Electronic structure and phonon thermodynamics of iron alloys

Thesis by

Jorge Alberto Muñoz Jr.

In Partial Fulfillment of the Requirements

for the Degree of

Doctor of Philosophy

California Institute of Technology

Pasadena, California

2013

(Defended May 20, 2013)

I would like to dedicate this work to my brother Miguel.

Gratias vobis ago

I believe that the most complex material on this planet is the humanity. It is organic and elastic, with the ability to grow when resources are available, or recede when this is not the case. It is quantized. A quantum of humanity is called a person, in the spirit of photons and phonons. The definition of personhood is thorny and controversial, but we shall not deal with this topic here. There is no conservation of persons, and for the most part they are distinguishable. This material seems to be amorphous, but persons tend to build hollow, three-dimensional objects sometimes for themselves or for other persons with the intent of performing a variety of activities inside these objects, so some degree of ordering is possible. In large metropolis, grain boundaries could be argued to exist. Persons affect each other, but the strength of these interactions is not very related to the Euclidian distance between them. The strength and number of bonds are different for each person, but each of these persons contribute to the properties of humanity.

The most intriguing attribute of this material is that abstract concepts arise from single persons or from permutations of persons. These are usually called ideas and are incredibly powerful, with the ability to modify the properties of the material. They are the dominant long-range forces. Art, mathematics, science, economics, government, law, religion, exploration, language, music, philosophy, freedom, etc. are instances of ideas, shaped by humanity and with the potential to shape humanity. Interactions between the environment, persons, and their creations are complex and rich, and I feel incredibly lucky that I can observe, usually understand, often benefit, and sometimes contribute to these human creations.

It is an honor to be able to work with my body: to displace it, to subject it to different stimuli, to interact with the world, to push it to the limit for the heck of it. I am extremely grateful because it allows me to hug the people I love. It is an honor to be able to work with my mind: to grasp concepts, to learn, to construct scientific models, to create and visualize figures and colors, to appreciate music, to understand and accept its own limitations and the limitations of my body. The plethora of feelings is occasionally overwhelming and frequently unpleasant, but I am grateful that I can explore them all. My brain keeps memories that are valuable, joyous, or painful. I am happy that I can retrieve them, create new ones, and that one day they will disappear. Thus, I acknowledge consciousness, even in light of its variability, vulnerability, and non-uniqueness.

After that lengthy rant, I will try to focus on my real acknowledgements.

In my first coordination shell is my advisor Brent Fultz. He has my gratitude for allowing me to join his group and I hope he believes it was a good decision. For me it was life-changing. He has my admiration for his scientific talent and intelligence, his scientific contributions, and the role that he is playing in organizing and pushing forward his field. He has my respect because his scientific standards are the highest and the publications out of his group are all outstanding. He has my friendship for giving me time, space, and much research independence; for helping me when I really needed his help; and most importantly, for having coffee with me once in a while. I hope one day I can reciprocate his kindness. Thank you, Brent!

The members of my thesis committee made my defense very interactive and very enjoyable. I thank Julia Greer, Bill Johnson, and Bill Goddard. It was a pleasure to discuss my research with them and I appreciate their insightful questions, their thoughtful opinions, and their time. Along with Brent, they made that day memorable. I thank Harry Atwater for his willingness to be in my thesis committee. He was in my candidacy one and he destroyed me. Later, I joined his soccer team.

Matt Lucas, Lisa Mauger and Mike Winterrose were my close collaborators and my friends during my time at Caltech, and I have the quixotic hope that we can keep working together in the future, as it was always a pleasure in spite of the crushing beamtimes that we shared. Of our perpetual friendship, I am sure. I have learned so much from them, and embraced so many of their great personal qualities and scientific approaches that now I am and alloy of mercury, although the composition is difficult to determine. Deep conversations about serious topics were almost as good as trike racing and goofy conversations about serious topics. Our quad at the APS guesthouse, late night escapades, and beamtime karaoke with upbeat 80's songs suddenly come to my mind. Thanks for sharing the good and the bad. There was plenty of both.

Olivier Delaire was my mentor during my SURFs at Caltech in the summer of 2005 and in the summer of 2006. His broad knowledge of the field and almost every other field inspired me. His work ethic and scientific insight have always impressed me. The well-planned and well-thought research projects that he devised for my summers, and his continuous help and genuine interest are the most important reasons why I could hang around Tech. I can identify these attributes in all his work. I will never be as good as him, but most of the time I try and that makes better. Merci bien!

Brent always maintains a group that is dynamic and intellectually stimulating. This environment allows his students have brilliant ideas and I am always impressed by the intellectual creativity and innovativeness of many of them. (Ambiguity in the previous sentence is casu consulto.) I have been lucky to forge strong friendships with many of its members and I have certainly learned a great deal from all of them. Hongjin Tan, Justin Purewal and I shared many lunches together. I value and miss those times. Chen Li was trapped with me in the same office for two years and during that time I stopped reading solid state, programming, and computer science books. I almost stopped reading

wikipedia. There was no need when I could just ask Chen. I obviously implored him to review parts of my thesis. If there is a mistake, he did not read that part, otherwise he would have roundhouse kicked them out as he did with many others. Max Kresch is incredibly smart, and I really enjoy his cynicism and humour noir. I appreciate the affability and spirited help that I always received from everybody in the group, specially: Sally Tracy, Jiao Lin, Nikolay Markovskiy, Tian Lan, Itzhak Halevy, Dennis Kim. Until I broke the ball mill, also from Channing Ahn. Doug Abernathy and Matt Stone were always friendly and their solicitude was instrumental for my work at Oak Ridge. For making samples and doing measurements in the Johnson Lab, I had the help and guidance of: Marios Demetriou, Dale Conner, Aaron Wiest, Mary Laura Lind.

It would be impossible to describe in how many ways my friends at Caltech have made my life more fun and more pleasant. It might even be counterproductive, so I will not try. I will only mention that they saved my ass from near-death events. Scott Roberts, Aron Varga, Misha Kislitsyn, Nick Stadie, Pratyush Tiwary, Steve Demers, David Abrecht, Alex Romero, Mariel Tourani, Maribel López, Raúl Hernández, Mike Vondrus, Chatr Panithipongwut. Thank you very much. Adriana Martel got me started in physics. Daniel Smith and Donald Walter got me started in research. Jim Barry never criticized my terrible drawings. Doris Xin exhumed me. Tomas Hernández, Julian Antolín and Emilio Enriquez have seen me shattered and crazy, and they were there for me. They have never crumbled, but when conditions were less than auspicious for them, I was not nearly as good of a friend. As kids, writing 'novels' with Iván Ruiz let our imaginations go wild. His new books are masterpieces and I hope he gets discovered. I thank my mentor Jorge López, who helped me tremendously and in many ways during my college years at UTEP, and afterwards has remained a close friend. I thank Tilmann Hickel for his interest in my work and for inviting me to the Ringberg workshop, the highlight of my graduate career. In a parallel universe, Tilmann and I are working together. Pauline Ku is my trip partner and she has shown me the way. We like to escape to classy places like Tijuana and the nude beach. Happiness and Silver Linings are our favorite movies.

The support of my family has been gargantuan and vital. An increase in the bond length only increased the bond stiffness, although the bond has always been infrangible. My infancy and upgrowth were filled with immense love, and for this I am the luckiest. Only now I am able to realize and start to comprehend the tremendous efforts and sacrifices that my parents have made and continue to make for me and for my brothers. Their hard work, humility, and integrity set the bar way too high. The suffering that they have endured for us is a testament of their love and fortitude. It has always been an uphill battle and the terrain is about to become steeper, but we are together, and we are a resilient bunch. For my brothers I would do anything, but I hope they stop testing me and start behaving soon. Many of my aunts, uncles, and cousins have always been there for me, and the López family adopted me when I moved to Los Angeles. Ana Laura made me dream and love, and I made her dream and love. I know she knows that my achievements are her

achievements and my multiple failures are my own.

I thank the Bill and Melinda Gates Foundation. It would have been much more challenging to go to college without the extremely generous support of the Gates Millennium Scholarship. They also paid for the bulk of my graduate education. They want me to pay it forward, and I will certainly try. I am sure the huge investment that Bill and Melinda Gates are making to improve the educational opportunities of underserved communities will pay off by improving an ever-growing number lives.

Now I will tell a few science-related childhood stories, which seems appropriate now. I am sorry for bringing up all of this stuff here, but it is the only section of my thesis that my family will read and I wanted to remind them of those idyllic times. It is also not unreasonable to think that I will be related by blood to most of the people who will look at my thesis at all, so I am just trying to please the crowd. The utmost patience of my parents and grandparents for my early measurements and experiments allowed to satisfy my scientific curiosity and might be responsible for my career path. I am glad my schooling was sooo bad that it never interfered with my education. My grandfather's collection of National Geographic, medicine books, and classics opened my mind. Pursuing my childhood scientific interests, I ruined many things, hurt myself, and made huge messes, so I apologize to the affected people. I could not even get the 'speed' of falling objects, but I did not learn about quadratic functions until later. I got the speed of sound surprisingly accurately from echoes, though. Mixtures of cleaning products did produce a substance capable of killing insects, but they also produced toxic fumes. After getting a Ph. D. in Materials Science, I finally know why I was able to melt sugar in the stove, but not salt. Without her knowledge, I discovered that my mom's back could absorb skin lotion, but not the bouillon cubes that I had sort of dissolved in it. Flies stop flying, but can survive in the fridge for quite a while; they die in the freezer. For a time, I was very interested in electricity. I wrecked a considerable number of Christmas lights investigating the properties of batteries in parallel and in series, but nobody noticed until the following Christmas, of course. I was very excited when I learned that I could produce electricity with wires and magnets, although the implementation of a plan to light up bicycles and carts did not have the intended consequences; it had other consequences. I calmed down a little when Santa Claus brought me a telescope, its utilization being a little more observational. My mom still has my pre-internet (sounds quaint) compilation of facts and pictures of planets and other celestial objects. There is a picture of Stephen Hawking in there, and it was surreal for me when I met him in person here at Caltech. She also has the collected drawings and observations I made of the fish in my aquarium, but my attempts to preserve the fish in alcohol were not successful. When my parents finally got me a computer (Pentium 90 overclocked to 125 MHz), my dad was freaked out by my largely innocuous Visual Basic viruses, although his worries always disappeared when he started playing Age of Empires. Really, it was a lot of fun. Thanks for the memories.

Hey! I belong among the wildflowers; I hope to see you all there.

Abstract

Vibrational entropy makes major contributions to the free energies of alloy phases and their relative thermodynamic stabilities, and significant nonharmonic behavior has been found in many systems. Here we study the order-disorder phase transition in FeV, the miscibility gap in the Fe-Au system, and the high temperature phonon behavior of FeTi. The experimental results are based on the combination of inelastic neutron scattering (INS) and nuclear-resonant inelastic x-ray scattering (NRIXS), which allows an accurate determination of the total phonon density of states (DOS) curves as well as element-specific partial phonon DOS curves. Computer simulations were used to relate the experimental observations to changes in the electronic structures of the systems.

INS and NRIXS were used to measure phonon spectra of FeV as a $B2$-ordered compound and as a bcc solid solution. Contrary to the behavior of ordering alloys studied to date, the phonons in the $B2$-ordered phase are softer than in the solid solution. Ordering increases the vibrational entropy, which stabilizes the ordered phase to higher temperatures. Ab initio calculations show that the number of electronic states at the Fermi level increases upon ordering, enhancing the screening between ions, and reducing the interatomic force constants. The effect of screening is larger at the V atomic sites than at the Fe atomic sites.

The phonon spectra of Au-rich alloys of fcc Au-Fe were also measured. The main effect on the vibrational entropy of alloying comes from a stiffening of the Au partial phonon DOS with Fe concentration that increases the miscibility gap temperature. The magnitude of the effect is non-linear and it is reduced at higher Fe concentrations. Force constants were calculated for several compositions and show a local stiffening of Au–Au bonds close to Fe atoms, but Au–Au bonds that are farther away do not show this effect. Phonon DOS curves calculated from the force constants reproduced the experimental trends. The Au–Fe bond is soft and favors ordering, but a charge transfer from the Fe to the Au atoms stiffens the Au–Au bonds enough to favor unmixing. The stiffening is attributed to two main effects comparable in magnitude: an increase in electron density in the free-electron-like states, and stronger *sd*-hybridization.

INS and NRIXS measurements were performed at elevated temperatures on $B2$-ordered FeTi and NRIXS measurements were performed at high pressures. The high-pressure behavior is quasi-harmonic. The softening of the phonon DOS curves with temperature is strongly nonharmonic.

Calculations of the force constants and Born-von Kármán fits to the experimental data show that the bonds between second nearest neighbors (2nn) are much stiffer than those between 1nn, but fits to the high temperature data show that the former softens at a faster rate with temperature. The Fe–Fe bond softens more than the Ti–Ti bond. The unusual stiffness of the 2nn bond is explained by the calculated charge distribution, which is highly aspherical and localized preferentially in the t_{2g} orbitals, along the direction of the 1nn. Ab initio molecular dynamics (AIMD) simulations show a charge transfer from the t_{2g} orbitals to the e_g orbitals at elevated temperatures. The asphericity decreases linearly with temperature and is more severe at the Fe sites.

Contents

List of Figures

List of Tables

Introductory remarks

Context of the present work and prospects for future research

Alloy Thermodynamics

In thermodynamic equilibrium, the type and proportion of the elemental components of a system determine its phase and many of its properties. The stable phase is the one that minimizes the free energy

$$F = U - TS\,, \tag{1}$$

where U is the internal energy, T is the temperature, and S is the entropy. Other contributions to F include pressure, mechanical stress, and magnetism [1]. It is in principle straightforward to calculate the free energy, and a comparison with the values obtained for other phases could provide important information on the stability of the material under different experimental or operational conditions. Nevertheless, many of the contributions to F are not easy to measure or calculate. Some even lack a truly fundamental understanding. This is particularly true for $S = k_\mathrm{B} \ln \Omega$, where k_B is the Boltzmann constant and Ω is the number of ways in which a system may be arranged. The entropic contribution from lattice vibrations S_vib is the main quantity of interest of this thesis, and how it is affected by changes in the electronic structure of the material is the main subject.

The difference in F between phases is what determines which one is stable, and in many cases the assumption that the difference in S_vib is negligible has been made. The rationale is that harmonic oscillations of the atoms around their equilibrium position are not significantly affected by small changes in the bond length, or are affected in a predictable (quasiharmonic) way. This is of course not completely correct, and Fultz and collaborators showed that changes in S_vib upon ordering in systems with ordering tendencies can be comparable to the change in configurational entropy of the system S_conf, which depends on the number of possible atomic configurations [2]. Subsequent work, such as that in Ref. [3], has shown that electron-phonon interactions can explain the nonharmonic temperature behavior of several systems, and the results presented in this thesis builds on this insight.

The work in this thesis advances the field of thermodynamics of materials in a number of ways.

Here are the ones I consider most important:

- Investigating FeV as a model system for order-disorder phase transitions, we provided solid evidence that electron-phonon interactions will, in general, affect the thermodynamics of metals with a significant number of *d*-electrons at the Fermi level, and nonharmonic behavior can be expected when this number changes with temperature, composition, chemical order, etc., This is most likely when the Fermi level is at or close to an abrupt feature in the electronic density of states (DOS). To our surprise, owing to these electron-phonon interactions in FeV, S_{vib} can stabilize the ordered phase. We showed that the change in the total number of electrons at the Fermi level $\mathcal{N}_F$ is a good predictor of the total effect on the phonons in the case of systems with isotropic Fermi surfaces.

- It is shown that *sd*-hybridization can have thermodynamic effects in ways previously unknown. In Au-rich Fe-Au, the addition of Fe results in a stiffening of the Au-Au bonds of the Au atoms around the Fe atom, even though the Fe-Au bond is soft. The net effect is a decrease in the vibrational entropy that increases the miscibility gap temperature. This is a highly local effect and other Au atoms are not affected.

- The symmetry conditions of bcc-based structures that confine the *d*-electrons to e_g orbitals in the direction of the second-nearest-neighbors (nn) might result in charge transfer between the t_{2g} and e_g orbitals due to atomic motions, as is the case for $B2$ FeTi. Changes in $\mathcal{N}_F$ are different for t_{2g} and e_g states.

Methodology

The field of thermodynamics has benefited greatly from recent developments in experimental techniques, instruments, and sample environments that enable detailed and systematic studies of phonons in an ever-growing number of systems, and can provide detailed information on many of their trends. The experimental work presented in this thesis is based on the synergistic combination of inelastic neutron scattering (INS) and nuclear-resonant inelastic x-ray scattering (NRIXS). These are currently the state of the art techniques to measure phonon spectra. For binary alloys, this combination allows an accurate determination of the total phonon DOS curves as well as element-specific partial phonon DOS curves. This detailed information is helpful in assessing the relative contributions of the different components of the system to the vibrational entropy, but also improves the accuracy and quality of the computational results by providing additional benchmarks.

The research also benefits from the computational study of the properties of the individual components as well as their interactions. Significant nonharmonic behavior has been found in many cases, but it is difficult to discern the underlying causes by experiment alone. With robust and fast

algorithms and the advent of high performance computing, ab initio simulations can be useful to identify the cause of nonharmonicity and explain the behavior.

It is not feasible to study experimentally the near-infinite number of possible materials, but the hope is that computer simulations will eventually become powerful enough to predict the stability and properties of many of them in a much more cost-efficient way. It would then be possible to sort out promising materials for applications, and eventually, to design materials computationally from first principles. This is a challenging and ambitious task and current technology is not yet able to simulate all types of materials, but the accelerated growth of computing power and decreasing cost might make it possible [4]. Large efforts are already underway in both the public and private sectors, with the goal of cutting the time it takes to manufacture and deploy a new material from its discovery and development, currently about 10-20 years [5].

Several approaches are being developed for the prediction of stable structures that show great potential. A small number of calculations and the use of the cluster expansion technique can be used to explore free energy landscapes if these are relatively simple [6], but knowledge of the underlying crystal structure is needed. A more robust approach is that of simulated annealing which consists of perturbing a starting configuration and observing the change in energy to find a global minimum [7]. A genetic algorithm can be used for the same purpose if a penalty function is defined [8], and might be faster. A high-throughput approach combines ab initio calculations with data mining using supercomputer architectures [9]. Some applications of these approaches can be found in Ref. [10]. An accurate estimation (calculated or measured) of the vibrational and other entropic contributions is imperative to achieve these goals, although this is still emerging. The present work shows how computer simulations can be used to identify materials that are not accurately described by the quasiharmonic model.

Near-term possibilities

Calphad is a mature numerical technique for the construction of phase diagrams [11]. It is based on the parameterization of the free energy curves for each phase, calculated by fits to experimental data, and can predict metastable phases and produce phase diagrams for parameter-space regions for which no data is available. It has been successful in predicting phases for multicomponent systems, which are challenging with the approaches described above. The databases distributed with some commercial implementations of the code, such as Thermo-Calc [12], are very comprehensive, making the technique highly flexible, and facilitates its application for a large number of system. The future for Calphad includes the construction of first principles databases that can be used like the experimental ones. The research presented here is relevant because electron-phonon interactions, charge transfer, and *sd*-hybridization are factors that affect the vibrational entropy and the heat capacity, one of the key quantities used in Calphad calculations. Understanding the coupling between

phenomena such as ordering and magnetism is important to sort out as it complicates extracting information from lambda transitions, for example [13].

Some extensions of the research presented here are straightforward, although they could be labor intensive. For example, it would be extremely useful for applications to find a proportionality constant between the change in $\mathcal{N}_\mathrm{F}$ and the change in the average phonon energy, but more experimental and computational data are necessary. It depends on the crystal structure and other factors, but rules of thumb would still be helpful. The thermodynamic effects of the anisotropic electron phonon-interaction have not been studied in detail, but many technologically relevant or promising materials are anisotropic, such as graphene. The electronic DOS and lattice dynamics of Cr are very similar to FeTi, although they are richer because of its magnetic properties. Other materials in which the electron-phonon interaction is thermodynamically important include thermoelectric [14] and superconducting [15] materials.

An emerging field is that of high entropy alloys. While most of the entropy differences are configurational in entropy, vibrational entropy could become important when approximately six or more components are present [16], and some measurements of phonon spectra have already been done [17]. An explanation at the bond level such as that attempted in Chapter 5 can clarify, explain, and maybe predict electronic structures that are otherwise quite difficult to calculate from first principles. A similar case can be made about bulk metallic glasses.

Several research directions are more challenging and risky, since they might end with null results, but are interesting and potentially useful for applications. For example, very little is known about the vibrational entropy of systems under stress, generally an anisotropic quantity. Experimental measurements of the phonon DOS are not sensitive enough to detect these small variations, but they could be important for the stability or, more likely, for the growth of epitaxial structures or devices. S_vib could stabilize these structures, so devices not predicted by standard calculations could still exist; with knowledge of the effects, it might be possible to design novel structures. The recent development of a tensorial cluster expansion method [18] can be of great aid for calculations in these systems. The effects on the kinetics of *sd*-hybridization have not been measured, but the Fe-Au and similar systems might be ideal to check this. Since ^{57}Fe is a Mössbauer isotope, a Mössbauer spectra can be obtained by Nuclear Forward Scattering, and a diffusion coefficient at a given temperature and composition can be obtained from the broadening of the spectra. These values can be compared to the values obtained from more traditional methods, which usually are usually independent of composition, such as by tracking the diffusion of ^{59}Fe in Au. Variations between the two will probably be because of electronic effects. Although it would be very computation-intensive, a code like SISYPHUS [19] could be used to study this phenomenon and produce a stochastic phase diagram.

Intent and organization of this thesis

The theoretical framework presented in Chapter 1 is intended to be compact, to start from almost axiomatic definitions, and to discuss the essential aspects necessary to make this thesis reasonably self-contained. I sought a consistent and balanced chapter and section structure, trying to emphasize the connectedness, commonality, recycling, and logical flow of many of the concepts, both in the background and in the results chapters. I tried to motivate on a physical basis new concepts being introduced, and when necessary, physical clarity and intuition were chosen over mathematical rigor. Nevertheless, an extensive number of references is given where more formal approaches are presented. The large number of references throughout the text is intended to let the interested reader find original sources and be able to reconstruct the arguments, or disagree with them. As much as possible, seminal articles are cited and the names of the authors are given in the main text. These articles are usually accompanied by references to more recent work. The principles of scattering theory, and then more details on practical experimental measurements, and data reduction are given in Chapter 2. Each subsequent chapter treats a different Fe-containing system in which different phenomena was investigated: the ordering FeV system, the segregating Fe-Au system, and intermetallic FeTi. The chapters follow a common general format though, and I hope that this can facilitate comparisons between them.

In Chapter 3 I show results on the FeV ordering system. I describe a decrease in the phonon energies observed upon ordering that results in a higher S_{vib} in the ordered phase than in the disordered one. This had not been observed before in ordering systems with the same underlying lattice, and cannot be explained by the most common model. We attribute this to an increase in $\mathcal{N}_{\mathrm{F}}$ upon ordering that enhances the electronic screening of atom vibrations and stabilizes the ordered phase by more than 350 K. Anomalous softening and stiffening with temperature in other metallic systems with d-electrons are correlated to $\mathcal{N}_{\mathrm{F}}$ as well [3, 20, 21], as is the composition dependence of the phonon frequencies [22]. The present work also uncovered correlations between $\mathcal{N}_{\mathrm{F}}$ at specific atomic sites in FeV and the motions of the corresponding atoms, which are the first observations of this kind. Calculations of the generalized susceptibility of the ordered and disordered systems show that it is isotropic and has the same shape for both phases, but differs by a constant factor, simply the ratio of $\mathcal{N}_{\mathrm{F}}$ in the ordered and disordered phases. This shows that for at least this cubic, isotropic system, $\mathcal{N}_{\mathrm{F}}$ is directly related to the capacity for electronic screening of atomic motions. The combination of these results provides strong evidence that the correlation between changes in $\mathcal{N}_{\mathrm{F}}$ and nonharmonic changes in the phonon frequencies are quite general for metals with d-electrons. The transverse modes are affected more by ordering than the longitudinal ones, so the shear modulus decreases upon ordering. This behavior is probably a good indicator that electron-phonon effects stabilize the ordered phase in an order-disorder system, since the shear modulus is related to a Fermi

surface nesting effect in bcc metals [23].

Chapter 4 unveils that hybridization between s and d electrons can have thermodynamically important consequences and that vibrational entropy in noble metals can partially be explained with a free-electron gas model. In Au-rich Fe-Au, a segregating system, the excess vibrational entropy of mixing is negative for Au motions, and its magnitude increases up to a composition of about 20 at. % Fe. It is positive for Fe motions in that composition range and approximately constant, resulting in an overall negative quantity. This suggests that while Au-Fe bonds are soft, the Au-Au bonds become stiffer in the presence of Fe atoms. This is not an electron-phonon interaction effect since $\mathcal{N}_\mathrm{F}$ does not change much with increasing Fe content and most of the electrons at the Fermi level are s-electrons. Instead, ab initio calculations and the Wills-Harrison model [24] predict that a charge transfer from the Fe atoms to the Au atoms stiffens the Au-Au bonds of the Au atoms surrounding the Fe atom. In this case, the Au atoms are reacting similarly to a free-electron gas, and it accounts for about half of the observed magnitude of the excess vibrational entropy of mixing. The sd-hybridization is responsible for the difference in the measured bulk modulus of Au and that predicted by the free-electron gas model, so we attribute the remainder of the excess vibrational of mixing to it. The effect is quite local and Au atoms that are farther away from the Fe atom are not affected, but it is large enough to increase the miscibility gap temperature by up to 550 K, although this value depends on composition.

Chapter 5 presents experiments and calculations on $B2$ FeTi. The most interesting characteristic is that the Fermi level lies at the bottom of a pseudo-gap in the electronic structure, so the bonding and antibonding states are well separated. Most of the bonding states are in the t_{2g} orbitals, while most of the antibonding states are in the e_g orbitals. The t_{2g} state is a triplet and the e_g state is a doublet, so if they are filled in this proportion, the charge distribution is nearly spherical. In FeTi, the asphericity, defined by the ratio between the charge in the t_{2g} orbitals to that in the e_g orbitals, is the largest that has been reported for any material, and it is larger at the Fe sites than at the Ti sites. The 2nn longitudinal force constants in FeTi are stiffer than those of the 1nn, which is a peculiar behavior that we attribute to the charge distribution. The lobes of the e_g orbitals point in the direction of 2nn, while the t_{2g} ones tend to fill the rest of the space in the sphere. The de facto depletion of the e_g orbitals results in stiff 2nn force constants. At high temperatures, our measurements show that the 2nn longitudinal force constants decrease, while the 1nn remain almost unchanged. When temperature is increased and the atomic displacements become more pronounced, some electronic charge is transferred to the e_g orbitals to minimize the energy. This is the first system for which such behavior has been predicted. The thermal broadening of the electronic DOS results in the gradual filling of the pseudo-gap. This increases $\mathcal{N}_\mathrm{F}$, and the increase occurs mostly at the Fe sites and comes mostly from t_{2g} states. Although more calculations are needed to prove it, this phenomenon is probably common in bcc-based metals at high temperatures.

Chapter 1

Theoretical framework and computational tools

1.1 Lattice dynamics

1.1.1 Direct and reciprocal lattices

An ideal crystal lattice with long-range order periodicity is constructed by repetition of a unit cell defined by three non-coplanar lattice vectors $\mathbf{a_1}$, $\mathbf{a_2}$, and $\mathbf{a_3}$. A primitive unit cell in this context is the smallest cell that can generate the crystal. Labeling each unit cell by a triplet of integers l_1, l_2, and l_3, the equilibrium position of the origin of the unit cell l is

$$\mathbf{x}_l = l_1\mathbf{a_1} + l_2\mathbf{a_2} + l_3\mathbf{a_3} \ . \tag{1.1}$$

The lattice generated by Eq. 1.1 is the direct lattice $\mathbf{X}$, which is a Bravais lattice. The different types of atoms in the unit cell are denoted by κ, and their respective masses are M_κ. The atomic equilibrium positions with respect to the origin of a unit cell are described by the basis vectors $\mathbf{x}_\kappa$ for $\kappa = 1, 2, \ldots, N$, so the equilibrium position of an atom κ in cell l is

$$\mathbf{x}_{l\kappa} = \mathbf{x}_l + \mathbf{x}_\kappa \ . \tag{1.2}$$

It is possible to generate a Bravais lattice identical to that of Eq. 1.1 for each possible $\mathbf{x}_\kappa$, but displaced from the original by $\mathbf{x}_\kappa$. Each of these will be referred to as a sublattice. If there are N atoms in the unit cell, the crystal will consists of N interpenetrating lattices, each of which is a Bravais lattice. Atoms in a particular sublattice must be of the same type, but those on different sublattices need not.

Since $\mathbf{X}$ has a defined periodicity, there exist a set of plane waves $\mathbf{K}$, with the same periodicity.

In this case,

$$\exp(\imath \mathbf{K} \cdot \mathbf{R}) = 1 \ . \tag{1.3}$$

$\mathbf{K}$ is known as the reciprocal lattice of $\mathbf{X}$. It is generated by

$$\mathbf{G}_h = h_1 \mathbf{b_1} + h_2 \mathbf{b_2} + h_3 \mathbf{b_3} \ , \tag{1.4}$$

with reciprocal lattice vectors $\mathbf{b_1}$, $\mathbf{b_2}$, and $\mathbf{b_3}$, and the triplet of integers h_1, h_2, and h_3. For cubic crystals, the directions of the reciprocal lattice vectors correspond to the normals to the direct lattice planes. Their magnitudes are given in 'reciprocal length' and are equal to the reciprocal of the interplanar spacing of the direct lattice planes. Thus,

$$\mathbf{G}_h \cdot \mathbf{x}_l = 2\pi n \ , \tag{1.5}$$

where n is an integer. The reciprocal lattice generated by $\mathbf{G}_h$ is commonly called reciprocal space, k-space, etc.

1.1.2 Born-von Kármán model and related concepts

The model of lattice dynamics presented by Born and von Kármán [25] in 1912 is one of the cornerstones of solid state physics. It is a mechanical approach to the problem of lattice stability and it provides a powerful machinery to study lattice vibrations. The primary aspects are presented below. Excellent reviews can be found in Refs. [26–28].

Assume there are displacements of the atom $l\kappa$ around its equilibrium position at time t, for example, due to thermal fluctuations. These are described by the displacement vector $\mathbf{u}_{l\kappa}(t)$. The position of an atom at any t is

$$\mathbf{r}_{l\kappa}(t) = \mathbf{x}_{l\kappa} + \mathbf{u}_{l\kappa}(t) \ . \tag{1.6}$$

The potential energy U of the crystal at any t is a function of the instantaneous positions of the atoms in the system. Expanding it in a Taylor series of the atomic displacements in the Cartesian coordinates $\alpha = x, y, z$ yields

$$U = U_0 + \sum_{l\,\kappa} \sum_{\alpha} \phi_{l\kappa,\alpha}\, \mathrm{u}_{l\kappa,\alpha} + \frac{1}{2} \sum_{l\,\kappa} \sum_{l'\kappa'} \sum_{\alpha} \sum_{\alpha'} \phi_{l\kappa,l'\kappa',\alpha\alpha'}\, \mathrm{u}_{l\kappa,\alpha}\, \mathrm{u}_{l'\kappa',\alpha'} + \ldots , \tag{1.7}$$

Many of the displacements will be equivalent because of crystal symmetries. In Eq. 1.7, the coefficients of the Taylor series are the derivatives of U with respect to the displacements, so

$$\phi_{l\kappa,\alpha} = \frac{\partial U}{\partial \mathrm{u}_{l\kappa,\alpha}}\Big|_0 \tag{1.8}$$

and

$$\phi_{l\kappa,l\prime\kappa\prime,\alpha\alpha\prime} = \frac{\partial^2 U}{\partial \mathrm{u}_{l\kappa,\alpha}\partial \mathrm{u}_{l\prime\kappa\prime,\alpha\prime}}\Big|_0 \ . \tag{1.9}$$

The derivatives are evaluated at the equilibrium position, where all the displacements are equal to zero, so derivative in Eq. 1.8 is zero since particles feel no force in the equilibrium configuration. The derivative in Eq. 1.9 can be expressed in matrix form as

$$\Phi_{l\kappa,\,l\prime\kappa\prime} = \begin{bmatrix} \phi_{xx} & \phi_{xy} & \phi_{zz} \\ \phi_{yx} & \phi_{yy} & \phi_{yz} \\ \phi_{zx} & \phi_{zy} & \phi_{zz} \end{bmatrix},$$

the interatomic force constant matrix between the pair of atoms $l\kappa$ and $l\prime\kappa\prime$. The elements of $\Phi_{l\kappa,\,l\prime\kappa\prime}$ are also specific to $l\kappa$, $l\prime\kappa\prime$, but this was omitted for notational clarity. The physical meaning is transparent here: κ and $\kappa\prime$ will be specific types of atom, for example, Fe and Au, and the relative distance between cells l and $l\prime$ can be given in terms their relative nearest neighbor distance. If $l\kappa = l\prime\kappa\prime$, Φ is the 'self-force' constant matrix, which is the negative of the sum of all the other force constants. This sum rule ensures that there is no net force on the crystal causing an acceleration.

The interatomic force constants can be used to derive the equations of motion for all the atoms in the crystal

$$M_\kappa \ddot{\mathbf{u}}_{l\kappa} = -\sum_{l\prime\kappa\prime} \Phi_{l\kappa,l\prime\kappa\prime}\mathbf{u}_{l\prime,\kappa\prime} \ . \tag{1.10}$$

With periodic boundary conditions, the solution of Eq. 1.10 can be found in the form of plane waves (see, for example, Ref. [27]),

$$\mathbf{u}_{l\kappa} = \frac{1}{\sqrt{M_\kappa}}\mathbf{e}_{j\kappa}(\mathbf{q})\exp(\imath[\mathbf{q}\cdot\mathbf{x}_l - \omega_j(\mathbf{q})t]) \ , \tag{1.11}$$

with wave vector $\mathbf{q}$, angular frequency $\omega_j(\mathbf{q})$, and polarization $\mathbf{e}_{j\kappa}(\mathbf{q})$, where j is the branch index. The substitution of the propagating-wave displacements into the equations of motion is equivalent to taking a space Fourier transform on the right hand side these equations. The problem is thus reduced to solving the following equation:

$$\omega_j^2(\mathbf{q})\,\mathbf{e}_{j\kappa}(\mathbf{q}) = \sum_{\kappa\prime} \mathbf{D}_{\kappa\kappa\prime}(\mathbf{q})\,\mathbf{e}_{j\kappa\prime}(\mathbf{q}). \tag{1.12}$$

The corresponding eigenvectors will be the polarization vectors of the lattice vibrations $\mathbf{e}_{j\kappa}(\mathbf{q})$, which can be calculated for all the atoms κ in the basis, and their associated angular frequencies $\omega_j(\mathbf{q})$ can be calculated by diagonalizing the matrix $\mathbf{D}_{\kappa\kappa\prime}(\mathbf{q})$.

If there are N atoms in the basis κ, then $\mathbf{D}(\mathbf{q})$ will be a $3N \times 3N$ matrix constructed from the 3×3 submatrices $\mathbf{D}_{\kappa\kappa\prime}(\mathbf{q})$, which are the Fourier transforms of $\Phi_{l\kappa,\,l\prime\kappa\prime}$. The $3N$ eigenvectors and

eigenvalues of the dynamical matrix evaluated at a particular wave vector $\mathbf{q}$ corresponds to the $3N$ eigenmodes of the vibration of the crystal for that wave vector. $\omega_j(\mathbf{q})$ is called the dispersion of branch j. Each value of $\mathbf{q}$ represents a particular mode. $\mathbf{D}(\mathbf{q})$ is known as the dynamical matrix, it is Hermitian for any value of $\mathbf{q}$ [28], so its eigenvalues $\omega_j^2(\mathbf{q})$ are real and $\omega_j(\mathbf{q})$ is either real or purely imaginary. The system is not mechanically stable when $\omega_j(\mathbf{q})$ is imaginary.

Only particular values of $\mathbf{q}$ are allowed, those that can be sustained by the lattice, but periodic conditions are required to define these values in an infinite crystal. These are usually termed the Born-von Kármán boundary conditions [25]. They are applied by dividing the infinite crystal into an infinite number of finite cells, each containing a very large number N of primitive cells. For simplicity, consider that each finite cell is cubic and has dimensions $L\mathbf{a_1}, L\mathbf{a_2}, L\mathbf{a_3}$, so $N = L^3$. The condition is

$$\mathbf{u}_{l\kappa} = \mathbf{u}_{l\prime\kappa\prime} \tag{1.13}$$

with $l = l_1, l_2, l_3$ and $l\prime = l_1\prime + L_1, l_2\prime + L, l_3\prime + L$. This means that displacements of equivalent atoms in different finite cells are identical, but can differ by a phase factor. This supposition is adopted for mathematical convenience and it is not valid in all cases [29], but it is inherent in modern materials research. The lattice can sustain the waves given by Eq. 1.11, so

$$\mathbf{q} = \eta_1\mathbf{b_1} + \eta_2\mathbf{b_2} + \eta_3\mathbf{b_3} \ , \tag{1.14}$$

where $\eta_i = n_i/L$ for $i = 1, 2, 3$ and n_i is an integer. The density of q-points will be $N\upsilon/8\pi^3$, where $\upsilon = |\mathbf{a_1} \cdot (\mathbf{a_2} \times \mathbf{a_3})|$, the volume of the direct lattice primitive cell. This is an important quantity for calculations, as it determines the resolution of the results, such as dispersions and electronic band structures. The same methodology applies in the context of electronic structure calculations, most of which are performed in reciprocal space as discussed in section 1.2.4, but in this context $\mathbf{q}$ is changed to $\mathbf{k}$ and the q-points become k-points.

Another important and useful property of the reciprocal space representation is that not all the $\mathbf{q}$ values in Eq. 1.14 are physically distinct. Consider the plane wave of Eq. 1.11 at a given t. If a reciprocal lattice vector $\mathbf{G}_h$ is added to $\mathbf{q}$ and we denote this by $\mathbf{u}\prime_{l\kappa}$, the following ensues:

$$\begin{aligned}
\sqrt{M_\kappa}\,\mathbf{u}\prime_{l\kappa} &= \mathbf{e}_{j\kappa}(\mathbf{q})\exp(\imath[\mathbf{q} + \mathbf{G_h} \cdot \mathbf{x}_l]) \\
&= \mathbf{e}_{j\kappa}(\mathbf{q})\exp(\imath\mathbf{q} \cdot \mathbf{x_l})\exp(\imath\mathbf{G}_h \cdot \mathbf{x}_l) \\
&= \mathbf{e}_{j\kappa}(\mathbf{q})\exp(\imath\mathbf{q} \cdot \mathbf{x_l})\exp(\imath 2\pi n) \\
&= \sqrt{M_\kappa}\,\mathbf{u}_{l\kappa} \ .
\end{aligned} \tag{1.15}$$

This does not mean that plane wave can change its wave vector by $\mathbf{G}$, it just means that it can be represented again a distance $\mathbf{G}$ away in the reciprocal lattice. All the distinct values of $\mathbf{q}$ are obtained

by restricting them to just one primitive cell of the reciprocal lattice, called the Brillouin zone. The concept was developed by Brillouin [30], and it is ideal for computational implementations.

1.1.3 Phonon thermodynamics

The leading term in the expansion of the potential energy of the atoms in a crystal vibrating around their equilibrium positions in Eq. 1.7 describe a classical three-dimensional simple harmonic oscillator (SHO). The term U_0 is the binding energy of the system, so the partition function of the crystal with N atoms and $3N$ oscillators is [31]

$$\mathcal{Z}_N^{\mathrm{SHO}} = A^N \left(k_{\mathrm{B}}T\right)^{3N} \exp\left(-\frac{NU_0}{k_{\mathrm{B}}T}\right) \ , \tag{1.16}$$

where A is a constant and T is the temperature. k_{B} is the Boltzmann constant. The free energy $F = E + PV - TS = E + PV - k_{\mathrm{B}}T \ln \mathcal{Z}$, where E is the energy, P is the pressure, V is the volume, and S is the entropy. The entropy is obtained by differentiating F with respect to T. For the SHO, the constant-volume heat capacity is

$$C_V^{\mathrm{SHO}} = T\frac{\partial S}{\partial T}\Big|_V = 3Nk_{\mathrm{B}} \ . \tag{1.17}$$

This is the well-known Dulong and Petit limit [32], the value of the heat capacity of many solids at temperatures higher than about room temperature. Nevertheless, in real solids C_V goes to zero as the temperature decreases to 0 K. Attempting to solve this problem lead to the discovery that the energies of lattice vibrations are quantized.

The assumption that atoms are joined to each other in a crystal by massless springs and they move harmonically around their equilibrium position is not unreasonable, but it is not complete. Einstein proposed in 1907 [33] that the energy associated with a harmonic vibration is quantized. In a quantum harmonic oscillator (QHO) of frequency ω, the possible energies are given by $E_n = (n + \frac{1}{2})\hbar\omega$ [34], where n is the energy level. The partition function for a single oscillator of frequency ω_i is

$$\mathcal{Z}_1^{\mathrm{QHO}} = \frac{\exp\left(-\hbar\omega_i/2k_{\mathrm{B}}T\right)}{1 - \exp\left(-\hbar\omega_i/k_{\mathrm{B}}T\right)} \tag{1.18}$$

and the partition function for N atoms and $3N$ independent oscillators is

$$\mathcal{Z}_N^{\mathrm{QHO}} = \prod_i^{3N} \frac{\exp\left(-\hbar\omega_i/2k_{\mathrm{B}}T\right)}{1 - \exp\left(-\hbar\omega_i/k_{\mathrm{B}}T\right)} \ . \tag{1.19}$$

Following the thermodynamic relationships mentioned above,

$$S_{\text{vib}} = k_{\text{B}} \sum_{i}^{3N} \left[-\ln\left(1 - \frac{1}{\exp(\hbar\omega_i/k_{\text{B}}T)}\right) + \frac{\hbar\omega_i/k_{\text{B}}T}{\exp(\hbar\omega_i/k_{\text{B}}T) - 1} \right] \tag{1.20}$$

where the subscript 'vib' is to emphasize that this entropy is purely from the oscillators. Other sources of entropy are due to, e.g., the configuration of atoms of different species in a crystal S_{conf}, magnetism S_{magn}.

In the Einstein model, $\omega_i = \omega_E$ for all i, so the heat capacity is given by

$$C_V^{\text{Ein}} = 3Nk_{\text{B}} \left(\frac{\hbar\omega_E}{k_{\text{B}}T}\right)^2 \frac{\exp(\hbar\omega_E/k_{\text{B}}T)}{\left[\exp\left(\hbar\omega_E/k_{\text{B}}T\right) - 1\right]^2} \ , \tag{1.21}$$

where ω_E is a characteristic frequency that depends on the material. This result is used here to justify two properties of lattice vibrations. First, assuming a quantized harmonic oscillator reproduces qualitatively the heat capacity behavior of solids. This suggest that the energies of lattice vibrations are quantized. A quantum of vibrational energy is called a phonon. Second, the number of low-lying states that can be excited thermally decreases to zero as the temperature goes to zero. This suggests that phonons are bosons. Perhaps the strongest experimental evidence of these two points is the inelastic scattering of x-rays or neutrons by crystals. The energy and momentum changes correspond to the creation or annihilation of phonons (see, for example, Ref. [35]). By measuring the recoil of the scattered x-ray or neutron, the properties of phonons in materials can be investigated. Refs. [36] and [37] provide a formal quantum treatment of lattice vibrations.

Phonons are bosons, so they follow Bose-Einstein statistics. They are not conserved, so their chemical potential is zero and their occupation is described by the Planck distribution

$$\text{n}_T(E) = \frac{1}{\exp(E/k_{\text{B}}T) - 1} \ , \tag{1.22}$$

where $E = \hbar\omega$. Eq. 1.20 can then be reduced to

$$S_{\text{vib}} = Nk_{\text{B}} \left[(1 + \text{n}_T)\ln(\text{n}_T) - \text{n}_T \ln(\text{n}_T)\right] \ . \tag{1.23}$$

Assuming that the energies of the phonons follow a distribution $g(E)$ (defined in Eq. 1.50), and this distribution is normalized to 1, the phonon entropy of a harmonic material at any T is [38]

$$S_{\text{vib}}(T) = 3k_{\text{B}} \int_0^\infty g(E) \left[(1 + \text{n}_T(E))\ln(\text{n}_T(E)) - \text{n}_T(E)\ln(\text{n}_T(E))\right] dE \ . \tag{1.24}$$

$g(E)$, referred to as the phonon density of states (DOS), and S_{vib} are central quantities of the work presented in this thesis. The phonon DOS curves can be measured by inelastic neutron scattering or

obtained from experimental or calculated phonon dispersions, as described in section 1.2.5. In the following chapters, we show that S_{vib} has important implications in the phase stability of materials, and we study electronic effects that can affect the behavior of $g(E)$.

1.1.4 Quasiharmonic model and nonharmonic effects in crystals

The Einstein model is a mean field theory; its parameters do not depend on the spacing between atoms, which results in unphysical behavior. For example, if F does not depend on the volume V, the equilibrium pressure P is zero and the bulk modulus B is also zero, since

$$P = -\left(\frac{\partial F}{\partial V}\right)\Big|_{T,N} \tag{1.25}$$

and

$$B = -V\frac{\partial P}{\partial V}\Big|_{T,N} \ . \tag{1.26}$$

A realistic model would require the potential energy of an atom to depend on the distance to its neighbors, so the atomic motions must be cooperative, an effective phonon-phonon interaction. Other properties of solids such as thermal expansion, finite thermal conductivity and the increase of the specific heat beyond the classical limit at high temperatures are also due to these anharmonic terms (see, for example, Ref. [39]).

In the quasiharmonic model, the volume dependence is introduced explicitly by essentially varying the interatomic distance in a Lennard-Jones [40] or similar potential. The result is a wider potential that in the harmonic approximation is equivalent to softer force constants and softer phonons. This behavior is indeed observed in most solids. The change in frequency of all the phonons is proportional to the change in volume with increasing temperature, so

$$\frac{\Delta\omega}{\omega} = -\gamma\frac{\Delta V}{V} \ , \tag{1.27}$$

where γ is known as the Grüneisen parameter [41]. For most materials, its value is around 2. Another useful definition is the mode Grüneisen parameter γ_i, which considers differential changes in the frequency of different modes ω_i with volume. Nevertheless, there is a vast amount of work on the definition and the nature of Grüneisen parameters (see, for example, Refs. [26, 39, 42]), and it is used extensively in materials research. The anharmonic model is used in the work presented here to identify anharmonic or otherwise anomalous behavior and to assess its magnitude.

More realistic results can be obtained if more terms in the series expansion of Eq. 1.7 are included in the calculations, but this makes the problem considerably more difficult for computation due to the large size of the tensors. Several approaches have been taken. For example, the effects (but not the tensors) of anharmonic terms can be calculated by perturbation theory if the anharmonicity

is small [43]. In another case, the force constants were fitted to experimental third order elastic constants [44]. A recent study calculated directly from first principles the third order anharmonicity tensor [45], noting that in a single element 256-atom fcc supercell there are 55 independent harmonic force constants and 6205 independent third order anharmonic force constants. Recently, the negative thermal expansion of ScF_3 was attributed to quartic anharmonicity [46].

Electron-phonon interactions can also affect the interatomic force constants of metals, for example, by modifying the screening abilities of electrons, which depend mostly on the shape of the Fermi surface. A well-known phenomenon is when two sheets in the Fermi surface are parallel, separated by the wave vector $\mathbf{k}$, make a phonon with the same wave vector become 'soft.' The screening is particularly effective on the phonon, so it reduces its energy. This is usually called a Kohn anomaly [47], and many cases have been reported in different materials, the one in graphite being a recent one [48]. Other effects are discussed in detail in section 3.6.2. For solid treatments of the electron-phonon interaction, see Refs. [49] and [50]. Ref. [51] includes a section on thermodynamic effects of the electron-phonon interaction.

1.2 Density functional theory

1.2.1 Essential aspects

The development of density functional theory (DFT) is one the most important breakthroughs in the physical sciences in the last 50 years and its application to study a large number of aspects of real materials has seen an explosive growth. It is a parameterless method, so its results are considered fundamental (ab initio) in a physical sense. Currently, a considerable percentage of all the works published in scientific journals include DFT results, sometimes centrally and some other times peripherally, supporting experimental results, for example. The literature on the principles and applications of DFT is vast (Ref. [52] is a particularly good exposition) so here we present only a succinct description.

Materials are made of nuclei and electrons, which interact with one another. These interactions are responsible for the diversity of properties of materials and phenomena occurring in them. The Hamiltonian for such a system is

$$\hat{\mathcal{H}} = -\frac{\hbar^2}{2M_e}\sum_i \nabla_i^2 + \sum_{I,\,i}\frac{e^2 Z_I}{|\mathbf{r_i}-\mathbf{R_I}|} + \frac{e^2}{2}\sum_{i\neq j}\frac{1}{|\mathbf{r_i}-\mathbf{r_j}|} - \frac{\hbar^2}{2}\sum_I \frac{\nabla_I^2}{M_I} + \frac{e^2}{2}\sum_{I\neq J}\frac{Z_I Z_J}{|\mathbf{R_I}-\mathbf{R_J}|}. \quad (1.28)$$

Upper case indices refer to nuclear coordinates and lower case indices denote coordinates for the electrons. M_e is the mass of the electron, M_I and Z_I are the mass and charge of the nucleus I, and $\mathbf{r}$ and $\mathbf{R}$ are the positions of electrons and nuclei, respectively. The charge of the electron is e. The first operator is the electron kinetic energy, the second one is the Coulombic interaction

between electrons and nuclei, the third is the Coulombic interaction between electrons, the fourth is the kinetic energy of the nuclei, and the last one is the Coulombic interaction between the nuclei.

In the adiabatic approximation, also known as the Born-Oppenheimer approximation in the context of condensed matter [53], the electron potential due to the nuclei and due to the electrons themselves are treated separately. We call the first potential $\hat{\mathcal{V}}_{\text{ext}}$, and the second one is $\hat{\mathcal{V}}$. The approximation is justified because, in most cases, the ions move at about the speed of sound ($\sim 10^3$ m/s), while the electrons move faster by about three orders of magnitude. The Hamiltonian in Eq. 1.28 is thus reduced to

$$\hat{\mathcal{H}} = \hat{\mathcal{T}} + \hat{\mathcal{V}} + \hat{\mathcal{V}}_{\text{ext}} \ , \tag{1.29}$$

where $\hat{\mathcal{T}}$ is the electron kinetic energy operator. Nevertheless, the solution of $\hat{\mathcal{H}}$ is still intractable for systems with more than a few dozen atoms because the many-body wave function depends on at least $3N$ variables for a system with N interacting electrons.

The framework of DFT was developed by Hohenberg and Kohn [54], who in 1964 published two theorems. The first theorem states that $\hat{\mathcal{V}}_{\text{ext}}$ is, to within a constant, a unique functional of the electronic density as a function of position $\rho(\mathbf{r})$. The Hamiltonian is determined by $\hat{\mathcal{V}}_{\text{ext}}$, so all the properties of the many particle system follow from a specification of $\rho(\mathbf{r})$. The second theorem states that the lowest energy is obtained if and only if the ground state density $\rho_0(\mathbf{r})$ is used in the energy functional. It establishes a variational principle for the density functional $\mathfrak{E}[\rho_0(\mathbf{r})] \leq \mathfrak{E}[\rho(\mathbf{r})]$. It follows that

$$\mathfrak{E}[\rho(\mathbf{r})] = \left\langle \psi(\mathbf{r}) \,\middle|\, \hat{\mathcal{T}} + \hat{\mathcal{V}} \,\middle|\, \psi(\mathbf{r}) \right\rangle + \left\langle \psi(\mathbf{r}) \,\middle|\, \hat{\mathcal{V}}_{\text{ext}} \,\middle|\, \psi(\mathbf{r}) \right\rangle \tag{1.30}$$

$$= \mathfrak{F}_{\text{HK}}[\rho(\mathbf{r})] + \int \rho(\mathbf{r})\, U_{\text{ext}}(\mathbf{r})\, d\mathbf{r} \ , \tag{1.31}$$

where $\psi(\mathbf{r})$ is the electron wave function and U_{ext} is the external potential and $\mathfrak{F}_{\text{HK}}[\rho(\mathbf{r})]$ is known as the Hohenberg-Kohn functional, but is not known explicitly. To solve this vexatious problem, Kohn and Sham [55] introduced the exchange-correlation energy E_{xc}, which is the difference in energy between the independent electron system and the real system. Then,

$$\mathfrak{F}_{\text{HK}}[\rho(\mathbf{r})] = E_{\text{kin}}[\rho(\mathbf{r})] + E_{\text{HF}}[\rho(\mathbf{r})] + E_{\text{xc}}[\rho(\mathbf{r})] \ , \tag{1.32}$$

where $E_{\text{kin}}[\rho(\mathbf{r})]$ is the kinetic interaction energy and $E_{\text{HF}}[\rho(\mathbf{r})]$ is the Hartree-Fock Coulomb interaction energy. The exact form of $E_{\text{xc}}[\rho(\mathbf{r})]$ is not known, but several approximations have been developed and the most salient will be described in the following section. This final approximation makes DFT calculations feasible. The single particle Hamiltonian can be written as

$$\hat{\mathcal{H}}_1 = \hat{\mathcal{T}}_{\text{ø}} + \hat{\mathcal{V}}_{\text{HT}} + \hat{\mathcal{V}}_{\text{xc}} + \hat{\mathcal{V}}_{\text{ext}} \ , \tag{1.33}$$

where $\hat{\mathcal{T}}_{\emptyset}$ is the kinetic energy of the electrons in the non-interaction case. For a system with N particles, the Hamiltonian is solved as a one particle system in its N lowest eigenstates φ_i, usually referred to as the Kohn-Sham orbitals.

$$\hat{\mathcal{H}}_1 \varphi_i(\mathbf{r}) = E_i \, \varphi_i(\mathbf{r}) \ . \tag{1.34}$$

These N equations are the Kohn-Sham equations, the heart of DFT. They can be solved by expanding the single electron wave functions in a basis and diagonalizing the Hamiltonian matrix. The resulting orbitals are used to calculate the ground state electronic density of the interacting system,

$$\rho(\mathbf{r}) = \sum_{i=1}^{N} \varphi_i^*(\mathbf{r}) \times \varphi(\mathbf{r}) \ . \tag{1.35}$$

The Hohenberg-Kohn theorems assure that the ground state electronic density uniquely determines the Hamiltonian, so the Kohn-Sham Hamiltonian is expressed in terms of ρ. This means that the equations used to calculate ρ depend themselves on ρ. The problem is solved by guessing the initial charge density and then iterating to self-consistency.

1.2.2 Exchange-correlation term

The Kohn-Sham equations cannot be solved without knowledge of an exchange-correlation functional, and the accuracy and computational cost of DFT calculations depend greatly on which functional is chosen. The functional can be expressed as [56]

$$E_{\mathrm{xc}}[\rho_\uparrow(\mathbf{r}), \rho_\downarrow(\mathbf{r})] = \int \rho(\mathbf{r}) \, \epsilon_{\mathrm{xc}}[\rho_\uparrow(\mathbf{r}), \rho_\downarrow(\mathbf{r})] \, d\mathbf{r} \ , \tag{1.36}$$

where the integrand is an energy density and $\epsilon_{\mathrm{xc}}[\rho_\uparrow(\mathbf{r}), \rho_\downarrow(\mathbf{r})]$ is an exchange-correlation energy per electron. $\rho_\uparrow(\mathbf{r})$ and $\rho_\downarrow(\mathbf{r})$ refer to the spin up and spin down electronic densities, respectively. In the particular case when there is no spin polarization, one charge density is needed. Increasingly complex ingredients can be used to construct $\epsilon_{\mathrm{xc}}[\rho_\uparrow(\mathbf{r}), \rho_\downarrow(\mathbf{r})]$, and a hierarchical view is shown in Fig. 1.1. In the following paragraphs, the local spin density approximation (LDA) and the generalized gradient approximation (GGA), used for the work presented in this thesis, are briefly reviewed.

In the LDA, $\epsilon_{\mathrm{xc}}[\rho_\uparrow(\mathbf{r}), \rho_\downarrow(\mathbf{r})]$ of Eq. 1.36 is the exchange-correlation energy per particle of an electron gas with uniform spin densities $\rho_\uparrow(\mathbf{r})$ and $\rho_\downarrow(\mathbf{r})$. It is known accurately from the work of Ceperley and Alder [57], and several parameterizations [58–60] are currently available for use with DFT codes. It is exact for spin densities that vary slowly over space, but it has proven, surprisingly, to be accurate for many solids with rapid density variations. LDA is a better approximation of E_{xc} than of the exchange and the correlation energies separately. This is because these two different

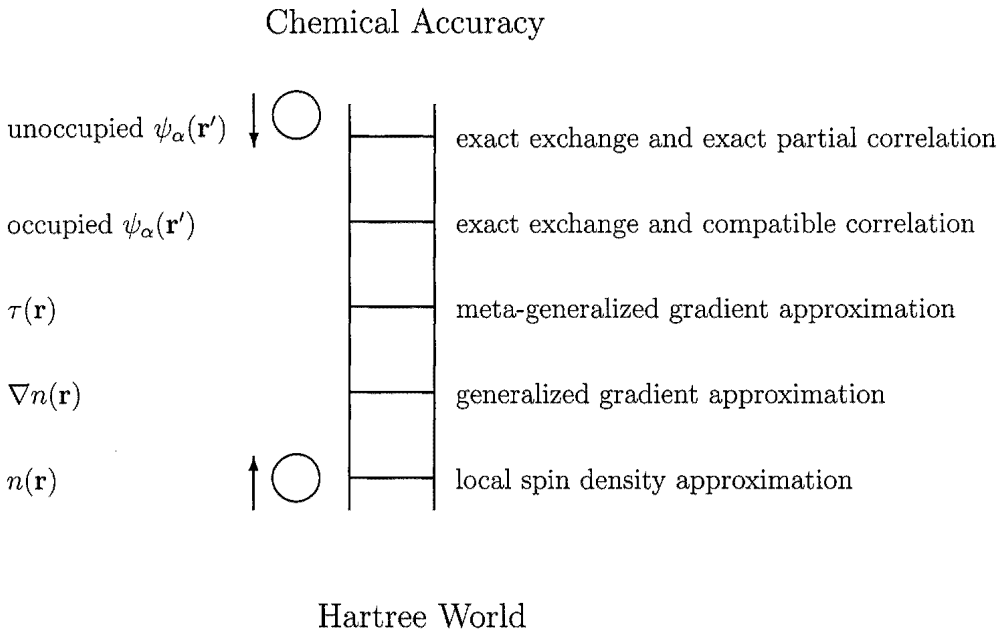

Figure 1.1: Jacob's ladder of density functional approximations. Any resemblance to the Tower of Babel is purely coincidental. Adapted from Ref. [56].

energies have opposing nonlocalities which tend to cancel. Applied to quantum chemistry problems, it yields reasonable geometries and vibration frequencies [61]. A notable failure of the approximation is that it predicts the nonmagnetic fcc and the antiferromagnetic fcc phases of pure Fe to be more stable than the ferromagnetic bcc phase [62].

When considering the gradients of the electronic densities, the exchange-correlation functional will have additional variables, $\epsilon_{\rm xc}[\rho_\uparrow(\mathbf{r}), \rho_\downarrow(\mathbf{r}), \nabla\rho_\uparrow(\mathbf{r}), \nabla\rho_\downarrow(\mathbf{r})]$. For spin densities that vary slowly over space, the leading correction to the LDA yields the second order gradient correction approximation (2GA) [55], but it provides a serious overcorrection for realistic densities. In the Kohn-Sham formalism, every electron in the system is effectively surrounded by an exchange-correlation hole, which results in a reduction of its potential energy (see, for example, Ref. [63]). This is the result of the electron number conservation, the Pauli exclusion principle, and Coulomb repulsion. The 2GA overcorrects because it breaks some hole rules. Langreth and Perdew [64] found that the correlation hole violates the sum rule that ensures that Coulomb repulsion does not change the hole charge integral even if it changes the shape of a hole. Perdew [65] also found that the exchange hole density is not negative everywhere. This means that a hole can exist where no electron is present. This spurious phenomena happens relatively far away from the center of the electron, and in the GGA [66], this is parametrized so that appropriate cutoffs can restore the properties of the holes. PBE-GGA [67] achieves the same results without introducing any parameters.

Several methods have the potential to provide more accurate results than LDA and GGA (Fig.

1.1), although they are currently considerably less robust. Meta-GGA [68] considers the kinetic energy densities $\tau(\mathbf{r})$, so $\epsilon_{\text{xc}}[\rho_\uparrow(\mathbf{r}), \rho_\downarrow(\mathbf{r}), \nabla\rho_\uparrow(\mathbf{r}), \nabla\rho_\downarrow(\mathbf{r}), \tau_\uparrow(\mathbf{r}), \tau_\downarrow(\mathbf{r})]$. LDA is a local functional of $\rho(\mathbf{r})$ since it requires only the density at a point. GGA is a semi-local functional of $\rho(\mathbf{r})$ since it requires the density in an infinitesimal region around a point. Meta-GGA is a non-local functional of $\rho(\mathbf{r})$. More information about the highest rungs of Jacob's ladder can be found in Ref. [56].

1.2.3 Pseudopotentials

As mentioned in section 1.2.1, the Kohn-Sham equations can be solved by expanding the single electron wave functions in a basis and diagonalizing the Hamiltonian matrix. This is an efficient strategy for valence electrons that are comparatively free-electron-like. Close to the nucleus, the Coulomb potential from the ion becomes substantially stronger, so the wave functions of the core electrons oscillate much faster. It is not efficient to expand the core state wave functions in plane wave basis sets. Nevertheless, the core electrons in many cases are quite insensitive to the bonding behavior of the atoms, and for the most part they only provide, along with the ions, the important but simple potential in which the valence electrons move.

In DFT calculations, it is customary to simulate the effect of the core electrons on the valence electrons with a pseudopotential (PP) to make the calculations more efficient. Older PPs, for example, norm-conserving [69] and ultrasoft [70, 71], are still in use and can be quite fast and accurate. In the norm-conserving PPs, the electron charge within the core part is equal to that of the actual atom. Ultrasoft PPs do not conserve charge, but they reduce the heights of the peak in the potential to reduce the number of necessary plane waves. The more recent projector augmented wave (PAW) method [72, 73] was used for the work presented in this thesis. A comparison of the constructions and performances of these three methods is given in Ref. [74]. The PAW method begins with the expansion of the wave functions in a plane wave basis set, but then it uses a set of projectors on radial grids at the atom centers to reintroduce the wave functions of the core electrons into the calculation. This is equivalent to a 'frozen core.' In principle, this method retains the full all-electron wave function and charge density while still being efficient computationally.

1.2.4 Electronic structure calculations

The eigenstates of any independent particle Schrödinger-like equation in which each electron moves in an effective potential $\hat{\mathcal{V}}_{\text{eff}}(\mathbf{r})$ satisfy the eigenvalue equation

$$\hat{\mathcal{H}}_{\text{eff}}(\mathbf{r})\psi_i(\mathbf{r}) = \left[-\frac{\hbar^2}{2M_e}\nabla^2 + \hat{\mathcal{V}}_{\text{eff}}\right]\psi_i(\mathbf{r}) = E_i\psi_i(\mathbf{r}) \ , \tag{1.37}$$

where $\hat{\mathcal{H}}_{\text{eff}}(\mathbf{r})$ is the effective Hamiltonian. The Kohn-Sham equations (Eq. 1.34) evidently satisfy the equation above. Imposing Born-von Kármán boundary conditions [25] on 1.37, will make ψ_i

periodic, so it can be expanded in the complete set of Fourier components:

$$\psi_i(\mathbf{r}) = \sum_q \zeta_{i,\mathbf{q}} \times \frac{1}{\sqrt{V}} \exp(\imath \mathbf{q}\cdot\mathbf{r}) \equiv \sum_{\mathbf{q}} \zeta_{i,\mathbf{q}} \times |\,\mathbf{q}\,\rangle \ . \tag{1.38}$$

The plane waves are orthonormal, so $\langle\,\mathbf{q\prime}\,|\,\mathbf{q}\,\rangle = \delta_{q,q\prime}$. In the equation above, V is the volume of the finite cell introduced in section 1.1.2, and $\zeta_{i,\mathbf{q}}$ is the expansion coefficient of ψ_i in the basis of orthonormal planes waves $|\,\mathbf{q}\,\rangle$. The reciprocal lattice representation of the Schrödinger equation is given by

$$\sum_{\mathbf{q}} \langle\,\mathbf{q\prime}\,|\,\hat{\mathcal{H}}_{\text{eff}}\,|\,\mathbf{q}\,\rangle\,\zeta_{i,\mathbf{q}} = E_i \sum_{\mathbf{q}} \langle\,\mathbf{q\prime}\,|\,\mathbf{q}\,\rangle\,\zeta_{i,\mathbf{q}} = E_i\,\zeta_{i,\mathbf{q\prime}} \ . \tag{1.39}$$

$\hat{\mathcal{V}}_{\text{eff}}(\mathbf{r})$ is also periodic, so it has a reciprocal lattice representation. The matrix elements of the potential in the reciprocal lattice are [52]

$$\langle\,\mathbf{q\prime}\,|\,\hat{\mathcal{V}}_{\text{eff}}\,|\,\mathbf{q}\,\rangle\,\zeta_{i,\mathbf{q}} = \sum_m \hat{\mathcal{V}}_{\text{eff}}(\mathbf{G}_h)\delta_{\mathbf{q\prime}-\mathbf{q},\mathbf{G}_h} \ . \tag{1.40}$$

In this case, the Kronecker delta is nonzero only if $\mathbf{q}$ and $\mathbf{q\prime}$ differ by some reciprocal lattice vector $\mathbf{G}_h$. The notation can be simplified by defining $\mathbf{q} = \mathbf{k} + \mathbf{G}_h$ and $\mathbf{q\prime} = \mathbf{k} + \mathbf{G}_{h\prime}$. The kinetic energy operator is $(\hbar^2/2M_e)\,|q|^2\,\delta_{\mathbf{q},\mathbf{q\prime}}$, so the Schrödinger equation for any given $\mathbf{k}$ can be written in matrix form as

$$\sum_{h\prime} \hat{\mathcal{H}}_{h,h\prime}(\mathbf{k})\,\zeta_{i,h\prime}(\mathbf{k}) = E_i(\mathbf{k})\,\zeta_{i,h}(\mathbf{k}) \ . \tag{1.41}$$

As mentioned in section 1.1.2, only $\mathbf{k}$-points within the Brillouin zone are distinct, so only these need to be considered. As V increases, the $\mathbf{k}$-points become more dense and tend to a continuum. At each $\mathbf{k}$ there are a discrete set of eigenstates $i = 1, 2, \ldots$ with eigenvalues E_i that become continuous bands. This is known as the electronic band structure, and provides rich information. In this thesis, we usually show electronic DOS curves, a sum over all the bands and k-points

$$\mathfrak{g}(E) = \frac{1}{N_k} \sum_{i,\mathbf{k}} \delta(E_i(\mathbf{k}) - E) \ , \tag{1.42}$$

where N_k, the total number of k-points, is a normalization factor. As a side note, it is interesting to note that the electronic entropy is given by (see, for example, [75])

$$S_{\text{elec}}(T) = -3k_{\text{B}} \int_0^\infty \mathfrak{g}(E)\,[(1 - f_T(E))\ln(1 - f_T(E)) + f_T(E)\ln(f_T(E))]\,dE \ , \tag{1.43}$$

which is analogous to S_{vib} (Eq. 1.24), but the electron occupancy follows the Fermi-Dirac distribution

$$f_T(E) = \frac{1}{\exp(E/k_{\text{B}}T) + 1} \ . \tag{1.44}$$

The most computation intensive task in a DFT calculation is the diagonalization of the Hamiltonian matrix (Eq. 1.41), which is intractable for real systems if attempted to perform directly. The general approach is to diagonalize the matrix iteratively until it converges to a value. Convergence is defined as a change in a parameter between contiguous diagonalizations that is smaller than a specified value. This parameter could be the total free energy, the eigenvalues, etc. Several flavors of this approach exists, like the block Davidson [76, 77], Conjugate Gradient [78, 79], and the Residual Minimization Method [80, 81] algorithms.

Other factors that affect the performance of the calculations are the number of k-points in the Brillouin zone and the number of plane waves. Most calculations are done considering just the k-points in the irreducible Brillouin zone, which is the Brillouin zone reduced by the symmetries in the point group of the lattice. In cubic symmetries, for example, the Brillouin zone can be reduced to 1/48 of the original one. The most common way to distribute k-points within the Brillouin zone is

$$\mathbf{k}_{n_1,n_2,n_3} \equiv \sum_{i}^{3} \frac{2n_i - N_i - 1}{2N_i} \mathbf{G}_i \ , \tag{1.45}$$

where $n_i = 1, 2, \ldots, N_i$. This scheme was proposed by Monkhorst and Pack [82] and its main advantage is that it leads to a uniform set of points that is valid for any crystal structure. The number of plane waves in VASP [83, 84], the code used for the shown in this thesis, is determined by specifying a value for the cutoff energy E_{cut} so that

$$\frac{\hbar^2}{2M_e} |\mathbf{G} + \mathbf{k}|^2 < E_{\text{cut}} \ . \tag{1.46}$$

This implies that the number of plane waves is different of each k-point. This is convenient because the number of plane waves changes smoothly when the volume is varied. This improves the accuracy of energy-volume calculations that are used, e.g., to determine the equilibrium lattice parameters of a system. Generally, the number of k-points and the value of E_{cut} are converged with respect to the free energy of the system. It is desirable to find the values that result in the required accuracy and economizes computational resources.

An important aspect for the calculation of the electronic structure of metals, such as the ones studied in this thesis, is the interpolation of the energy between k-points in the neighborhood of the Fermi surface (the partial occupancy). The Fermi surface can be extremely intricate and vary sharply in some cases, but quantities such as the total electron density, energy, and interatomic forces, depend on the accuracy with which it can be discerned [52]. The tetrahedron method [85–88] is the most widely used for this purpose. The simplest version is a linear interpolation between the values known at the k-points at the vertices, but higher order schemes are available. It is also convenient because tetrahedra can be used to fill all space for any grid. Smearing methods replace

the step function at the Fermi surface with a smooth function such as a finite-temperature Fermi-Dirac distribution [89], a Gaussian [90], or even a complete orthonormal set of functions [91]. These methods are discussed in more detail in section 5.5.1.

1.2.5 First principles lattice dynamics

As mentioned in section 1.1.2, phonon dispersions can be calculated from the dynamical matrix $\mathbf{D}(\mathbf{q})$ and the required ingredient is the force constant tensor $\Phi_{l\kappa,\,l'\kappa'}$. In principle, the latter can be calculated from first principles, and several approaches have been developed to achieve this. The main ones are briefly summarized here.

The first attempt was the 'frozen-phonon' method developed by Wendel and Martin in 1977 [92, 93], which is extremely intuitive. It consists of displacing atoms in a supercell in a way that is consistent with particular phonon modes, and calculating the change in total energy as a function of displacement. Its main drawback is that it is restricted to wave vectors for which the phonon displacement pattern is commensurate to the supercells used in the calculations. Therefore, it is an extremely inefficient way to calculate full phonon dispersions, but it is used to obtain elastic constants. For example, the shear elastic constants G in the FeV cubic lattice shown in Table 3.4 were calculated from a volume-conserving monoclinic deformation of the cell

$$\begin{bmatrix} 0 & \varepsilon & 0 \\ \varepsilon & 0 & 0 \\ 0 & 0 & \varepsilon^2/(1-\varepsilon^2) \end{bmatrix} . \tag{1.47}$$

The corresponding strain energies were calculated as a function of the displacement ε and fitted to the total energy $E(\varepsilon) = E_0 + 2VG\varepsilon^2$.

A more thorough method that has reach maturity is the 'direct' method, in which forces on atoms are calculated directly. The Hellman-Feynman theorem states that the first derivative of the eigenvalues of $\hat{\mathcal{H}}_\lambda$, a Hamiltonian that depends on the parameter λ, is given by the expectation value of the derivative of the Hamiltonian

$$\frac{\partial E_\lambda}{\partial \lambda} = \left\langle \psi_\lambda \left| \frac{\partial \hat{\mathcal{H}}_\lambda}{\partial \lambda} \right| \psi_\lambda \right\rangle . \tag{1.48}$$

In the case of a system of nuclei and electrons, $\hat{\mathcal{H}} = \hat{\mathcal{V}} + \hat{\mathcal{V}}_{\text{ext}}$, Feynman proved [94] that the force on any nucleus at any given time is the classical electrostatic attraction exerted on this nucleus by the other nuclei and by the electron charge density distribution of the system $\rho(\mathbf{r})$ at that time. Since $\rho(\mathbf{r})$ can be easily calculated using DFT, the forces on a displaced atom in a crystal and all other atoms in the crystal can be found. This allows for several independent force constants to be

determined from a single calculation [95]. Furthermore, symmetry arguments can be used to find atomic displacements from which all the force constants can be determined [96, 97]. This is the method used for the work presented in this thesis. The algorithm proposed by Parlinski, Li, and Kawazoe [98], which considers interatomic interactions between atoms in different supercells, was used to calculate the force constants from the direct forces on atoms.

Another approach is the linear response method. In the series expansion of the potential energy of a system (Eq. 1.7), the force constant between two atoms is given by Eq. 1.9, the second derivative of the energy with respect to the positions of those two atoms. In this case, Eq. 1.48 yields

$$\frac{\partial^2 E^{\diamondsuit}}{\partial \mathbf{R_I} \partial \mathbf{R_J}} = \int \frac{\partial \rho^{\diamondsuit}(\mathbf{r})}{\partial \mathbf{R_J}} \frac{\partial \mathcal{V}_{\text{ext}}(\mathbf{r})}{\partial \mathbf{R_I}} d\mathbf{r} + \int \rho^{\diamondsuit}(\mathbf{r}) \frac{\partial^2 \mathcal{V}_{\text{ext}}(\mathbf{r})}{\partial \mathbf{R_I} \partial \mathbf{R_I}} d\mathbf{r} + \frac{\partial^2 \mathcal{V}^{\diamondsuit}}{\partial \mathbf{R_I} \partial \mathbf{R_I}} \ , \tag{1.49}$$

where $E^{\diamondsuit}$ and $\mathcal{V}^{\diamondsuit}$ are the total energy of the system and the electrostatic interaction between different nuclei, respectively, in the atomic configuration $^{\diamondsuit}$. Eq. 1.49 is the derivative of the force on nucleus I with respect to the position of nucleus J (or vice versa), and it depends on $\rho^{\diamondsuit}(\mathbf{r})$ as well as on $\partial \rho^{\diamondsuit}(\mathbf{r}) / \partial \mathbf{R_J}$, the linear response to a distortion of the nuclear geometry. A variational DFT method known as density functional perturbation theory (DFPT) is used to compute Eq. 1.49 [99, 100]. A review is offered in Ref. [101]. The main advantage of this approach is that it does not require a supercell. The disadvantage is that, being perturbative, it is not valid for large atomic displacements.

In this thesis, direct measurements of the phonon DOS curves $g(E)$ are presented. For comparison with the experimental data, phonon DOS curves are obtained from the calculation of the phonon dispersions $E_j(\mathbf{q})$ by

$$g(E) = \frac{1}{N_q} \sum_{j,\mathbf{q}} \delta(E_j(\mathbf{q}) - E) \ , \tag{1.50}$$

where j is the phonon branch and N_q is the number of q-points.

1.2.6 Generalized electronic susceptibility

One of the earliest approaches that took advantage of electronic structure calculations for the study of phonon anomalies was the generalized susceptibility one, of which a simplified case will be discussed below. As mentioned briefly in section 1.1.4, Kohn anomalies are observed at phonon wave vectors that are equal to those that separate Fermi surface sheets. For example, in a free-electron gas, this is equal to twice the momentum of the electrons at the Fermi surface (the diameter of the sphere). The observation of soft phonons in several systems was correlated to peaks in their generalized susceptibilities [102–106]. We used this method to study the screening behavior of FeV and the results are discussed in section 3.5.2 .

The linear response of the conduction electron system to an external potential such as a phonon

can be described in terms of a dielectric matrix [107]

$$\varepsilon(\mathbf{q}+\mathbf{G}_h,\mathbf{q}+\mathbf{G}_{h\prime}) = \delta_{\mathbf{G}_h,\mathbf{G}_{h\prime}} + \nu(\mathbf{q}+\mathbf{G}_h)\times\chi(\mathbf{q}+\mathbf{G}_h,\mathbf{q}+\mathbf{G}_{h\prime}) \ , \tag{1.51}$$

where $\chi(\mathbf{q}+\mathbf{G}_h,\mathbf{q}+\mathbf{G}_{h\prime})$ is the static generalized susceptibility matrix, $\nu(\mathbf{q}+\mathbf{G}_h)$ is the Fourier transform of the Coulomb interaction between electrons, and $\mathbf{G}_h$ and $\mathbf{G}_{h\prime}$ are reciprocal lattice vectors. In the random phase approximation (RPA) [108–110], the electronic susceptibility for one atom per unit cell is given by

$$\begin{aligned}\chi(\mathbf{q}+\mathbf{G}_h,\mathbf{q}+\mathbf{G}_{h\prime}) = &\sum_{n,n\prime,\mathbf{k},\mathbf{k}\prime}\frac{f(E_{n,\mathbf{k}})-f(E_{n\prime,\mathbf{k}\prime})}{E_{n\prime,\mathbf{k}\prime}-E_{n,\mathbf{k}}}\\ &\times\langle\, n,\mathbf{k}\,|\exp(\imath(\mathbf{q}+\mathbf{G}_h)\cdot\mathbf{x}_l)|\,n\prime,\mathbf{k}\prime\,\rangle\times\langle\, n\prime,\mathbf{k}\prime\,|\exp(\imath(\mathbf{q}+\mathbf{G}_{h\prime})\cdot\mathbf{x}_l)|\,n,\mathbf{k}\,\rangle \ .\end{aligned} \tag{1.52}$$

where $f(E_{n,\mathbf{k}})$ is the Fermi-Dirac distribution (Eq. 1.44), n and $n\prime$ are band indices, and $\mathbf{k}$ is restricted to the first Brillouin zone. Considering only diagonal elements ($\mathbf{G}_h = \mathbf{G}_{h\prime}$), Eq. 1.51 reduces to

$$\varepsilon(\mathbf{q}) = 1+\nu(\mathbf{q})\,\chi(\mathbf{q}) \tag{1.53}$$

and

$$\chi(\mathbf{q}) = \sum_{n,n\prime,\mathbf{k},\mathbf{k}\prime}\frac{f(E_{n,\mathbf{k}})-f(E_{n\prime,\mathbf{k}+\mathbf{q}})}{E_{n\prime,\mathbf{k}+\mathbf{q}}-E_{n,\mathbf{k}}}\times\left|\langle\, n,\mathbf{k}\,|\exp(\imath\mathbf{q}\cdot\mathbf{x}_l)|\,n\prime,\mathbf{k}+\mathbf{q}\,\rangle\right|^2 \ . \tag{1.54}$$

The oscillator strength matrix element

$$\Upsilon_{n\mathbf{k},n\prime\mathbf{k}\prime}(\mathbf{q}) = \langle\, n,\mathbf{k}\,|\exp(\imath\mathbf{q}\cdot\mathbf{x}_l)|\,n\prime,\mathbf{k}\prime\,\rangle \tag{1.55}$$

imposes the restriction $\mathbf{k}\prime = \mathbf{k}+\mathbf{q}+\mathbf{G}_h$. Thus, eq. 1.54 can be written as

$$\chi(\mathbf{q}) = -\sum_{n,n\prime,\mathbf{k},\mathbf{k}\prime}\frac{f(E_{n,\mathbf{k}})-f(E_{n\prime,\mathbf{k}+\mathbf{q}})}{E_{n\prime,\mathbf{k}+\mathbf{q}}-E_{n,\mathbf{k}}}\,|\Upsilon_{n\mathbf{k},n\prime\mathbf{k}\prime}|^2 \tag{1.56}$$

$$= -2\sum_{n,n\prime,\mathbf{k},\mathbf{k}\prime}\frac{f(E_{n,\mathbf{k}})[1-f(E_{n\prime,\mathbf{k}\prime})]}{E_{n\prime,\mathbf{k}+\mathbf{q}}-E_{n,\mathbf{k}}}\,|\Upsilon_{n\mathbf{k},n\prime\mathbf{k}\prime}|^2 \tag{1.57}$$

For 'nesting' features, i.e., flat and parallel areas of the Fermi surface, the denominator in eq. 1.57 is vanishingly small giving rise to a large peak in $\chi(\mathbf{q})$ at the nesting wave vector. When nesting features are important, it is possible to ignore the effect of the oscillator strength matrix elements in favor of the energy denominator part of $\chi(\mathbf{q})$, so

$$\chi(\mathbf{q}) = 2\sum_{n,n\prime,\mathbf{k},\mathbf{k}+\mathbf{q}}\frac{f(E_{n,\mathbf{k}})(1-f(E_{n\prime,\mathbf{k}+\mathbf{q}}))}{E_{n\prime,\mathbf{k}+\mathbf{q}}-E_{n,\mathbf{k}}} \tag{1.58}$$

This approximation is usually taken with the assumptions: (1) $\Upsilon_{n\mathbf{k},n\prime\mathbf{k}\prime}(\mathbf{q})$ depends very weakly on $\mathbf{k}$ and is a smoothly and slowly varying function of $\mathbf{q}$ only; and (2), the position of the peak in $\chi(\mathbf{q})$ will be determined largely from the intraband nesting features of the Fermi surface or from volume effects. It is clear from Eq. 1.55 that in the $\mathbf{q} \to 0$ limit, the interband matrix elements vanish while the intraband matrix elements tend to unity, so $\chi(\mathbf{q})$ tends to the number of electronic of states at the Fermi level. In the large $\mathbf{q}$ limit, the intraband matrix elements will be negligible and the interband contributions will dominate.

Eq. 1.57 shows that, from a simplified perspective, nesting features in the Fermi surface will be related to soft phonons. The situation in reality could be much more complicated, since the off-diagonal elements of $\varepsilon(\mathbf{q}+\mathbf{G}_h, \mathbf{q}+\mathbf{G}_{h\prime})$ can be important, and $\Upsilon_{n\mathbf{k},n\prime\mathbf{k}\prime}(\mathbf{q})$ can have large peaks of its own in some cases.

1.3 Cluster expansion

The cluster variation method, a generalization of the mean-field approximation, was first proposed by Kikuchi in what is now a classic paper in the field [111]. Its original purpose was to treat cooperative phenomena in periodic systems, like the shape of the heat capacity below and above the disordering temperature in system with ordering tendencies. It is based on a parameterization of the free energy $F = E + PV - k_{\mathrm{B}}T \ln \Omega$ by clusters of atoms that describe the local chemical configuration. The energy and the entropy are those at the given configuration. The energy is a linear function of the cluster concentration and the entropy is obtained from the equilibrium cluster distribution. The variational principle of statistical mechanics is then applied on the free energy functional by varying the configuration. Each cluster is defined by n, the number of sites p it contains (the order of the cluster); and by $\mathfrak{k}$, the relative distance between sites (first nearest neighbors, second nearest neighbors, etc.). The spin variables σ_{p_i} take numerical values according to the type of atom at site p_i. The numerical values are arbitrary, but values that are symmetric around zero are more convenient. For example, the Ising model simplifies calculations in the case of A-B binary alloys, so $\sigma = +1$ for A atoms and $\sigma = -1$ for B atoms. When a third component is added, $\sigma = 0$ for C atoms. Some clusters for fcc alloys with $\mathfrak{k} = 1$ are illustrated in Fig. 1.2, which was obtained from Ref. [112].

The inclusion of larger clusters generally gives more accurate results [113], but the original formulation of Kikuchi based on combinatorics makes it impractical for this purpose. Simplifications and reformulations such as those of Refs. [114–117] can make the problem more tractable. Sanchez, et al. [118] showed that the set of clusters of all sizes are orthogonal to each other and form a basis,

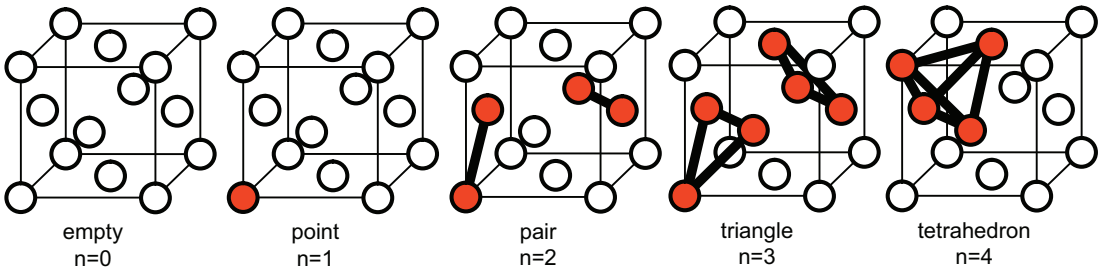

Figure 1.2: First nearest neighbors clusters for the fcc structure. Adapted from Ref. [112].

so any thermodynamic function $\mathcal{F}$ can be mapped into this basis,

$$\mathcal{F} = \sum_{n,\,\mathfrak{k}} \nu_{n,\mathfrak{k}}(r)\, \xi_{n,\mathfrak{k}}\,. \tag{1.59}$$

In Eq. 1.59, $\nu_{n,\mathfrak{k}}(r)$ is a many-body interaction function (a potential if $\mathcal{F}$ is an energy, etc.), r is a lattice parameter, and $\xi_{n,k}$ is a multisite correlation function. The correlation function expresses with a scalar the chemical configuration of a given cluster in a system,

$$\xi_{n,\mathfrak{k}} = \frac{1}{N_{n,\mathfrak{k}}} \sum_{n,\,\mathfrak{k}} \sigma_{p_i} \cdots \sigma_{p_n}\ , \tag{1.60}$$

where the inverse of the normalization constant $N_{n,\mathfrak{k}}$ is the number of clusters of type $n, \mathfrak{k}$. It averages over symmetry-equivalent configurations. The formalism of Sanchez, et al. is known as the cluster expansion (CE) method. In practice, the number of clusters will be finite and relatively small. Another apparent shortcoming of the method is that the interaction functions should have a composition dependence in order to converge [119,120]. This composition dependence is introduced in the generalized cluster expansion (GCE) [121]. Nevertheless, the GCE is seldom used, and a very large body of work based on the CE exists. Extensive application of the method thus seems to show that the CE is enough to describe and even predict the behavior of many systems. Recent efforts by van de Walle have been directed towards the extension of the CE method to tensorial quantities [18], which allow to study anisotropic properties such as elasticity and stress.

An immediate application of the CE formalism is to 'interpolate' the properties of random solid solutions of arbitrary compositions from values obtained for ordered structures, which are attainable by, e.g, density functional theory with periodic boundary conditions. This is usually known as the cluster inversion technique [122]. In a random solid solution there is no correlation in the occupation of the atomic sites. It can be proved by induction that in this case the value of the correlation function

for an A-B binary alloy is

$$\xi_{n,\mathbb{k}} = (1 - 2x_B)^n \ , \tag{1.61}$$

where x_B is the concentration of B atoms. A measurable thermodynamic quantity or function $\mathcal{F}$ in a known configuration $^\diamond$ can be expressed in terms of the correlation functions that parameterize the chemical order of the configuration, $\xi^\diamond_{n,\mathbb{k}}$. For the rest of this section, we consider this function to be the phonon DOS, $g^\diamond(E)$, since this is the case studied in section 3.4. The correlation functions of different configurations can be arranged in the matrix $[\xi^\diamond_{n,\mathbb{k}}]$. If $g^\diamond(E)$ is measured in different configurations of the same system and the correlation functions are calculated, the result is be a system of linear equations. In matrix notation,

$$g^\diamond(E) \cdot \left\langle \frac{M}{\varrho_{sc}} \right\rangle = \sum \mathcal{G}_{n,\mathbb{k}}(E) \cdot [\xi^\diamond_{n,\mathbb{k}}] \ , \tag{1.62}$$

where $\mathcal{G}_{n,\mathbb{k}}$ is a basis vector of the cluster expansion and the sum is over all the available values of $n, \mathbb{k}$ in configuration $^\diamond$. $\langle M/\varrho_{sc} \rangle$ is the average inverse scattering efficiency of the alloy, and is a necessary correction when working with neutron-weighted DOS (NWDOS) curves such as in the present work. The cluster inversion technique [122] consists of solving this system of equations to find the basis vectors:

$$\mathcal{G}_{n,\mathbb{k}}(E) = \sum g^\diamond(E) \cdot \left\langle \frac{M}{\varrho_{sc}} \right\rangle \cdot [\xi^\diamond_{n,\mathbb{k}}]^{-1} \ . \tag{1.63}$$

These basis vectors are known as interaction parameters and are configuration-independent. In the case of the phonon NWDOS curves, they are interaction phonon NWDOS (IPDOS) functions. They convey important information about the system: the empty term, $\mathcal{G}_{0,0}$, is the phonon NWDOS of an equiatomic random solid solution of A and B atoms; the point term, $\mathcal{G}_{1,1}$, shows the effect of composition; the pair term is the effect of the number of like and unlike pairs of atoms in the system. It can be shown that the pair term is completely equivalent to the Warren-Cowley SRO parameters so that $\xi_{2,1} = \alpha_1$, $\xi_{2,2} = \alpha_2$, etc.

1.4 Simulation of disordered structures

Disorder, including chemical disorder, can dramatically change the mechanical, electrical, semiconducting, magnetic, etc. properties of a material compared to the ordered state. The literature on the topic is impossible to review here, but Ref. [123] provides a thorough, if dated, description of the different types of disorder. The simulation of disorder is difficult because of the inherent limitations of existing computational tools and resources, which routinely make use of periodic systems to facilitate computation. Several approximations are available, the most basic being the virtual crystal approximation (VCA), that assumes that the interatomic potential between all atoms in the

system is the same. In a binary alloy, it is the concentration-average of the potentials of atoms A and B. It is a natural idea and has been applied since the 1930s for the calculation of electronic structures, perhaps for the first time by Nordheim [124]. It is in use today, but it has problems predicting even trends in, e.g., the lattice parameter. It works for some systems though, and it is not more computationally expensive that calculations on ordered structures. The coherent potential approximation (CPA) [125–127] improves over the CPA by assuming that the potentials of the A and B atoms, separately, are embedded in a uniform, average potential. It works well in a greater number of cases than the CPA. For a review of the VCA and CPA methods, see Ref. [128].

Other approaches take better advantage of modern techniques. The CE method described above can use calculations performed using, e.g., DFT with the projector augmented wave method [72], on ordered structures to predict the properties of disordered alloys. It is a substantial improvement over the VCA and CPA, but a deficiency is that atomic relaxations cannot be taken into account. Generally, the distances between A atoms, B atoms, and A and B atoms will be slightly different in the disordered phase, even in a cubic lattice. This can change the bandwidth in semiconductors (for example, Ref. [129]), have thermodynamics implications in a wide variety of materials (for example, Ref. [130], and subsequent chapters in this thesis), etc.

Randomly populating the lattice sites of a very large supercell with the ratios of the composition of the system and performing DFT calculations can, by exhaustion, provide accurate results that include atomic relaxation effects. Nevertheless, DFT calculations are computationally expensive and are currently limited to a few hundred atoms. Semi-empirical potentials allow to extend this to a few thousand atoms, but could decrease the accuracy of the calculations. It is possible to build and ensemble of supercells of a few thousand atoms each and then take the average, which might be a decent approximation of the disordered state if the semi-empirical potential used is of good quality.

An elegant and effective approach is the construction of special quasirandom structures (SQSs) [131]. It is currently the method of choice for the simulation of disordered structures because of its relatively low computation cost (compared to the brute force method) and excellent accuracy when the SQS is of sufficient quality. It is based on the CE formalism described in section 1.3, and consists of designing a structure that has the same $\xi_{n,\bar{k}}$ values as the disordered structure of interest. With a small number of atoms, from two to a few tens, it is possible to achieve this for the first few or more nearest neighbors, deferring periodicity errors to more distant neighbors that have significantly less influence. The improvement over the CE method is that the SQSs can be relaxed and atomic relaxation effects are included in the calculations. It is also straightforward to extend the method to multicomponent systems, such as in Ref. [132], although it is not a simple task. A rigourous optimization will also consider the particular system at hand, although this is usually not essential. Different SQSs might have parameters that are similar to each other, or different values for which a preference does not exists a priori. Standard optimization benchmarks currently does not exist, but

several attempts have been made to characterize the error [133, 134]. The ATAT code (Ref. [135]) is currently widely used for the construction and optimizations of SQSs. The SQS approach was chosen to simulate the properties of disordered compounds studied in this thesis with excellent results.

1.5 Molecular dynamics

The concept of molecular dynamics (MD) is perhaps the quintessence of computer simulations: given a collection of N particles $i = 1, 2, \ldots, N$ with positions $\mathbf{r}_i$ at time t_0, in which at least one particle has a nonzero velocity, $\dot{\mathbf{r}} \neq 0$, predict $\mathbf{r}_i$ for $t > t_0$. This approach could provide a wealth of information on almost any system imaginable, but the details of the implementation make it a nontrivial task. Currently, this is one of the most active and most diverse fields in science, and it is impossible to summarize the literature here, but Refs. [19, 21, 136] show applications of MD calculations to systems that are relevant to the work presented here.

The first 'details' in the implementation of MD are the size and initial configuration of the system. The first one is limited by computational capabilities, so boundary conditions are necessary. The second one requires knowledge of the velocities of the particles. In most cases, their motion will be assumed to be classical, described by second order differential equations that require both $\mathbf{r}_i(t_0)$ and $\dot{\mathbf{r}}(t_0)$. These issues are not main concerns for crystalline systems because Born-von Kármán boundary conditions [25] can be used and the energies of the atoms follow a Maxwell-Boltzmann distribution at temperature T, so the initial velocities can be generated. More complicated is to keep T constant during the calculation, although several types of 'thermostats' are available to regulate it. In general, these couple the particles to a heat bath, e.g., directly [137], stochastically [138], via a fictitious mass [139].

The second consideration is that the force exerted on a particle is proportional to the change in energy when that particle is displaced, so accurate potentials or force fields are required, along with appropriate truncation schemes and values. Understandably, the development of these potentials is one of the main foci of the MD community. The simplest ones are the Lennard-Jones potential [40], the Morse potential [140] and the Buckingham potential [141]. Although all of them are almost one hundred years old, they provide decent results in many cases if attention is paid to the parameterization. A much more recent development that is illustrative of the advances in the field is the ReaxFF [142], which is able to simulate chemical reactions by allowing bonds to break and form. For metals, embedded atom methods [143–145], which parameterize the electronic charge density, ordinarily give the best results.

Another source of uncertainty in MD calculations is the discretization of t. The configuration at each t, separated from the previous by Δt, is approximated with a Taylor expansion. The errors from neglecting terms in the approximation are rapidly accumulated and set the calculation on a

path to failure, e.g., divergent particles. In principle this can be fixed by calculating $\ddot{\mathbf{r}}_\mathbf{i}$, $\dddot{\mathbf{r}}_\mathbf{i}$, $\ddddot{\mathbf{r}}_\mathbf{i}$, ..., but this is too computationally expensive. Instead, several algorithms have been developed to reduce the error. The Verlet methods, in which the error scales as $(\Delta t)^2$, are the most widely used (for a review, see Ref. [146]). As often happens with calculations of any type, an optimization of the computation cost and simulation accuracy should be made.

Some of the results shown in Chapter 5 are from ab initio molecular dynamics (AIMD) simulations. All the aspects mentioned above are relevant, but there is no empirical potential. Instead, the forces at each time step are obtained from DFT calculations. Two general categories of AIMD simulations exists. In what is usually known as Born-Oppenheimer MD, the forces are calculated as described in section 1.2.5, after electronic states are relaxed to their ground state. Information on the forces are part of the standard output of most modern DFT codes, so the implementation is straightforward. This method was used for the calculations presented here. In Car-Parrinello MD [147], the electronic degrees of freedom are coupled to the classical coordinate system. By giving the orbitals a fictitious mass, the set of coefficients of the plane wave basis set is treated classically as an additional set of coordinates. In this case the electronic states are not at their ground states, but the calculations are faster. The combination of MD and DFT is a powerful one, but their respective limitations are also combined. Of particular importance is the heavy computational cost of DFT, which currently limits AIMD to systems with a few hundred atoms and a few thousand fs. The use of supercomputers can alleviate the latter, but can do less for the former.

The quantities of interest for the work presented here obtained from AIMD simulations are the electronic DOS curves $g(E)$ and the phonon DOS curves $g(E)$. $g(E)$ is acquired from the DFT calculation at each time step as described in section 1.2.4. $g(E)$ is obtained from the Fourier transform of the velocity autocorrelation function of the particles (for example, [148])

$$g(E) = \frac{1}{2\pi}\left[\int_{-\infty}^{\infty} C(t)\exp(\imath E t)\,dt\right]^2 , \tag{1.64}$$

where

$$C(t) = \frac{\langle \dot{\mathbf{r}}(0)\cdot\dot{\mathbf{r}}(t)\rangle}{\langle \dot{\mathbf{r}}(0)\cdot\dot{\mathbf{r}}(0)\rangle} . \tag{1.65}$$

Chapter 2

Scattering basics and experimental methods

2.1 Time-of-flight inelastic neutron scattering

2.1.1 Elements of neutron scattering

An important fraction of the experimental work presented here made use of the inelastic scattering of 'thermal' neutrons as the probe to study phonons in materials. Scattering off a material is possible because the wave length of thermal neutrons is comparable to the typical interatomic spacing between ions. Neutrons can be produced in a nuclear reactor by a chain reaction of nuclear fission or by spallation of heavy metals. The time-of-flight inelastic neutron scattering (INS) was performed with the Wide Angular-Range Chopper Spectrometer (ARCS) [149] at the Spallation Neutron Source (SNS) at the Oak Ridge National Laboratory. The source of the neutrons is the spallation of a mercury (Hg) target bombarded with high energy protons. The initial energies of the neutrons are too high for materials science research, so they are slowed down ('thermalized') to useful energies by passing them through cells filled with water. The SNS is currently the brightest source of neutrons in the world.

Scattering is a wave phenomenon and as such it can be studied via plane waves and spherical waves. The methodology presented in sections 1.1.1 and 1.1.2 becomes then particularly appropriate. A short review of the basics is given here, although more focus is placed on the physical interpretation than on a formal development, in the spirit of Ref. [150]. The theory of scattering is very well developed and it is treated in detail in many advanced textbooks, such as Refs. [39] and [151]. The theory of neutron scattering is also presented in works such as Refs. [152] and [153].

For a set of N atoms fixed in space, the modulus squared (the intensity) of a classical scattered wave is

$$|\psi_{\rm sc}(\mathbf{Q},\mathbf{r_d})|^2 = \frac{1}{\mathrm{r}_d^2}\left|\sum_{i=1}^{N} b_i(\mathbf{Q})\exp(\imath\mathbf{Q}\cdot\mathbf{r_i})\right|^2 , \tag{2.1}$$

where $\psi_{\mathrm{sc}}(\mathbf{Q},\mathbf{r})$ is the scattered wave at position $\mathbf{r_d}$, the point where the wave is detected; the magnitude of $\mathbf{r_d}$ will be much larger than $\mathbf{r_i}$, the position of the scattering particle i; the scattering amplitude is b, which for neutron scattering is largely independent of $\mathbf{Q}$ due to the small size of the nucleus compared to the neutron wavelength; finally

$$\mathbf{Q} \equiv \mathbf{q}_0 - \mathbf{q}_f, \tag{2.2}$$

the wave vector transfer from the plane wave to the sample. In the equation above, $\mathbf{q}_0$ and $\mathbf{q}_f$ are the initial and final wave vectors. This approach is correct if the wave is scattered only once by the material. Also, the (unknown) short-range nuclear interaction between the neutron and the nucleus that defines the atomic form factor is replaced by a δ-function potential with a strength that is adjusted to measured results. The differential cross section $d\sigma$ for scattering into unit solid angle $d\Omega$ is given by the expression

$$\begin{aligned}
\frac{d\sigma}{d\Omega} = |\mathfrak{F}(\mathbf{Q})|^2 &= \left| \sum_{i=1}^{N} b_i \exp(\imath \mathbf{Q}\cdot\mathbf{r_i}) \right|^2 \\
&= \sum_{i}^{N} b_i^2 + \sum_{i\neq j}^{N} b_i b_j \exp(\imath \mathbf{Q}\cdot\mathbf{r_i} - \mathbf{r_j}) \\
&= N\left\langle b^2 \right\rangle + \sum_{i\neq j}^{N} \langle b \rangle^2 \exp(\imath \mathbf{Q}\cdot(\mathbf{r_i} - \mathbf{r_j})) \\
&= N\left[\left\langle b^2 \right\rangle - \langle b \rangle^2 \right] + \left| \sum_{i}^{N} \langle b \rangle \exp(\imath \mathbf{Q}\cdot\mathbf{r_i}) \right|^2 \\
&= N\left\langle b^2 \right\rangle + N\langle b \rangle^2 \left[\int P(\mathbf{r}) \exp(\imath \mathbf{Q}\cdot\mathbf{r}) \mathbf{dr} \right] .
\end{aligned} \tag{2.3}$$

The whole derivation is shown to emphasize two aspects. The first one is the definition of the Patterson function $P(\mathbf{r})$. To convert the square of the discrete sum into a continuous integral over the whole space, the introduction of a Dirac delta $\delta(\mathbf{r} - \mathbf{r_i})$ is necessary to account for the discrete positions of the atoms in the lattice. $P(\mathbf{r})$ is therefore the position autocorrelation function that represents the probability that, given a particle at the origin, a distinct particle will be found at position $\mathbf{r}$ at the same time. The most important property of $P(\mathbf{r})$ is that its Fourier transform is the total diffracted intensity $I(\mathbf{Q})$. The second aspect is that the expression consists of two terms, one that is independent of $\mathbf{Q}$ and another one that depends on $\mathbf{Q}$. The former is basically the sum of the 'intensities' contributed by the various nuclei separately and it is called incoherent scattering. The latter involves the interference of waves scattered by different nuclei and it is called coherent scattering.

Van Hove showed that Eq. 2.3 can be extended to include time correlations [154], so

$$|\mathfrak{F}(\mathbf{Q},t)| = \int G(\mathbf{r},t)\exp(\imath\mathbf{Q}\cdot\mathbf{r})d\mathbf{r} \tag{2.4}$$

and

$$|\mathfrak{S}(\mathbf{Q},E)| = \frac{1}{2\pi}\int_{-\infty}^{\infty}\mathfrak{F}(\mathbf{Q},t)\exp(\imath Et)d\mathbf{t}\ . \tag{2.5}$$

$G(\mathbf{r},t)$ is the time dependent position autocorrelation function. Compare the equation above to Eq. 1.64, which is the phonon density of states obtained from the velocity autocorrelation function. Van Hove also showed that the partial differential scattering cross section per unit angle per unit energy is given by

$$\frac{d^2\sigma}{d\Omega dE} = b^2\left(\frac{E_f}{E_0}\right)^2|\mathfrak{S}(\mathbf{Q},E)|\ . \tag{2.6}$$

It is important to notice that $\mathfrak{S}(\mathbf{Q},E)$ also consists of an incoherent and a coherent part. In this case, the former is the sum of the intensities of the phonons at each $\mathbf{Q}$ and E, while the latter includes effects such as phonon dispersions. Now consider Eq. 1.11, the plane waves solution to the equations of motion for all atoms in a crystal. If this equation is substituted in Eqs. 2.5 and 2.6, the phonon expansion in powers of $\mathbf{u}_{l\kappa}$ will have terms having as factors [150]

$$\begin{gathered}\exp(\imath\mathbf{Q}\cdot\mathbf{r_i})\exp(-\imath\omega t)\\ \exp[\imath(\mathbf{Q}+\mathbf{q})\cdot\mathbf{r_i}]\exp(-\imath\omega t\pm\imath\omega_j(\mathbf{q})t)\\ \exp[\imath(\mathbf{Q}\pm\mathbf{q_1}\pm\mathbf{q_2})\cdot\mathbf{r_i}]\exp[\imath(-\omega\pm\omega_j\mathbf{q_1}\pm\omega_j(\mathbf{q_2}))t]\\ \vdots\end{gathered} \tag{2.7}$$

These various terms correspond to processes involving no phonons (elastic scattering), one phonon, two phonons, etc. and provide their respective selection rules. The point to make here is that INS measurements will include contributions from neutrons that were scattered more than once by the nuclei in the sample.

2.1.2 Technique

The diagram shown in Fig. 2.1 illustrates the basic principles of INS with time-of-flight instruments. After thermalization, the pulsed neutron beam is directed to the instrument through 'neutron guides.' Inside of these guides, the neutrons undergo total reflection so the loss of intensity is negligible. Two choppers rotating with different frequencies allow to select the incident energy E_0 of the neutron bunch. The first chopper is usually more massive and stops high energy neutrons and other background radiation. The second chopper, usually called a Fermi chopper, is smaller and used for fine tuning the energy distribution of the neutron bunch. Neutrons are weakly interacting,

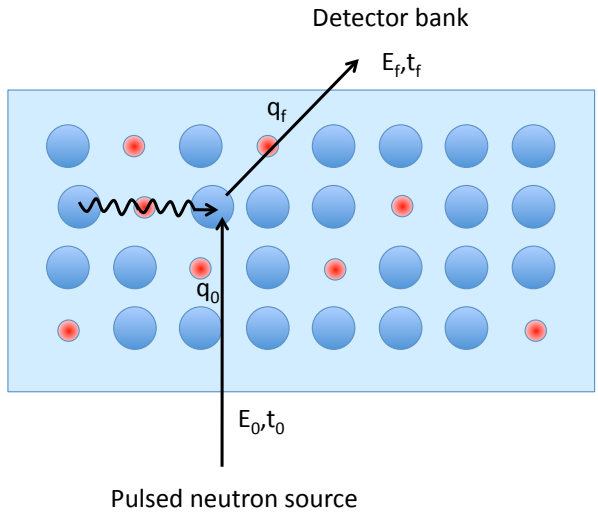

Figure 2.1: Schematic of an inelastic neutron scattering measurement. Straight lines are neutron paths, the wavy line represents a lattice vibration, and the circles of different colors and sizes represent two different types of atoms with different neutron scattering cross sections.

so their detection is difficult. Usually ^{3}He-filled tubes are used for this purpose, since a charge is produced after neutron capture by the ^{3}He. ARCS has 115 'packs' of eight 1-meter-long tubes each that are sensitive to the linear position.

The times t_0 and t_f at which the neutrons leave the Fermi chopper and are detected, respectively, are known. Also know is the distance from the chopper or another check point to the sample and from the sample to each 'pixel' in the detector bank. The time the neutrons take to reach the sample is fixed, while the time they take to reach the detector depends on the distance to that particular pixel and the energy lost to or gained from phonons in the sample $\Delta E = E_f - E_0$. The change in neutron momentum $\hbar\mathbf{Q}$ is also calculated from the position of the detector, which will make an angle with respect to the initial momentum. In fact, the raw data from ARCS is a 'neutron event' list; for every neutron detected, the detector number and position, as well as the time-of-flight of the neutron are saved into a file. $|\mathfrak{S}(\mathbf{Q}, E)|$ can then be calculated if the scattering cross sections b^2 are known, although if there is more than one type of scatterer, i.e., atoms of different elements, $d^2\sigma/d\Omega dE$ will be neutron-weighted by the neutron scattering efficiency of each element. This is represented in Fig. 2.1 by showing atoms with a larger cross section, although the cross section is not related to the mass of the atom, i.e., the red atoms are not necessarily less massive than the blue ones.

2.1.3 Data reduction

The INS data from polycrystalline samples historically has been quite challenging to reduce, although with technical improvements in the instruments many issues have become less serious. In particular

for ARCS, the incident energy is more accurately determined by the chopper settings than in older instruments. The performance of the detectors is also superior, so detector masking and efficiency corrections are perhaps not as essential as for previous generations, but it is still an important issue. The wide angular-range of ARCS samples a larger part of $(\mathbf{Q}, E)$, which improves the accuracy of experimental phonon DOS curves. Still of uttermost importance is the removal of the background and multiphonon scattering contributions (derivation 2.7). The removal of multiple scattering is more complicated, but this is a significantly smaller contribution to the measured intensities.

For each data set, the following reduction procedures were performed using DrChops, part of the DANSE software [155]. Differences in the sensitivity of the detectors were assessed by measuring a vanadium rod. Vanadium is an almost completely incoherent scatterer of neutrons (99%), so it is ideal for this application. The differences were found to be very small for each data set, but they were normalized nevertheless. Bad detectors were masked so that they do not give spurious intensity minima in the measured $\mathfrak{I}(\mathbf{Q}, E)$, the intensity as a function of $(\mathbf{Q}, E)$ (closely related to $\mathfrak{S}(\mathbf{Q}, E)$ of Eq. 2.6). This would happen because of the dynamic nature of the measurements, so the intensity at a particular $(\mathbf{Q}, E)$ is not determined by a single detector. For the Fe-V data set, which was obtained shortly after the commissioning of ARCS, about 5% of the detectors were masked. For the Fe-Au and FeTi data sets, less than 1% of the detectors were masked. Finally, the raw data was processed to obtain $\mathfrak{I}(\mathbf{Q}, E)$ histograms. The binning of the energy transfer and the momentum transfer are the main variable at this stage, and there is a trade-off between the two axis in terms of counting statistics, although the binning used for the present work, 0.5 meV per energy bin and 0.1 Å^{-1} per momentum bin, is fairly standard and was also chosen to coincide with the x-ray measurements explained in the following section (section 2.2). Results for some Fe-V alloys are shown in Fig. 2.2. Very detailed descriptions of the reduction procedures are given in Refs. [155–157].

The background subtraction is performed next. A measurement under the same experimental conditions and sample environment is done, but without the sample. This amounts to most of the real contribution from the background, although the presence of the sample can slightly change the background since the neutrons can get scattered by the sample before or after being scattered by the sample holder. At ARCS the instrument background is quite low because it is almost completely shielded by neutron-absorbing materials, including in between detector packs. Most of the background comes from the sample environment. The Fe-V and FeTi measurements presented here were performed in a low-background furnace which consisted of heat cartridges (outside of the beam path) and thin aluminum shielding (Al is a weak scatterer of neutrons). The Fe-V samples were measured in Al sachets and the FeTi in Al canisters. For the Fe-Au measurements, the samples consisted of rolled sheets suspended that were suspended from a stick, so no container was necessary. In general, background subtraction was not an issue for the data reported here.

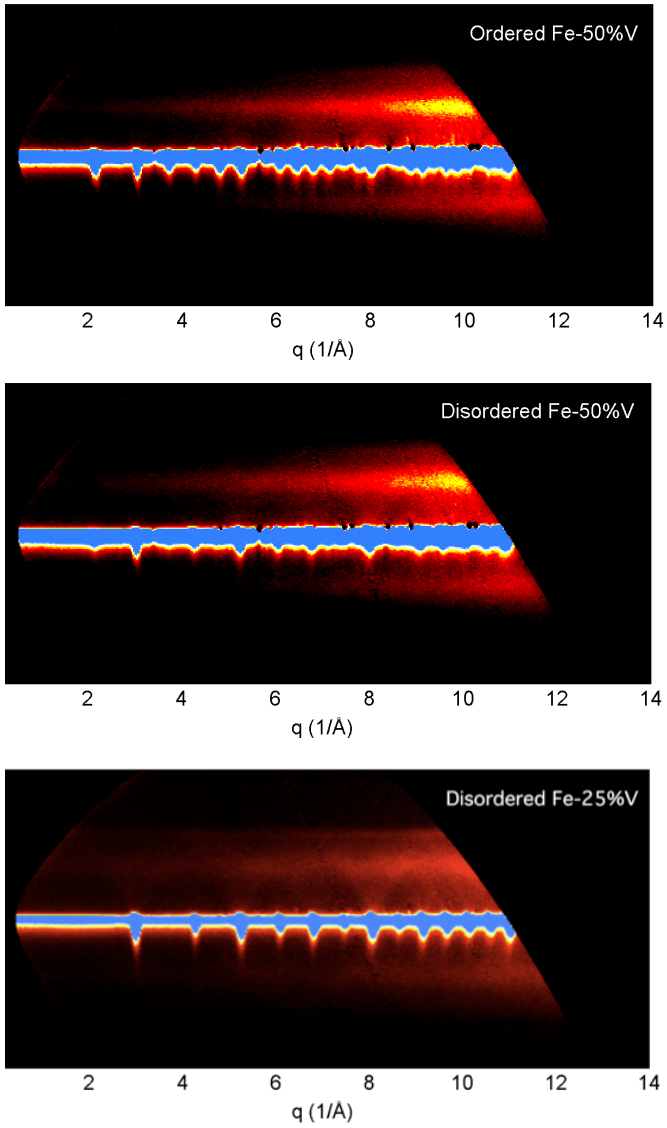

Figure 2.2: Energy and momentum dependence of inelastic neutron scattering $\mathfrak{I}(\mathbf{Q}, E)$ from ordered (top panel) and disordered (middle panel) FeV. Incoherent scattering from the V atoms contributes a broad background that goes as Q^2, but streaks from angle-averaged phonon dispersions emanate upwards from the strong Bragg diffractions at $E = 0$. Dispersions are more evident in the $\mathfrak{I}(\mathbf{Q}, E)$ from a chemically disordered Fe-25%V alloy (bottom panel). The dispersions are broadened largely by how the elastic anisotropy is averaged in the scattering from a polycrystalline sample.

Neutron-weighted phonon DOS curves $g(E)$ were obtained from the $\mathfrak{I}(\mathbf{Q}, E)$ histograms, using getDOS, part of the DANSE software [155]. For incoherent scatterers of neutrons, the phonon DOS is obtained by integrating over the $\mathbf{Q}$ axis. Most isotopes will scatterer some part of the neutrons coherently though, and in some cases this is the dominant type of scattering. The incoherent approximation is used in the case of coherent scatterers, which consists in assuming that

$$\int_{\infty}^{\infty} \left(\frac{d^2\sigma}{d\Omega dE}\right)_{\text{coherent}} \mathbf{Q}\, d\mathbf{Q} = \int_{\infty}^{\infty} \left(\frac{d^2\sigma}{d\Omega dE}\right)_{\text{incoherent}} \mathbf{Q}\, d\mathbf{Q} \tag{2.8}$$

for a sufficiently large $\mathbf{Q}$-sampling, where the expression on the right refers to a theoretical incoherent scatterer. One of the biggest advantages of ARCS is that its wide angular-range (it is in the name of the instrument) allows the measurements to comply with the condition of the approximation, so phonon DOS curves obtained by integrating over the $\mathbf{Q}$ axis are accurate. The subtraction of the elastic scattering (the high intensity part at $E = 0$ in the panels of Fig. 2.2) is done by assuming an E^2 scaling of the intensity of the phonon DOS (Eq. 2.6) and fitting the elastic peak to a Gaussian. The main issue this code deals with is the determination and subtraction of multiphonon scattering, which it solves by an iterative method: the n-phonon scattering can be written as the convolution of the 1- and $(n-1)$-phonon scattering and this leads to a recursion relation for all the orders of scattering, with one adjustable parameter. A heuristic penalty function is defined to find the parameter that results in the 'best' multiphonon scattering subtraction. The parameter should be same for measurements under the same conditions, although a variation is expected with temperature, for example, since the multiphonon contribution to $\mathfrak{I}(\mathbf{Q}, E)$ will increase. Finally, getDOS applies an analytical phonon occupancy correction. This is necessary because less energetic vibrations have larger amplitudes, so they are sampled preferentially. A very detailed description of the getDOS and underlying principles is given in Ref. [157].

2.2 Nuclear-resonant inelastic x-ray scattering

2.2.1 Elements of nuclear-resonant scattering

The other pivotal technique used for the research presented here is nuclear-resonant inelastic x-ray scattering (NRIXS). It is based on the Mössbauer effect [158], the recoilless absorption of gamma (or high energy x-ray) radiation by a nucleus. For example, ^{57}Fe has a nuclear excited state 14.413 keV above its ground energy, so it is capable of absorbing radiation of this energy. The NRIXS work presented here was performed at beam line 16ID-D, maintained by the High Pressure Collaborative Access Team (HP-CAT), at the Advanced Photon Source (APS) at the Argonne National Laboratory. In this facility, x-rays are produced by electrons moving at relativistic speeds through an undulator. The required electron speeds are reached by directing the electrons through a linear accelerator and

then a booster synchrotron. They are finally 'stored' in a ring where beamlines have access to them.

The Mössbauer effect can be understood in classical terms. The momentum of a high energy gamma-ray is large enough to produce a large recoil in a free nucleus absorbing it, so the energy of the gamma-ray changes. The recoil energy $E_R = E_0^2/2M_nc^2$, where E_0 is the nuclear transition energy, M_n is the mass of the nucleus and c is the speed of light. Low nuclear transition energies are in the keV to tens of keV range, so the recoil energy will be a few meV. The width of the nuclear transition energies is very narrow, of the order of a few neV, so the difference is six orders of magnitude. Other nuclei cannot absorb the reemitted gamma-ray and it escapes the material.

Consider a system like the one described in section 1.1.2 in which all nuclei are joined by springs to each other. When a photon is absorbed by one of the nuclei there are two limiting cases: the ion suffers a recoil that is damped by the restoring forces of the springs, but propagates throughout the crystal as a wave; or the restoring forces are large enough that springs are 'rigid' and the energy is transmitted to the crystal as a whole, so the ion itself does not recoil. The first case is similar to that of the free nucleus and the reemitted photon does not have the appropriate energy to be reabsorbed by other nuclei. In the second case M_n becomes the mass of the whole crystal and E_R is negligible, so other nuclei can reabsorb the photon creating a resonance. Classically, the first case is always going to happen unless the restoring force is infinite, but this limit does not have to be reached as we can define 'rigid' as having a restoring force large enough to make reabsorption of the photon by other nuclei possible. Lattice vibrations are quantized, but the model is close to reality. Intuitively, there will be a probability distribution for the events, and this distribution will depend on the energy of the photon being absorbed. Isotopes with nuclear transition energies low enough that the probability of recoilless absorption is not negligible are called Mössbauer isotopes. The probability of resonant absorption is called the Lamb-Mössbauer factor f_{LM}.

The theoretical framework for nuclear-resonant inelastic scattering was largely developed by Singwi and Sjölander [159]. They started with the Hamiltonian $\hat{\mathcal{H}}_{\mathrm{nr}}$ of a nucleus in an interacting system in which the nucleus goes from state A to state B and at the same time, the system makes a transition from state n_i to state n_j. This is the interaction between the radiation field and the nucleus, so it is in the form of plane waves. The interaction between nucleons is much stronger than between nuclei, so the total wave function is a product of the wave function from each interaction. The transition matrix element corresponding to the absorption of a photon of wave vector $\mathbf{k}$ is $\left\langle Bn_j \left| \hat{\mathcal{H}}_{\mathrm{nr}} \right| An_i \right\rangle$. The part that corresponds to the change in the state of the collective motions is per nucleus is $\left\langle n_j \left| \exp(\imath \mathbf{k} \cdot \mathbf{r}) \right| n_i \right\rangle$, where $\mathbf{r}$ is the position of nucleus. The absorption cross section resulting from this matrix element is [159]

$$\sigma(E) = C\,\Gamma^2 \sum_{i,j} g_{n_0} \frac{\left| \langle n_j \left| \exp(\imath \mathbf{k} \cdot \mathbf{r}) \right| n_i \rangle \right|^2}{(E_0 - E + \epsilon_{n_j} - \epsilon_{n_i})^2 + \Gamma^2/4} \ , \tag{2.9}$$

where C is a constant, E_0 is the energy difference between the final and the initial nuclear states of the absorbing nucleus, ϵ_{n_i} and ϵ_{n_i} are the energies of the states $|n_i\rangle$ and $|n_j\rangle$ of the interacting system, Γ is the width of the excited state of the nucleus, and g_{n_0} is the statistical weight factor for the state $|n_i\rangle$. Using similar arguments as in Eq. 2.3,

$$\sigma(E) = \frac{C\,\Gamma}{\hbar}\int_{-\infty}^{\infty} \exp[\imath t(E-E_0) - \Gamma/(2)|t|]\,\langle \exp[\imath \mathbf{k}\cdot\mathbf{r}(0)]\exp[-\imath \mathbf{k}\cdot\mathbf{r}(t)]\rangle\, dt\ , \tag{2.10}$$

where $\mathbf{r}(t)$ is a Heisenberg operator. By analogy to Eqs. 2.4 and 2.5,

$$\langle \exp[\imath \mathbf{k}\cdot\mathbf{r}(0)]\exp[-\imath \mathbf{k}\cdot\mathbf{r}(t)]\rangle\ = \int \exp(\imath \mathbf{k}\cdot\mathbf{r}) G_x(\mathbf{r},t) d\mathbf{r}\ . \tag{2.11}$$

The interpretation of the Van Hove function $G_x(\mathbf{r},t)$ is not as straightforward as in the classical limit because it is a complex quantity. Nevertheless, the real part is the emission or absorption probability [159]. Performing a phonon expansion for incoherent scattering like that of Eq. 2.7, the 0-phonon (elastic scattering) becomes the recoilless radiation absorption peak of width Γ, while the rest of the terms are the same as in the case of neutrons: 1-phonon scattering, 2-phonon scattering, etc. The main difference with respect to INS is that the change in energy is not measured. Instead, the incident energy is known and the number of nuclear-resonant fluorescence photons directly determines the phonon DOS.

The different elements of the transition matrix give all the possible scattering channels. If the system interacts with the x-ray, the eigenstates of the radiation field will be different. Coherent scattering occurs if the eigenstates of the nucleus remain the same, $|A\rangle \neq |B\rangle$, and it is further divided into coherent elastic if the eigenstates of system do not change, $|n_j\rangle = |n_i\rangle$, and coherent inelastic if they do. Incoherent scattering is the case discussed above when $|A\rangle \neq |B\rangle$, and for nuclear-resonant scattering, it implies a change in the system eigenstate, $|n_j\rangle \neq |n_i\rangle$. Furthermore, there are several incoherent scattering channels, such as nuclear-resonant fluorescence and atomic fluorescence after nuclear absorption. The nuclear-resonant fluorescence is specifically what is measured with NRIXS. Detailed descriptions and derivations (in the framework of quantum electrodynamics) are given in Ref. [160]. An excellent discussion of the coherent/incoherent - elastic/inelastic combinations can be found in Ref. [151].

The nature of NRIXS has important implications. Since it is completely incoherent, the (normalized) phonon DOS curves do not have any $\mathbf{Q}$ dependence. The incoherent approximation that must be followed when acquiring phonon DOS curves from INS is exact in the case of NRIXS, so phonon DOS curves from NRIXS are very accurate, but cannot provide direct information on the phonon dispersions. It is possible to calculate the dispersion by fitting the NRIXS data with a Born-von Kármán model such as in section 5.4. It can only be used to measure Mössbauer isotopes, so the motions of the other elements in the system are not measured. When there is more than one

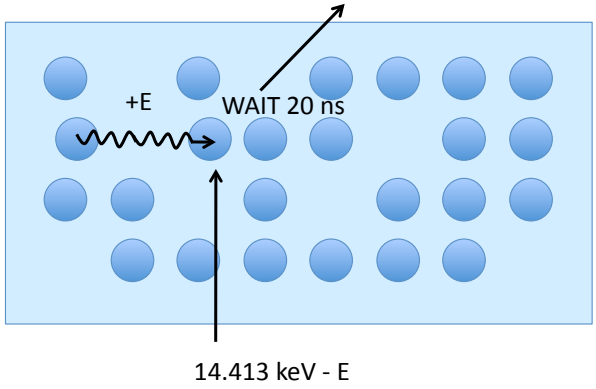

Figure 2.3: Schematic of a nuclear-resonant inelastic x-ray scattering measurement. Straight lines are x-ray paths, the wavy line represents a lattice vibration, the blue circles represent the nuclei of a Mössbauer isotope, and the empty sites represent that NRIXS is only sensitive to the motion of these nuclei.

element, the phonon DOS curves are 'partial.' For the work presented here, the motions of the ^{57}Fe isotope were measured and are referred to as Fe partial phonon DOS curves.

2.2.2 Technique

As mentioned in the previous section, it was predicted early (in 1960) that lattice vibrations could be obtained experimentally from the nuclear-resonant absorption of radiation, but the cross sections are too small to be measured by radioactive sources available at the time. Ruby proposed to use synchrotron radiation with time discrimination to excite the nuclear state [161], which was eventually achieved by three groups in 1995 [162–164] when technical developments finally allowed it.

Because of its small scattering cross section, NRIXS measurements require a bright source of x-rays of the appropriate energy to excite the nuclear state of the Mössbauer isotope at hand. Currently, this is possible at third-generation synchrotron facilities: SPring-8 in Japan, the European Synchrotron Radiation Facility in France, and the Advanced Photon Source in the U.S.A. The energy has to tuned to the nuclear transition energy the Mössbauer isotope of interest. Radiation of this energy is produced by setting the separation of the poles in an undulator inserted into the storage ring. The beam is then monochromatized by a water-cooled high-heat-load monochromator (composed of two diamonds at the APS) and a silicon crystal high-resolution monochromator decreases the bandwidth to a few meV. The energy selection is achieved through the crystal reflections. Finally, the beam is focused with Kirkpatrick-Baez (KB) mirrors [165]. The beam size at HP-CAT 16ID-D is 30 $\times$ 50 μm using 1-meter-long KB mirrors. Samples with an area much larger than that are not necessary for NRIXS measurements. This also allows to measure samples in a diamond-anvil cell (DAC). Another requisite for the technique is that the radiation has a pulsed

structure, and the pulses are separated by long intervals relative to the decay time of electronic excitations, usually around 200 ns. The timing is used to discriminate photons produced by nuclear scattering from those that are scattered by electrons or pass through the sample without interacting. Nuclear-resonant-scattered photons are delayed due to the finite lifetime of the nuclear excited state, while scattering due to electrons happens almost instantly. Vetoing the first few ns assures that the radiation detected is from nuclear x-ray scattering.

The diagram in Fig. 2.3 shows the basic principle of NRIXS. X-ray radiation detuned from the nuclear-resonant energy (14.413 keV for ^{57}Fe) by an amount E is directed towards the sample. This differential is of a few tens of meV or less and is obtained with the high-resolution monochromator. Radiation of this energy can create or annihilate a phonon (or a combination of phonons) of energy E in the material, losing or gaining an energy equal to that of the phonon. This interaction tunes the photon energy to exactly the resonance energy, so it can be absorbed and reemitted a few ns later. Fast electronics are synchronized with the revolutions of the electron beam in the storage ring. Avalanche photodiode detectors (APD) are placed as close as possible to the sample to cover the largest solid angle and are programed to start detecting radiation a fixed time after the electron pulse, usually 10 to 20 ns, and to keep doing it until a few ns before the next pulse. Measurements are taken for a few seconds at each energy in the energy range of the measurement, with an energy step of 0.5 meV and ranges of between $\pm$80 to $\pm$120 meV for the experiments presented here. Scans usually take between 30 minutes and 1 hour, and several scans are taken with the same experimental conditions. When the APD has to be farther away from the sample because of the sample environment (a DAC and a furnace for the work presented here), more scans are necessary to improve the counting statistics. A second APD is placed a meter or so in from of the sample. The radiation that goes through the sample at the resonance energy is coherent, so this measures the resolution function of the instrument. Finally, notice that atoms are missing in the lattice shown in Fig. 2.3. This is to represent that only the motions of the Mössbauer isotope of interest, the blue atoms, can be detected. More details about the experimental setup are given in Ref. [166].

2.2.3 Data reduction

The reduction of NRIXS data is comparatively easy and was performed using the program PHOENIX [167]. The elastic peak is removed using the resolution function $\mathcal{R}(E)$, either measured in situ or simulated using a function consisting of a Gaussian-like fit to the elastic peak minus the 1-phonon contribution expected from a Debye solid. The multiphonon scattering is then removed using the Fourier-log method [168]. In this method, the measured intensity

$$\mathcal{I}(E) = c\,\mathcal{R}(E) + a\,f_{\mathrm{LM}} \sum_{n}^{\infty} \int g_n(E\prime)\mathcal{R}(E - E\prime)dE\prime \,, \tag{2.12}$$

where a and c are normalization constants and the n-phonon DOS curve $g_n(E)$ depends recursively on the 1-phonon function

$$g_{n+1}(E) = \frac{1}{n+1} \int g_n(E\prime) g_1(E - E\prime) dE\prime \ . \tag{2.13}$$

Eqs. 2.12 and 2.13 have a simple representation in reciprocal space,

$$\tilde{g}_1(E) = \ln \left[1 + \frac{\tilde{\mathfrak{J}} - c\,\tilde{\mathcal{R}}}{a\, f_{\mathrm{LM}} \tilde{\mathcal{R}}} \right] \ , \tag{2.14}$$

where the tilde indicates the Fourier transform. $\mathfrak{S}(E)$ is then the inverse Fourier transform of $\tilde{g}_1(E)$.

Chapter 3

Order-disorder phase transition in FeV

3.1 Introduction

Vibrational entropy makes major contributions to the free energies of alloy phases and their relative thermodynamic stabilities [38]. For chemical ordering transitions in alloys, the changes of vibrational entropy can be comparable to the large decrease in configurational entropy that accompanies ordering [2]. Ordering transitions are driven by the energetics: the bonds between atoms of different elements are, on average, more energetically favorable than bonds between atoms of the same type. An intuitive model using Lennard-Jones potentials developed by Garbulsky and Ceder [169] predicts that bonds that minimize the energy are also stiffer. This explains the usual thermodynamic effect of the vibrational entropy on systems that undergo chemical ordering but keep the same underlying lattice, which is to stabilize the disordered phase with respect to the ordered one. Experimental work regarding this effect can be found in Refs. [2, 170–177] and computational work in Refs. [178–185]. The behavior in FeV is the opposite, and to the best of our knowledge it is the first and (so far) only system in which such exceptional behavior has been observed experimentally. We attribute this effect to a difference in the electronic screening between the two phases and our arguments are presented in the next few sections. The vibrational entropy difference between disordered and ordered phases for several systems is given in Table 3.1.

The Fe-V system has been fertile ground for experimental studies of the relationship between structure and magnetism and it has been investigated thoroughly. The phase diagram for the Fe-V system is shown in Fig. 3.1. The two elements form a bcc random solid solution at high temperatures for all compositions. The sigma phase, a low-symmetry tetragonal phase with 30 atoms distributed in a nonstoichiometric way over 5 crystallographic sites, is thermodynamically stable around the equiatomic composition at lower temperatures, but it can be avoided easily by quenching. Quenched samples typically have a small degree of $B2$ ordering, but almost complete order can be achieved

Table 3.1: Experimental and calculated values for the difference in vibrational entropy between disordered and ordered phases in selected systems. References are given.

System	Transformation	Experimental	Calculated
FeV	$B2 \rightarrow$ bcc	-0.22 [186]	-
Ni_3Al	$L1_2 \rightarrow$ fcc	0.10–0.30 [2, 172]	0.00–0.29 [178–181]
Fe_3Al	$D0_3 \rightarrow$ bcc	0.10 [174]	0.11 [185]
Cu_3Au	$L1_2 \rightarrow$ fcc	0.14 [173]	0.08–0.12 [181–183]
Co_3V	$L1_2 \rightarrow$ fcc	0.15 [175]	-
FeCo	$B2 \rightarrow$ bcc	0.03 [177]	-
Pd_3Cu	$L1_2 \rightarrow$ fcc	-	0.03 [184]
Pd_3Au	$L1_2 \rightarrow$ fcc	-	0.07 [184]
Cu_3Pd	$L1_2 \rightarrow$ fcc	-	0.03 [184]
CuAu	$L1_0 \rightarrow$ fcc*		0.18 [182]
Pd_3V	$D0_{22} \rightarrow$ fcc*	0.04 [176]	-0.07 [130]
Ni_3V	$D0_{22} \rightarrow$ fcc*	0.04 [187]	-
$AlTi_3$	$L1_2 \rightarrow$ fcc	-	0.12 [188]
Al_3Ti	$L1_2 \rightarrow$ fcc	-	0.23 [188]
$AlHf_3$	$L1_2 \rightarrow$ fcc	-	0.18 [188]

* The $L1_0$ and $D0_{22}$ are tetragonal structures based on the cubic fcc structure.

by annealing [189, 190]. The magnetic moment decreases from the value of the bulk Fe as the V concentration increases until it disappears at a composition of about 70 at. % V [191–193], although it depends strongly on its state of order [193–196]. First principles calculations by several methods have successfully reproduced the trends in the magnetism [22, 193, 197–202] and predict a small charge transfer from the V to the Fe atoms and the development of an antiparallel magnetic moment at the V atoms.

This chapter presents inelastic neutron scattering (INS) and nuclear resonant inelastic x-ray scattering (NRIXS) measurements performed on FeV in two different states of $B2$ order. The two methods are complementary as discussed in Chapter 2, and combining the data sets allows the determination of motions of the Fe and V atoms separately. The main observation is that the phonons in FeV become softer upon ordering, so the vibrational entropy is higher in the ordered phase than in the disordered phase. It is also observed that the softening is greater for the V atoms than for the Fe atoms, and for the transverse modes than for the longitudinal modes. The number of Fe–V bonds increases upon ordering and are energetically favorable. The measured difference in vibrational entropy at room temperature is $0.14 \pm 0.02\, k_B$/atom and we estimate that the difference is $0.22 \pm 0.03\, k_B$/atom between the states of perfect order and perfect disorder. The error margins are from counting statistics and propagation of error, but are on the conservative side.

A cluster expansion analysis was performed on the neutron-weighted phonon density of states (NWDOS) curves obtained from INS to study the effects of composition and ordering. By measuring the system in two degrees of order, it was possible to discriminate the effect of first and second nearest

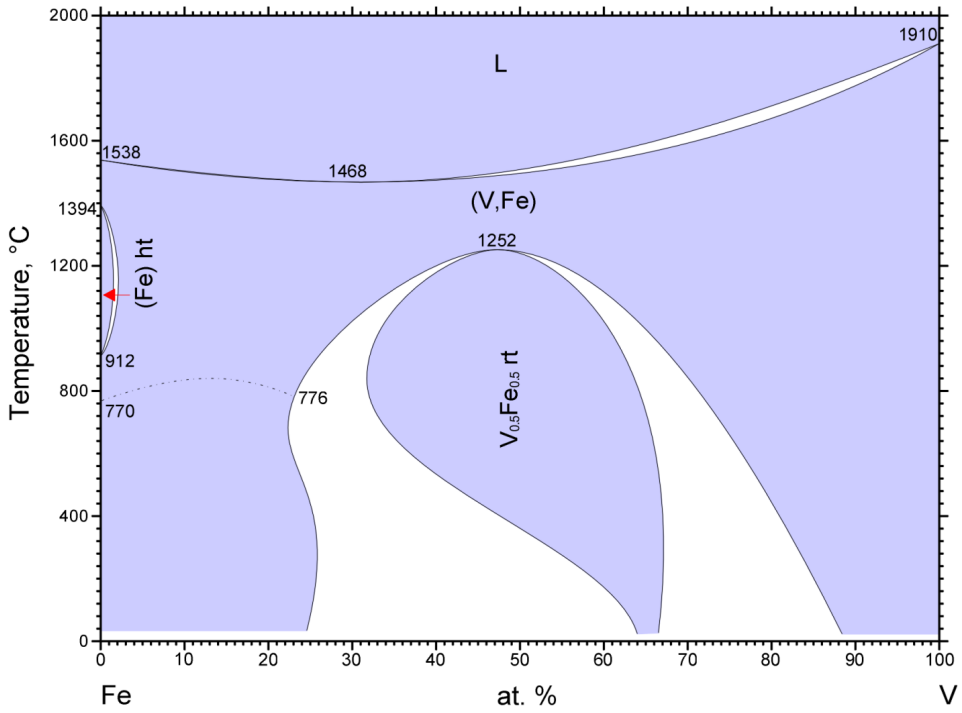

Figure 3.1: Fe-V phase diagram adopted from ASM International Alloy Phase Diagrams Center [203].

neighbors (nn) on the NWDOS curves. In the $B2$ structure, the 1nn are Fe–V bonds and the 2nn are Fe–Fe or V–V bonds. It was observed that an increase in the number of Fe–V 1nn bonds results in an overall softening of the NWDOS curves while the increase in the number of Fe–Fe and V–V bonds produces a stiffening, but of smaller magnitude than the 1nn effect. This phenomenological result is consistent with softer Fe-V bonds.

An analysis was performed at the electronic structure level to explain the phenomenon. First principles calculations show how the better electronic screening can cause a decrease of the average energy of the phonons in the ordered phase. At the Fermi level, the projected electronic DOS at the V atoms undergoes a larger increase with ordering than the projected electronic DOS at the Fe atoms, correlating with the larger phonon softening of the V motions. The measured shear modulus G, which is related to the transverse atomic motions, decreases upon ordering, consistent with the observed softening of the transverse modes. The bulk modulus B, which is related to the longitudinal modes, increases upon ordering, but the effect of ordering on the high energy peak is small. The intraband generalized susceptibility as a function of the phonon wavevector $\chi(\mathbf{q})$ was calculated along high-symmetry directions for the majority band electrons. Although the

generalized susceptibility cannot discriminate between transverse and longitudinal modes, it shows that the combined electronic response is isotropic. It also shows that electronic screening is better in the ordered state than in the disordered state by the same ratio in all reciprocal space directions and that its efficiency decreases for motions of higher frequency. The high temperature behavior of the phonon NWDOS curves was successfully explained using a quasiharmonic model.

3.2 Experimental

3.2.1 Sample preparation

A FeV sample for INS measurements was prepared by arc-melting vanadium slugs of 99.8% purity and iron lumps of 99.98% purity in the stoichiometric ratio under a high-purity argon atmosphere. There was no detectable mass loss and no visible oxidation after melting. The ingots were cold-rolled in between steel sheets to a thickness of 1.1 mm corresponding to a neutron scattering probability of about 10%. Additional samples of elemental Fe and V of the purity specified above were also prepared for INS measurements by cold-rolling them to a thickness of 0.7 and 1.9 mm, respectively. The as-prepared FeV sample was mostly in the (disordered) $A2$ phase as evidenced by the low intensity of the superlattice diffraction peaks in the diffraction pattern obtained from the neutron scattering measurements (Fig. 3.2). The sample was then annealed in situ during the experiment at 773 K for 8 hours under vacuum and then cooled down to room temperature over 2 hours. The annealing induced $B2$ ordering as shown by the increase in the intensity of the superlattice diffraction peaks.

Two FeV samples for NRIXS measurements were prepared as described above, but they were 96.06% enriched with ^{57}Fe. The small ingots were cold-rolled to a thickness of 200 μm. One of them was annealed at 773 K in a sealed quartz tube under vacuum for 8 hours and then cooled down in the furnace to room temperature over 2 hours to reproduce the anneal treatment of the INS sample. A thin foil of the elemental ^{57}Fe used to make the FeV sample was also measured.

A third set of FeV samples was prepared for pulse-echo ultrasonic measurements. One sample received the same annealing treatment described before to induce ordering. Additionally, ingots of composition $Fe_{75}V_{25}$ and $Fe_{25}V_{75}$ as well as pure Fe and pure V were prepared. The ingots were cut with a diamond blade to obtain two parallel faces, then sanded to ensure parallelism, and finally polished to improve the quality of the measurements. The thickness of the samples varied between 0.7 and 1.2 cm. A digital point micrometer was used to measure the thickness in different parts of the samples and the parallelism was assessed to be better than 1 μm.

3.2.2 Scattering measurements

INS measurements were performed with the wide Angular-Range Chopper Spectrometer (ARCS) [149]. The nominal incident neutron energy was 80 meV. The energy resolution (FWHM) was 1.7 meV at 40 meV neutron energy loss, and 3.1 meV at the elastic line. The cold-rolled FeV sample was mounted in thin aluminum foil and held by an aluminum frame shielded with cadmium and placed inside a custom-built low background resistive furnace with thin aluminum shielding. Measurements were performed at room temperature on the as-prepared sample, at 773 K after the 8-hour anneal, and again at room temperature on the then $B2$-ordered sample. For measurements on elemental Fe and V at room temperature, the cold-rolled samples were mounted in thin aluminum foil and held by an aluminum frame shielded with cadmium.

NRIXS measurements [204] were performed at beamline 16ID-D of the Advanced Photon Source on elemental ^{57}Fe and the two ^{57}FeV samples with different degrees of $B2$ order. The incident photon energy was scanned from –80 to +80 meV in steps of 0.5 meV around the nuclear resonance energy (14.413 keV) of ^{57}Fe. The instrument resolution function measured in situ was 2.2 meV (FWHM). Each sample was placed on Kapton tape at a grazing angle to the incident x-ray beam. The NRIXS signal was measured with two avalanche photodiode detectors (APDs) with active areas in close proximity to each other, positioned 90° from the direction of the beam. All measurements were performed at room temperature.

3.2.3 Ancillary measurements

X-ray diffractometry with a Cu Kα (8.0 keV) source was performed on all the samples. Radiation of this energy does not produce detectable superlattice diffraction peaks because the difference of the atomic scattering factors of Fe and V is very small, but it was useful to show that the samples were bcc-based and to measure their lattice parameters. No oxidation or traces of the sigma phase were detected. High temperature measurements were performed in a commercial furnace in the temperature range 300 – 900 K. The lattice parameter at room temperature a and the coefficient of linear thermal expansion α for all samples are shown in Table 3.2.

The transverse and longitudinal sound velocities of the Fe-V samples were measured with ultrasonic pulse-echo instrumentation. An electrical pulser/receiver device was used with two 25 MHz transducers, one capable of producing shear waves and the other longitudinal waves. An oscilloscope was used for detecting and monitoring the waves and a computer program was used to record the signal. Bee honey was used to couple the transducers to the samples. More details on the instrumentation and technique are given in Ref. [205]. Densities were calculated from the lattice parameters obtained by x-ray diffractometry and B and G were obtained. Results are shown in Table 3.2.

Table 3.2: Measured and calculated composition dependence of the lattice parameter a, linear thermal expansion coefficient α, bulk modulus B, and shear modulus G for as-prepared Fe-V alloys. Experimental errors from standard deviations.

		Fe	$Fe_{75}V_{25}$	FeV	$Fe_{25}V_{75}$	V
a (± 0.003 Å)	Exp.	2.858	2.886	2.914	2.963	3.042
	Calc.	2.833	2.880	2.938	2.959	2.999
α ($\pm 0.5 \times 10^{-6}$ K^{-1})	Exp.	11.8	11.0	-	9.3	8.4
B (± 5 GPa)	Exp.	170	166	161	182	163
	Calc.	188	179	182	202	183
G (± 0.5 GPa)	Exp.	82.0	81.1	74.4	64.7	48.1
	Calc.	-	-	76.4	-	-

3.3 Experimental results

3.3.1 Short-range and long-range order

The raw INS spectra were re-binned into intensity I as a function of momentum transfer Q and energy transfer E as described in section 2.1.3. Neutron diffraction patterns were obtained by integrating $I(Q, E)$ over the energy range –5 to 5 meV and are shown in Fig. 3.2. The measurements were normalized by the number of incident neutrons on the samples. No other scaling was necessary because the mass, shape, and position of the sample were the same after the in situ anneal. The intensities of the fundamental bcc diffraction peaks did not change after the anneal.

The long-range order (LRO) parameter L is given by

$$L^2 = \frac{\mathcal{I}_s \bar{u}(\theta_f)^2 |b_{\mathrm{Fe}} + b_{\mathrm{V}}|^2 \mathcal{L}_f(\theta) m_f}{\mathcal{I}_f \bar{u}(\theta_s)^2 |b_{\mathrm{Fe}} - b_{\mathrm{V}}|^2 \mathcal{L}_s(\theta) m_s} \ , \tag{3.1}$$

where $\mathcal{I}$ is the integrated intensity of the appropriate peak, $\bar{u}(\theta)$ is the Debye-Waller amplitude as a function of the scattering angle θ, b is the neutron coherent scattering length, $\mathcal{L}$ is the Lorentz factor, and m is the multiplicity of the diffracting planes. The subscripts f and s refer to the fundamental and superlattice diffraction peaks. To calculate $\bar{u}(\theta)$, a thermal atomic displacement factor of 2.8×10^{-3} Å^2 was used [196]. Results for L calculated using the (110) fundamental diffraction peak and the (100) superlattice diffraction peak are: 0.34 for the as-prepared sample and 0.87 for the annealed sample (Table 3.4).

The diffuse scattering intensity from the as-prepared sample in the region from, e.g., 1 to 2 Å^{-1}, is from short-range order (SRO) in the sample, and it disappeared after the sample was annealed. The Warren-Cowley parameters were determined from the diffraction patterns following the method

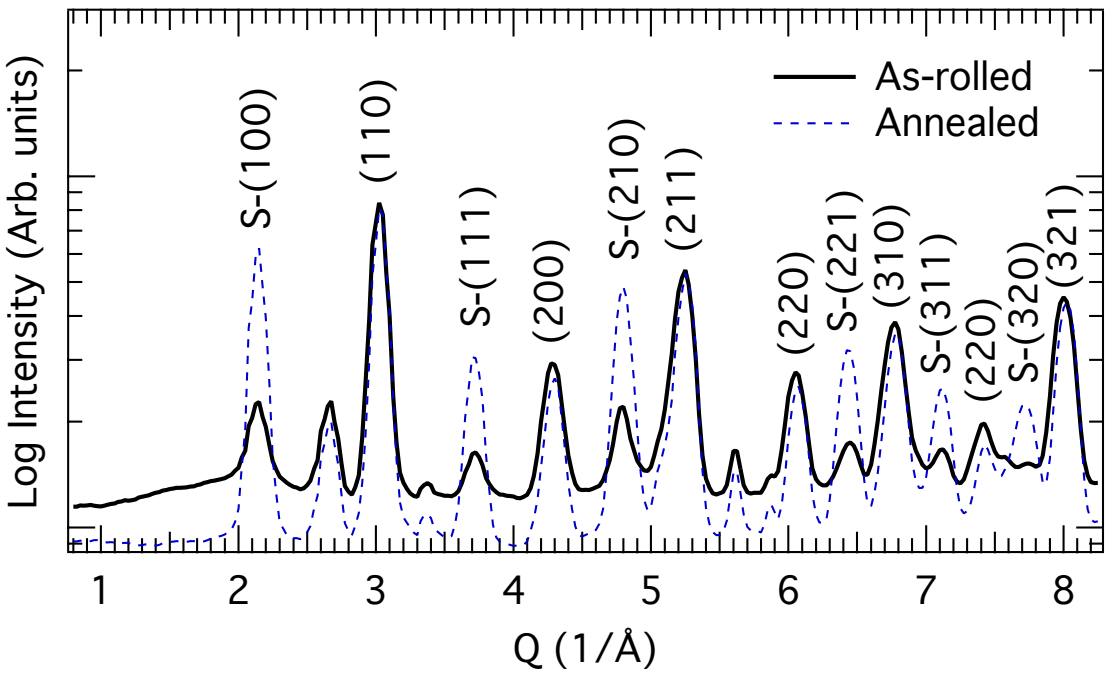

Figure 3.2: Neutron diffraction patterns of FeV samples obtained by integrating over the energy in the elastic region of $I(Q, E)$ (see text for details). Fundamental and superlattice diffraction peaks are marked. Unmarked peaks are from the Al shielding.

of B. E. Warren [206], fitting the diffuse intensity to the series representation of the ratio of the SRO intensity I_{SRO} to the Laue monotonic scattering I_{LMS}

$$\frac{I_{\mathrm{SRO}}}{I_{\mathrm{LMS}}} = 1 + n_1\alpha_1\frac{\sin kr_1}{kr_1} + n_2\alpha_2\frac{\sin kr_2}{kr_2} + \ldots \tag{3.2}$$

where n_i and r_i are the coordination number and radius of shell i, and $k = 4\pi\sin\theta/\lambda$ (λ is the incident neutron wavelength). To separate the effects of SRO from other contributions to the diffuse scattering, the difference in diffuse scattering between the as-rolled and annealed samples was used to evaluate I_{SRO}. The resulting Warren-Cowley parameters are: $\alpha_1 = -0.29$, $\alpha_2 = 0.05$, and $\alpha_3 = -0.11$. The parameters are consistent with partial $B2$ ordering.

3.3.2 Phonon DOS curves and vibrational entropy

NWDOS curves were obtained from INS data reduced by the method described in section 2.1.3 and the results are shown in Figs. 3.3 and 3.5. Fe partial phonon DOS curves were obtained from NRIXS data reduced by the method described in section 2.2.3 and the results are shown in the middle panel of Fig. 3.4. The neutron scattering efficiency of each element is proportional to the neutron scattering cross section divided by the molar mass, σ/M, which is 0.208 and 0.100 barns/amu for Fe and V, respectively. Thus, Fe motions are overemphasized in the NWDOS curves by about a 2:1

ratio. Subtracting the excess weight of the Fe partial phonon DOS obtained from NRIXS gives the neutron-weigh corrected phonon DOS (top panel of Fig. 3.4), and subtracting all the Fe weight gives the V partial phonon DOS (bottom panel of Fig. 3.4). All the phonon DOS curves show significant softening after the alloy was annealed to develop $B2$ order. The whole spectrum softens, but the low-energy modes are affected most. The general softening upon ordering in the V partial phonon DOS is larger than in Fe. The larger V uncertainties are due to their lower neutron scattering efficiency.

The vibrational entropy per atom S_{vib} was calculated in the quasiharmonic formalism [38]. From the phonon DOS curves shown in Fig. 3.3, the vibrational entropy per atom at room temperature was found to be 3.15 ± 0.01 k_{B} in pure Fe and 3.64 ± 0.01 k_{B} in pure V. The results for the FeV samples are given in Table 3.4. The vibrational entropy of formation $\Delta S_{\mathrm{vib}}^{\mathrm{form}} = -0.07 \pm 0.02\, k_{\mathrm{B}}$/atom for the as-rolled sample and $+0.07 \pm 0.02\, k_{\mathrm{B}}$/atom for the annealed sample. For our samples in an initial state of partial disorder, the vibrational entropy of ordering $\Delta S_{\mathrm{vib}}^{\mathrm{ord}} = +0.14 \pm 0.02\, k_{\mathrm{B}}$/atom. From the change upon ordering of the V partial phonon DOS and the Fe partial phonon DOS, the V and Fe contributions to the vibrational entropy of ordering are $+0.16 \pm 0.05\, k_{\mathrm{B}}$ per V atom, and $+0.08 \pm 0.02\, k_{\mathrm{B}}$ per Fe atom. L changed from 0.34 to 0.87, and we can use this information to obtain $\Delta S_{\mathrm{vib}}^{\mathrm{A2}\rightarrow\mathrm{B2}} = 0.22 \pm 0.03\, k_{\mathrm{B}}$/atom, the total change of vibrational entropy expected between states of full disorder and full order. For this estimate, we assumed that the change in vibrational entropy scales with the fractional change of Fe–V bonds. The total fraction of Fe–V bonds is $(1 + L^2)/2$. As it will be shown in section 3.4, the cluster expansion formalism predicts the same number. The same correction was used for the partial vibrational entropies for Fe and V atoms in Table 3.4.

3.3.3 Thermal Grüneisen parameter

The thermal softening of phonons in the $B2$ phase of FeV, shown in Fig. 3.5, is consistent with expectations from the quasiharmonic approximation. The thermal Grüneisen parameter is given by

$$\bar{\gamma} = -\frac{Bv\beta}{C_{\mathrm{P}}}, \tag{3.3}$$

where B is the bulk modulus, v is the specific volume, β is the volume thermal expansion, and C_{P} is the heat capacity at constant pressure. We obtained $\bar{\gamma} = 1.45$ using our values for the nominator of Eq. 3.3 and the values from Ref. [207] for the denominator. The curve labeled 'QH' in Fig. 3.5 was obtained by compressing the energy scale for the curve for 300 K by the quantity $\bar{\gamma}\beta\Delta T$ and renormalizing the total intensity.

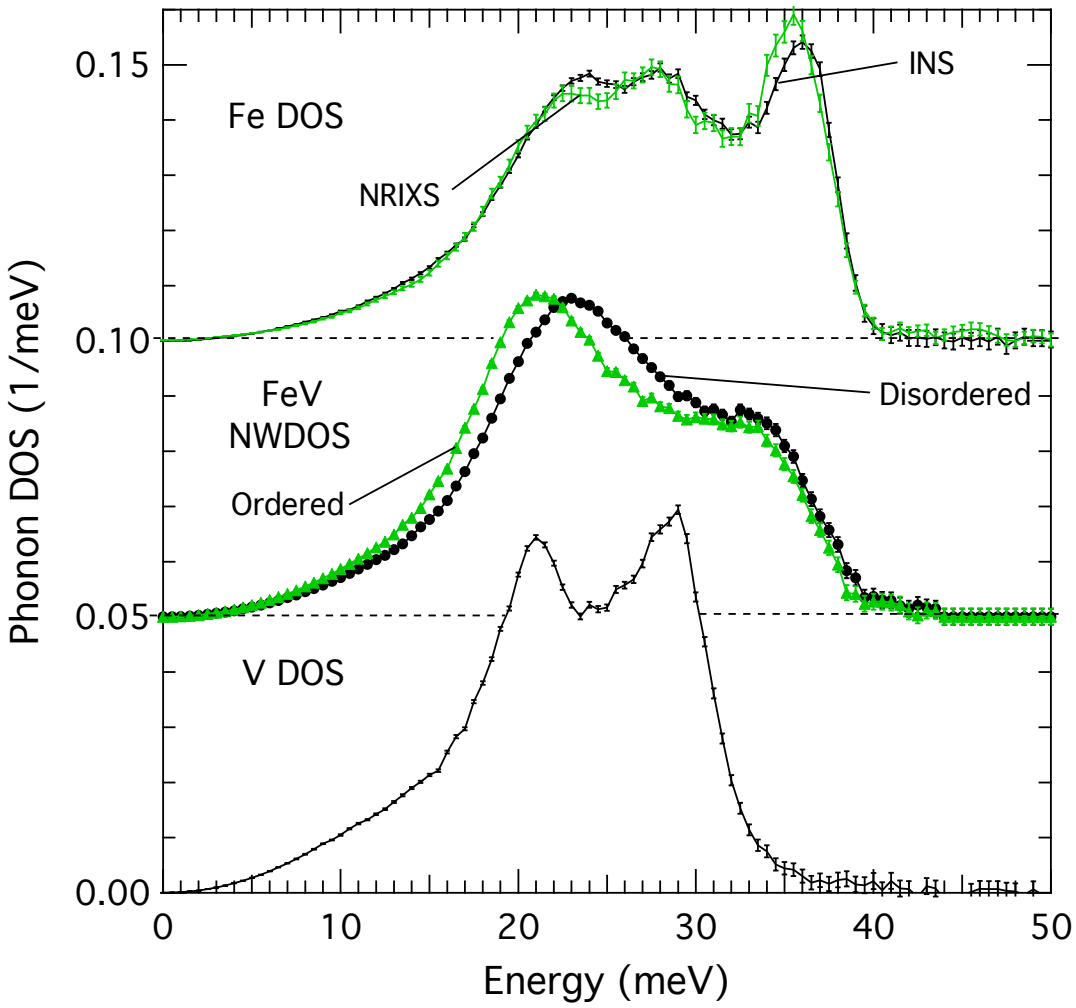

Figure 3.3: Phonon DOS curves of pure Fe measured by INS and NRIXS (top panel). Neutron-weighted phonon DOS curves of FeV alloys (middle panel), and pure V (bottom panel) measured by INS. Error bars are from counting statistics.

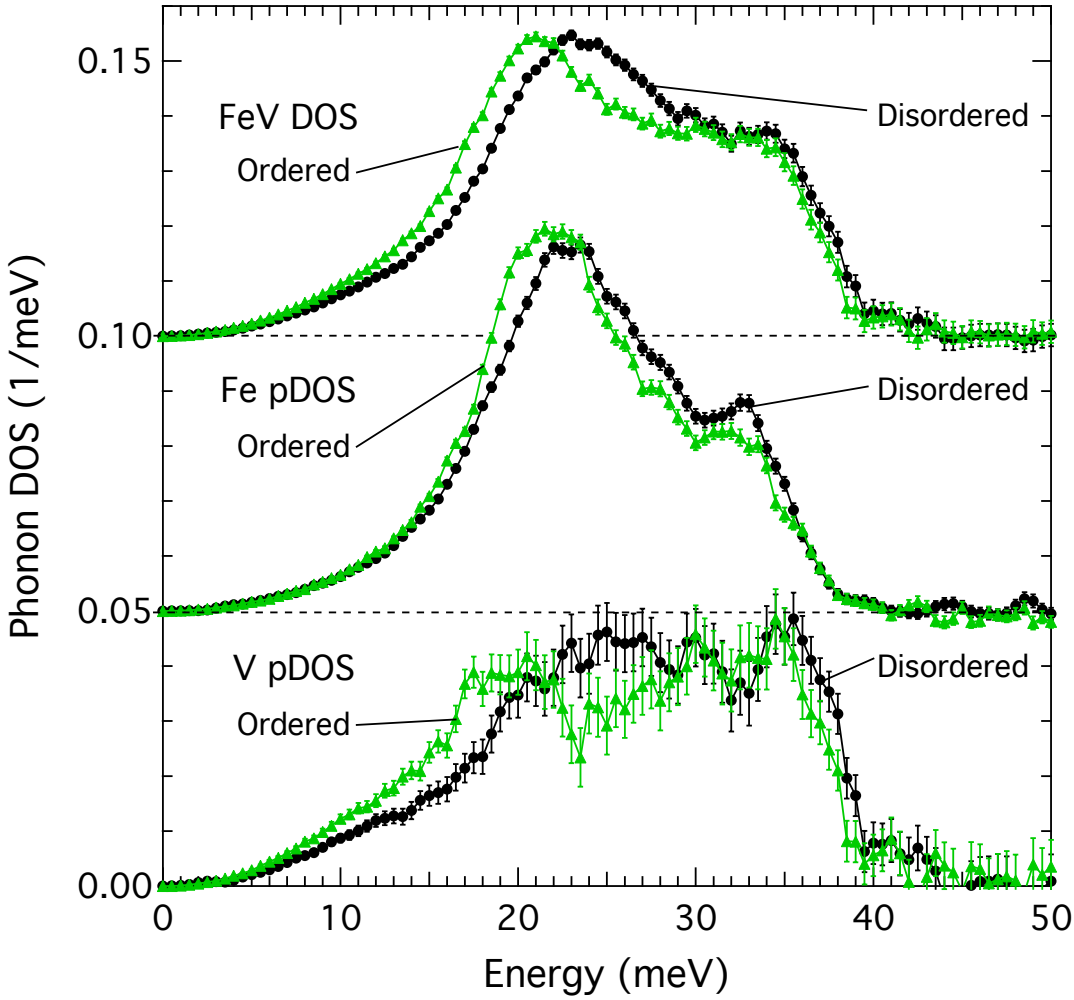

Figure 3.4: Neutron-weight-corrected phonon DOS curves of FeV samples (top panel), along with Fe partial phonon DOS curves (middle panel), and V partial phonon DOS curves (bottom panel). The Fe partial phonon DOS curves were determined directly by NRIXS measurements; the total FeV DOS curves and the V partial phonon DOS curves were obtained by combining INS and NRIXS spectra. Error bars are from counting statistics in the Fe partial phonon DOS, and propagation of error in the other curves.

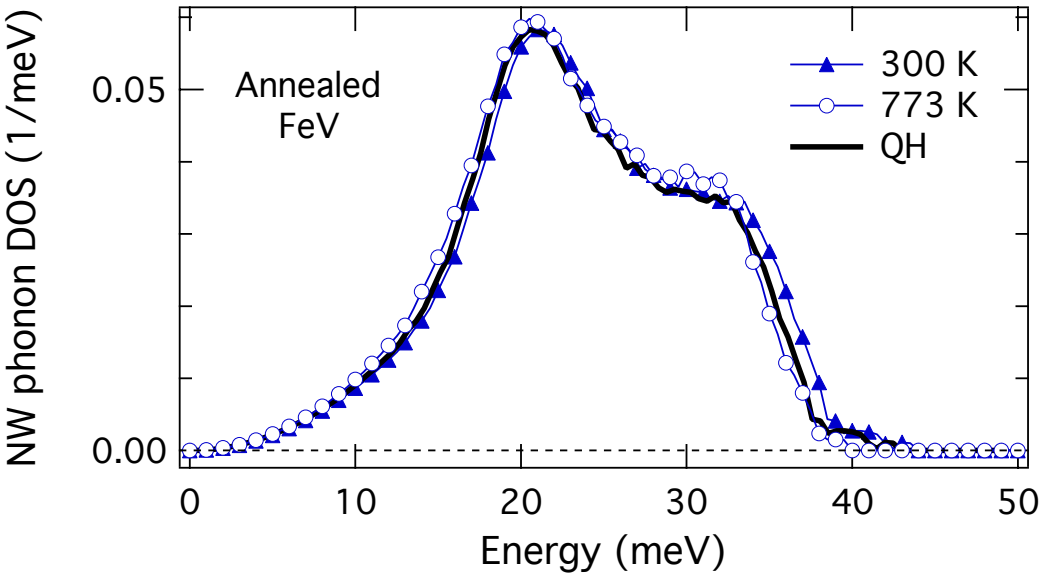

Figure 3.5: Neutron-weighted phonon DOS curves of $B2$ FeV at room temperature and at 773 K, along with the quasiharmonic model prediction at 773 K.

3.4 Cluster expansion

The cluster expansion and cluster inversion methods were developed for scalar quantities, but have been successfully used on phonon DOS curves obtained by NRIXS [208] and INS [177, 209]. A correction is necessary to account for the different phonon cutoff energies E_c of the different systems, which are mainly dependent on the bond length *vs* bond stiffness relation. The cluster expansion space is technically infinite-dimensional, but the technique is robust because the convergence to valid results is very rapid. The theoretical background is summarized in section 1.3.

For the present analysis, we used the NWDOS curves of the as-prepared and annealed FeV, along with measurements on pure Fe and pure V (Fig. 3.3) to calculate the neutron-weighted interaction phonon DOS (IPDOS) curves $\mathcal{G}_{n,k}$ for the Fe-V system. The spin variables σ_p were assigned a value of $+1$ for an Fe occupied site and -1 for a V occupied site, therefore the correlation functions $-1 \leq \xi_{n,k} \leq +1$. As mentioned before, n is the order of the cluster and k is the relative distance between sites, and the correlation function (Eq. 1.60) is a scalar value that represents an atomic configuration. The numerical values that can be assigned to σ_p have some geometric constrains but are not unique. Nevertheless, an Ising-like assignment of the variables is simple and convenient for the case of a binary system. The advantages will be discussed below.

In previous work on the Fe-Cr [208, 209] and Fe-Co [177] systems, k was neglected by grouping together 1nn and 2nn, which is an acceptable simplification in bcc-based systems because the difference in bond length is small. More information is available on the Fe-V system because phonon

Table 3.3: Values of the cluster expansion correlation functions and cutoff energy of the measured FeV samples and interpolated $A2$ and $B2$ structures.

Correlation	Fe	$A2$	As-prepared	Annealed	$B2$	V
$\xi_{0,0}$	+1	+1	+1	+1	+1	+1
$\xi_{1,1}$	+1	0	0	0	0	-1
$\xi_{2,1}$	+1	0	-0.34	-0.87	-1	+1
$\xi_{2,2}$	+1	0	+0.05	+0.87	+1	+1
Cutoff (meV)	40.5	43.0	42.4	41.4	41.2	35.2

DOS curves of the same composition with different degrees of order were obtained. When $\sigma_p = \pm 1$, the correlation functions for the pair contributions $\xi_{2,k}$ can be mapped to the Warren-Cowley SRO parameters for the k-th nearest neighbors, so we expanded the method accordingly. The IPDOS curves are the basis of the cluster expansion, but at least the low order terms have clear physical meaning: the empty term (null vector) $\mathcal{G}_{0,0}$ is the phonon NWDOS of an equiatomic random solid solution of A and B atoms; the point term $\mathcal{G}_{1,1}$ shows the effect of composition; in the $B2$ structure, the pair term $\mathcal{G}_{2,k}$ is the effect of the number of like ($k = 1$) and unlike ($k = 2$) pairs of atoms in the system.

The cutoff energy of each NWDOS curve (Table 3.3) is different, so we normalized the energy range to 1 and the IPDOS curves of Fig. 3.6 are a function of the rescaled energy $\mathcal{E}$. For consistency, the cutoff energy was defined to be $x_0 + 2s$ where x_0 is the centroid and s the standard deviation of a Gaussian fitted to the high energy peak of each NWDOS. The cutoff energy in the $A2$ and $B2$ cases was extrapolated by assuming a linear relation with the degree of order, since the lattice parameter decreases linearly with the degree of order [196].

For $\mathcal{G}_{n,k}$ with $n \geq 1$, the conservation of normal modes condition requires that for rescaled energy $\mathcal{E}$,

$$\mathcal{G}'_{n,k}(\mathcal{E}) = \frac{1}{K}[\mathcal{G}'_{0,0}(\mathcal{E}) + \mathcal{G}_{n,k}(\mathcal{E})] - \mathcal{G}'_{0,0}(\mathcal{E}) \ . \tag{3.4}$$

Here, $\mathcal{G}'_{0,0}$ is the normalized empty term IPDOS curve and

$$K = \frac{\sum_{\mathcal{E}=0}^{1} \mathcal{G}'_{0,0}(\mathcal{E})}{\sum_{\mathcal{E}=0}^{1} [\mathcal{G}'_{0,0}(\mathcal{E}) + \mathcal{G}_{n,k}(\mathcal{E})]}. \tag{3.5}$$

This is a useful way to present IPDOS curves because $\mathcal{G}'_{n,k}(\mathcal{E})$ is the magnitude of the effect of a higher order ($n \geq 1$) IPDOS on the cluster expansion reconstructed DOS curve of an equiatomic random solid solution ($\mathcal{G}'_{0,0}$). Simple scaling by the value of the appropriate correlation function $\xi_{n,k}$ gives the contribution to the NWDOS from the atoms in the cluster n and shell k. The values

for the correlation functions using $\sigma_p \pm 1$ are shown in Table 3.3. $\xi_{0,0} \cdot \mathcal{G}_{0,0}$ is the null vector of the basis, so $\xi_{0,0}$ is always $+1$ for every composition and configuration. $\xi_{1,1} \cdot \mathcal{G}_{1,1}$ is the effect of composition, so $\xi_{1,1}$ goes from $+1$ for pure Fe to -1 for pure V and it is zero at the equiatomic composition. $\xi_{2,1} \cdot \mathcal{G}_{2,1}$ is the effect of ordering in the 1nn shell, so $\xi_{2,1}$ goes from $+1$ when the an atom A has a 100% chance of having an atom B as a 1nn to 0 when there is no correlation to -1 when the an atom A has a 100% chance of having an atom A as a 1nn. Similarly for $\xi_{2,2} \cdot \mathcal{G}_{2,2}$ in the case of 2nns. With this information, it is possible to interpolate the phonon NWDOS curves of FeV for any composition and state of order.

In Fig. 3.6 we observe that when $B2$ order develops, $\xi_{2,1}$ is negative, and the effect of forming pairs of unlike atoms in the first coordination shell is given by the negative of $\mathcal{G}'_{2,1}$. The method predicts that ordering in the first shell will produce a general increase in the number of low energy phonons, particularly between $\mathcal{E} = 0.35$ and $\mathcal{E} = 0.55$, and a decrease in the number of higher energy phonons (a softening). Ordering in the second shell, which is between pairs of like atoms in the $B2$ structure, partially offsets this effect by reducing the number of phonons in the range $0.4 < \mathcal{E} < 0.7$ while increasing the number of phonons above this energy (a stiffening). Nevertheless, the positive area under $\mathcal{G}'_{2,2}$ (the number of phonons affected) is only 58% that of $\mathcal{G}'_{2,1}$, which is intuitively expected because the distance between second nearest neighbors is greater than between first nearest neighbors and the number of second nearest neighbors is smaller. The combined effect of ordering in the first and second shells is also shown in Fig. 3.6.

The IPDOS functions were used to reconstruct the NWDOS of the equiatomic FeV in the $A2$ and $B2$ cases and the results are shown in Fig. 3.7. There is very little difference between the reconstructed NWDOS for the perfect $B2$ case and the annealed sample. The reconstruction for the $A2$ case is considerably stiffer than the as-prepared sample, although the higher cutoff energy is partially responsible for this. The vibrational entropies for the $A2$ and $B2$ cases were 3.28 and $3.50 \pm 0.03\, k_B$ per atom, a difference of $\Delta S_{\text{vib}}^{\text{A2}\rightarrow\text{B2}} = 0.22 \pm 0.04\, k_{\text{B}}$ per atom, in agreement with the value obtained in section 3.3.2.

3.5 Computational

3.5.1 Electronic structure

The electronic DOS was calculated from first principles using DFT for the $A2$ and $B2$ cases (Fig. 3.8). The disordered structure was simulated with the 16-atom special quasirandom structure (SQS) of Jiang et al. [210]. This defers errors due to periodicity to distant neighbors which have considerably smaller effects. More details about the construction of SQSs and their application are given in section 1.4. The correlation functions of the SQS used for the calculations are identical to the random solid solution up to the fifth nearest neighbors.

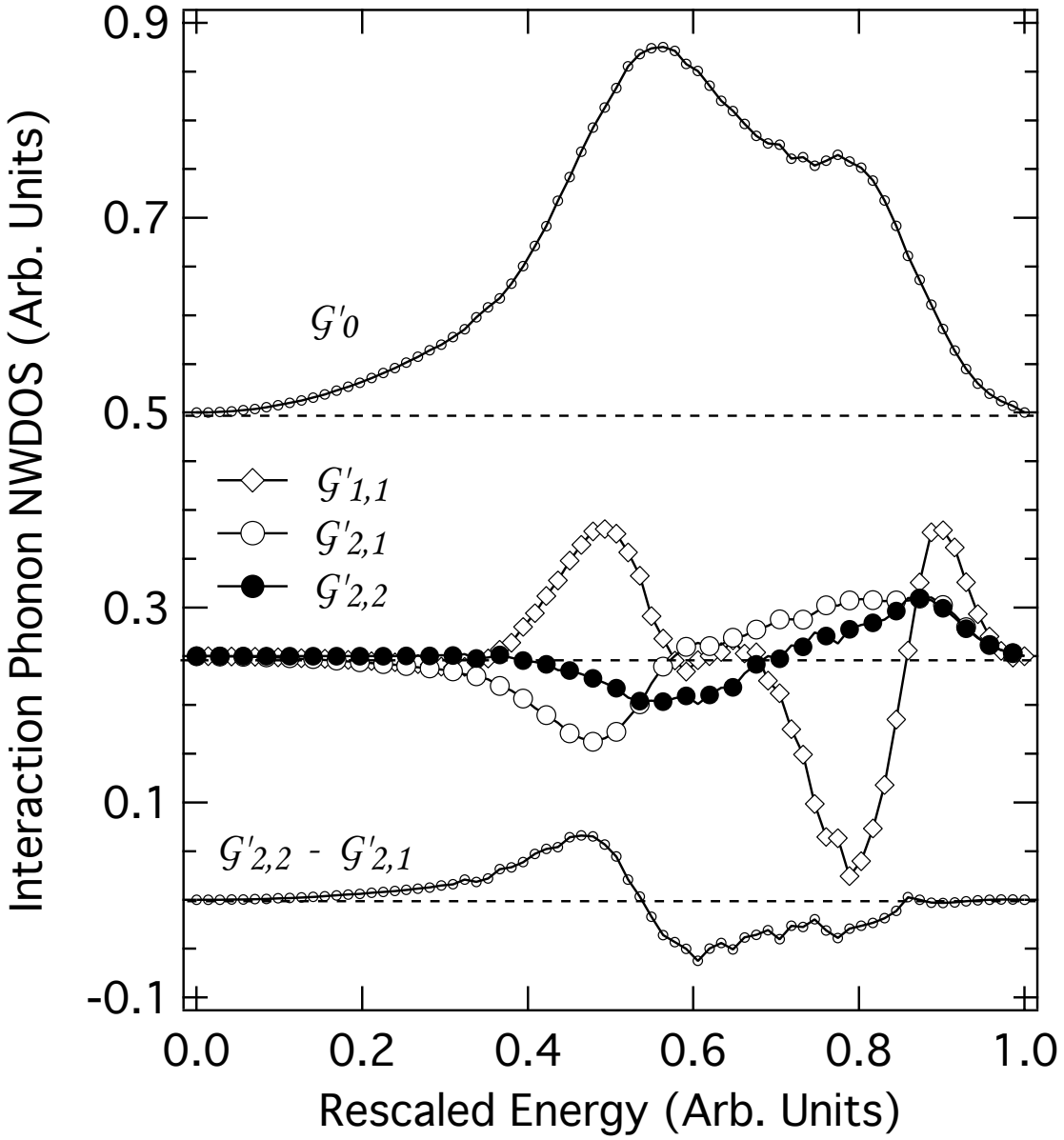

Figure 3.6: Phonon-conserving Interaction Phonon NWDOS curves obtained from the cluster inversion method. The effect of ordering in the system is $\mathcal{G}'_{2,2} - \mathcal{G}'_{2,1}$.

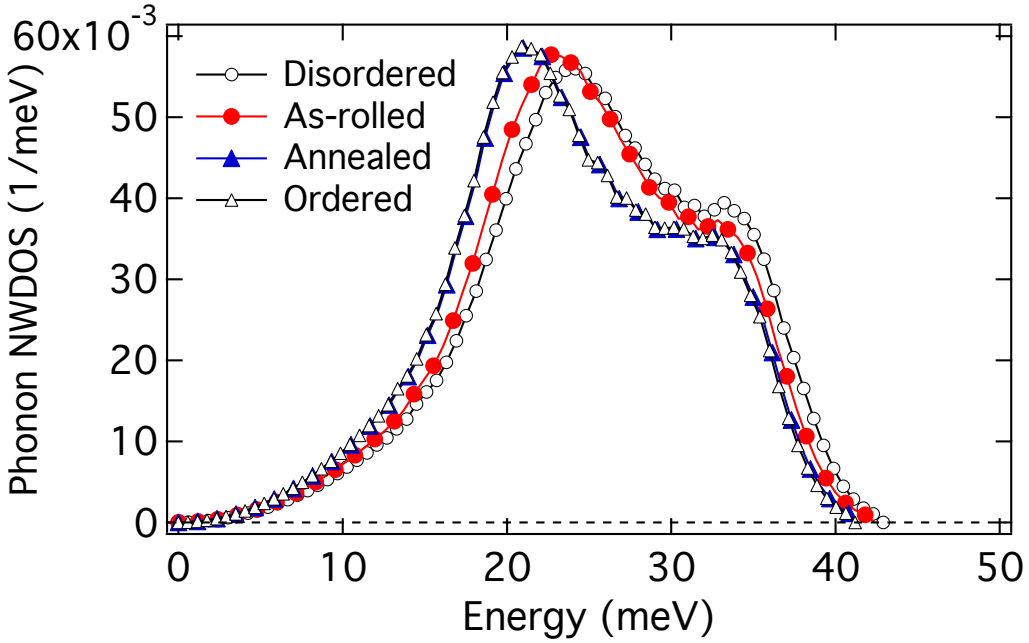

Figure 3.7: Measured NWDOS curves for the as-rolled and annealed samples and cluster expansion extrapolation for the perfect order and perfect disorder cases.

The spin-polarized calculations used VASP [83, 84] with the projector augmented wave method [72, 73] and the generalized gradient approximation (GGA) of Perdew, Burke, and Ernzerhof [67]. Convergence with respect to the kinetic energy cutoff and the sampling of k-points in the Brillouin zone was achieved. The k-point meshes for Brillouin zone sampling were constructed using the Monkhorst-Pack scheme [82] and the total number of k-points times the total number of atoms per unit cell was 8192 in both cases. The plane wave cutoff energy was set at 420 eV. The SQS and the $B2$ structures were fully relaxed with respect to volume, the position of the atoms, and the shape of the unit cell using a conjugate-gradient scheme. For the relaxation the cutoff energy was set at 550 eV to minimize the Pulay stress. The distortions on the cell vectors due to relaxation are very small, indicating that the bcc phase is stable. The bulk moduli, ground state energy, and equilibrium lattice parameter were found by a fit of the energy-volume relationship obtained from the calculations to the third order Birch-Murnaghan equation of state [211]. The shear modulus was calculated from a volume-conserving monoclinic deformation of the cell. These procedures are explained in section 1.2.5. The trends in the calculated lattice parameter and elastic moduli are in good agreement with experimental data (Table 3.4). The calculations predict the ordered structure to be more stable than the disordered one, with ground state energies E_0 of -17.498 eV/unit cell and -17.462 eV/unit cell, respectively.

To test the applicability of SQSs and their accuracy, the electronic structure for the compositions $Fe_{75}V_{25}$ and $Fe_{25}V_{25}$ (Fig. 3.9) were calculated and the trends in lattice parameter and bulk modulus

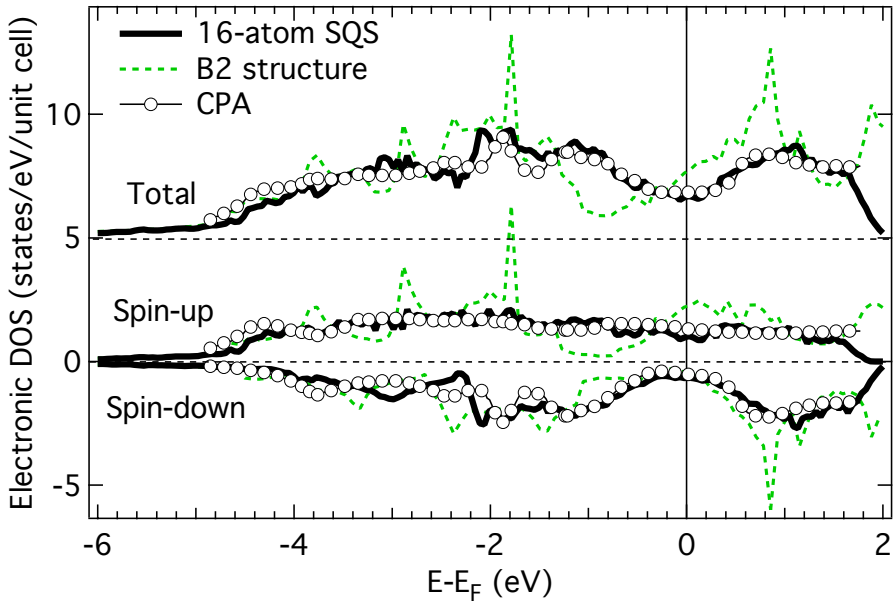

Figure 3.8: Spin-polarized electronic DOS computed from first principles for equiatomic FeV in the B2 structure, and in a 16-atom SQS. Calculations performed using a CPA method from Ref. [198] are included for comparison. The total electronic DOS is offset for clarity.

were in agreement to the experimental results in the Fe-V system. The SQSs for these compositions were also obtained from Ref. [210]. The electronic structure was calculated using SQSs designed with 2 and 8 atoms and the differences with respect to the 16-atom one were small.

The electronic structure in the $B2$ case is in good agreement with the results of Moruzzi and Marcus [200] obtained by the local density approximation to DFT using the augmented-spherical wave method. These authors used the atomic-sphere approximation which assumes that the charge density and the potential is spherical within a given radius, and they used the same radius for both Fe and V atoms. This is less sophisticated than our approach, but the approximation is valid for cubic systems. The electronic DOS for the disordered structure is in good agreement with the results of Johnson, Pinski and Staunton [198] calculated in the coherent phase approximation.

The calculated electronic structure was projected onto the Fe and V atomic sites on both the SQS and the $B2$ structure (Fig. 3.10). The total and element-projected magnetization M and number of electrons at the Fermi level $\mathcal{N}_F$ were calculated and shown in Table 3.4. An increase in $\mathcal{N}_F$ of about 1 state/eV/unit cell is observed upon ordering. The increase is larger at the V-projected sites, about 0.7 states/eV/unit cell. At the Fe-projected sites it is about 0.4 state/eV/unit cell. The calculations show a decrease in M upon ordering. The magnitudes in the ordered and disordered states, are in good agreement with experimental values [192–194, 196] and computational work [198–202].

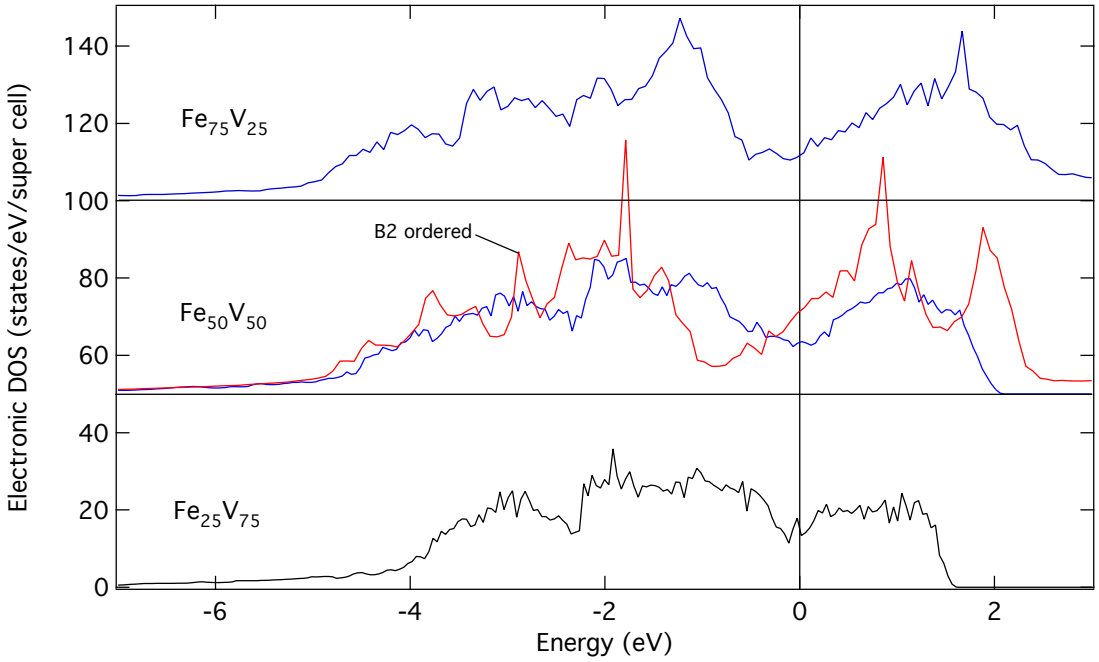

Figure 3.9: Total electronic DOS computed from first principles for the SQSs of $Fe_{25}V_{75}$, $Fe_{50}V_{50}$, and $Fe_{75}V_{25}$. The electronic structure of the $B2$-ordered is included for completeness. All the calculations are spin-polarized except for $Fe_{25}V_{75}$, which is paramagnetic. The electronic DOS curves are offset for clarity.

3.5.2 Generalized electronic susceptibility

The diagonal part (**G = G'**) of the generalized electronic susceptibility, given by

$$\chi(\mathbf{q}) = \sum_{n,n',\mathbf{k},\mathbf{k}'} \frac{f(E_{n,\mathbf{k}}) - f(E_{n',\mathbf{k}+\mathbf{q}})}{E_{n',\mathbf{k}+\mathbf{q}} - E_{n,\mathbf{k}}} \times \left| \langle n,\mathbf{k} \mid e^{-i\mathbf{q}\cdot\mathbf{r}} \mid n',\mathbf{k}+\mathbf{q} \rangle \right|^2, \tag{3.6}$$

was calculated for the $B2$-ordered and disordered cases of FeV. The generalized susceptibility in the random phase approximation was explained in Chapter 1.2.6. In Eq. 3.6, $\mathbf{q}$ is the wave vector of the perturbation, in this case a phonon; $f(E_{n,\mathbf{k}})$ is the Fermi distribution at the energy $E_{n,\mathbf{k}}$; n and n' are band indices; $\mathbf{k}$ is a wave vector in the first Brillouin zone. In the present calculations, $\mathbf{k}' = \mathbf{k} + \mathbf{q}$ is zero if it lies outside of the n^{th} Brillouin zone. The off-diagonal elements of the susceptibility represent non-central forces, which are not present in free-electron systems, but are not necessarily insignificant in transition metals [212, 213]. The occurrence of anomalies in the phonon spectra of metals has been related to sharp features in $\chi(\mathbf{q})$ [102–106]. These anomalies originate with nesting features, where the denominator in Eq. 3.6 is vanishingly small for many pairs of electronic states. Looking at the second term on the right, the intraband matrix elements tend to unity in the long wavelength limit, while the interband matrix elements vanish. The intraband contribution is due to the existence of the Fermi surface and results in additional softening in metals [214].

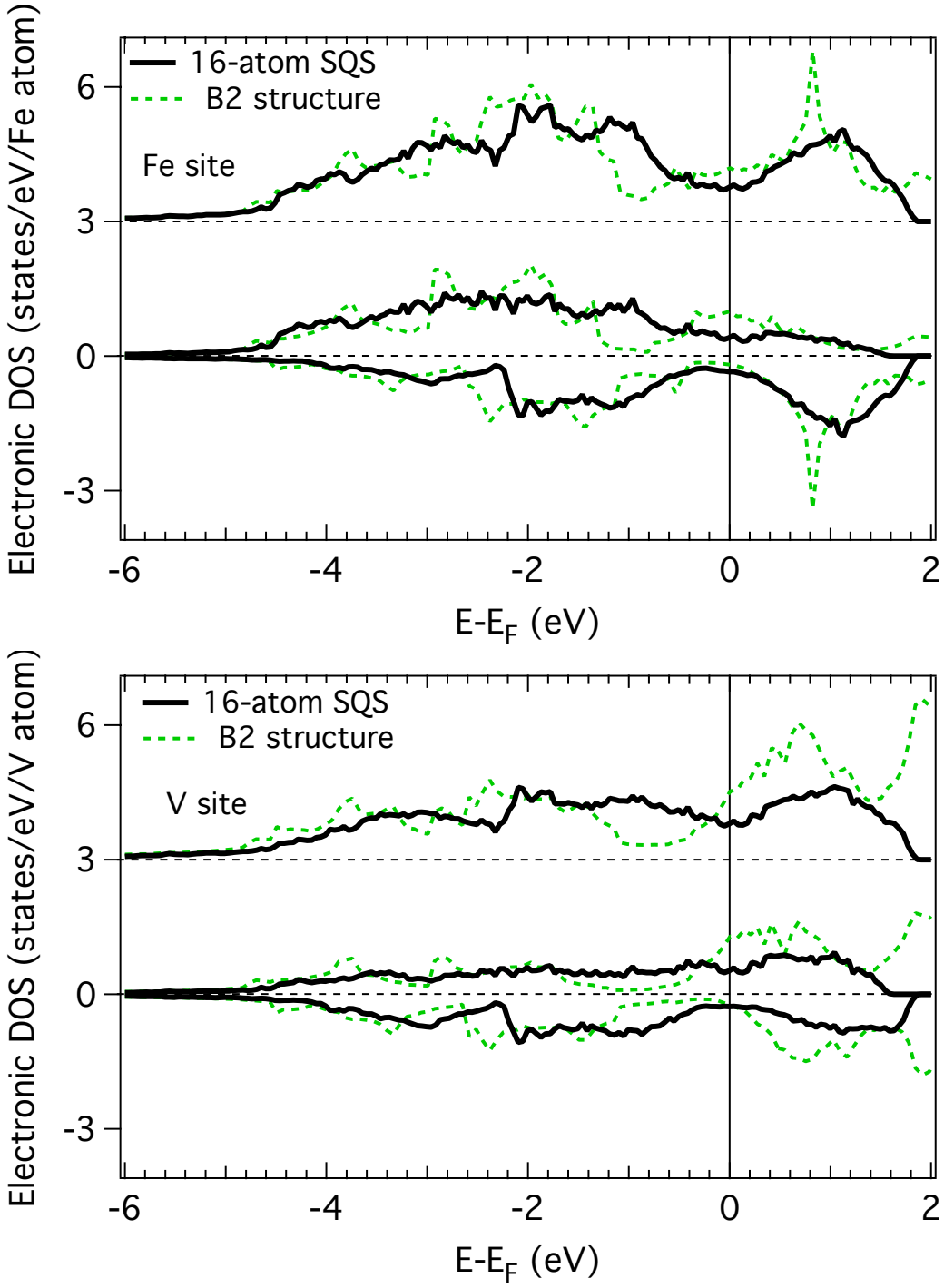

Figure 3.10: Spin-polarized electronic DOS computed from first principles at the Fe sites (top) and at the V sites (bottom) for equiatomic FeV in the B2 structure, and in a 16-atom SQS. Calculations performed using a CPA method are included for comparison. (See text for details.) The total electronic DOS is offset for clarity.

For the calculation of the intraband generalized susceptibility for $B2$-ordered FeV and the 2-atom SQS of FeV, spin-polarized electronic structure calculations similar to those described in Chapter 3.5.1 were performed, but the method of Methfessel and Paxton [91] was used for partial occupancies instead of the tetrahedron method [88]. This resulted in a difference of 0.1% in the Fermi energy in the ordered structure and 0.4% in the 2-atom SQS of FeV. The electronic DOS curves were in excellent agreement with those shown in Fig. 3.8. Only the generalized susceptibility of the majority spin electrons was calculated, since there are no studies on the generalized susceptibility including spin interactions and mixing different types of perturbation energies is not in the spirit of the generalized susceptibility. A 2-atom SQS was used to facilitate direct comparison with the $B2$ structure, and the Brillouin zone construction of the bcc structure was imposed on the Fe and V atoms in the SQS and $B2$ structure. The 16-atom SQS used to study the electronic DOS was not practical for the calculation of the generalized susceptibility. For example, if a bcc construction is imposed on the atoms, the band structure would still have to be unfolded. This is a considerable effort [215] and might not be well-defined for supercell structures with relaxed atomic positions that are different from those of the basic cell. If the Brillouin zone constructions are different, an extended scheme band structure would be necessary. In this case the intraband versus interband distinctions are difficult to define.

The electronic band structure was calculated at 17,241 k-points evenly distributed in one-half of the Brillouin zone. Due to computer memory limitations, the DFT calculations were performed on 5 different subsets of the total number of k-points with evenly distributed k-points and then assembled together. This approach precluded us from using the tetrahedron method, but was deemed as a more direct approach than unfolding the band structure from the irreducible representation used by VASP calculations. A program was written to find the pairs of k-points $\mathbf{k}$ and $\mathbf{k}+\mathbf{q}$ in the same band with non-vanishing nominator in Eq. 3.6 and to calculate the denominator. To have a non-vanishing nominator at $\mathbf{q}$, one of the k-points must have an energy above the Fermi energy and the second k-point must be below the Fermi energy. The k-point structure was translated to the neighboring Brillouin zones (12 for the bbc structure) to ensure that the number of elements in the summation of Eq. 3.6 was the same for every $\mathbf{q}$ point, but the energy of the bands was set to zero in this region to make the calculations analogous to the Lindhard function, named after the physicist who first derived it [216]. An octree [217] was used to divide the Euclidean space and improve the speed of the calculations. The code was parallelized in a simple way to calculate the generalized susceptibility at different values of $\mathbf{q}$ at the same time.

To test the approach, the intraband generalized susceptibility for a free-electron gas in a bcc Brillouin zone was calculated in the Γ-H direction. The analytical solution is the Lindhard function, and a comparison is shown in Fig. 3.11. This indicates that variations of less than about 5% are not physically significant with our k-point resolution. The work of Landa et al. [106] for the case of

Nb, which also has a bcc structure, was reproduced using VASP ab initio calculations and the code described above. The results are in good agreement and shown in Fig. 3.12. The same data were used to obtain the Fermi surface, and a MATLAB routine was developed to perform the rendering. The results for the third Brillouin zone are shown in Fig. 3.13, and are in good agreement with experimental [218] and computational [219–221] results. Finally, the convergence of the generalized susceptibility curve with increasing number of k-points was checked.

The intraband susceptibilities of the spin-up electrons of the two bands that cross the Fermi surface in the 2-atom SQS and the $B2$ structure were added together. Results for the high-symmetry directions Γ-H, Γ-P, and Γ-N are shown in Fig. 3.14. The generalized susceptibility is fairly isotropic and consistently 2.5 times larger in the $B2$ structure than in the 2-atom SQS. This is the ratio of electronic states at the Fermi level between both structures.

3.6 Discussion

3.6.1 Ordering tendencies

The main experimental observation presented in this chapter is a general softening of the phonon DOS curves upon ordering in the FeV system, so the vibrational entropy is higher in the ordered state. As mentioned in section 3.1, the ordered and disordered phases have the same underlying lattice, and these are the first experimental measurements that show that the vibrational entropy of ordering in such systems can be a positive quantity. The common underlying lattice is important because, in general, the behavior of the vibrational entropy cannot yet be predicted when significant changes occur in the structure of a material, such as in coordination number or lattice parameter. These changes do not take place or are negligible in the FeV system, so measured quantities are directly related to the state of order. From a computational point of view, the common underlying lattice makes it is possible to study both systems in a consistent way using the same Brillouin zone construction. The choice of Brillouin zone does not affect averaged quantities such eDOS curves, but is important for more detailed calculations such as the generalized susceptibility. The combination of experimental and computational work presented here permits to relate changes in the vibrational entropy to changes in the electronic structure.

The model presented in Ref. [169] predicts a bond stiffening and therefore a decrease in the vibrational entropy upon ordering, which is the common effect. It uses the Lennard-Jones potential [40] to describe the bonding between atoms. The Lennard-Jones potential has two adjustable parameters: the depth of the potential well and the distance at which it reaches a minimum. In an AB binary alloy there are three potentials: between A atoms, between B atoms, and between A and B atoms. In an ordering alloy, the A–B bond is more energetically favorable than the average of the A–A and B–B bonds (the opposite is true for systems with unmixing tendencies). Lennard-Jones

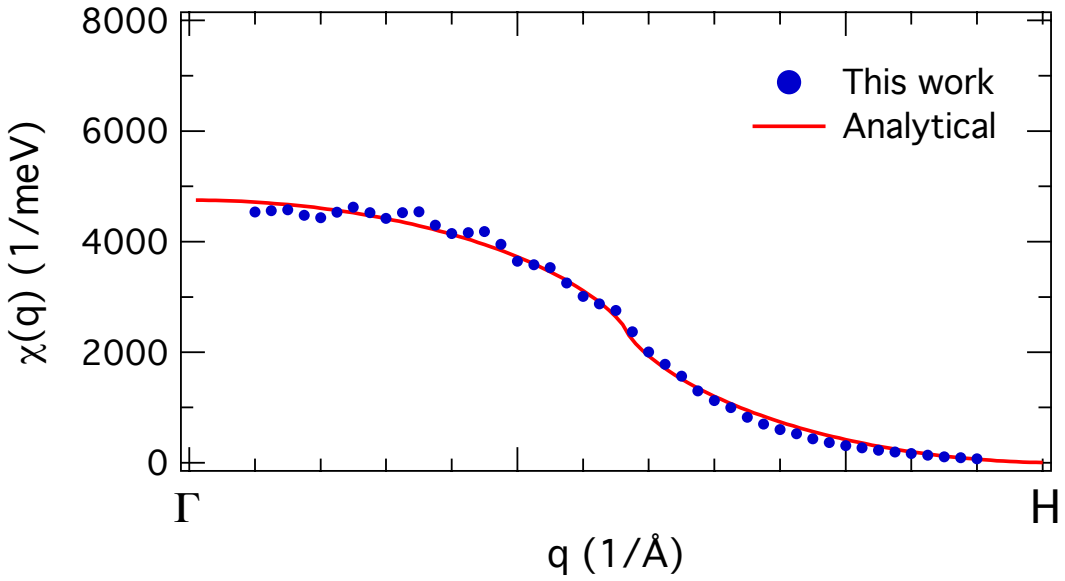

Figure 3.11: Intraband generalized susceptibility for an unperturbed free-electron gas (Lindhard function).

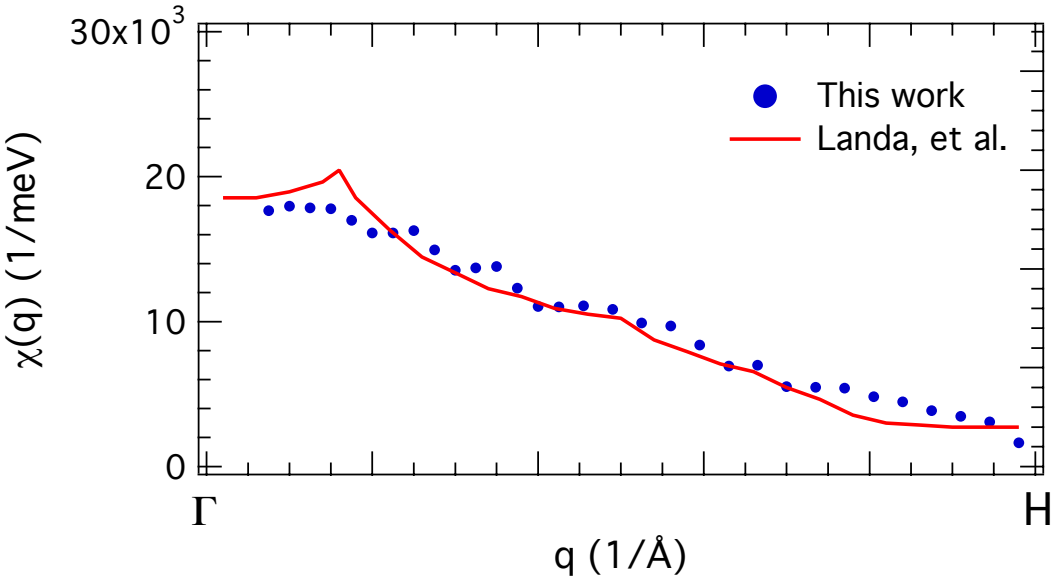

Figure 3.12: Intraband generalized susceptibility for the 3rd band in pure Nb in the Γ-H direction.

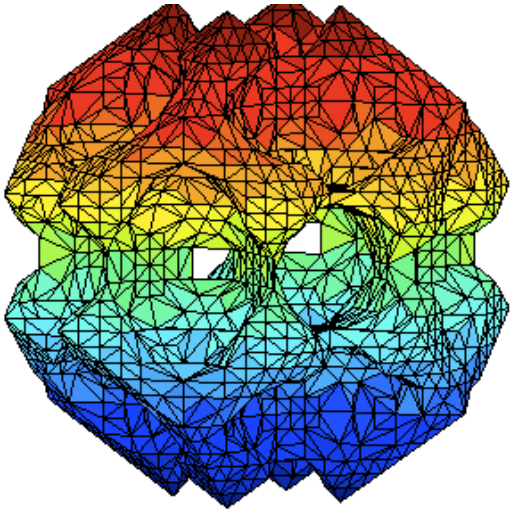

Figure 3.13: Fermi surface for the third Brillouin zone of Nb.

potentials for an ordering system with very small variations in bond length are shown in Fig. 3.15. In the harmonic model, the bottom of the potential can be fitted by a quadratic expression with a proportionality constant that defines how narrow the potential is - an effective spring constant. This quadratic dependence arises from the assumption of the harmonic model that atoms in a crystal are joined by independent springs. A deeper Lennard-Jones potential will also be narrower and will have a stiffer spring constant (larger magnitude). A stiffer spring constant results in a lower vibrational entropy [38]. Since the Lennard-Jones potential is generally a good approximation of the interaction between atoms, we can expect the model of Ref. [169] to predict the correct behavior for most systems. Nevertheless, the authors identify a region in parameter space in which the simple picture provided by the Lennard-Jones potentials breaks down. FeV falls in this category and implies that a more fundamental mechanism affects bonding in the system. In the following section (section 3.6.2) we identify electronic screening as this mechanism.

A higher vibrational entropy for the $D0_{22}$-ordered phase compared to the fcc phase in Pd_3V was predicted by calculations [130]. The $D0_{22}$ structure is based on the cubic fcc structure, but it is tetragonal. The tetragonality is small in Pd_3V, with a difference between the a and c lattice parameters of 0.03 Å [222]. The bonds follow a linear bond length vs bond stiffness relation. The authors attribute the phenomenon to symmetry constraints in the ordered structure that force the bond length to be different from the one that optimizes its free energy. They call this an 'ideal' bond length and define it as the bond length in the disordered structure. The calculations presented in section 3.5.1 show that the length of the bonds in the Fe-V system does not vary much between the ordered and disordered states or even with composition. The lattice parameter depends more on the number of (shorter) Fe–V bonds. By this definition, the FeV bond is always at its ideal length and lattice relaxation effects are negligible.

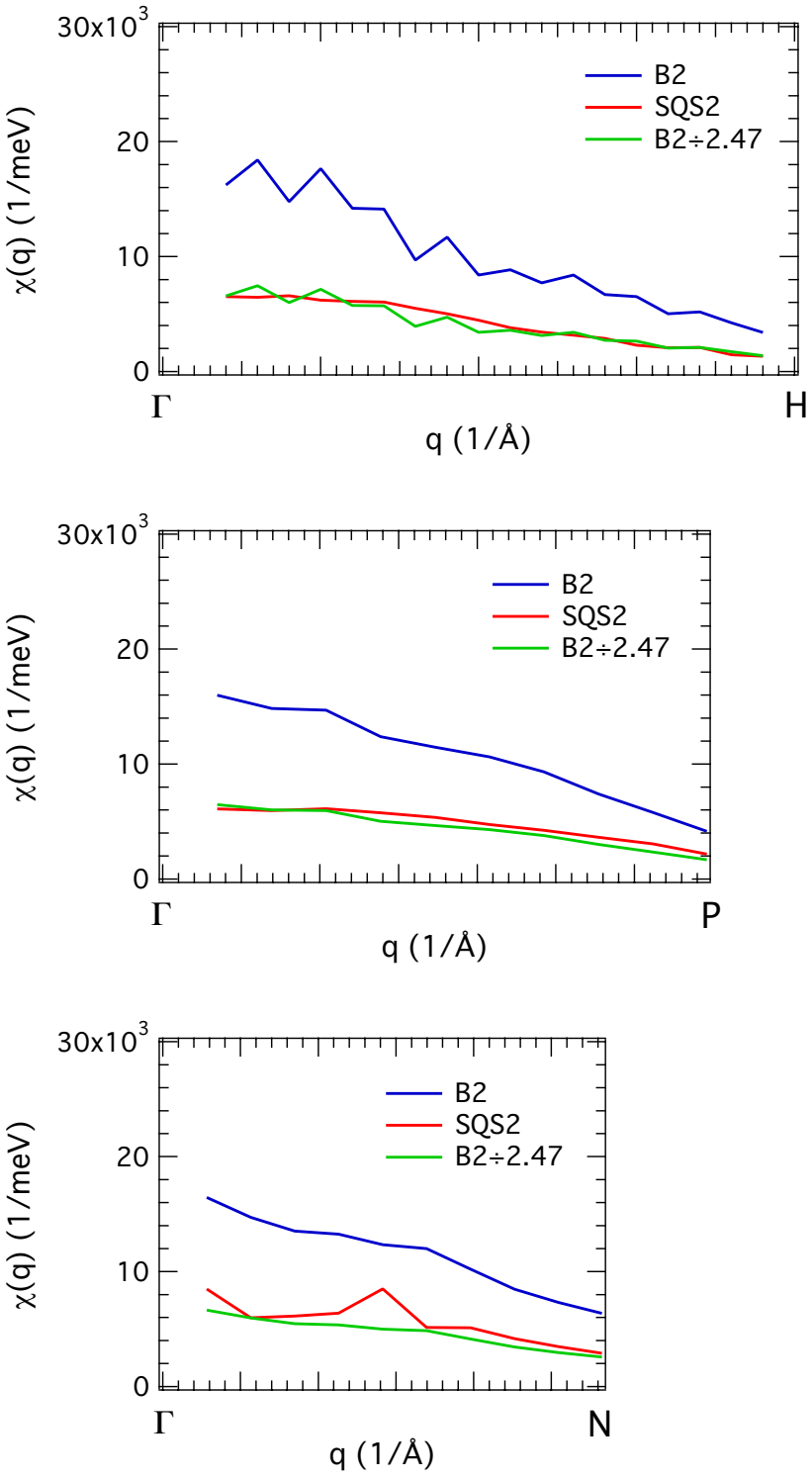

Figure 3.14: Sum of the intraband generalized susceptibilities of the majority band electrons in the three high-symmetry directions in the $B2$-ordered FeV and a 2-atom SQS of FeV. The curve marked '$B2 \div 2.47$' is the $B2$ result scaled by the ratio of the electronic DOS at the Fermi level for the two systems.

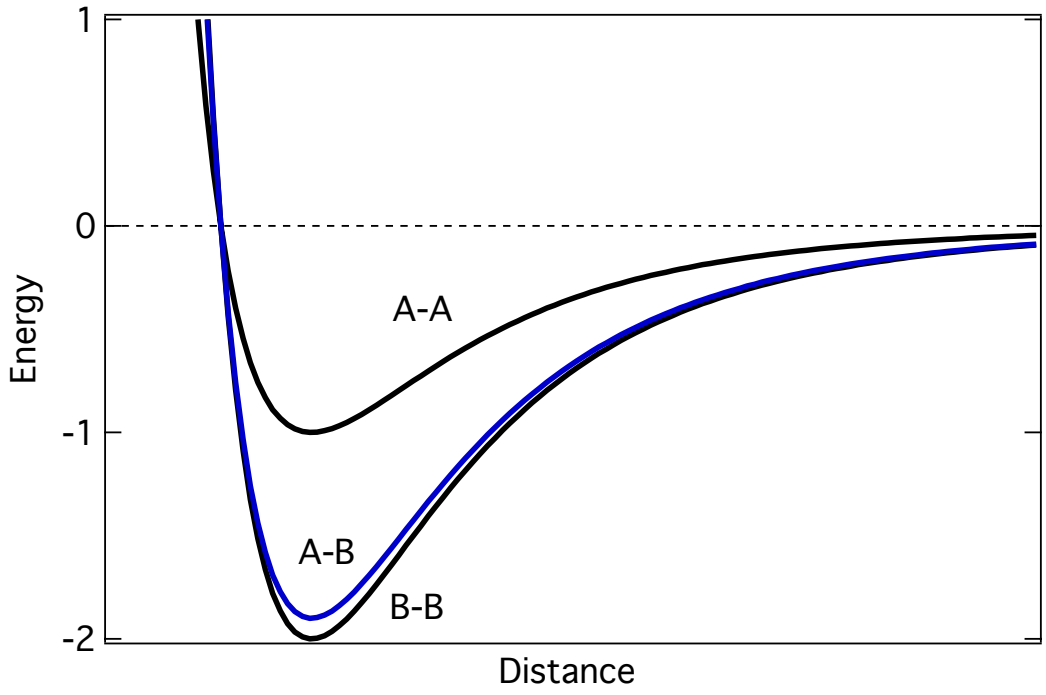

Figure 3.15: Lennard-Jones interatomic potentials for an ordering system. A and B represent atoms of different types.

Low-symmetry ordered compounds may also have soft phonons and large vibrational entropies. For example, the vibrational entropy is believed to stabilize the θ phase (tetragonal $C16$) against the metastable θ' phase (cubic $C1$) in the important intermetallic alloy Al_2Cu [223]. Both are ordered structures, but the θ phase has a layered structure that facilitates the motion of a transverse optical mode, making the mode soft and increasing the vibrational entropy.

3.6.2 Electronic screening

The effect of screening in the bcc transition metals Zr, Nb, and Mo was explored computationally from first principles in early work by Ho, Fu, and Harmon [90,224]. The authors conclude that as the number of valence electrons increases, the additional charge density is accommodated in directional bonds between 1nn atoms. This is a result of the additional occupied d-states which have e_g and t_{2g} symmetries. The larger screening effects in transition metals compared to simple metals occurs because there are more localized d-electrons to screen than free-electron orbitals.

The thermodynamic importance of the electron-phonon interaction at elevated temperatures has been the subject of controversies. The calculations in Ref. [50] imply that the effect dissipates at temperatures higher than the characteristic phonon frequency, which in most transition metals would

be in the range 50 – 200 K. The results of Allen and Hui [225] predict that the adiabatic part of the interaction will persist at temperatures above the Debye temperature, which is considerably higher than the characteristic phonon energy, but the magnitude of the effect was deemed an overestimation by Wallace [226]. The adiabatic component of the electron-phonon interaction is due to low frequency ionic motions which are much slower than the electronic response time, so the electronic density is reconfigured to minimize the energy accommodating the lattice distortion (effectively a frozen phonon). The adiabatic component therefore averages electronic properties over thermal nuclear displacements. The nonadiabatic component of the electron-phonon interaction refers to the scattering of electronic states by phonons whose wave vectors span the Fermi surface (the nuclear kinetic energy operator operates on the electronic wave functions) and is responsible for, e.g., conventional superconductivity [227]. In a more detailed computational study of the high temperature behavior of each component of the electron-phonon interaction in the simple metals Na, K, Al, and Pb, using nearly-free-electron pseudopotentials, Bock, Wallace, and Coffey concluded that the nonadiabatic term vanishes at elevated temperatures while the adiabatic contribution increases [228,229]. They also calculated that the magnitude of the effect on the free energy of the system is close to that predicted by Allen and Hui.

The effect of the adiabatic electron-phonon interaction on the phonon thermodynamics of several metallic systems as a function of temperature was investigated by a combination of lattice dynamics measurements and first principles simulations by Delaire et al. In pure V [20], the phonon DOS curves do not soften with temperature even though the material expands normally. The normal softening behavior is recovered with small additions of Co, but not with additions of Nb, which is isoelectronic with V and has a similar band structure. The strength of the electron-phonon interaction is proportional to the number of electrons at the Fermi level [230], as is the electronic screening in the long wavelength limit. At high temperatures, the phonons disrupts the periodicity of the lattice, decreasing the lifetime of the electronic states and broadening them. This broadening smears sharp features in the electronic DOS. If the Fermi level lies close to a peak in the electronic DOS, the decrease in the number of electrons at the Fermi level can be substantial. This is the case in pure V, so while the phonon softening effect with the thermal expansion is present, it is canceled out by a stiffening effect due to the decrease in the number of electrons at the Fermi level that are available for screening. With the addition of Co, the Fermi level moves to a valley in the electronic DOS where the effects of thermal broadening are less severe. The mechanism is the same for the $A15$ superconductors V_3Si and V_3Ge [3], but the effects are larger. In all three systems (V, V_3Si, and V_3Ge) the effects are present at temperatures above 1000 K. In another experiment, the opposite effect is observed (an anomalous softening) when the narrow band-gap in FeSi is filled at high temperatures due to thermal broadening, improving the electronic screening efficiency [21].

The inverse correlation between the number of electrons at the Fermi level and the phonon

behavior (which can be acceptably characterized by the average phonon energy) was also used by Lucas et al. [22] to explain the compositional trends in the Fe-V system. For a higher number of electrons at the Fermi level, the electronic screening will be better and the average phonon energy will be lower. The strongest evidence of the inverse correlation in the Fe-V system is perhaps the excellent agreement between the average phonon energy and the inverse of the electronic heat capacity (proportional to the number of electrons at the Fermi level) measured by Cheng, Wei, and Beck [231]. There is a discontinuity in both quantities at the 70 at. % V which is the critical composition for magnetism and the electronic structure changes substantially. The behavior of the lattice parameter also changes at this composition. This information is shown in Fig. 3.16. This strongly suggest that the same phenomenon is responsible for the softening of the phonons upon ordering in FeV since the number of electrons at the Fermi level increases as shown in Fig. 3.8.

The density of electronic states in FeV at the Fermi level projected onto V atoms undergoes a larger increase with ordering than for Fe atoms (Table 3.4) by a factor of 1.7. This suggests that screening of the displacements of V atoms may be more effective than for Fe atoms. This is consistent with the experimental data as the phonon partial DOS of V atoms softens (Fig. 3.4) more upon ordering than the Fe phonon partial DOS. Although correlations have been reported previously between the total electron DOS at the Fermi level and softening of the phonon DOS, we know of no other correlations between the projected electronic DOS at an atom and the softening of its partial phonon DOS.

In general, the electronic screening can be complicated and sometimes it is not very well described by the number of electrons at the Fermi level. This is the case in highly anisotropic materials in which the electron-phonon interaction varies greatly in different directions in the Brillouin zone or for certain wave vectors. A good example is MgB_2 [214, 232]. As mentioned before, the ability of electrons to screen phonon perturbations depends on the wave vector of the phonon (see, e.g., Ref. [233]). In the long wavelength limit, the phonon is screened out almost entirely by electrons and the screening is proportional to the number of electrons at the Fermi level. On the other hand, electrons cannot effectively screen motions with large wavevectors. A generalized susceptibility study of ordered and disordered FeV was presented in section 3.5.2. The results in Fig. 3.14 show that it decreases with increasing wave vector in all three high-symmetry directions. The main observations are that there are no sharp features within the margin of error of the calculations, the susceptibility decreases monotonically and isotropically, and the ratio of the susceptibility between the ordered and the disordered systems is constant at any wavevector. This is perhaps not surprising for a cubic system, but it validates the assumption that the phonon softening is related to the number of electrons at the Fermi level in the FeV system.

The final important feature in the data (Fig. 3.4) is the differential softening of the low energy transverse and the high energy longitudinal modes. The generalized susceptibility cannot distinguish

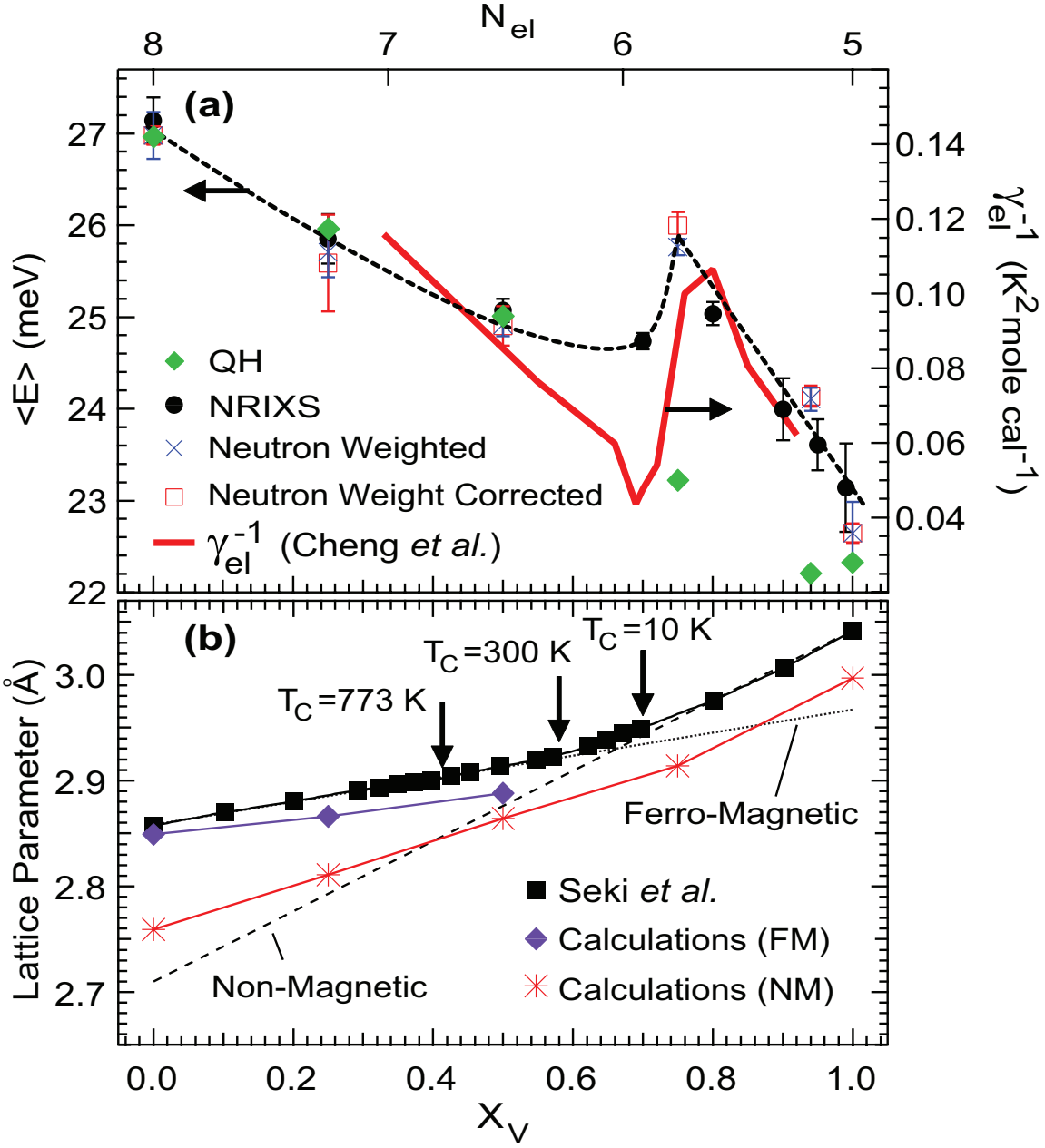

Figure 3.16: (Top panel) Left axis: average phonon energy from INS and NRIXS. Dashed lines with markers were obtained from the quasiharmonic model. Right axis: inverse of the electronic contribution to the low-temperature heat capacity [231] shown as a thick solid line. (Bottom panel) Lattice parameter of Fe-V alloys [189] and first principles calculations [22]. Dashed lines are extrapolations of the experimental results on Fe-rich (ferromagnetic) and V-rich (nonmagnetic) alloys.

between them, but the C_{44} elastic constant is particularly sensitive to the electronic structure of bcc transition metals and alloys. For example, the C_{44} elastic constant shows an anomalous temperature dependence in bcc Nb and V that is electronic in origin [23,234]. Atoms in these metals have a region of high electron density situated between the jungle-gym and the ellipsoid parts of the Fermi surface (Fig. 3.13) that is disturbed mainly by a C_{44} type of deformation [235]. The electronic structure of FeV is similar to that of these elements, so it is plausible that the softening of the transverse modes upon ordering is because the increase in the number of electronic states is mostly in this area of the Brillouin zone. The larger softening of the transverse modes in V than in Fe is consistent with the larger increase in the number of electrons at the Fermi level at the V sites (Fig. 3.9 and Table 3.4). Most of the increase of the states is in the same region of the Brillouin zone at the V sites. It is important to note the bulk modulus is greater in the ordered alloy, which implies a stiffening of the high energy longitudinal modes, and is the usual behavior of ordering alloys. Therefore, the longitudinal modes might stiffen slightly upon ordering, decreasing the vibrational entropy, but the large softening of the transverse modes increases the overall vibrational entropy and stabilizes the ordered phase. The preferential softening of the low energy transverse modes has also been observed in several $A15$ superconductors with increasing temperature [3,236].

3.6.3 Phonon thermodynamics

As seen in Figs. 3.3 and 3.4 and discussed in section 3.6.2, ordering affects transverse phonons more than longitudinal phonons. From our measurements with long-wavelength ultrasonic waves, we find that the bulk modulus increases upon ordering, although the shear modulus decreases (Table 3.4). The different behaviors upon ordering of phonons with different polarizations and wavelengths show that simple parameterizations of the phonon spectra are not adequate to determine the change in vibrational entropy. For example, the Debye-Grüneisen model [237] predicts a vibrational entropy of ordering of -0.11 k_B/atom, which has the wrong sign. It uses an estimate of the Debye temperature with just the experimental bulk modulus.

The cluster expansion work presented in section 3.4 provides the tools to interpolate the phonon DOS curves for any composition and state of order. It is a phenomenological model, but it can provide real space predictions of reciprocal space quantities such as the phonon DOS that are the result of simple parameters. The main result (Fig. 3.6) is that the formation of A-B bonds between 1nn atoms increases the intensity in the low energy transverse mode region of the phonon DOS at the expense of higher energy modes. The longitudinal and transverse modes are degenerate at the H and P points of the Brillouin zone for Fe [238], V [239], and related systems such as Nb [240] and Ta [241], so it is possible that ordering breaks this 'average' degeneracy in the disordered system. The opposite effect is seen with the formation of A–A and B–B bonds, but these are 2nn bonds and their effect is smaller.

The quasiharmonic model predicts a stiffening of phonons with the decrease in volume that accompanies ordering. For the sample with $B2$ order, Fig. 3.5 shows that the thermal expansion and the quasiharmonic model can account for the thermal softening of the phonon DOS from 300 to 773 K, so the $B2$ phase itself exhibits a normal bond-stiffness versus bond-length relationship. In the framework discussed in section 3.6.2, this is to be expected since the Fermi level does not lay at a peak in the electronic DOS (Fig. 3.8). Although the electron-phonon interaction in the system is large, it is invariant with temperature.

The effect of the vibrational entropy on the order-disorder transition temperature can be estimated from simple thermodynamic arguments. Consider two cases: one in which the whole entropic contribution to the free energy comes from configurational entropy, and a second in which both configurational and vibrational degrees of freedom are accounted. When the free energies of these two cases are equal,

$$T^{\mathrm{A2}\to\mathrm{B2}}_{\mathrm{config\ +\ vib}} = T^{\mathrm{A2}\to\mathrm{B2}}_{\mathrm{config}} \cdot \left(1 + \frac{\Delta S^{\mathrm{A2}\to\mathrm{B2}}_{\mathrm{vib}}}{\Delta S^{\mathrm{A2}\to\mathrm{B2}}_{\mathrm{config}}}\right)^{-1}, \tag{3.7}$$

and the relative importance of the vibrational entropy in phase transitions (cf. Eq. 4.10) can be assessed. In Eq. 3.7, $T^{\mathrm{A2}\to\mathrm{B2}}_{\mathrm{config\ +\ vib}}$ is the transition temperature considering both configurational and vibrational contributions, $T^{\mathrm{A2}\to\mathrm{B2}}_{\mathrm{config}}$ is the transition temperature taking only configurational contributions into account, and $\Delta S^{\mathrm{A2}\to\mathrm{B2}}_{\mathrm{config}}$ is the change in configurational entropy upon ordering. In the point approximation, the configurational entropy per atom is

$$S_{\mathrm{config}} = -\frac{k_{\mathrm{B}}}{2}[(1+L)\ln(1+L) + (1-L)\ln(1-L)]. \tag{3.8}$$

Using the values listed for our samples in Table 3.4, $\Delta S^{\mathrm{A2}\to\mathrm{B2}}_{\mathrm{vib}} = 0.22 \pm 0.03\, k_{\mathrm{B}}$/atom and $\Delta S^{\mathrm{A2}\to\mathrm{B2}}_{\mathrm{config}} = -0.69\, k_{\mathrm{B}}$/atom, so vibrational entropy stabilizes the ordered phase, increasing the order-disorder temperature achieved by configurational entropy alone by 47 ± 11 %. The transition temperature in equiatomic FeV is 1150 K [189], so vibrational entropy is responsible for an increase in the order-disorder temperature of about 367 ± 40 K. From the phonon DOS curves in Fig. 3.3, the vibrational entropy per atom was found to be $3.15 \pm 0.01\, k_{\mathrm{B}}$ for pure Fe and $3.64 \pm 0.01\, k_{\mathrm{B}}$ for pure V. The vibrational entropy of formation $\Delta S^{\mathrm{form}}_{\mathrm{vib}}$ is $-0.07 \pm 0.02\, k_{\mathrm{B}}$/atom for the as-prepared sample and $+0.07 \pm 0.02\, k_{\mathrm{B}}$/atom for the annealed sample. The vibrational entropy of formation is positive for the $B2$ ordered phase, but negative for the solid solution, although the total entropy of formation of the solid solution has a dominant positive contribution from the configurational entropy.

3.7 Conclusion

The softening in the phonon DOS that accompanies the ordering transition in equiatomic FeV was investigated. The electronic structures of the $B2$-ordered phase and a SQS with 16 atoms to simulate the disordered phase were calculated from first principles. The decrease in the average phonon energy is the result of an increase in the number of electrons at the Fermi level upon ordering. These electrons are available to screen atomic motions. Electronic susceptibility calculations show that the system is isotropic and that the ratio of the magnitude of the susceptibility in the ordered and disordered phases is the same for any perturbation (phonon) wave vector, showing that the number of electrons at the Fermi level is a good descriptor of the total screening and the phonon softening. The screening upon ordering is better at the V sites than at the Fe sites. A decrease in the shear modulus upon ordering and a preferential softening of the low energy transverse modes observed in the data suggests that the increased screening of these modes upon ordering is the main contribution to the overall softening of the phonon DOS. A cluster expansion analysis supported this explanation. The softening results in the stabilization of the ordered phase and it is estimated that the increase in vibrational entropy increases the order-disorder temperature by about 370 K. The $B2$ phase exhibits a normal quasiharmonic behavior at high temperatures.

Table 3.4: Values of the vibrational entropy per atom $S_{\rm vib}$ ($k_{\rm B}$/atom) and average phonon energy $\langle E\rangle$ (meV) from experimental data for each sample and each atom species in FeV. The change in vibrational entropy, $\Delta S_{\rm vib}^{\rm A2\to B2}$, is estimated for transition from full disorder ($A2$) to full $B2$ order. The values in parentheses are uncertainties in the last significant digit. Number of electronic states at the Fermi level $\mathcal{N}_{\rm F}$ (states/eV/atom) and magnetic moment M (μ_B) were calculated for the FeV alloy, and at the Fe and V sites. Lower rows are long-range order parameters L, lattice parameters a (from neutron diffraction), shear modulus G, and bulk modulus B, for the disordered (SQS) and ordered (B2) samples.

	Disordered		Ordered		Transition	SQS		$B2$	
	$S_{\rm vib}$	$\langle E\rangle$	$S_{\rm vib}$	$\langle E\rangle$	$\Delta S_{\rm vib}^{\rm A2\to B2}$	$\mathcal{N}_{\rm F}$	M	$\mathcal{N}_{\rm F}$	M
FeV	3.33(2)	25.1(2)	3.47(2)	24.2(2)	0.22(3)	1.66	0.62	2.67	0.40
Fe atom	3.44(1)	24.2(1)	3.52(1)	23.6(1)	0.12(3)	0.76	1.67	1.18	1.16
V atom	3.24(4)	26.0(4)	3.40(4)	24.8(4)	0.25(8)	0.80	-0.39	1.50	-0.33
L	0.34		0.87			0.00		1.00	
a	2.938(2) Å		2.931(3) Å			2.938 Å		2.870 Å	
G	74.4(5) GPa		65.6(5) GPa			76.4 GPa		68.7 GPa	
B	161(5) GPa		176(5) GPa			182 GPa		195 GPa	

Chapter 4

Miscibility gap in the Fe-Au system

4.1 Introduction

Fe and Au, in their pure forms and in alloys, are elements known since antiquity and are of major importance in many areas such as industry, technology, economics, etc. Perhaps as a testament to their importance, one of the three human prehistoric ages is the Iron Age, and a comparatively benevolent or productive time period is often referred to as a Golden Age. The scientific literature on the Fe-Au system is vast. The alloys have interesting magnetic properties. For example, Fe atoms can have larger magnetic moments than in pure Fe [242], and magnetism can stabilize pseudomorphic Fe-Au mixtures on surfaces [243]. It is also possible to prepare Fe-Au spin glasses [244–246]. In medicine, nanoparticles of Fe-Au alloys [247–250] are promising for cancer treatment applications [251] owing to the biocompatibility of Au [252]. Nevertheless, bulk mixtures of Au and Fe atoms have few applications because these elements are largely immiscible at low temperatures, as can be observed in the Fe-Au phase diagram (Fig. 4.1). The lifetime of alloys quenched from high temperatures, where Fe is soluble in $A2$ (fcc) Au, is of the order of days to months at room temperature, depending on the composition [253].

It has been mentioned that vibrational entropy can severely impact the thermodynamics of systems with strong mixing tendencies (see section 3.1), but it can also be a dominant contribution to the free energy of systems with segregation tendencies. In these systems, contributions to the entropy that are not configurational in origin can be comparable to the large entropy gain that comes from mixing. Important properties of the system, e.g., the solubility limit and the miscibility gap, will be largely dependent on these additional sources of entropy. In the well-studied NiAu alloy, with a miscibility gap temperature of about 1050 K [254], the total configurational entropy was found to account for only one-half of the total entropy of mixing [255]. Several computational assessments of the miscibility gap temperature considering only configurational contributions to the

free energy overestimated it by as much as a factor of 2 [256–258]. Since magnetic and electronic contributions are expected to be small in this system [259, 260], the excess entropy of mixing likely has a vibrational origin, and it decreases the miscibility gap temperature by about 1000 K [255]. Nevertheless, only the equiatomic composition has been investigated, so there is no information on the compositional trends. Vibrational entropy is relevant in other segregating systems. For example, the miscibility gap in the Ag-Cu system [261], the spinodal decomposition in FeCr [262], and the observed retrograde solubility in several dilute vanadium alloys [263], are all affected by it.

Measurements of phonons in Fe-Au alloys are challenged by the x-ray and neutron absorbing properties of Au. Nevertheless, INS measurements have been performed with direct geometry chopper spectrometers [264,265], and modern instruments make such measurements more practical [149,204]. An early Mössbauer spectrometry study assessed the force constant of Fe impurities in fcc Au [266] using the impurity model developed by Mannheim [267]. Recent studies on Fe-Au alloys have investigated the phonon spectra of Fe atoms in multilayers [268, 269] and nanoclusters [270] using the technique of nuclear resonant inelastic x-ray scattering (NRIXS), which probes specifically the motions of Fe atoms. The results presented here are the first direct measurements of the phonons of Fe atoms in bulk Fe-Au.

In this chapter, we present measurements of samples of varying Fe content that show that the vibrational entropy increases the miscibility gap temperature in the Fe-Au system by as much as a factor of 4 (about 550 K) at 10 at. % Fe but the effect is smaller for higher Fe contents. A computational study of the electronic origin of the decrease in vibrational entropy upon mixing is presented. A physical picture is obtained with the Wills-Harrison model [24]. The Fe-Au bonds are soft, favoring mixing, but hybridization between the *s*-electrons in Au and the *d*-electrons in Fe, and an increase in electron density in the Au free-electron-like states, stiffens the bonds between Au atoms surrounding a Fe atom enough to favor unmixing. This is a local effect and Au atoms that are farther away from the Fe atom are not affected [271]. This might be the first case in which these electronic effects have been found to be thermodynamically important for determining the vibrational entropy.

4.2 Experimental

4.2.1 Sample preparation

Fe-Au alloys of stoichiometric Fe_xAu_{1-x} with nominal compositions $x = 0$, 0.03, 0.20, and 0.50 were prepared for INS measurements by arc-melting gold foils of 99.999% purity and iron lumps of 99.98% purity under a high-purity argon atmosphere. There was no detectable mass loss and no visible oxidation after melting. Electron microprobe measurements confirmed the compositions to be accurate to 0.6 at.%. Because of the large neutron absorption cross section of Au, the ingots

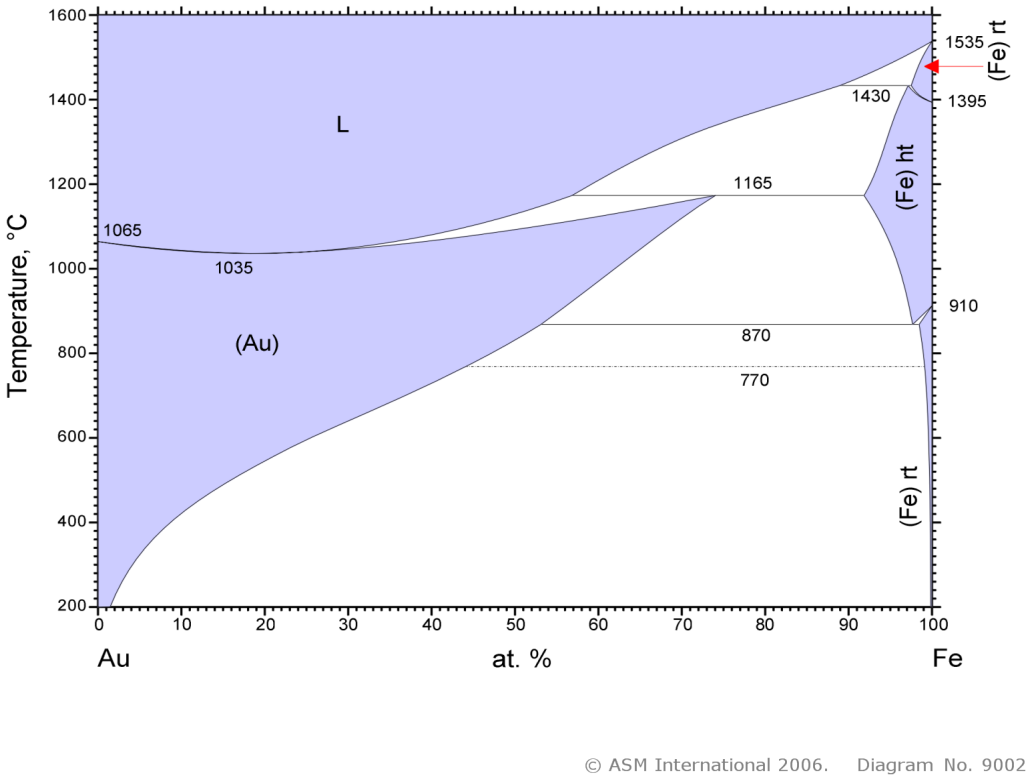

Figure 4.1: Fe-Au phase diagram adopted from ASM International Alloy Phase Diagrams Center [275].

were cold-rolled to a thickness of 120 μm to ensure the transmission of neutrons through the sample. To reduce strains, the samples were sealed in quartz tubes in an argon atmosphere, annealed, and quenched into iced brine. All the samples were annealed at temperatures between 1220 and 1375 K for 30 minutes. Higher temperatures were used for higher Fe concentrations to avoid forming the $A2$ bcc phase (Fig. 4.1). X-ray diffractometry showed all the samples to be in the $A1$ fcc phase. The lattice parameter decreased with increasing Fe concentration (Table 4.3) in good agreement with previous results [272–274].

Fe-Au samples for NRIXS measurements were prepared in the way described above for compositions $x = 0$, 0.03, 0.10, 0.20, 0.30, 0.40, 0.50, and 0.60, but they were 96.06% enriched with ^{57}Fe. The small ingots were cold-rolled to thicknesses between 10 and 50 μm. The heat treatment was the same as described above.

4.2.2 Scattering measurements

INS measurements were performed with the wide Angular-Range Chopper Spectrometer (ARCS). The nominal incident energy was 40 meV. The energy resolution (FWHM) was 1.6 meV at the elastic

line, although the energy resolution of a direct energy spectrometer improves with increasing energy transfer. The Fe-Au samples were mounted on a frame masked with cadmium foil so that the only scattering was from the samples. The flat plate geometry was placed at a 45 ° angle with respect to the incident beam to suppress self-shielding.

NRIXS measurements were performed at beamline 16ID-D of the Advanced Photon Source. The incident photon energy ranged from −80 to +80 meV in steps of 0.5 meV around the nuclear resonance energy (14.413 keV) of ^{57}Fe. The incident beam was at a grazing angle to the sample, and the NRIXS signal was measured with two avalanche photodiode detectors (APDs) monitoring both sides of the sample. The monochromator resolution function was measured in situ using a single APD in the forward direction, and was 2.2 meV (FWHM). All measurements were performed at room temperature.

4.2.3 Ancillary measurements

The magnetization of the Fe-Au samples was measured with a vibrating sample magnetometer (VSM) up to an applied field of 2 T. Transmission Mössbauer spectrometry was performed with a conventional constant acceleration spectrometer. Both the VSM and Mössbauer results indicate that at room temperature the samples with compositions $x = 0.03$, 0.10, and 0.20 are paramagnetic with no Fe clustering and the samples with higher Fe concentration are ferromagnetic. The magnetic properties are consistent with previous results [242], as are the room temperature Mössbauer spectra [276].

4.3 Experimental results

4.3.1 Phonon DOS curves and vibrational entropy

Fe partial DOS curves were obtained from NRIXS data reduced by the method described in section 2.2.3 and the results are shown in Fig. 4.2. NWDOS curves were obtained from INS data reduced by the method described in section 2.1.3 and the results are shown in Figs. 4.3 and 4.4. Different chemical elements have different neutron scattering efficiencies, so data obtained from INS are neutron-weighted. The neutron weights are the ratios of neutron cross section to molar mass, σ/M, which are 0.208 and 0.039 barns/amu for Fe and Au, respectively, so the motions of Fe atoms are overemphasized by a 5:1 ratio. A neutron-weight correction was made possible by combining the INS neutron-weighted phonon DOS spectra with the NRIXS Fe partial phonon DOS spectra, as mentioned in Chapter 2. A comparison between the INS and the NRIXS data is shown in the top panel of Fig. 4.3. The curves in Fig. 4.4 show the NWDOS curves along with the neutron-weight-corrected DOS curves and the Fe partial phonon DOS for the compositions $Au_{0.80}Fe_{0.20}$ and

$Au_{0.50}Fe_{0.50}$.

The vibrational entropy per atom $S_{\rm vib}$ was obtained in the quasiharmonic formalism from the normalized phonon DOS as described in section 1.1. The excess vibrational entropy of mixing as a function of Fe concentration x due to motions of atoms of type $d = \{\text{Au, Fe}\}$ in $Au_{1-x}Fe_x$ is

$$\Delta S^d_{\rm vib}(x) = S^d_{\rm vib}(x) - \mathcal{S}^d_{\rm vib}, \tag{4.1}$$

where $\mathcal{S}^d_{\rm vib}$ is the vibrational entropy of pure element d. As shown in Table 4.3, $\mathcal{S}^{\rm Au}_{\rm vib} = 5.6\,k_{\rm B}$ per atom, but fcc Fe is not stable at room temperature, so we use $\mathcal{S}^{\rm Fe}_{\rm vib} = 3.5\,k_{\rm B}$ per atom, which is the phonon entropy of ^{57}Fe in $^{57}Fe_{0.50}Ni_{0.50}$ from NRIXS measurements at 300 K [277]. Phonon DOS curves of solid solutions of fcc Fe-Ni, and therefore their vibrational entropies, do not change much with composition [278] and are in very good agreement with those of fcc Fe precipitates in Cu [279], pseudomorphic fcc Fe films, [280] and fcc Fe at high temperature [281]. We expect the true $\mathcal{S}^{\rm Fe}_{\rm vib}$ to be $3.5 \pm 0.3\,k_{\rm B}$ per atom, with a conservative range estimate, but corrections of this magnitude do not substantially change the values of the excess vibrational entropy of mixing for Fe-Au alloys shown in Fig. 4.5. The excess vibrational entropy of mixing for the alloy $Au_{1-x}Fe_x$ is the concentration-weighted sum of the curves obtained from Eq. 4.1 for Au and Fe motions

$$\Delta S_{\rm vib}(x) = [1-x]\Delta S^{\rm Au}_{\rm vib}(x) + [x]\Delta S^{\rm Fe}_{\rm vib}(x). \tag{4.2}$$

The neutron-weighted phonon DOS of $Fe_{0.03}Au_{0.97}$ is presented in the top panel of Fig. 4.3 along with the measured partial phonon DOS of the Fe modes. Both curves are normalized, but the vertical axes were adjusted to emphasize that the peak centered at 20.1 meV is mainly due to a local Fe mode. This value is 4.3% higher than the pure Au cutoff energy, $E_c = 19.3$ meV [282]. The general shape of the Au partial phonon DOS of $Fe_{0.03}Au_{0.97}$ does not differ much from that of pure Au. There is a very small stiffening due to the reduction in lattice parameter and the transverse and longitudinal peaks are centered at the same energies. Nevertheless, there is some intensity at energies higher than E_c, in the region where the Fe mode is located, and this intensity in the Au partial DOS curve is the main contribution to the reduction in vibrational entropy in $Fe_{0.03}Au_{0.97}$ with respect to pure Au.

4.4 Computational

4.4.1 Electronic structure

Total energy calculations were performed with density functional theory (DFT) on fcc Au, an fcc structure with 1 Fe atom and 31 Au atoms, a $L1_2$ ordered structure of $FeAu_3$, and four 32-atom

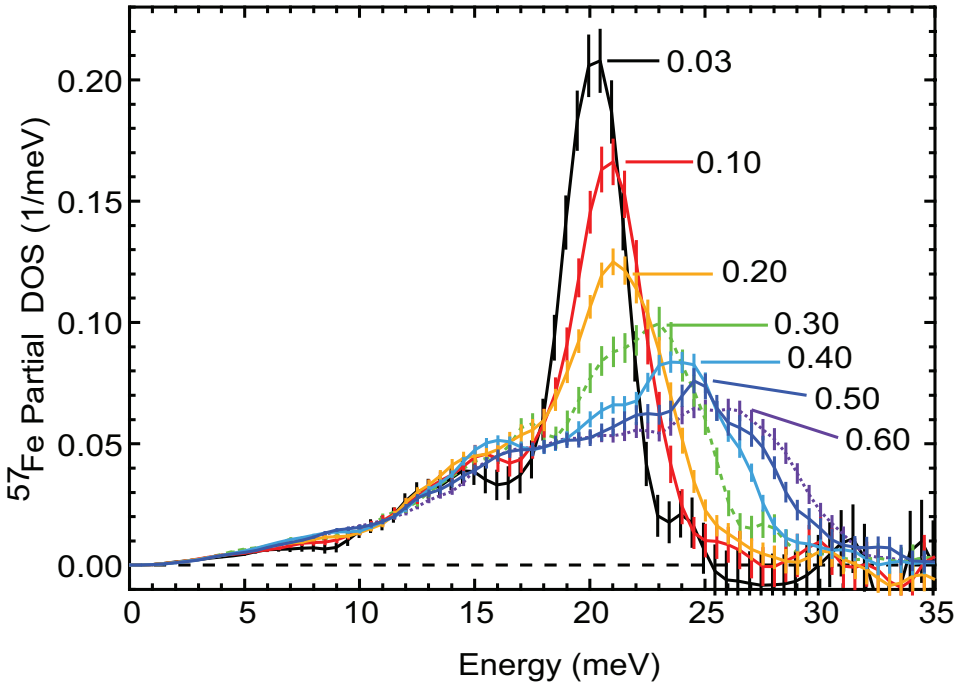

Figure 4.2: ^{57}Fe partial phonon DOS curves for the Fe_xAu_{1-x} alloys at 300 K from NRIXS measurements. The Fe content x for each curve is indicated in the figure.

special quasirandom structures (SQSs) with 2, 4, 6, and 8 Fe atoms, respectively. An SQS is a specially designed periodic structure with the same values of atomic correlation functions (in the cluster expansion formalism [111,118]) as the random solid solution [131]. More details are given in section 1.4. The SQSs of von Pezold et al. [133] were used.

The package VASP [83,84] was used with projector augmented wave (PAW) potentials with the local density approximation (LDA) exchange-correlation [57,58] functional. The electronic structure was calculated for pure Au and $L1_2$ Au_3Fe using four-atom unit cells with a 24×24×24 k-point mesh generated with the Monkhorst-Pack scheme [82] and a plane wave kinetic energy cutoff of 450 eV. For the structures with 32 atoms, the k-point mesh consisted 8×8×8 k-points and the kinetic energy cutoff was 500 eV. In all cases the total energy converged to less than 1 meV. The calculations were spin-polarized in the cases of the SQS of $Au_{24}Fe_8$ and Au_3Fe, which are ferromagnetic at room temperature, giving magnetic moments of 2.75 and 3.00 μ_B/Fe atom, respectively, which are comparable to the value of 2.9 μ_B/Fe atom measured on a solid solution of the same composition [242]. The ground state lattice parameter in each case was found by fitting the energy-volume relationship to the third-order Birch-Murnaghan equation of state [211], giving results within a few percent of the experimental values and reproducing the trend observed in Table 4.3. Electronic DOS curves for pure Au and the Au- and Fe-projected d-electrons in the four SQSs are shown in Fig. 4.6.

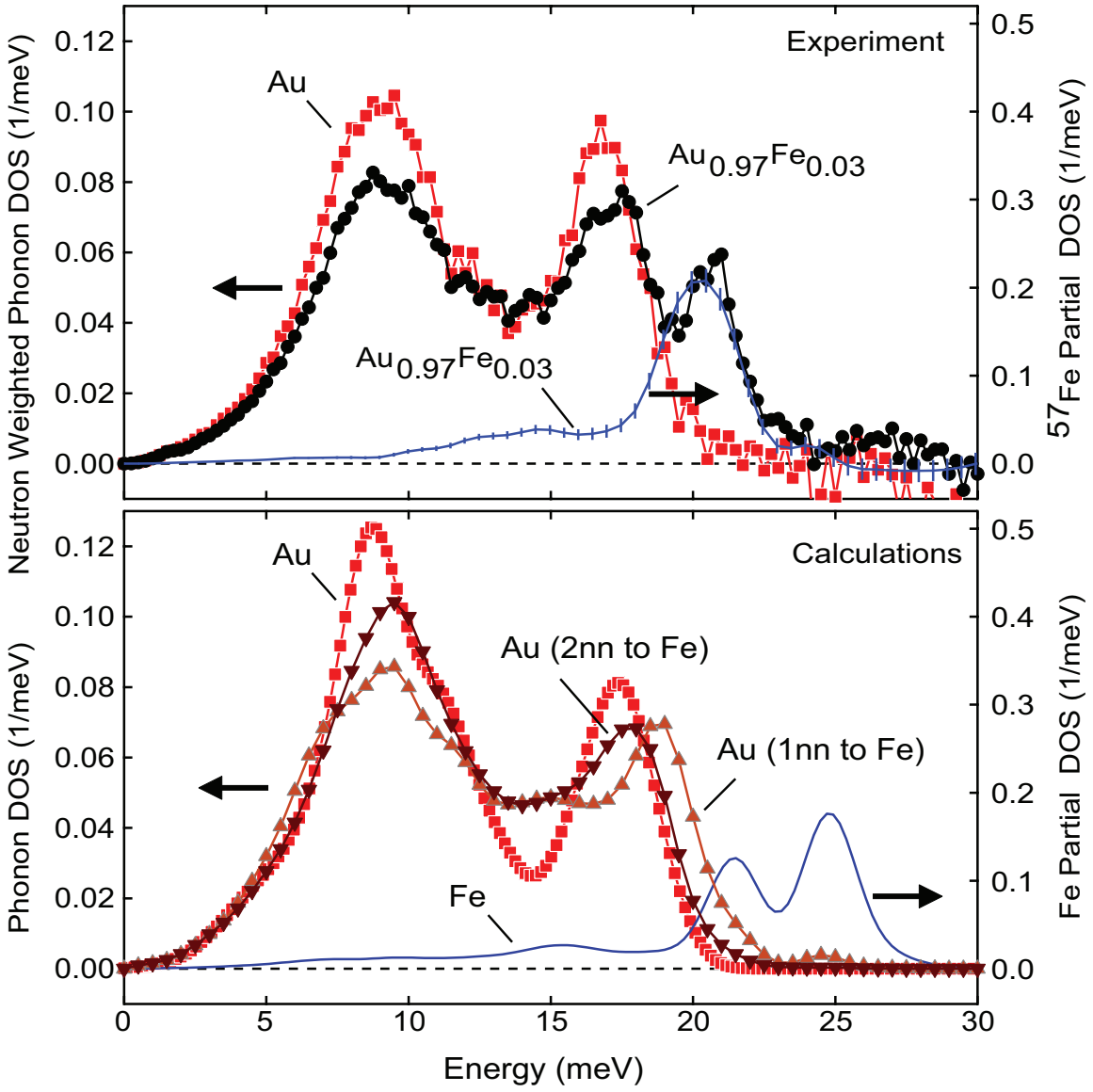

Figure 4.3: Experimental (top) and calculated (bottom panel) phonon DOS curves. (Top) Left axis is the neutron-weighted phonon DOS curves for pure Au and $Fe_{0.03}Au_{0.97}$ from INS measurements and the right axis is the ^{57}Fe partial phonon densities of states for $^{57}Fe_{0.03}Au_{0.97}$ from NRIXS measurements. (Bottom) Analogous curves were calculated for pure Au and an SQS of Fe_2Au_{30}, but the motions of Au atoms that are 1nn to a Fe atom and those that are 2nn are plotted separately.

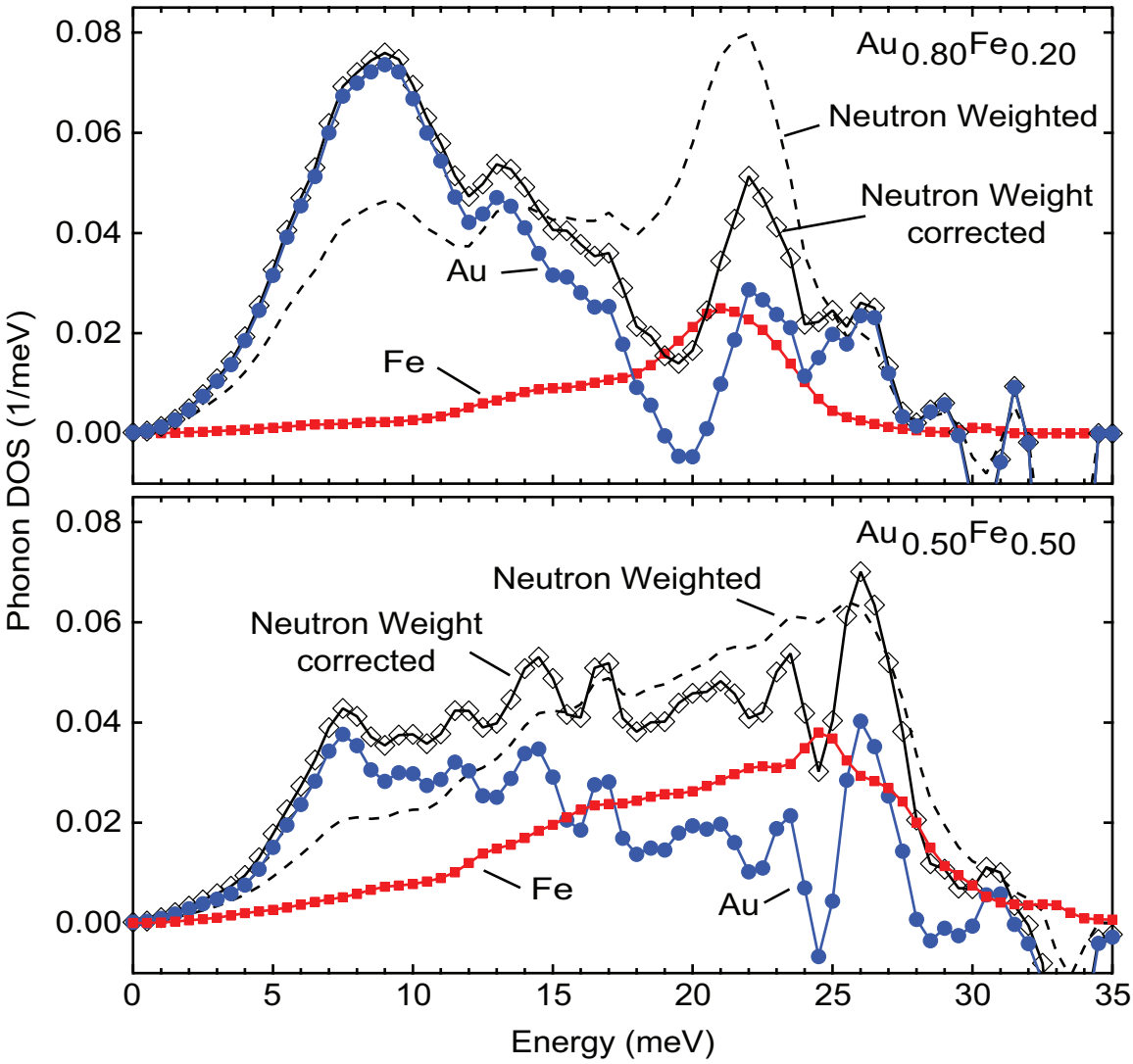

Figure 4.4: Neutron-weighted (dashed curves without markers) and neutron-weight-corrected (open diamonds) phonon DOS curves, along with the concentration-weighted Fe (solid squares) and Au (solid circles) partial phonon DOS curves for $Fe_{0.20}Au_{0.80}$ (top) and $Fe_{0.50}Au_{0.50}$ (bottom).

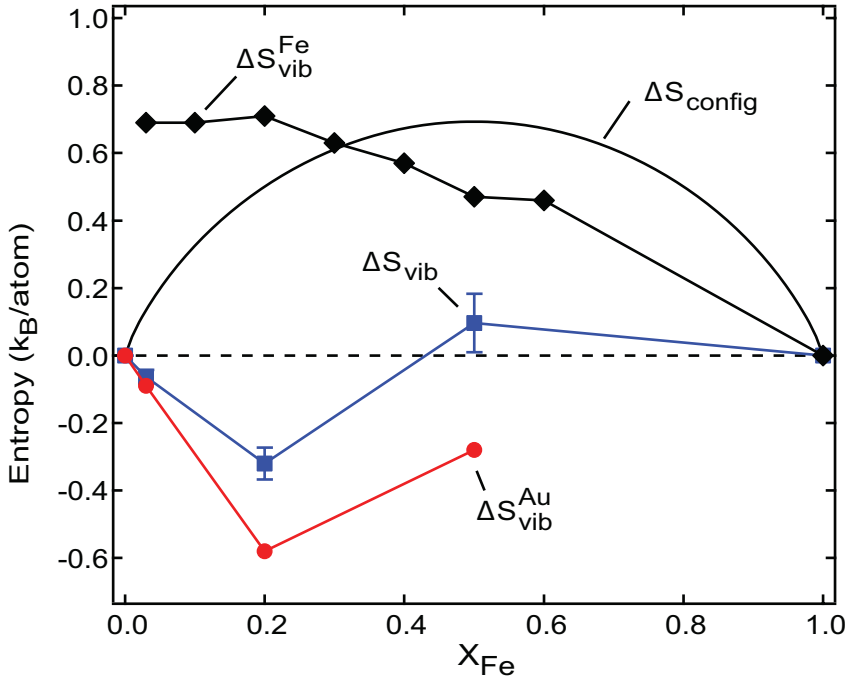

Figure 4.5: Configurational entropy of mixing (ΔS_{config}) and excess vibrational entropy of mixing (ΔS_{vib}) for Fe_xAu_{1-x} alloys with respect to ideal mixing of fcc Au and fcc Fe. Excess vibrational entropy contributions from Au and Fe are ΔS_{Au} and ΔS_{Fe}.

4.4.2 Interatomic force constants

To calculate the interatomic force constants for pure Au and Au_3Fe, a 108-atom supercell (3×3×3 times the standard fcc unit cell) and a 3×3×3 k-point mesh were used. For $Au_{31}Fe_1$ and the SQS structure of $Au_{30}Fe_2$ a 256-atom supercell (4×4×4 times the conventional fcc unit cell) and a 2×2×2 k-point mesh were used. In all cases the atom displacements were 0.01 Å. The grid used to store the wave function and charge density coefficients (basicGrid) included all wave vectors up to twice the cutoff energy to avoid wrap-around errors, and the grid used to calculate the augmentation charges was 8 times denser than the basicGrid. This is necessary for accurate thermodynamic calculations in Au-based systems [283]. Force constants were calculated by the Parlinski-Li-Kawazoe method [98] as implemented in the PHONOPY code [284] and were found to be in good agreement with both experimental fits [282] and calculated results [45,285]. The elements of the interatomic force constant tensor and the resulting bond-stretching force constant are listed in Table 4.4. Dynamical matrices were calculated from the force constants, and phonon DOS curves were computed on 16×16×16 q-meshes using the Monkhorst-Pack scheme [82]. Results for pure Au and the SQS of $Au_{30}Fe_2$ are shown in the bottom panel of Fig. 4.3.

In Fig. 4.3, the Au motions in the SQS are further separated into those of Au atoms that have a Fe atom as 1nn and Au atoms that have a Fe atom as a 2nn but not as a 1nn. Although the composition is slightly higher than in the experimental sample, the trends are satisfactorily

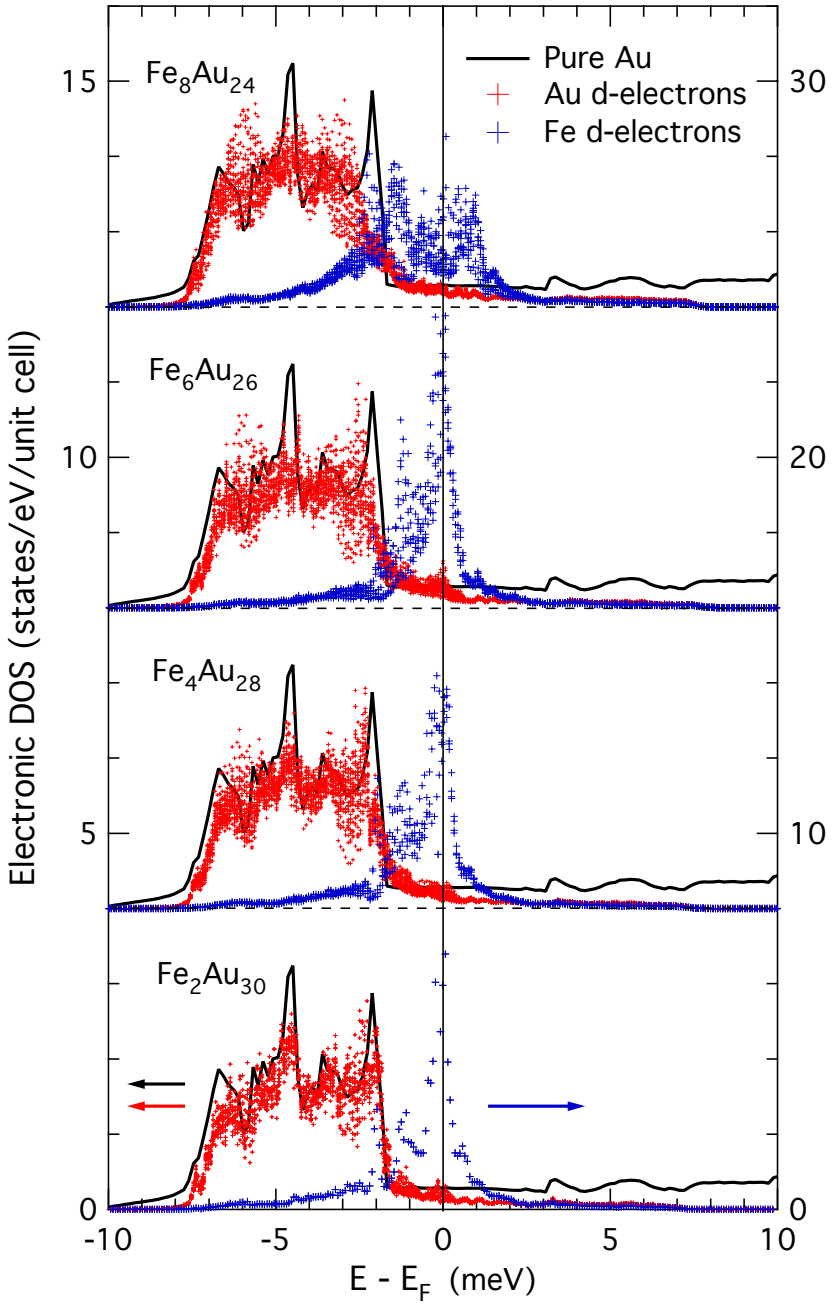

Figure 4.6: Calculated electronic DOS curves for d-electrons at the Fe (left axis) and Au (right axis) sites in the SQSs of $Au_{30}Fe_2$, $Au_{28}Fe_4$, $Au_{26}Fe_6$, and $Au_{24}Fe_8$. The solid line is the electronic DOS of pure Au (right axis). The vertical line marks the Fermi energy.

reproduced. The Fe modes are mostly at energies higher than the calculated value of E_c, which is in agreement with the experimental value. There is a small bump in the Au partial phonon DOS of $Au_{0.97}Fe_{0.03}$ in the same energy range. There is also some stiffening of the rest of the Au modes with respect to pure Au, consistent with a decrease in lattice parameter, although the motions of Au atoms close to Fe atoms are affected more by the (local) decrease in lattice parameter. The Au vibrations with energies greater than E_c come from Au atoms that are 1nn to a Fe atom. This can also be seen in Table 4.4, which shows that the Au-Au bonds that have at least one Fe atom as a nearest-neighbor are substantially stiffer than those that are farther away from Fe atoms.

4.5 Wills-Harrison model

As shown in Fig. 4.5, the excess vibrational entropy of mixing is negative up to at least compositions of 20 at. % Fe, mostly because of the stiffening of the Au partial phonon DOS. A convenient way to study this phenomenon is by looking at the bulk modulus B, the resistance of a system to uniform compression, which is a measure of the stiffness of longitudinal long wavelength motions. It is given by

$$B = -V \frac{d^2E}{dV^2}\Big|_T . \tag{4.3}$$

There are several contributions to the total energy E. For example, a textbook treatment of Au as a free-electron gas yields a bulk modulus of 35 GPa [39], but its experimental value is 171 GPa [286]. Hybridization between the s- and d-electrons accounts for the large difference. Other effects such as electron-phonon interactions are expected to be small in this system due to the low density of states at the Fermi level [230]. Hybridization effects can be incorporated with the Wills-Harrison model [24], which extends the nearly-free-electron theory of simple metals to include the effects of sd-hybridization. Although it is based on bonding between two atoms, an adjustable parameter is fitted to experimental values, so it probably accounts for some longer-range forces and, inadvertently, for other phenomena like electron-phonon interactions or magnetism.

The Wills-Harrison model provides an approximation of the total energy of a metal including contributions from: 1) the nearly-free-electron gas, 2) hybridization between the s-electrons and the d-band, and 3) nonorthogonality of hybridized d-states. It is based on three parameters. The first one, r_0, is the radius of a sphere equal to the atomic volume. The second one is the d-state 'radius,' r_d, which is an element-specific constant that describes the coupling of s- and d-electrons in the pseudopotential perturbation formalism [287]. It originates with the hybridization matrix element,

$$\langle k|\Delta|d\rangle = \left[\frac{\hbar^2 k^2}{N_a^{1/2} m_e}\right]\left[\frac{r_d}{r_0}\right]^{-3/2} Y_2^m(\theta_k, \phi_k) e^{-ikr_j} , \tag{4.4}$$

where $\langle k|$ and $|d\rangle$ are the s and d atomic states, and Δ is the hybridization potential. In Eq. 4.4, N_a

Ti		V		Cr		Mn	Fe		Co		Ni		Cu	
2.2	48%	3.52	46%	4.14	45%		3.09	46%	2.72	44%	2.03	47%	1.03	50%
-1.76	39%	-2.96	39%	-3.67	40%		-2.5	37%	-2.11	34%	-1.24	29%	-0.33	16%
0.6	13%	1.09	14%	1.43	15%		1.1	17%	1.31	22%	1.07	24%	0.67	34%
1.04		1.65		1.9			1.69		1.92		1.86		1.37	
		Nb					Ru						Ag	
		2.92	35%				3.34	29%					0.34	21%
		-3.38	40%				-4.09	36%					-0.29	18%
		2.16	25%				3.96	35%					0.97	61%
		1.7					3.21						1.02	
		Ta					Os						Au	
		3.03	31%				2.85	21%					0.58	17%
		-3.87	40%				4.82	36%					-0.81	24%
		2.84	29%				5.7	43%					1.97	59%
		2					3.73						1.74	

Figure 4.7: Wills-Harrison periodic table. The three rows below the symbol of each element are the values of $B_{\rm fe}$, B_b, and B_c, respectively (see text for details). Percentages are the relative weigh of each contribution to the total bulk modulus B, which is listed in the last row for each element. All values are in GPa.

is the number of atoms in the system and Y_2^m is the spherical harmonic. Δ is spherically symmetric around the nucleus, so only terms for $l = 2$ contribute, and in the (θ_k, ϕ_k) coordinate system, only the term with $m = 0$ with respect to k will contribute. The z-axis for the spherical coordinates is taken to be along the direction of the atom containing the $|d\rangle$ state to the equivalent state in a neighboring atom. Solving for r_d yields

$$r_d^{3/2} = -\frac{1}{5}\left[\frac{4}{3}\pi\right]^{1/2}\frac{m_e}{\hbar}\int_0^\infty r^4 R_2(r)\Delta dr, \tag{4.5}$$

where $R_2(r)$ is the radial d-state wave function, which can be obtained in the Hartree-Fock formalism. It is also possible to fit r_d to d-electron bandwidths from calculations. Finally, r_c is the radius of the Ashcroft empty-core pseudopotential [288]. It is adjustable, but it is correlated to the core radii calculated from the ionization energy of the atom.

The nearly-free-electron gas contribution to the total energy is given by

$$E_{\rm fe} = \frac{3}{5}Z_s\frac{\hbar^2}{2m_e}k_F^2 - \frac{3Z_s e^2 k_F}{4\pi} - \frac{Z_s^2 e^2 \alpha k_F}{(18\pi Z_s)^{1/3}} + \frac{2Z_s}{3\pi}e^2 r_c^2 k_F^3 \ , \tag{4.6}$$

where Z_s is the charge in the outermost s-electron shell, e and m_e are the electron charge and mass, α is the Madelung constant, and the Fermi wavevector k_F is

$$k_F = \frac{1}{r_0}\left(\frac{9\pi Z_s}{4}\right)^{1/3} \ . \tag{4.7}$$

On the right side of Eq. 4.6, the first term is the kinetic energy, the second term is the exchange energy, the third term is the Madelung energy, and the last term is a correction to the Madelung energy when used with the Ashcroft empty-core pseudopotential. The contributions from sd-hybridization

Table 4.1: Total stiffness of the bond between several pairs of elements predicted by the Wills-Harrison model, and contributions from $B_{\rm fe}$, B_b, and B_c (see text for details). All the bulk moduli have units of GPa.

	Au–Au	Au–Fe	Co–Co	Co–Fe	V–V	V–Fe	Fe–Fe
$B_{\rm fe}$	0.58	1.58	2.72	2.91	3.52	3.30	3.09
B_b	-0.81	-1.79	-2.11	-2.27	-2.96	-3.03	-2.50
B_c	1.97	1.64	1.31	1.10	1.09	1.18	1.10
B	1.74	1.43	1.92	1.74	1.65	1.45	1.69

and from the nonorthogonality of the hybridized d-states are

$$E_b = -\frac{1}{2} Z_d \left[1 - \frac{Z_d}{10}\right] (30.9) n^{1/2} \frac{\hbar^2 r_d^3}{m_e d^5} = -\frac{1}{2} Z_d \left[1 - \frac{Z_d}{10}\right] W_d \tag{4.8}$$

and

$$E_c = Z_d n (11.4) \frac{\hbar^2 r_d^6}{m d^8} \ , \tag{4.9}$$

respectively. The numerical values arise from the d-state coupling, n is the number of 1nn atoms for the crystal structure of the system and d is separation between 1nn atoms. The Friedel model is used to approximate the shape of the density of states of the d-electrons [289]. The height of the rectangle is the number of electrons at the Fermi level, $\mathcal{N}_{\rm F}$, and the width $W_d = 10/\mathcal{N}_{\rm F}$. The bulk modulus contributions can be obtained by taking the appropriate energy derivatives with respect to volume, which are denoted $B_{\rm fe}$, B_b, and B_c, respectively.

For the present analysis, empty-core pseudopotential radii, r_c, were fitted while using the values for the other two parameters listed in Ref. [24] to obtain accurate bulk moduli for several elemental metals. The results were sorted in a 'Wills-Harrison periodic table' and are shown in Fig. 4.7. Several trends can be observed. $B_{\rm fe}$ is larger for elements towards the middle of the transition metal rows and is particularly small for the noble metals, generally tracking the experimental bulk modulus of each element. The relative weight of $B_{\rm fe}$ remains about the same for elements in the same row, although it decreases with row number. The relative weight of B_c generally increases with row number. As a result, B_c, arising from the nonorthogonality of hybridized d-states is the most important contribution to the bulk modulus of Au.

The parameters obtained for the elemental metals were used to calculate the bulk moduli of bonds between these elements by considering the geometric mean of r_0, r_d, and r_c for each pair of elements. Several results are shown in Table 4.1. The Wills-Harrison model predicts that the Co–Fe and V–Fe bonds are softer than the average of Co–Co and Fe–Fe, and V–V and Fe-Fe bonds, respectively, which is accurate (see, for example, Refs. [177, 186]). This results in an ordering tendency if the depth of the potential scales with the stiffness (section 3.6.1). The model predicts that the Au-Fe bond is softer than the average of Au–Au and Fe–Fe bonds, but Fe-Au is a system with unmixing tendencies.

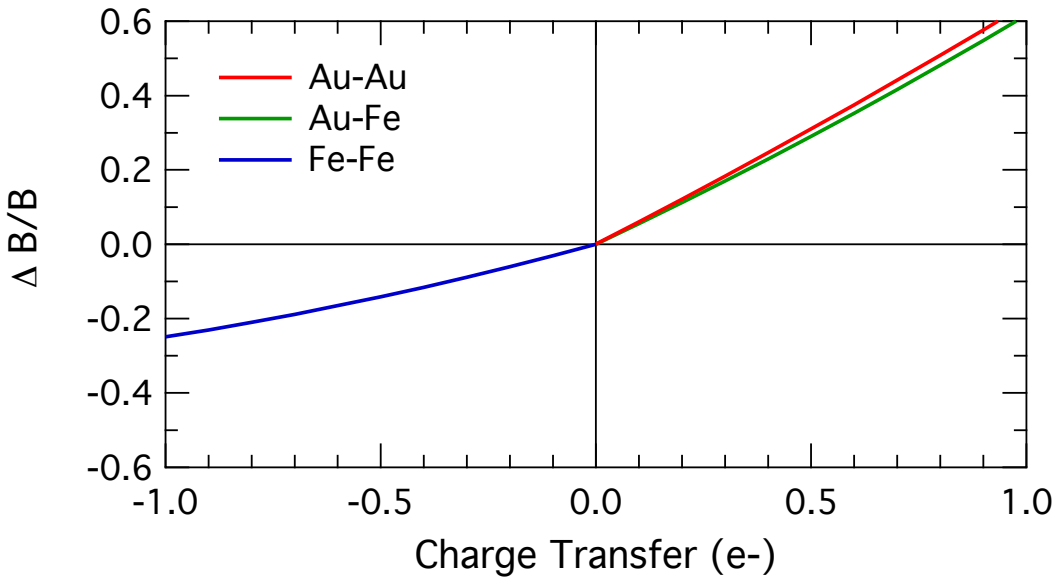

Figure 4.8: Percent change of the bond stiffness when charge is increased or decreased in the atomic spheres of each pair of atoms in the Fe-Au system.

This apparent contradiction is solved when considering charge transfer, which is negligible in the Fe-V and Fe-Co systems, but is significant in the Fe-Au system (see section 4.6.2). As shown in Fig. 4.8, the model predicts a significant increase in the stiffness of the Au-Au and Fe-Au bonds when the charge is increased that is not completely offset by the softening of Fe-Fe bonds when the charge is reduced by the same amount. This eventually makes the unmixing of the system more energetically favorable. The stiffening of Au-Au bonds with increasing charge comes mostly from changes in B_b, *sd*-hybridization.

4.6 Discussion

4.6.1 Phonon thermodynamics

The vibrational entropies of pure Au and pure Fe (Table 4.3 and section 4.3.1) can be used to obtain an ideal vibrational entropy of mixing of $-2.14\,k_{\mathrm{B}}$/atom/(at. fraction Fe). However, a fit to the data in Fig. 4.5 up to 20 at. % Fe gives a slope of $-3.75\,k_{\mathrm{B}}$/atom/ (at. fraction Fe), 75% larger than the value from a simple substitution. A way to assess the thermodynamic effects of the vibrational entropy is by comparing the observed miscibility gap temperatures as a function of Fe content x, $T^{\mathrm{mix}}_{\mathrm{config\,+\,vib}}(x)$, which includes vibrational and configurational contributions to those expected from

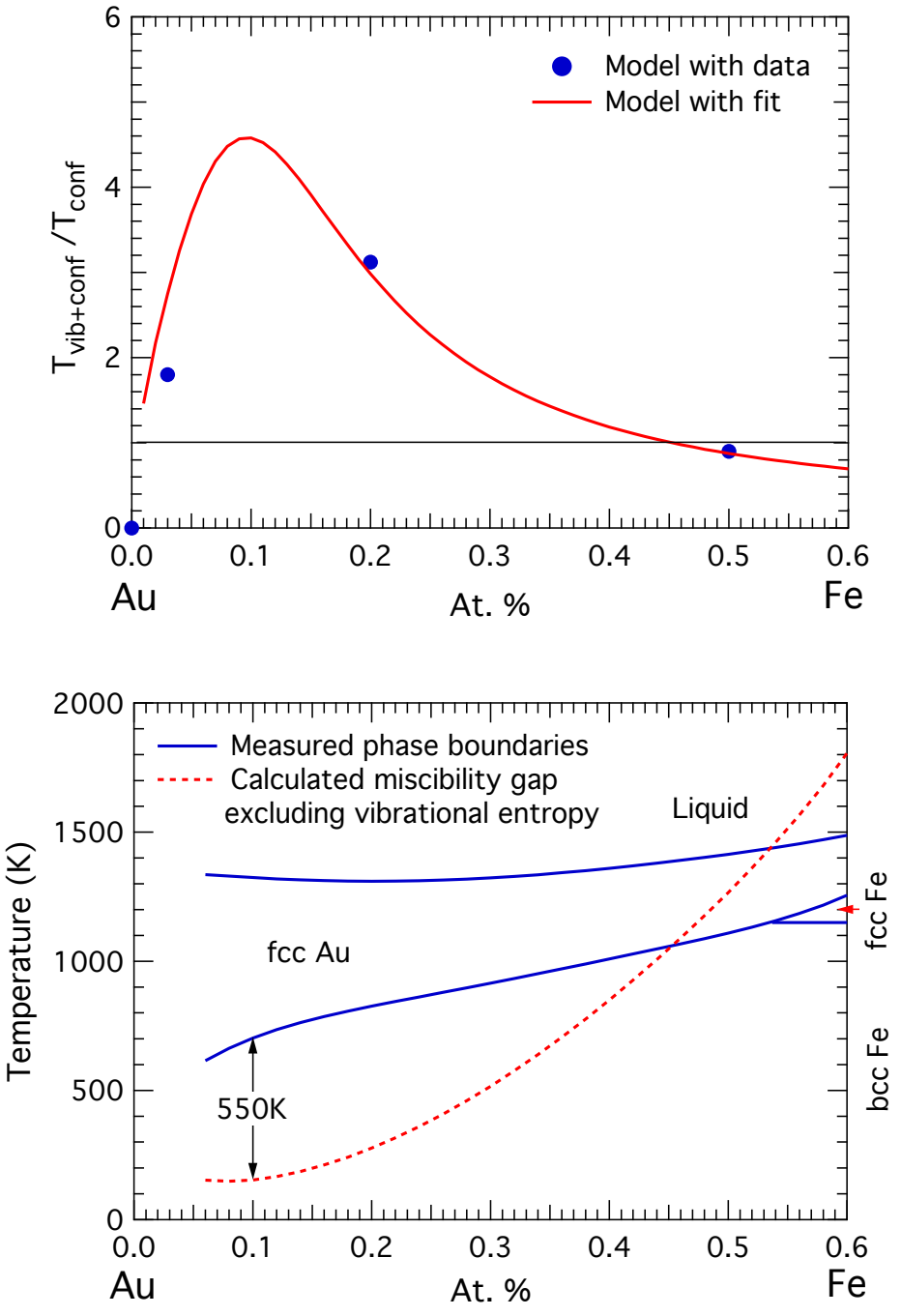

Figure 4.9: (Top) Percent increase of the miscibility gap temperature as a function of Fe content in the Fe-Au system when considering vibrational and configurational entropies versus the configurational contribution alone. (Bottom) Comparison of the observed phase boundaries with the calculated phase boundaries if only configurational entropy is considered.

configurational entropy alone, $T^{\mathrm{mix}}_{\mathrm{config}}(x)$. A simple estimation of this relationship (cf. Eq. 3.7) is

$$T^{\mathrm{mix}}_{\mathrm{config\ +\ vib}}(x) = T^{\mathrm{mix}}_{\mathrm{config}}(x) \cdot \left(1 + \frac{\Delta S^{\mathrm{mix}}_{\mathrm{vib}}(x)}{\Delta S^{\mathrm{mix}}_{\mathrm{config}}(x)}\right)^{-1} , \tag{4.10}$$

where $\Delta S^{\mathrm{mix}}_{\mathrm{vib}}(x)$ is the excess vibrational entropy of mixing shown in Fig. 4.5 and $\Delta S^{\mathrm{mix}}_{\mathrm{config}}(x)$ is given, in the point approximation, by

$$\Delta S_{\mathrm{config}}(x) = -k_{\mathrm{B}}[(1-x)\ln(1-x) + x\ln(x)] \ . \tag{4.11}$$

The plot in the top panel of Fig. 4.9 is obtained from a polynomial fit to the measured excess vibrational entropy of mixing and from Eq. 4.11. It shows that the vibrational entropy has a very large effect at low Fe concentrations which can more than triple the miscibility gap temperature. After a peak at about 10 at. % Fe, the magnitude of the effect decreases with increasing Fe concentrations, and it is close zero at the equiatomic composition. The model predicts a reversed effect of the vibrational entropy on the miscibility gap temperature in the Fe-rich region, but its validity is less clear due to the richer complexity of the phase diagram in this region (see Fig. 4.1). There are several sources of uncertainty in the values, e.g., short-range ordering in the system which may decrease the configurational entropy, the estimation of the vibrational entropy of fcc Fe, but these are small corrections. Perhaps the most significant unknown is the temperature dependence of the vibrational entropy, which was not part of this study, but has been observed to be anharmonic in other systems with segregation tendencies such as Cu-Ag [290].

The lower panel of Fig. 4.9 shows a comparison between the observed phase boundaries of the system and the phase boundaries considering only configurational entropy. The vibrational entropy shifts the phase boundaries up in temperature. The same analysis was performed for several systems using the values calculated by Ozoliņš, Wolverton, and Zunger [291] and the results are presented in Table 4.2. The ratios between critical temperatures with and without vibrational entropy contributions is of the same order of magnitude as those observed in the Fe-Au system. The effect of the excess vibrational entropy of mixing is to decrease the miscibility gap temperature in $Cu_{0.859}Ag_{0.141}$ and NiAu. It increases the order-disorder transition temperature in AgAu and reduces it in CuAu. In the Fe-Au system, the vibrational entropy hinders mixing when Fe is the solute, but it seems to assist it when Fe becomes the solvent. Fig. 4.4 shows a large increase in the number of Au modes near 8 meV at compositions higher than 20 at. % Fe. Although data are not available for the Fe-rich part of the phase diagram, this behavior seems to be consistent with a Au resonance mode due to ordering observed by Bogdanoff et al. [265] in Au-Cu alloys. The resonance mode in Cu_3Au decreases the vibrational entropy of mixing with respect to the disordered sample by about 0.22 k_{B}/atom due to the increase in the number of bonds between light Cu atoms and heavy

Table 4.2: Measured disordering temperature $T^{\mathrm{mix}}_{\mathrm{config\ +\ vib}}$ and disordering temperature accounting only for configurational entropy $T^{\mathrm{mix}}_{\mathrm{config}}$. Change in configurational entropy $\Delta S^{\mathrm{mix}}_{\mathrm{config}}$ and excess vibrational entropy of mixing $\Delta S^{\mathrm{mix}}_{\mathrm{vib}}$ upon disordering for the ordering systems CuAu and AgAu and the segregating systems $Cu_{0.859}Ag_{0.141}$ and NiAu. Shift in the disordering temperature due to vibrational entropy alone $T^{\mathrm{mix}}_{\mathrm{vib}}$.

System	$T^{\mathrm{mix}}_{\mathrm{config\ +\ vib}}$	$\Delta S^{\mathrm{mix}}_{\mathrm{config}}$	$\Delta S^{\mathrm{mix}}_{\mathrm{vib}}$	$T^{\mathrm{mix}}_{\mathrm{config\ +\ vib}}/T^{\mathrm{mix}}_{\mathrm{config}}$	$T^{\mathrm{mix}}_{\mathrm{vib}}$
	K	k_{B}/atom	k_{B}/atom		K
CuAu	800	0.57	0.16	0.78	-225
AgAu	800	0.62	-0.10	1.19	129
$Cu_{0.859}Ag_{0.141}$	1052	0.40	0.37	0.52	-973
NiAu	1100	0.56	0.48	0.54	-943

Au atoms and perhaps a decrease in the lattice parameter. This shows that the overall vibrational entropy in these noble-metal-like systems is not trivially related to the bond proportion or other simple quantities, but it is the result of different phenomena like charge transfer, hybridization, or mass ratios acting constructively or destructively. These phenomena will be discussed below for the Fe-Au system.

The combination of INS and NRIXS measurements provides information of the individual motion of Au and Fe atoms. The Au partial phonon DOS stiffens considerably with increased Fe concentration, mostly because the Au–Au bonds that have a Fe atom as a nearest neighbor stiffen substantially and this raises the energies of some Au modes above the cutoff energy of pure Au. This is a local effect and the Au atoms that are not close to Fe atoms have force constants that are much closer to that of pure Au, as indicated by the calculations (Table 4.4). This stiffening trend continues as the Fe concentration is increased and is the main reason why the vibrational entropy of mixing in Fig. 4.5 is negative at Fe concentrations up to 20%. The magnitude of the excess phonon entropy of mixing is more than half the configurational entropy of mixing and opposite in sign. Although chemical mixing is favored in the fcc phase by the configurational entropy, the phonon entropy favors chemical unmixing, and contributes to the miscibility gap in the Fe-Au phase diagram shown in Fig. 4.1.

At dilute concentrations, Fe atoms vibrate in a local mode at an energy higher than E_c, as shown in the top panel of Fig. 4.3, and this is reproduced by the calculations using an SQS. The 1nn force constants are dominant in the system and Au atoms are four times more massive than Fe atoms. A quick calculation with a classical harmonic oscillator model using the force constants from Table 4.4 shows that the average energy of the Fe vibrations should be about 40% higher than those of Au. The Mannheim model [267] can be used with the Green's function formalism of Seto, et al. [292] to obtain the ratio between the longitudinal force constants of the Au-Au and Fe-Au bonds from

the phonon DOS curves. The ratio obtained by this procedure was 1.55 [293], comparable to 1.80 obtained from the ab initio results.

With increasing composition there are more Fe atoms in the nearest neighbor shells of other Fe atoms, and this distribution of local environments may be responsible for much of the increase in the peak width of the Fe modes at modest concentrations observed in Fig. 4.2. The mean energy of this local mode of Fe atoms does not change enough with Fe concentration to have a substantial effect on the vibrational entropy, however.

4.6.2 *sd*-hybridization

Fig. 4.6 shows a sharp peak in Fe 3*d*-electrons at the Fermi level of the SQS for Fe_2Au_{30}. This peak grows and broadens with increased Fe concentration (considering that there are more Fe atoms). The Fe 3*d*-electrons at the Fermi level may facilitate the screening of the Fe atom motions [3,20,21,186], perhaps counteracting somewhat the tendency for phonons to stiffen with the decrease in lattice parameter. Nevertheless, from Fig. 4.5 we see that the larger effect on the vibrational entropy is from the stiffening of the vibrations of Au atoms.

The Wills-Harrison model (see section 4.5) predicts a value of 143 GPa for the bulk modulus of the Fe–Au bond, compared to 174 and 169 GPa for Au–Au and Fe–Fe bonds, respectively. This is in agreement with the ab initio calculations which predict that the Fe–Au bond is softer than the Au–Au bond. For Fe–Au bonds, the relative weight of each contribution, B_{fe}, B_b, and B_c, is intermediate between that of noble metal and transition metal bonds, and B_b and B_c almost cancel each other out. As the Fe concentration increases, the phonon DOS stiffens and both the Au-Au and Fe-Au bonds stiffen (Table 4.4). This stiffening is predicted by the Wills-Harrison model when charge is increased in these bonds (Fig. 4.8) and comes mostly from B_b, the coupling between occupied *d*-states and unoccupied plane wave states. The model also predicts an overall increase in the hybridization contribution to the bulk modulus (B_b and B_c) when the lattice parameter is reduced in the case of noble metals. The electronic origin of the change of Au atom stiffness is from *s*-states near the Fermi level and from *sd*-hybridization. Considering just the free-electron like contributions, we would expect a stiffening of the Au–Au bonds with Fe concentration for two reasons.

First, there is a charge transfer from Fe to Au. It is difficult to quantify the charge transfer with respect to pure fcc Fe, but the charge in a sphere of radius 1.503 Å about Au atoms in the SQSs that are next to Fe atoms is larger than the charge around Au atoms that are not, indicating a transfer from Fe atoms to each 1nn Au atom of about 0.04 electrons. The electronic DOS of Au in Fig. 4.6 can be approximated as a band of nearly-free-electrons with 0.2 /states/eV/atom at a Fermi level that lies 10 eV above the bottom of the band. For a Fe concentration of 10%, if each Fe atom contributes half an electron to the nearly-free-electron band, B_{fe} for the Au–Au bonds will

increase by 5%.

Second, the lattice parameter is reduced with Fe concentration, giving an increase in nearly-free-electron density that is proportional to the modulus. For a Fe concentration of 10%, using the lattice parameters of Table 4.3, this gives an increase of 1.7%. The Au-Au bond bulk modulus stiffening due to free-electron like contributions is therefore 6.7% for a Fe concentration of 10%.

The elastic constants for the Au–Au bonds in pure Au, $Au_{31}Fe_1$, and Au_3Fe were calculated following the analysis in Ref. [206] and the interatomic force constants given in Table 4.4. The results for the bulk modulus are 185, 193, and 246 GPa, respectively. The value for pure Au is in good agreement with experiments [286]. For the Fe–Au bond in $Au_{31}Fe_1$ we obtained 63 GPa. These values come from DFT calculations, so they include all the electronic contributions, including hybridization. The increase in the bulk modulus is linear and predicts a stiffening of the Au–Au bond of 13% at a composition of 10% Fe. We estimated above that about half (6.7%) comes from filling of the nearly-free-electron band and thus, the other half results from changes in the *sd*-hybridization. According to the Wills-Harrison model, the stronger hybridization is mainly the result of changes in B_b. Assuming the interatomic force constants increase by this total of 13 %, Eq. 1.24 predicts that the vibrational entropy will decrease by 0.12–0.20 k_B/atom. This assumes that all the Au atoms are affected, while hybridization happens around Fe atoms, so the interpolation might be off at very small Fe concentrations. Nevertheless, this shortcoming is less serious at 10 at. % Fe, and results in a change of vibrational entropy that is close to the experimental result of about 0.16 k_B/atom.

4.7 Conclusion

In the present study using NRIXS and INS, the local modes of Fe atoms in an fcc Au host are identified. The change in both Fe and Au vibrations with increasing Fe composition and the effects of both species on the vibrational entropy of the solid solution were investigated. First principles calculations of the force constants and electronic structures of Fe-Au compounds were used to interpret the phonon DOS curves. The phonon partial DOS of Au atoms depends strongly on the Fe concentration, with an increase in energy (stiffening) of the Au vibrations with increasing Fe content. This stiffening of the Au modes dominates the alloy vibrational entropy but, contrary to transition metal alloys [3,20,22,186], cannot be fully explained by changes in lattice parameter or the overall electronic DOS at the Fermi level. We suggest that its origin is twofold. First, the donation of charge from Fe atoms to a nearly-free-electronic band causes a stiffening of the elastic constants. Second, the increase in the number of available *d*-electrons from the Fe affects the *sd*-hybridization and, according to the Wills-Harrison model [24], results in stiffer bonds.

Table 4.3: Measured lattice parameter a and vibrational entropy S_{vib} of Fe-Au alloys at 300 K from x-ray diffraction, nuclear resonant inelastic x-ray scattering, and inelastic neutron scattering. $S_{\mathrm{vib}}^{\mathrm{Fe}}$ and $S_{\mathrm{vib}}^{\mathrm{Au}}$ denote the vibrational entropy of the Fe and Au atoms, $S_{\mathrm{vib}}^{\mathrm{NW}}$ is the average vibrational entropy per atom as obtained from the neutron-weighted INS data, and S_{vib} is the neutron-weight-corrected average entropy per atom obtained by combining the INS and NRIXS results as described in the text.

Sample	a (x-ray) $\pm$ 0.002 Å	a (neutron) $\pm$ 0.008 Å	$S_{\mathrm{vib}}^{\mathrm{Fe}}$ k_{B} /atom	$S_{\mathrm{vib}}^{\mathrm{Au}}$ k_{B} /atom	$S_{\mathrm{vib}}^{\mathrm{NW}}$ $\pm$ 0.01 k_{B} /atom	S_{vib} k_{B} /atom
Au	4.0786	4.0693	-	5.64 $\pm$ 0.01	5.64	5.64 $\pm$ 0.01
$Au_{0.97}Fe_{0.03}$	4.0721	4.0638	4.19 $\pm$ 0.06	5.56 $\pm$ 0.02	5.36	5.52 $\pm$ 0.02
$Au_{0.90}Fe_{0.10}$	4.0555	-	4.19 $\pm$ 0.05	-	-	-
$Au_{0.80}Fe_{0.20}$	4.0262	4.0256	4.21 $\pm$ 0.04	5.07 $\pm$ 0.06	4.58	4.89 $\pm$ 0.05
$Au_{0.70}Fe_{0.30}$	3.9913	-	4.13 $\pm$ 0.04	-	-	-
$Au_{0.60}Fe_{0.40}$	3.9492	-	4.07 $\pm$ 0.03	-	-	-
$Au_{0.50}Fe_{0.50}$	3.9084	3.9001	3.97 $\pm$ 0.03	5.36 $\pm$ 0.17	4.19	4.67 $\pm$ 0.09
$Au_{0.40}Fe_{0.60}$	3.8607	-	3.96 $\pm$ 0.03	-	-	-

Table 4.4: Interatomic force constant tensor elements and bond-stretching (longitudinal) force constants for pure Au, ordered $Au_{31}Fe_1$ and $L1_2$ Au_3Fe, and the SQS of $Au_{30}Fe_2$ from first principles calculations for first, second and third nearest-neighbors (nn). For the longitudinal force constants, denoted by ϕ_{zz}, the bond direction was rotated to be along the z-axis by covariant transformation. For $Au_{31}Fe_1$, the values reported for the Au-Au bonds are for Au atoms that have at least one Fe atom as a 1nn. The forces reported for the SQS of $Au_{30}Fe_2$ are average forces and two sets of Au-Au forces are given, one for Au atoms that have a Fe atom as a 1nn (denoted by the superscript '1') and another for Au atoms that are 2nn to Fe atoms (denoted by the superscript '2'). All force constants have units of N/m.

		Au	$Au_{31}Fe_1$		Au_3Fe			$Au_{30}Fe_2$ (SQS)		
		Au-Au	Au–Au	Fe–Au	Au–Au	Fe–Au	Fe–Fe	Au-Au[1]	Au-Au[2]	Fe–Au
1nn	ϕ_{11}	16.63	18.43	5.49	23.15	7.39	-	-	-	-
	ϕ_{12}	20.82	23.43	5.78	26.88	12.65	-	-	-	-
	ϕ_{33}	-8.62	-7.16	-0.38	-12.46	-2.67	-	-	-	-
	ϕ_{zz}	37.44	41.86	11.27	50.04	20.04	-	45.80	36.57	20.76
2nn	ϕ_{11}	4.90	4.52	2.64	3.59	-	0.63	-	-	-
	ϕ_{22}	0.07	0.81	-0.88	0.09	-	0.89	-	-	-
	ϕ_{zz}	4.90	4.52	2.64	3.59	-	0.63	4.05	4.42	2.84
3nn	ϕ_{11}	1.07	1.16	0.26	1.82	0.69	-	-	-	-
	ϕ_{22}	1.01	1.06	0.01	1.38	0.07	-	-	-	-
	ϕ_{12}	0.43	0.53	0.58	1.25	-0.11	-	-	-	-
	ϕ_{23}	0.12	-0.15	0.00	-2.06	0.24	-	-	-	-
	ϕ_{zz}	1.59	1.67	0.62	4.15	0.59	-	0.53	0.58	1.25

Chapter 5

Phonon-induced charge transfer in FeTi

5.1 Introduction

The FeTi system has been the subject of numerous experimental and computational studies due to its various properties and characteristics. It has a simple $B2$-ordered structure that is extremely stable, with a melting point of almost 1600 K (Fig. 5.1), so it was the subject of some of the first electronic structure calculations on transition metal alloys [294–296]. The predictive power of these early calculations was tested by comparing the results to measurements of the Fermi surface [297], specific heat [298], isomer shift [299], x-ray emission [300] and band structure [301]. The discovery of the shape-memory effect in NiTi in 1962 [302, 303] made CoTi and FeTi interesting for comparative studies of the electronic structure [304, 305]. Finally, it became interesting in its own right with the discovery in 1974 of its significant hydrogen absorption capabilities [306]. Since then, most of the work on FeTi has been in this context.

The previous two chapters explored the relationship between the local atomic arrangement and the vibrational entropy at the electronic structure level. In this chapter we study the effects of temperature, and also pressure, on the interplay between phonons and electrons. As discussed in section 1.1.4, anharmonic behavior is expected to become stronger at higher temperatures, and there are several techniques that allow studies of this kind of behavior. The simplest is perhaps measuring the heat capacity as a function of temperature. Deviations from the Dulong and Petit limit beyond that of the expected contributions from electrons and thermal expansions is the signature of effects that cannot be accounted for by the quasiharmonic model. This approach has been used to assess the anharmonic entropies in a number of cases, for example, for fcc and bcc metals [307–309], in which the electron-phonon interaction might be relevant. More detailed information can be obtained by measuring the phonons directly at elevated temperatures. This has been done by triple-axis inelastic neutron scattering in a number of relevant systems, such as Cr [310], bcc Ti [311] ,

and Zr [312]. Time-of-flight inelastic neutron scattering has been used to measure V-rich alloys at elevated temperatures [3, 20], as discussed in chapter 3. Nevertheless, in general it is necessary to perform computer simulations to understand if the anharmonic behavior is due to changes in the electronic structure, an increase in the phonon-phonon interaction, or something else.

In this chapter we present a unique set of measurements on FeTi. NRIXS measurements, which probe exclusively the Fe vibrations, were performed in a diamond-anvil cell up to a pressure of 47 GPa and in a different setup, in a custom-built resistive furnace that heated from room temperature to a temperature of 1035 K. These are the first NRIXS results available for any material in this temperature range, which is too low to be attainable by conventional laser heating. INS measurements were performed at cryogenic temperatures in a closed-cycle helium refrigerator and up to a temperature of 750 K in a resistive heating furnace. This allowed for the determination of the Ti-specific motions as a function of temperature. The high temperature and high pressure measurements are complementary and they allow for an experimental assessment of the explicit anharmonicity, which proves substantial in the system.

FeTi is isoelectronic with Cr and has a similar electronic structure. The interatomic longitudinal force constants between 2nn atoms are stiffer than those between 1nn atoms in both systems. This is explained by a charge distribution model that allocates most of the valence electrons in the direction of the 1nn atoms. Ab initio calculations in the quasiharmonic limit reproduce the pressure dependence of the phonons, but not the temperature dependence. Ab initio molecular dynamics calculations were performed to study the temperature dependence of the charge distribution. It becomes more isotropic at high temperatures due to a shift of the charge to orbitals of higher energy, which explains the preferential softening of the 2nn longitudinal force constants with temperature. Phonon DOS curves generated from these calculations reproduce the observed experimental softening with temperature. It was determined that the charge redistribution is a response in the adiabatic limit to the phonon perturbation, providing evidence of a phonon-induced charge transfer. This phenomenon might also occur in other bcc metals or bcc-based alloys with strong quasi-ionic bonding

5.2 Experimental

5.2.1 Sample preparation

The $B2$ FeTi neutron-scattering sample was synthesized by arc-melting shots of 99.98% pure Ti and 99.97% pure Fe in the stoichiometric ratio under an argon atmosphere. The samples were crushed and melted again several times to ensure homogeneity. There was negligible mass loss and no visible oxidation after melting. The same procedure was followed to prepare $B2$ FeTi for NRIXS measurements, but the samples were isotropically enriched with 96% ^{57}Fe. In both cases, x-ray diffraction with Cu K_α radiation showed the underlying bcc structure.

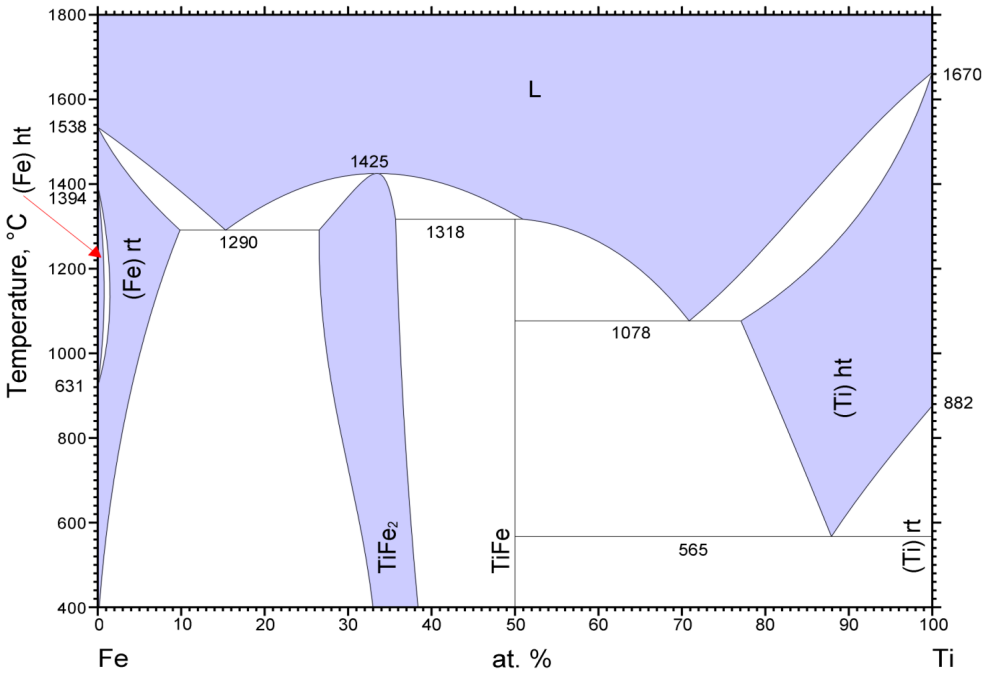

Figure 5.1: Fe-Ti phase diagram adopted from ASM International Alloy Phase Diagrams Center [313].

5.2.2 Scattering measurements

INS measurements were performed with the ARCS spectrometer [149] at the Spallation Neutron Source at the Oak Ridge National Laboratory. The arc-melted sample was crushed and loaded into a 5/8-inch diameter aluminum can with a 3/8-inch diameter annulus. The can was mounted in a low-background resistive furnace with thin aluminum shielding for thermal radiation for measurements at 300, 523, and 748 K. Components of the sample environment not exposed to the beam were covered with neutron-absorbing cadmium or boron nitride to reduce the background. The nominal incident energy was 80 meV and a chopper frequency of 600 Hz was used for all measurements. The energy resolution has a full-width-at-half-maximum (FWHM) of 1.7 meV at 40 meV neutron energy loss, increasing to 3.1 meV at the elastic line. The empty Al sample container was measured at all temperatures and was subtracted from the measured spectra of the samples.

NRIXS measurements were performed at high temperatures and high pressures at beam line 16ID-D at the Advanced Photon Source at the Argonne National Laboratory with an incident x-ray beam with an energy of 14.413 keV, the resonant energy of ^{57}Fe. The monochromator resolution function was measured in situ with an avalanche photodiode detector (APD) and determined to be

2.2 meV FWHM. For measurements at high temperatures (300, 523, 748, and 1035 K), the arc-melted and crushed sample was loosely dispersed between two Kapton polyimide films, making a thin and flat square. This was then accommodated in a custom-built furnace, close to a thermocouple and a resistive heating element. The sample was enclosed in two concentric niobium foil cylinders from which a small area had been stripped off for x-ray access. The whole device was enclosed in a steel tube and connected in series to a mechanical and a turbomolecular pump. The steel tube had a window cut off for x-ray access which was covered by Kapton tape and kept in place with ceramic adhesive. The sample was fixed at a grazing angle to the x-ray beam and an APD was set on top of the furnace at a right angle with the beam. NRIXS data was collected in scans of incident photon energy from −90 to +90 meV around the resonant energy.

For NRIXS measurements at high pressures, the arc-melted and crushed sample was loaded into a panoramic piston-cylinder-type diamond-anvil cell (DAC) optimized for use in NRIXS measurements [314]. Three APDs were positioned 90° from the direction of the beam. Several ruby chips were loaded into the pressure chamber along with the sample and were used for pressure calibration [315]. Beryllium was used as a gasket material to allow transmission of x-rays. The culets of the diamonds had diameters of 500 μm and the hole had a diameter of 200 μm. No pressure medium was used, but measurements of rubies in several places around the pressure chamber ruled out any large pressure gradients. NRIXS data was collected in scans of incident photon energy from −90 to +90 meV around the resonant energy for measurements at 0, 10, 19, and 33 GPa, and from −120 to +120 meV for measurements at 47 GPa.

High pressure angle-dispersive x-ray diffraction (ADXD) was performed on the $B2$ FeTi sample with natural enrichment at beamline X17C at the National Synchrotron Light Source at the Brookhaven National Laboratory up to 26 GPa. A Merrill-Bassett-based [316, 317] DAC was used. The culets of the diamonds had a diameter of 500 μm and the hole drilled in a 301 stainless steel gasket had a diameter of 250 μm. Silicone oil was used as the pressure medium. The pressure calibration was done by the fluorescence of ruby technique [315], and measurements of several ruby chips in the pressure chamber proved the pressure to be homogeneous. A monochromatic x-ray beam of energy 30.4912 keV (wavelength of 0.4066 Å) was used and a charge-coupled device (CCD) detector was placed at a distance of 256.55 mm from the sample.

5.2.3 Ancillary measurements

The sample density was calculated from the lattice parameters obtained by x-ray diffractometry. The lattice parameters as a function of temperature were also measured in the temperature range 300–900 K using a commercial furnace, and the coefficient of linear thermal expansion α was calculated.

5.3 Experimental results

5.3.1 Phonon DOS curves at elevated temperatures

NWDOS curves were obtained from INS data reduced by the method described in section 2.1.3 and the results are shown in the top panel of Fig. 5.2. The ^{57}Fe partial DOS curves obtained from NRIXS data, which were reduced by the method described in section 2.2.3, are also shown in this figure. The neutron scattering efficiency of each element is proportional to σ/M. This ratio is 0.208 for Fe and 0.091 for Ti, so the Ti motions in the NWDOS curves are underrepresented by a factor of about 2. The excess weight of the Fe partial phonon DOS obtained from NRIXS gives the neutron-weight-corrected DOS curves in Fig. 5.2. Subtracting all the weight gives the V partial phonon DOS shown in the same figure. The larger error bars are due to the lower neutron scattering efficiency of these atoms.

In FeTi, the vibrational entropy per atom increases linearly with temperature at temperatures above 300 K. For the Fe motions, it increases from $3.17 \pm 0.01\,k_B$/atom at room temperature to $7.00 \pm 0.01\,k_B$/atom at 1035 K. For the V motions, it increases from $3.00 \pm 0.04\,k_B$/atom at room temperature to $5.84 \pm 0.04\,k_B$/atom at 750 K. INS measurements were performed at ARCS in a closed-cycle helium refrigerator at 10 and 150 K, but there was no difference in their DOS curves with respect to those measured at 300 K and that is why they were not included in Fig. 5.2. The phonon entropy of pure Fe is $3.15 \pm 0.01\,k_B$/atom (see Section 3.3.2), while the phonon entropy of pure hcp Ti was estimated from the measurements of Stassis et al. [318] to be $4.2\,k_B$/atom. The decrease in the vibrational entropy in the $B2$ phase as compared to the elemental components is thus $0.62\,k_B$/atom. This is large, equivalent to 0.07 eV at the melting temperature, but the energy of formation is –0.42 eV per unit cell [319] with respect to the pure elements, which makes the intermetallic phase very stable. FeTi is nonmagnetic, whereas Fe is ferromagnetic in its pure form, so we expect changes in magnetic entropy to be negligible. The average phonon energy decreases linearly at temperatures above room temperature. Results for the total DOS curves and the Fe and Ti partial DOS curves are shown in Fig. 5.3.

5.3.2 Phonon DOS curves at elevated pressures

The ^{57}Fe partial DOS curves obtained from NRIXS data, reduced by the method described in section 2.1.3, are shown in Fig. 5.4. The larger error bars at higher pressures stem from a thinning of the sample that reduces the number of counts per unit time, and from the reduced sampling of high energy phonons due to their smaller vibration amplitude. The ^{57}Fe vibrational entropy decreases linearly with pressure from $3.17 \pm 0.01\,k_B$/atom at ambient pressure to $2.44 \pm 0.01\,k_B$/atom at 47 GPa. It is evident in the figure that the main (localized) peak shifts to higher energies with pressure, but the appearance of a high energy shoulder can also be observed.

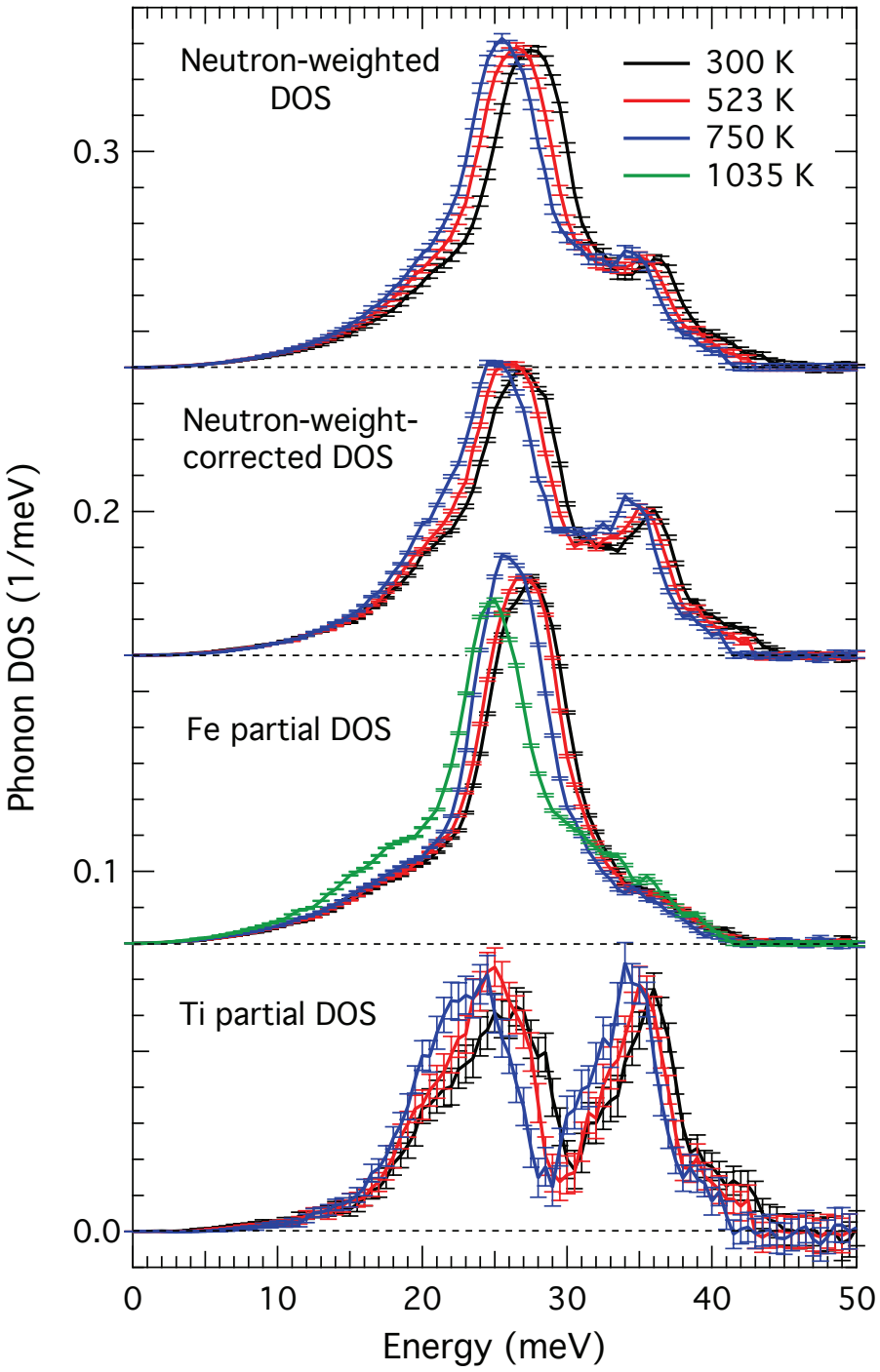

Figure 5.2: Phonon DOS curves for FeTi at elevated temperatures. The neutron-weighted DOS curves were obtained from INS measurements and the Fe partial DOS curves from NRIXS measurements. The two data sets were combined to obtained neutron-weight-corrected DOS curves and Ti partial DOS curves. See text for details.

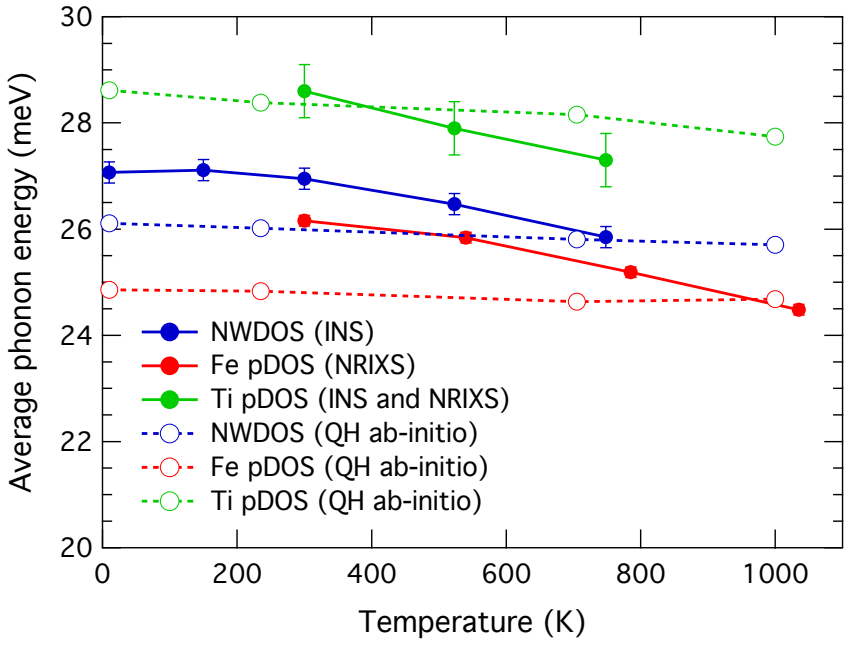

Figure 5.3: Experimental and calculated average phonon energy as a function of temperature for the Fe- and Ti-specific motions, as well as total neutron-weight-corrected DOS curve for FeTi. Error bars are from counting statistics.

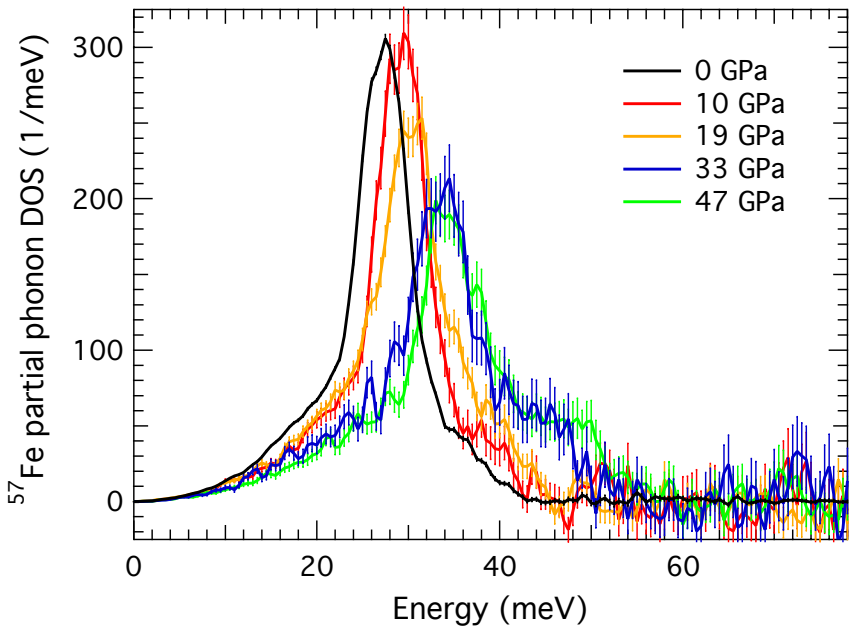

Figure 5.4: ^{57}Fe partial phonon DOS curves for FeTi at elevated pressures from NRIXS measurements in a diamond-anvil cell at room temperature.

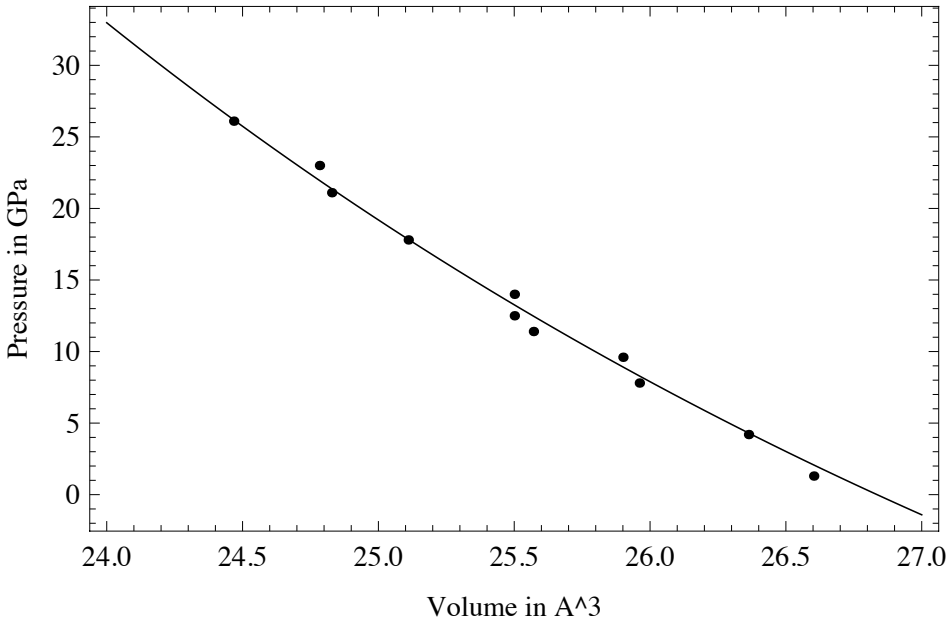

Figure 5.5: Volume-pressure relationship in the FeTi system measured by high-pressure x-ray diffraction in a diamond-anvil cell at room temperature. The solid line is a fit to the data using the third-order Birch-Murnaghan equation.

The relationship between the pressure and the volume was obtained by fitting the pressure variant of the Birch-Murnaghan equation of state [211] to the high-pressure diffraction measurements. The equation is

$$P(V) = \frac{3B_0}{2}\left[\left(\frac{V_0}{V}\right)^{\frac{7}{3}} - \left(\frac{V_0}{V}\right)^{\frac{5}{3}}\right]\left\{1 + \frac{3}{4}\left(B_0' - 4\right)\left[\left(\frac{V_0}{V}\right)^{\frac{2}{3}} - 1\right]\right\}, \tag{5.1}$$

where B_0' is the pressure derivative of the bulk modulus and was given a value of 4.0, which provided the best fit and is a common value for metals. The data and the fit are shown in Fig. 5.5. A value of 212 GPa was obtained for the bulk modulus, which is in reasonable agreement with the value of Buchenau et al. [320] of 193 GPa obtained from the force constants of a Born-von Kármán fit to phonon dispersions. Liebertz, Stähr, and Haussühl [321] obtained a value of 160 GPa from pulse-echo measurements. The ab initio results presented below gave a value of 192 GPa, and Zhu et al. [319] obtained the same value. Using the pressure-volume relationship, the average phonon energy as a function of volume compression is shown in Fig. 5.6.

5.3.3 Explicit anharmonicity

The assumption of the harmonic model is that a phonon has a well-defined, harmonic-like frequency with an infinite lifetime. The quasiharmonic model expands this by assuming that a change in volume, which can originate with a change in pressure or temperature, will change the energy of the

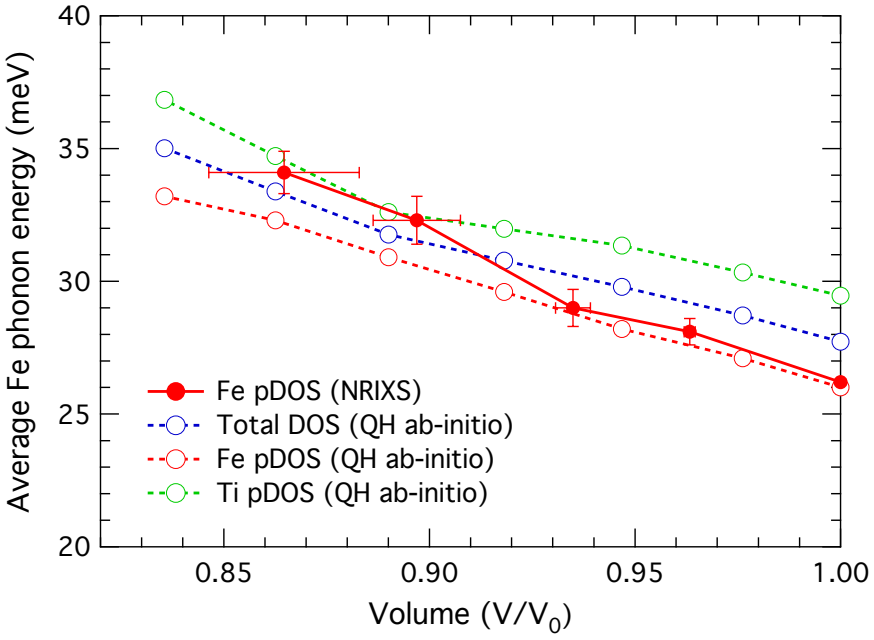

Figure 5.6: Experimental and calculated average phonon energy as a function of volume compression for the partial phonon DOS of Fe in FeTi at room temperature. Energy error bars are from counting statistics. Volume error bars are from the distribution of pressures measured for the rubies inside the diamond-anvil cell.

phonon, but not its lifetime. The change in the average energy of the phonon is thus given by

$$\frac{\Delta E}{E} = \gamma \frac{\Delta V}{V}, \tag{5.2}$$

where the proportionality constant γ is called the Grüneisen parameter, after the scientist that first postulated this definition [41]. In the quasiharmonic model, the average Grüneisen parameter of all the phonon modes, $\bar{\gamma}$, should be equal to the thermal Grüneisen parameter, $\gamma_{\rm th}$ (see, for example, Ref. [322]), which is given by

$$\gamma_{\rm th} = -\frac{Bv\beta}{C_{\rm P}}, \tag{5.3}$$

where B is the bulk modulus, v is the specific volume, β is the volume thermal expansion, and $C_{\rm P}$ is the heat capacity at constant pressure. Our x-ray diffraction measurements gave $\beta = 2.90\times10^{-5}{\rm K}^{-1}$ and $v = 1.53\times10^{-4}{\rm m}^3/{\rm Kg}$. Measurements of $C_{\rm P}$ with an adiabatic calorimeter by Ikeda, Nakamichi, and Yamamoto [323] gave a value of 428J/Kg·K. The main source of uncertainty is B, since there is some scattering in the values reported in the literature. Using the values mentioned in the previous section, we estimate that $\gamma_{\rm th}$ is between 1.7 and 2.1. Using the high temperature data shown in Fig. 5.2, along with Eq. 5.2, the temperature Grüneisen parameter $\gamma_T = 2.94$ from 300K to 750 K. Analogously, using the high pressure data shown in Fig. 5.4, the proportionality constant from 0

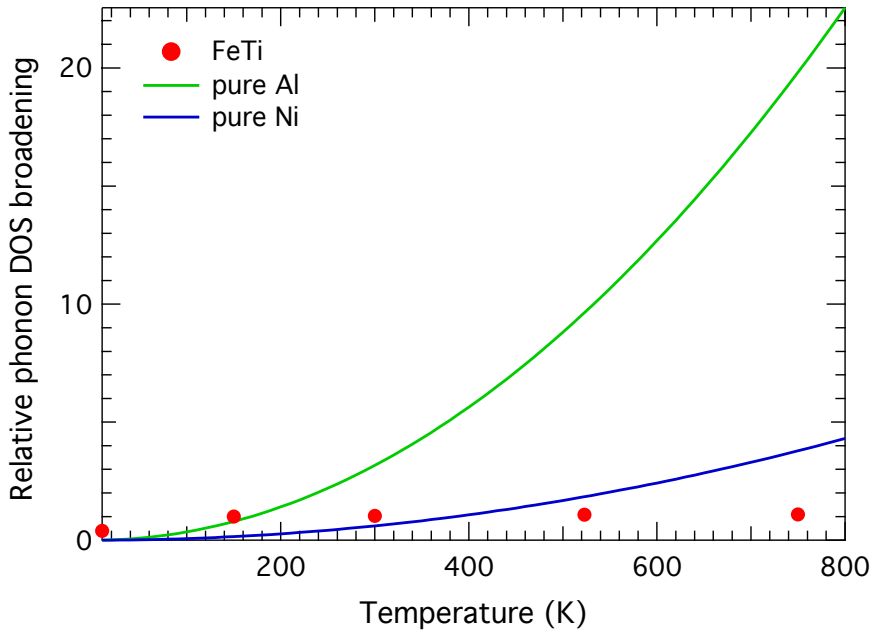

Figure 5.7: Relative broadening of the phonon DOS curves at different temperatures. The solid lines are fits to INS data given in Refs. [156] and [325] for Al and Ni. See text for details.

GPa to 47 GPa is $\gamma_P = 1.97$.

Anharmonic behavior is identified as a change in phonon frequencies that is inconsistent with Eq. 5.2 (see, for example, Ref. [324]). This could be the result of phonon-phonon interactions which tend to reduce the phonon lifetime and therefore broaden the phonon DOS curves, although this does not occur in FeTi. To verify, the method of Refs. [156] and [325] was used. The broadening due to phonon-phonon scattering is expected to take the form of a damped harmonic oscillator [312,326,327]. The neutron-weighted DOS curve at 10K was convoluted with the function of a damped harmonic oscillator with a quality factor $\mathcal{Q}$, and the $\mathcal{Q}$ that best reproduces the shape of the DOS curves at each elevated temperature was found, accounting for the energy shifts due to thermal expansion.

In FeTi, the inverse of the quality factors are very small and do not change with temperature (Fig. 5.7), indicating that the effect of cubic anharmonicity is negligible, although quartic anharmonicity could still be present since if does not broaden the peaks.

Explicit anharmonicity can be separated from quasiharmonic effects if it is known how the phonons change with temperature at constant pressure and with pressure at constant temperature, since

$$\left(\frac{\partial \ln \langle E \rangle}{\partial T}\right)_P = -\beta B_T \left(\frac{\partial \ln \langle E \rangle}{\partial P}\right)_T + \left(\frac{\partial \ln \langle E \rangle}{\partial T}\right)_V . \tag{5.4}$$

The second term on the right of Eq. 5.4 is the pure temperature contribution to the frequency shift from explicit anharmonicity. From our data, the constant pressure derivative has a value of

$-8.90\times10^{-5}\,\mathrm{K}^{-1}$ and the constant temperature derivative has a value of $-3.03\times10^{-5}\,\mathrm{K}^{-1}$, so 2/3 of the thermal phonon softening is due to anharmonic effects. We used the ^{57}Fe partial phonon DOS curves measured by NRIXS for the calculation of the first term on the right because it is the only data available at high pressures, but the decrease in the average phonon energy seems to be very similar for the Fe and Ti vibrations, as seen in Fig. 5.3.

5.4 Born–von Kármán fits to the phonon DOS curves

The experimental neutron-weight-corrected and partial phonon DOS curves were fit to a Born-von Kármán model (Ref. [26], also summarized in section 1.1.2) considering the first four coordination shells. This is ongoing work, but some preliminary results are presented here. The set of experimental force constants of Buchenau, et al. [320] was taken as the initial guess for the iterative procedure to obtain force constants [157]. The force constants were then optimized to converge on the measured phonon DOS curves, taking into account the experimental resolution functions, using a differential evolution algorithm implemented in the MYSTIC software package [328]. More details on the fitting algorithms will be provided in a future publication [329].

For the high temperature fits, the force constants were set to optimize both the Fe partial DOS and the neutron-weight-corrected curves. This limited the maximum temperature to 750 K. The values of all the force constants at room temperature are in good agreement with those of Buchenau, et al. The results for the first and second nearest-neighbor longitudinal force constants are shown in Fig. 5.8. There is a large decrease in the 2nn force constants for both the Fe and Ti atoms. For the Fe atoms, the decrease at 750 K from room temperature is about 18 N/m (60%). For the Ti atoms it is about 9 N/m (20%), so the average decreases by about 13.5 N/m (40%). There is little change in the 1nn longitudinal force constants, and the behavior is nonmonotonic, but they seem to increase with temperature. Initially, the average of the 2nn force constants was larger than that of the Fe–Ti 1nn bond, which is peculiar in this system. At elevated temperatures, the 1nn bonds become stiffer than the average of the 2nn bonds. Similar behavior was also observed in Cr [310].

Only NRIXS data was available for the high pressure fits, so the force constants between Ti atoms were kept constant while those that involved Fe atoms were allowed to diverge. The results for the first and second nearest-neighbors longitudinal force constants are shown in Fig. 5.8. In this case, the 1nn force constant was substantially stiffer and the 2nn Fe force constant substantially softer than those obtained by Buchenau, et al. Both force constants stiffen with pressure, although the 1nn force constant stiffens more.

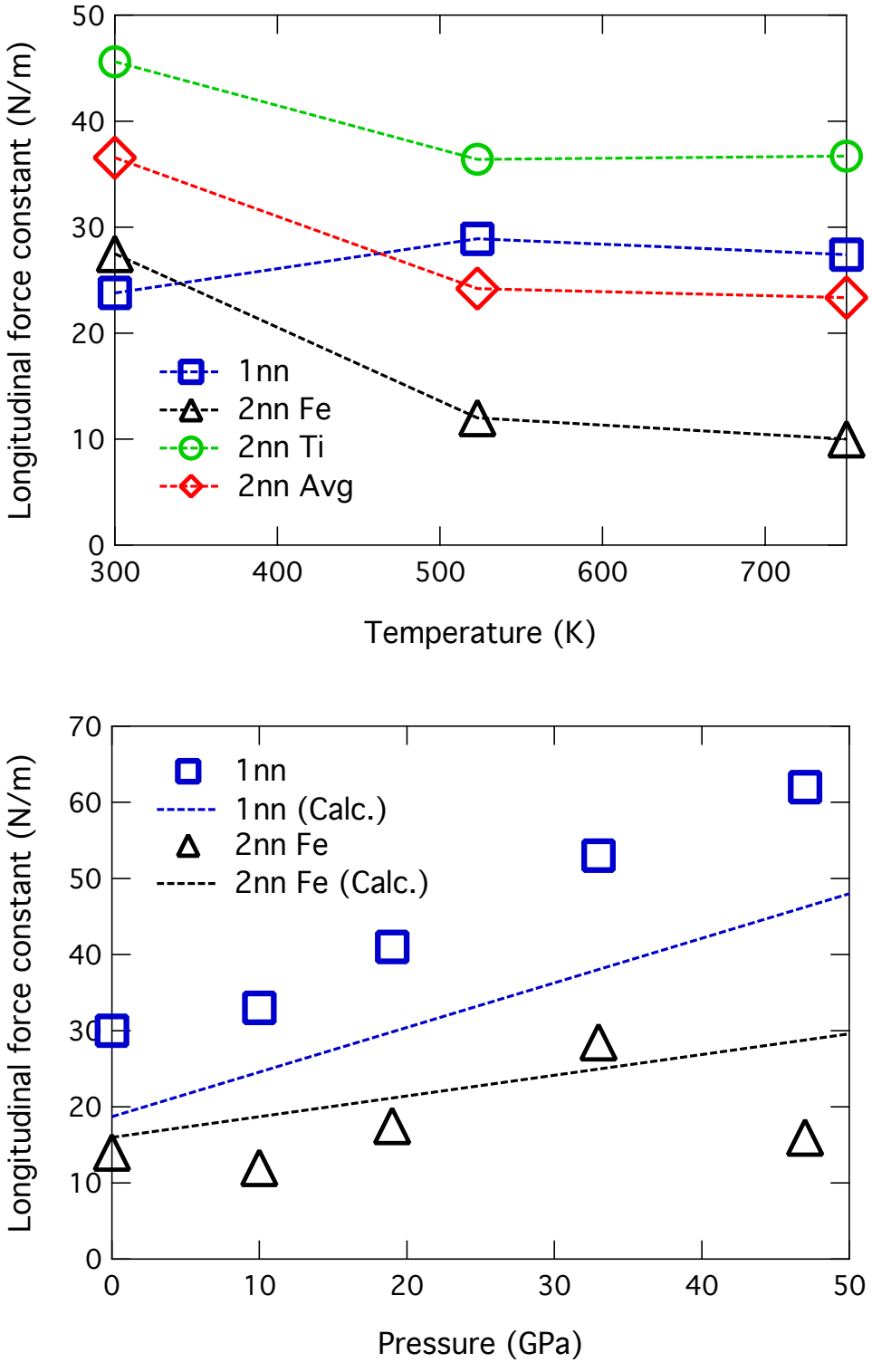

Figure 5.8: Force constants from BvK fits to the experimental data. Temperature above and pressure below.

5.5 Computational

5.5.1 Ground state electronic structure and lattice dynamics

Total energy calculations were performed with density functional theory using VASP [83,84] with projector augmented wave potentials [72,73] with the generalized gradient approximation [67] exchange-correlation functional on $B2$ FeTi. The k-point meshes for Brillouin zone sampling were constructed using the Monkhorst-Pack scheme [82]. The total number of k-points in the Brillouin zone was 29^3. The plane wave cutoff energy was 450 eV. Spin-polarized calculations gave a negligible magnetic moment for the $B2$ structure, in agreement with experimental results [330]. The kinetic energy cutoff and the sampling of k-points was converged to less than 1 meV. The volume of the structure was found by fitting the relationship between the internal energy U_{el} and the volume V to the third-order Birch-Murnaghan equation of state [211], giving results within less than one percent of the experimental values. Simulations of an SQS of FeTi were performed as described in section 3.5.1. The $B2$ ordered structure is substantially more stable than the SQS, as expected from the strong ordering tendency of FeTi, with U_{el} in the ground state of -17.0436 eV/unit cell and -16.3073 eV/unit cell, respectively. This gives an energy of formation of -0.422 eV for the ordered structure [319] and +0.314 eV for the SQS with respect to the pure elements, which practically forbids the existence of the disordered phase, although the formation of an amorphous phase with mechanical alloying has been observed [331].

In electronic structure calculations, the total energy of a configuration is given by

$$E_0 = \sum_n \frac{1}{\Omega_{BZ}} \int_{\Omega_{BZ}} \epsilon_{n,\mathbf{k}} \Theta(\epsilon_{n,\mathbf{k}} - E_F)\, d\mathbf{k}\,, \tag{5.5}$$

where $\epsilon_{n,\mathbf{k}}$ is the energy of band n at k-point $\mathbf{k}$, Ω_{BZ} is the volume of the Brillouin zone, and $\Theta(x)$ is the Heaviside step function at x. For numerical calculations, it is necessary to substitute the integral in the equation above by the sum

$$\sum_k \Omega_k\, \epsilon_{n,\mathbf{k}}\, \Theta(\epsilon_{n,\mathbf{k}} - E_F)\,, \tag{5.6}$$

where Ω_k is the volume around the k-point. This summation is practical for an insulator or a semiconductor with no electrons at the Fermi energy, i.e., partial occupancies, but the convergence with increasing number of k-points is too slow to be practical in metals. Several methods have been developed to approximate Eq. 5.6 and improve the convergence speed. A simple way is to substitute $\Theta(x)$ by the Fermi-Dirac distribution $f_F(x)$ with a thermal energy $\varsigma = k_{\mathrm{B}}T$ [89]. This corresponds to a convolution of the true electronic structure with the derivative of $f_\varsigma(x)$, whose FWHM will tend to zero (a δ-function) as ς tends to zero. The finite width of the convolution function allows more

k-points to be used to determine the partial occupancies. The number of k-points necessary for the convergence of E_0 increases rapidly with decreasing ς, so a reasonable compromise between ς and number of k-points that results in energy convergence must be found. Other smearing functions have been used for the convolution, e.g., a Gaussian [332], a complete orthonormal set of functions with a Gaussian as the null vector [91]. The former technique reintegrates the charge after smearing to place the Fermi level at the right energy, while the latter uses an approximation scheme that correctly places the Fermi level without reintegrating. In the two cases mentioned above, ς is still proportional to a physical temperature, although not in a simple way as when the derivative of the Fermi-Dirac distribution is used. The tetrahedron method [88] interpolates the value of $\epsilon_{n,\mathbf{k}}$ between k-points, so no smearing of the electronic DOS is necessary.

Electronic DOS curves calculated with the method of Methfessel and Paxton [91] for the partial occupancies are shown in Fig. 5.9. The t_{2g} and e_g electronic states are projected at the Fe and Ti sites. The total t_{2g} and e_g electronic densities, the total densities at the Fe and Ti sites, and the electronic DOS of the system are also shown. The different curves correspond to different values of ς, an electronic smearing parameter that introduces a fictitious finite electronic temperature. Piscanec et al. used this method to study Kohn anomalies and electron-phonon interactions in the highest optical branches in graphite and graphene at Γ and $\mathbf{K}$ points at finite temperatures [48]. From this study, and the Raman measurements of Calizo et al. of the temperature dependence of the graphene modes at the Γ point [333], we estimated that the proportionality constant between the Methfessel-Paxton ς and temperature is about 1.2×10^{-3} eV/K. This 'calibration' does not necessarily hold in general, but it gives a reasonable temperature estimate of the different curves in Fig. 5.9 compared to those obtained by ab initio molecular dynamics in Fig. 5.15. The largest ς (purple line) is equivalent to about 915 K.

There is little difference in the number of electronic states at the Fermi level for ς smaller than about 0.5 eV, as expected because it lies at the bottom of a pseudogap. The sharp features in the electronic DOS are smoothed substantially. No change in the relative populations of t_{2g} and e_g electrons was detected with increasing ς, in contrast with the results from ab initio molecular dynamics presented in section 5.5.3. For values of ς larger than 0.5 eV, there is an increase in the number of electrons at the Fermi level, which is associated with enhanced electronic screening in other transition metal alloys as discussed in section 3.6.2. In particular, it can be seen that the increase is mostly at the Fe sites and, within the Fe, due to the t_{2g} electrons. The increase at $\varsigma = 1.1$ eV is about 1.2 states/electron/atom. This is comparable, for example, to that in FeV upon ordering (section 3.5.1).

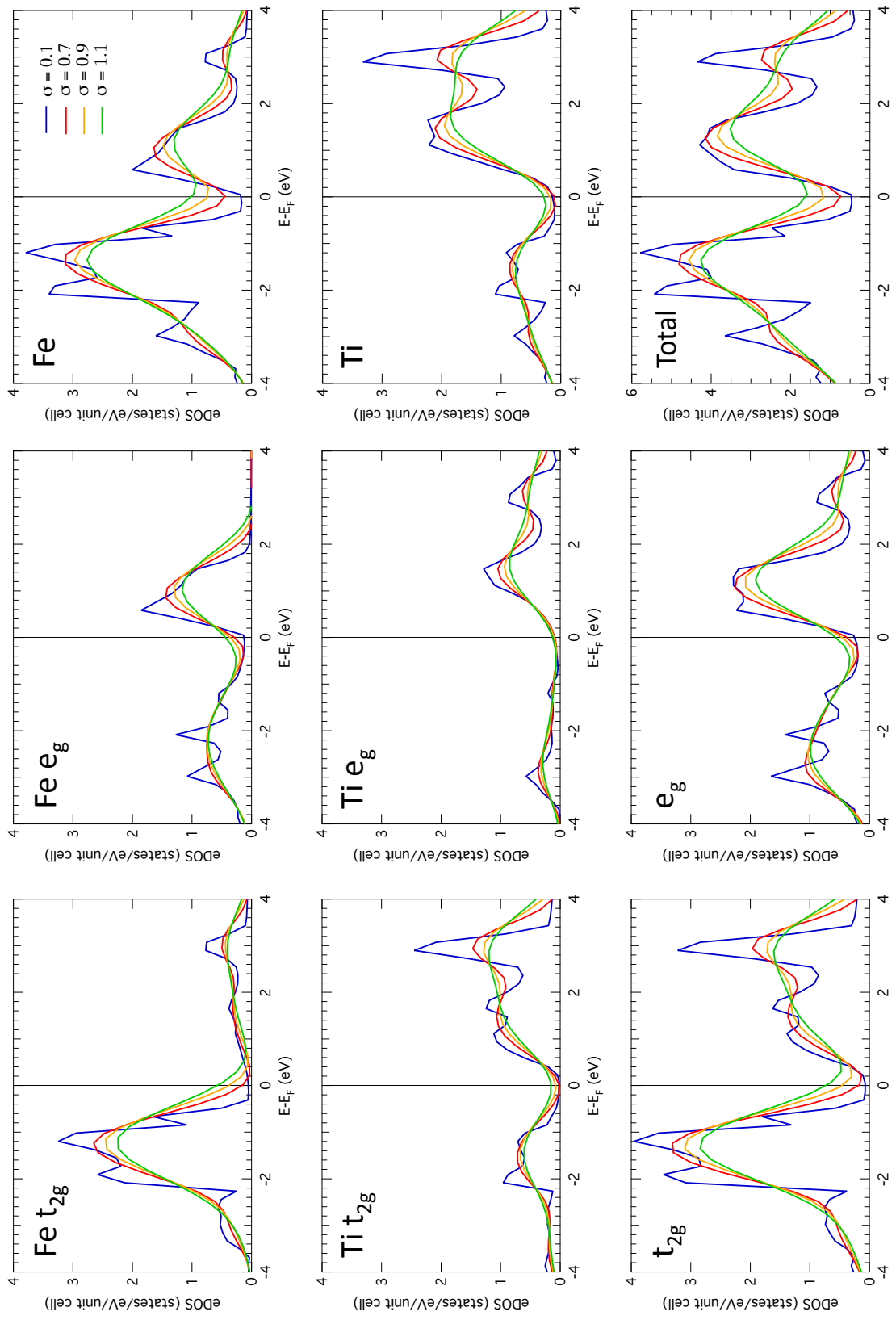

Figure 5.9: Site- and momentum-projected electronic structures for different broadening parameters. Using the 'calibration' discussed in the text, the four broadening parameters $\sigma = 0.1$, 0.7, 0.9, 1.1, are equivalent to 85, 585, 750, and 915 K, respectively.

Forces on atoms after displacing one of them were calculated using the configuration described in the previous section. A 54-atom supercell (3×3×3 times the $B2$ structure unit cell) of FeTi with a 9^3 k-point mesh and atom displacements of 0.01 Å was used. Interatomic force constants were calculated using the Parlinski-Li-Kawazoe method [98] as implemented in the PHONOPY code [284] and are in excellent agreement with Born-von Kármán fits to experimental results [320], as shown in Table 5.1. The dynamical matrix was calculated from the force constants, and the phonon dispersions are shown in Fig. 5.14. Phonon DOS curves were computed on 16^3 q meshes using the Monkhorst-Pack scheme [82] and the results are presented in Fig. 5.13. This results are shown in section 5.5.2 since they are part of the study on the volume dependence of the lattice dynamics. The agreement between the measured and calculated Fe phonon DOS curve is excellent, with a difference in the energy of the center of the main peak of about 1 meV. The calculated Ti partial phonon DOS curve shows a distinct peak centered at 20 meV and a broader feature at energies higher than about 24 meV. The agreement with the experimentally derived Ti partial DOS curve is worse than in the case of the Fe motions, but there are significantly larger experimental uncertainties in the case of the Ti motions.

Longitudinal and transverse force constants were obtained by spin-polarized electronic structure calculations for the $B2$ Fe-based alloys: FeTi, FeV, FeCr, FeFe, and FeCo. It is important to note that equiatomic FeCr undergoes spinodal decomposition and the $B2$ structure is not observed in nature. The forces considering the average of A-A and B-B bonds are shown on Figs. 5.10 and 5.11. In the $B2$ structure, the 1nn and 4nn bonds are between different atoms, while the 2nn, 3nn, and 5nn are between atoms of the same species. The longitudinal force constants were obtained by projecting the appropriate force constant tensor onto the direction that connects the nth nearest neighbors. If the symmetry is axial, one of the eigenvectors of the force constant tensor will be equal to the longitudinal force constant. The other two eigenvectors form a 2-dimensional space that is orthogonal to the longitudinal force constant. We consider the average their magnitudes be the transverse force constant. If the model is realistic, the values of the longitudinal force constants tend to be very robust and model independent [157]. For example, if the number of nearest neighbors is enough to describe the system, considering more will only nominally affect the values of closer neighbors. The values for the transverse force constants are certainly less robust, but they might be informative. The results shown here omit the values of 4nn, which are not axial.

A peculiarity of the FeTi system is that the 2nn longitudinal force constants are stiffer than those of the 1nn. This has been observed experimentally in elemental Cr as well [310], a strongly anharmonic system with an anharmonic phonon entropy of 0.83 k_B/atom at its melting temperature [307]. In the other $B2$ systems investigated, the longitudinal force constants decay with the order of the nearest neighbor, which is the usual behavior as long-range forces become weaker. When the longitudinal force constants are plotted against the number of d-electrons, the 1nn force constants

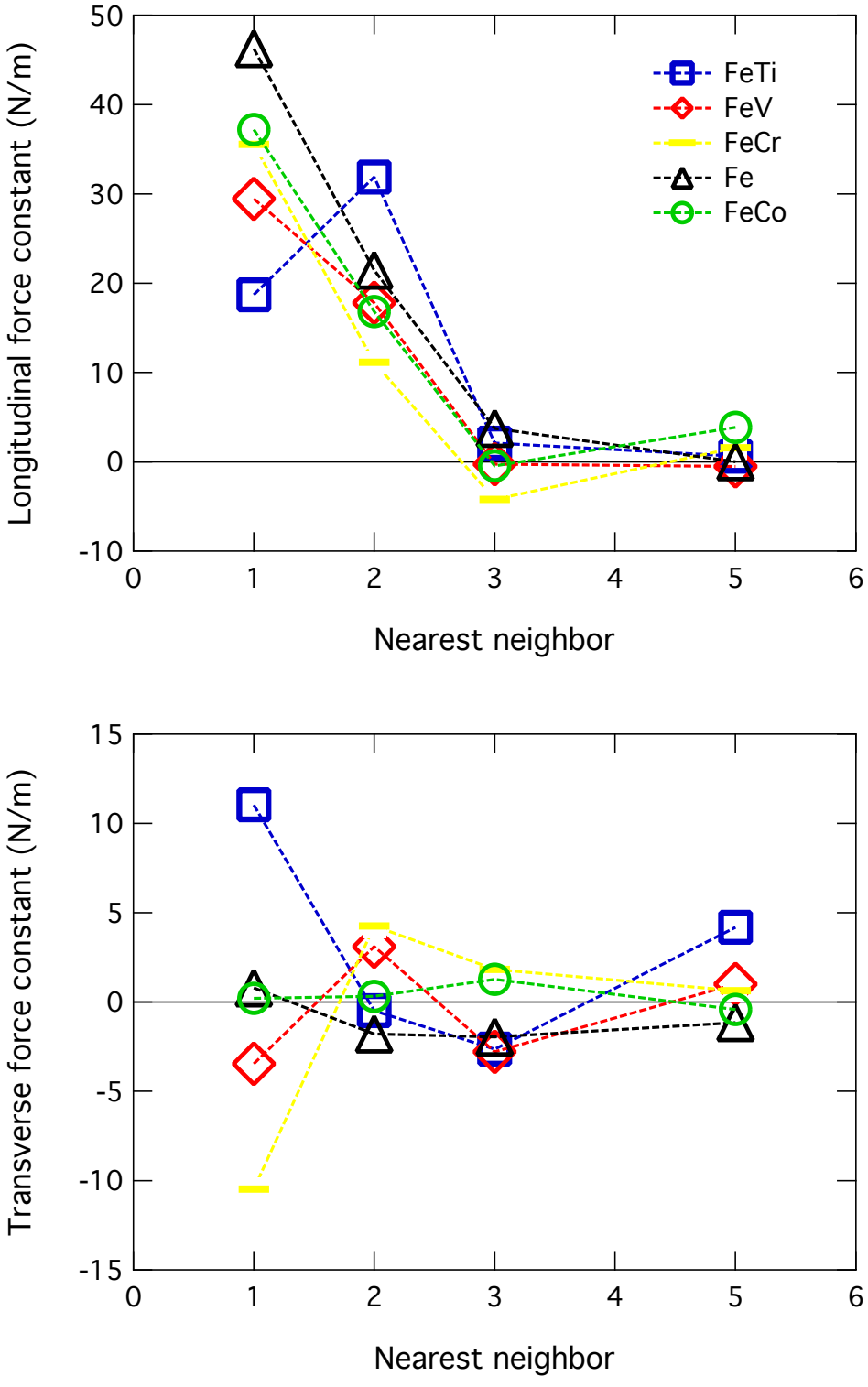

Figure 5.10: Transverse and longitudinal force constants calculated for several $B2$-ordered Fe-based compounds

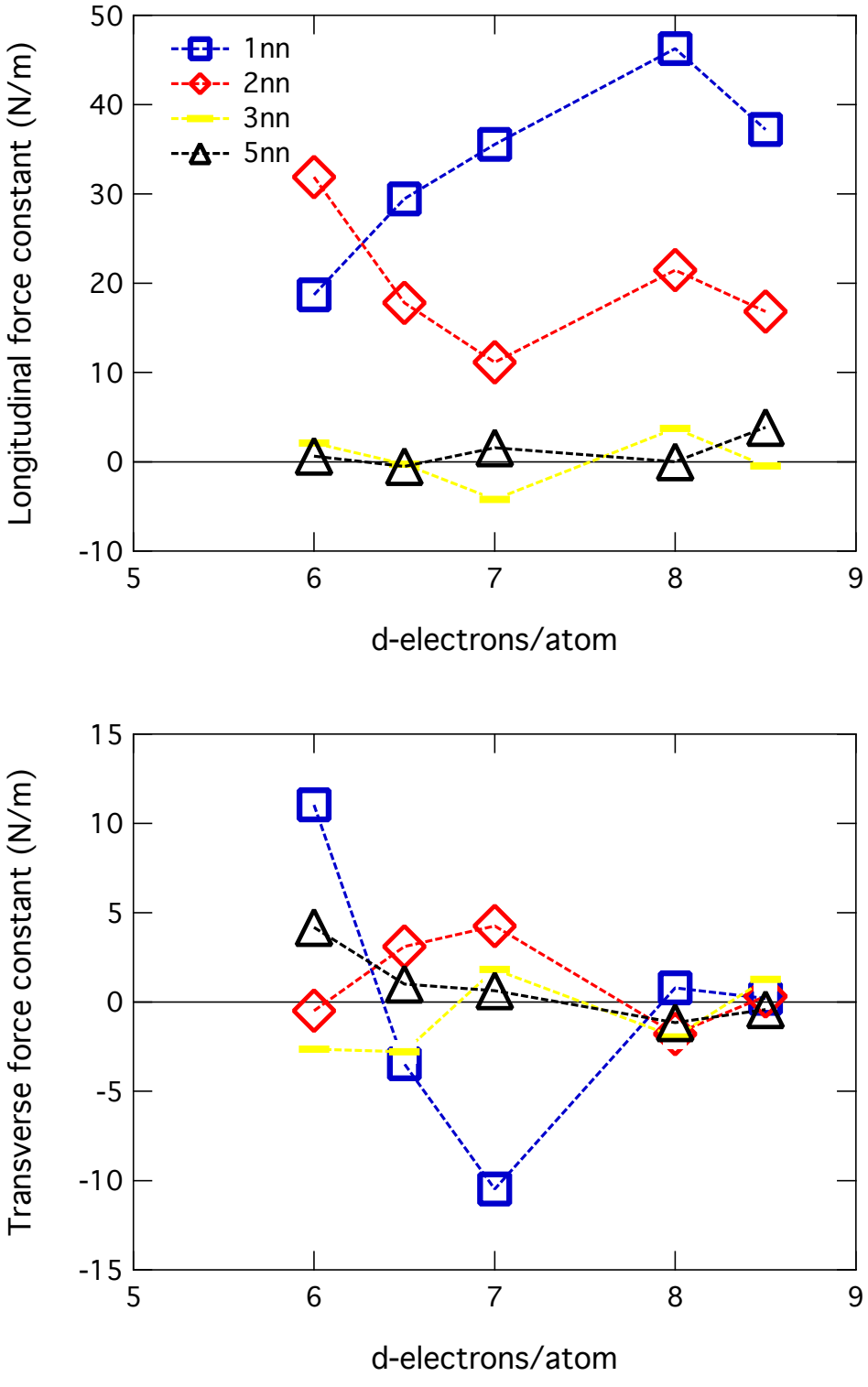

Figure 5.11: Calculated transverse and longitudinal nearest neighbors force constants as a function of the number of *d*-electrons per atom.

Table 5.1: Measured and calculated interatomic force constant tensor elements for FeTi (N/m).

Neighbor	FeTi (exp)			FeTi (calc)		
and indices	Fe	Ti	Avg	Fe	Ti	Avg
$1xx$		12.15			13.59	
$1xy$		7.69			2.55	
$2xx$	25.9	48.7	37.3	15.9	47.8	31.9
$2yy$	9.6	-9.6	0	7.1	-8.1	0.5
$3xx$	0.4	4.3	2.4	0.4	3.7	2.1
$3zz$	-3.7	-0.5	-2.1	4.1	5.3	4.7
$3xy$	3.6	2.3	2.95	-1.3	1.3	0

increase until up to Fe, but then decrease slightly in FeCo. The 2nn force constants decrease from FeTi to FeCr, while the 3nn and 5nn are close to zero for all systems. The 1nn transverse force constants are strongly 'positive' for FeTi and strongly 'negative' for FeCr. This is related to the mechanical stability of the compounds, and is consistent with the phase separation observed in FeCr.

5.5.2 High-temperature and high-pressure quasiharmonic behavior

A series of electronic structure calculations at increasing volumes were performed on the FeTi system. Phonon DOS curves were obtained as described in the previous section and the phonon free energies, F_{ph}, were computed from the calculated phonon DOS curves in the harmonic approximation,

$$F_{\mathrm{ph}}(T,V) = \int \left[\frac{E}{2} + k_{\mathrm{B}}T\ln x\right] g_V(E)\mathrm{d}E, \tag{5.7}$$

where T is the temperature, $g_V(E)$ is the phonon DOS curve calculated at V, and $x = (1 - e^{-E/k_{\mathrm{B}}T})$. At each temperature, the free energy of Eq. 5.7 was fitted to a polynomial in V and the minimum value of the Helmholtz free energy, $F_{\mathrm{tot}}(T,V) = U_{\mathrm{el}}(V) + F_{\mathrm{ph}}(T,V)$, was used to obtain a temperature-volume relationship. The Grüneisen parameter obtained from these calculations was γ_T=1.33. The quasiharmonic calculations predict that the 1nn and 2nn force constants for the Fe-Ti, Fe-Fe, and Ti-Ti bonds decay linearly with increasing V, as shown in Fig. 5.12.

Electronic structure calculations were performed at volumes smaller than the equilibrium volume. Phonon dispersions and phonon DOS curves were obtained by the method described previously and the results are shown in Figs. 5.13 and 5.14. The value obtained for the pressure Grüneisen parameter γ_P=1.60, and for the Fe-specific motions it was $\gamma_{P,\,\mathrm{Fe}}$=1.69. The agreement with the high pressure NRIXS measurements (Fig. 5.4) is excellent, as both the stiffening and the broadening of the main peak are reproduced. Also reproduced is the development, with decreasing volume, of a broad shoulder at energies higher than those of the main peak. The experimental and calculated average energy of the Fe vibrations agree to within a few meV and the volume derivatives are very

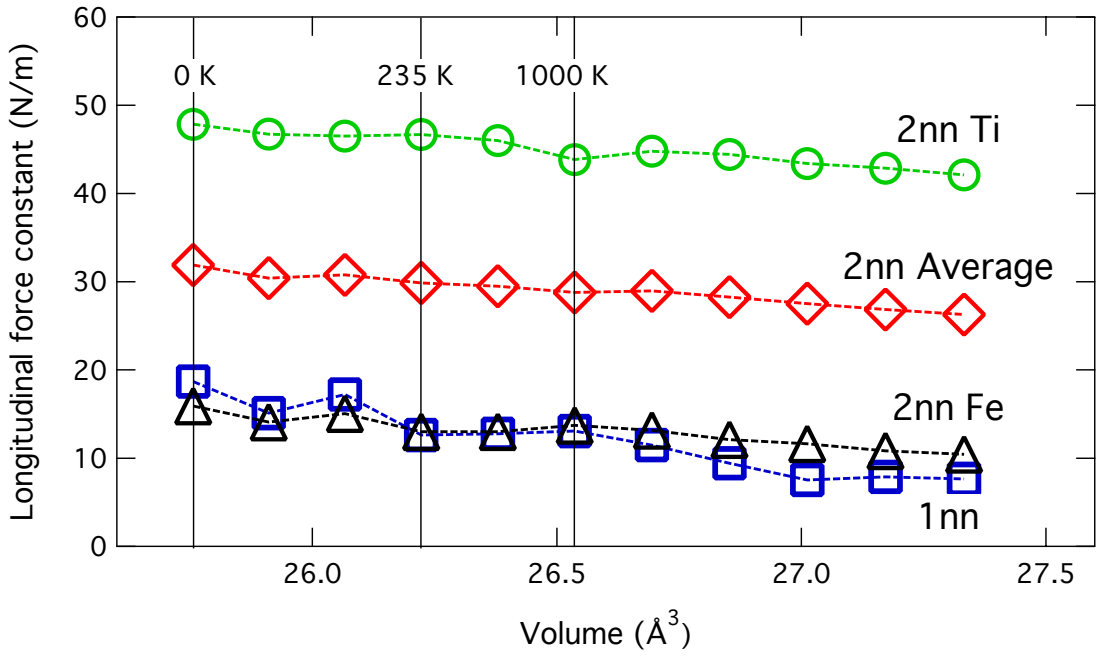

Figure 5.12: Calculated FeTi quasiharmonic longitudinal force constants for volume expansion.

similar, as can be seen in Fig. 5.6. There is no data on the Ti vibrations at high pressure, but the calculations predict severe changes in the shape of the Ti partial phonon DOS with a particularly large stiffening of the highest energy peak.

The dispersions show that all the modes stiffen with pressure, but the high energy optical modes at the M point stiffen the most. These have mixed character, but are mostly Ti motions [334]. The force constants increase linearly from a normalized volume of 1 to 0.836, although the 1nn force constants are more sensitive to volume. The longitudinal 1nn increases from 18.69 to 48.06 N/m, whereas the longitudinal Fe-Fe 2nn increase from 15.92 to 29.62 N/m and the longitudinal Ti-Ti 2nn increase from 47.85 to 69.78 N/m. The average of the 2nn longitudinal force constants at V/V_0=0.836 is 49.70 N/m, so the difference between the 1nn and 2nn force constants observed at ambient pressure is reduced at higher pressures.

5.5.3 High temperature electronic structure and lattice dynamics studied by ab initio molecular dynamics

Ab initio molecular dynamics calculations were performed using VASP [83,84] with same potentials on 128-atom super cells using a 2×2×2 k-point mesh. The energy cutoff was 350 eV and the Monkhorst-Pack scheme [82] was used to sample the Brillouin zone. Due to memory constraints, the fast Fourier transform vectors were set to 3/2 the length of the vectors of the basis set and the projection operators were evaluated in real space using the method of King-Smith, Payne, and

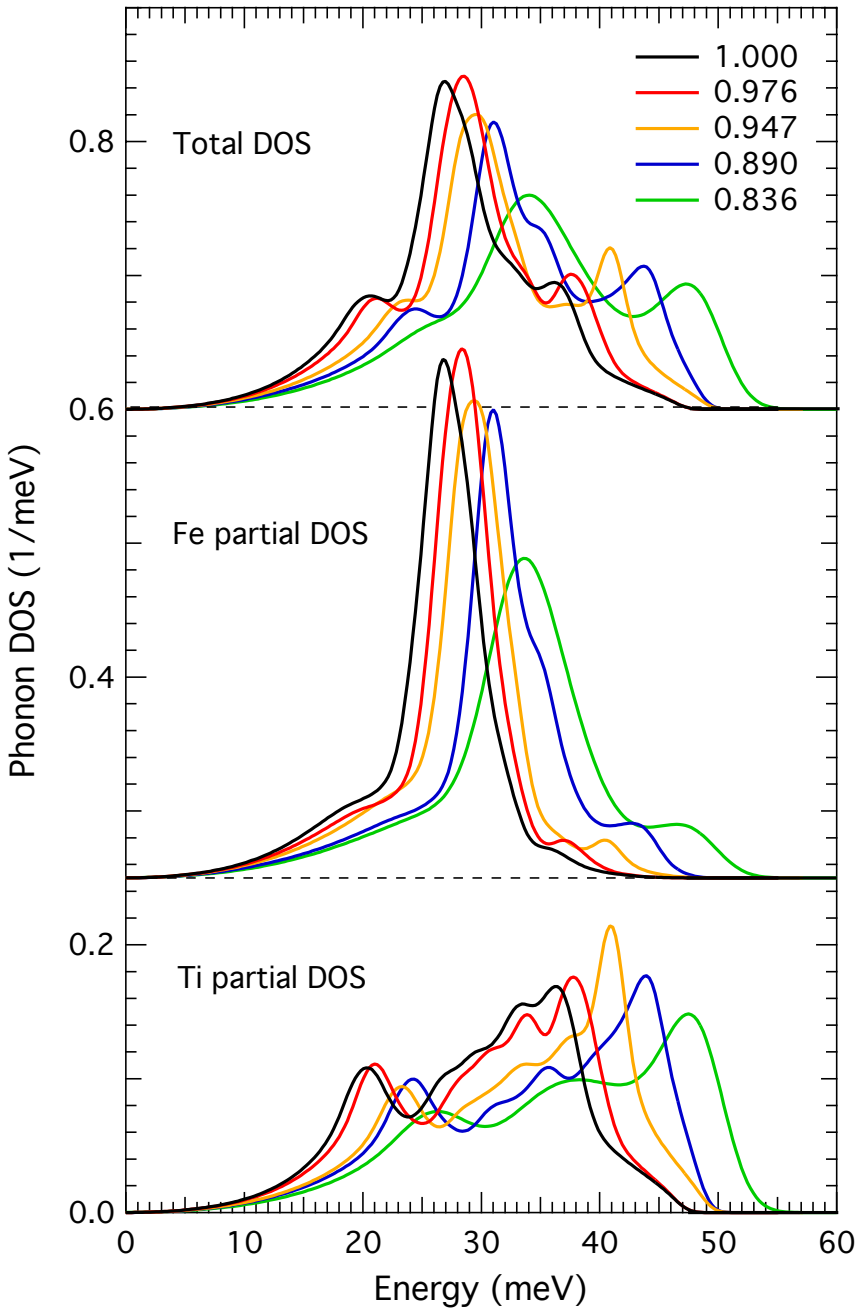

Figure 5.13: Calculated phonon DOS curves for FeTi at different volume compressions.

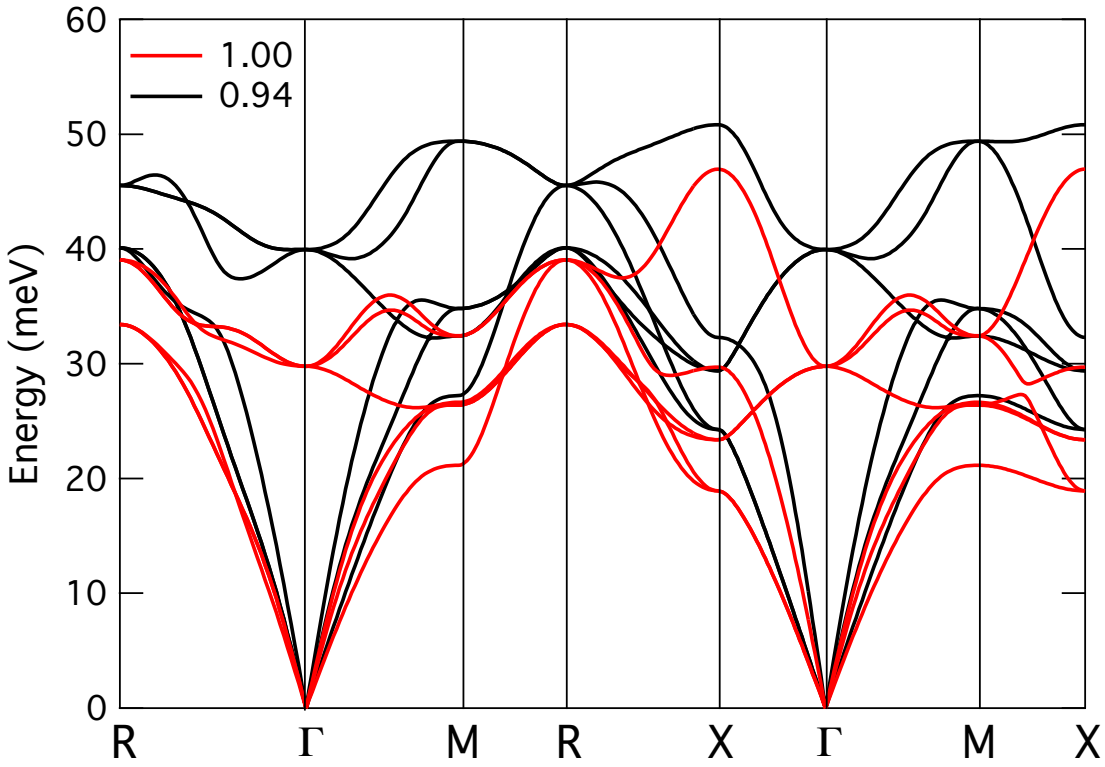

Figure 5.14: Phonon dispersions calculated for FeTi at the equilibrium lattice parameter and at a reduced lattice parameter.

Lin [335]. The simulations were carried out using a canonical ensemble and the standard Nosé thermostat [139]. Using 2-fs steps, the sample reached thermodynamic equilibrium after about 500 fs, based on the periodicity of the total energy as a function of time. There was no distinguishable difference in the time-energy relation when a 1-fs time step was used. The final electronic DOS curves were computed for each temperature by assembling the electronic DOS curves from each time step after reaching equilibrium and are shown in Fig. 5.15 for 600, 900, and 1200 K. The pseudogap at the Fermi level is filled gradually with temperature, and the number of electronic states at the Fermi level increases linearly. The electronic DOS curves are similar to those presented in section 5.5.1.

The *d*-electron cloud asphericity, defined by the ratio between the charge in the t_{2g} orbitals to that in the e_g orbitals, decreases with increasing temperature at the Fe sites, but not at the Ti sites, as show in Fig. 5.16. The t_{2g} state is a triplet and the e_g state is a doublet, so a perfectly spherical *d*-electron cloud has a ratio of 1.5. In the $B2$ structure, the t_{2g} orbitals point in the direction of the 1nn, while the e_g electrons point in the direction of the 2nn. A ratio higher than 1.5 implies that there is a preferential concentration of charge between the 1nn, while a ratio lower than 1.5 implies that the preferential concentration is in the direction of the 2nn. To obtain this ratio, 'screenshots'

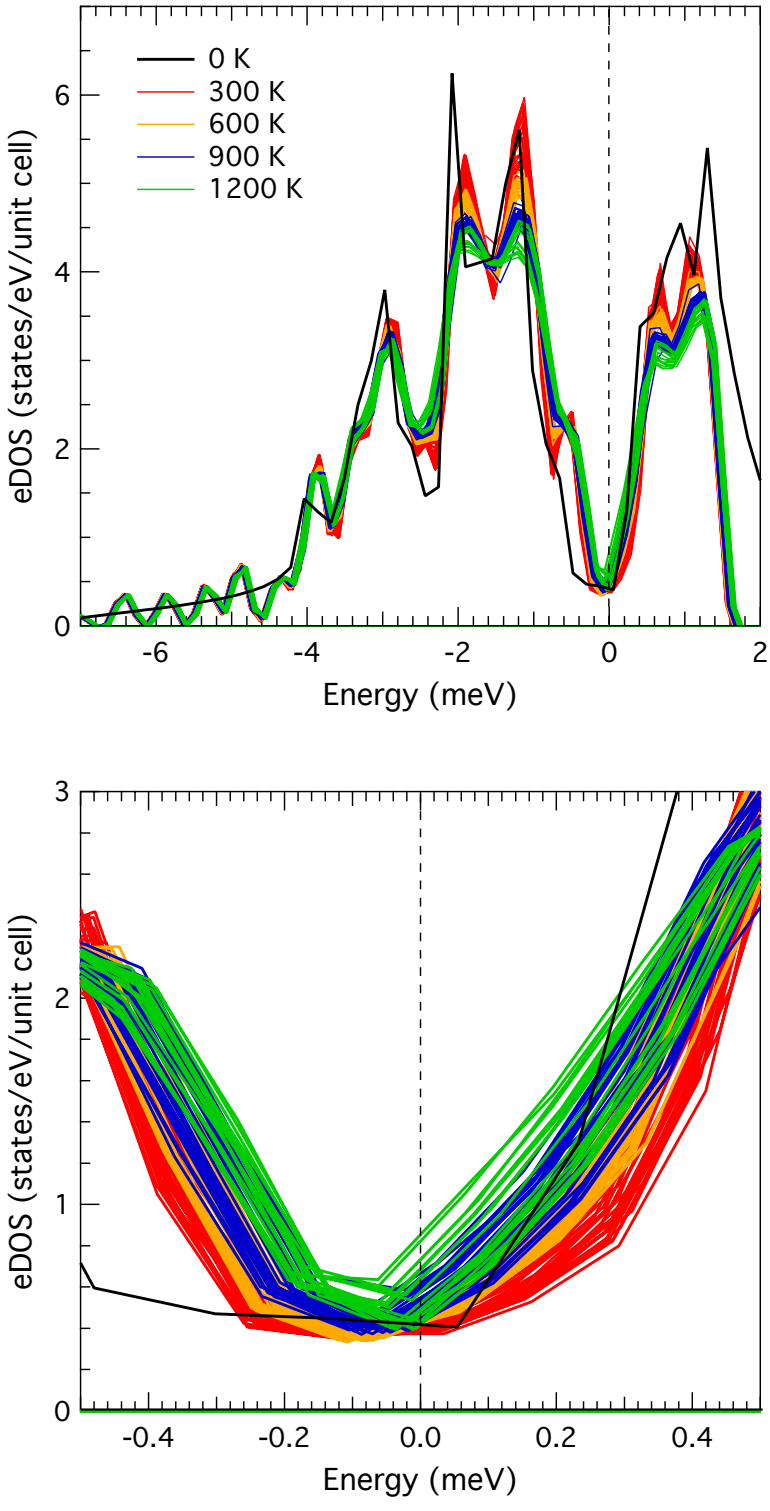

Figure 5.15: Electronic DOS for FeTi obtained at elevated temperatures from AIMD calculations.

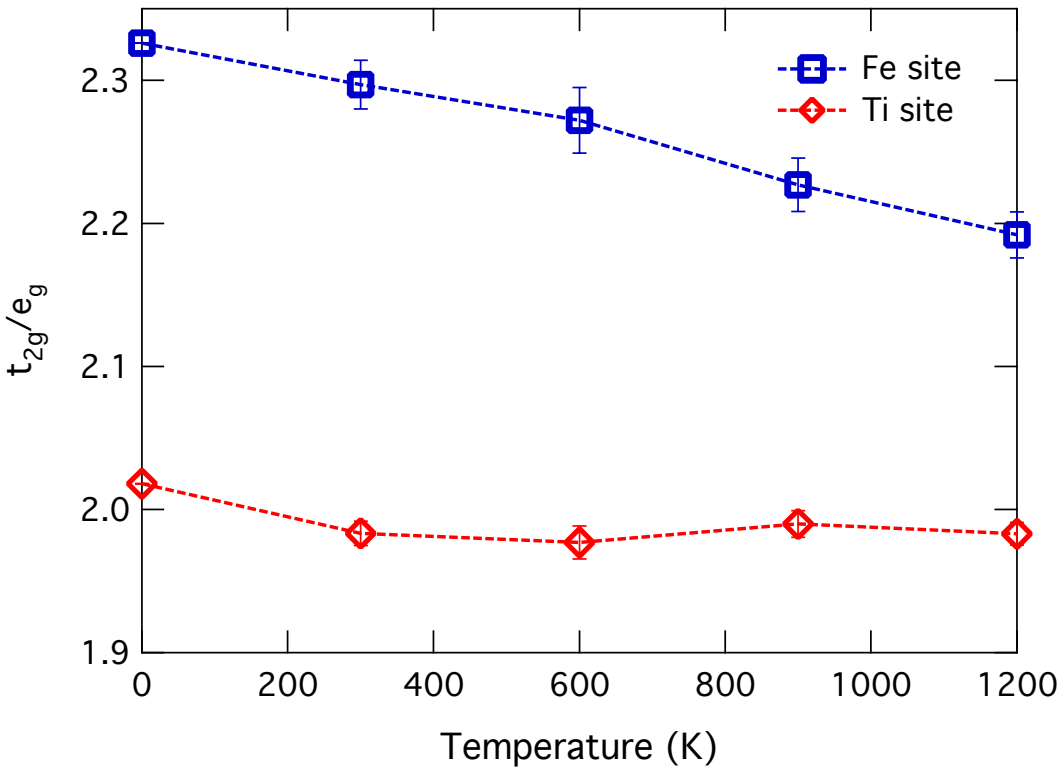

Figure 5.16: *d*-electron charge asphericity at the Fe and Ti sites calculated at elevated temperatures from AIMD results.

of the atomic positions in the super cell at twenty time steps between time step 1000 and time step 2000 (2 to 4 ps) were selected randomly. The electronic structure with momentum-projected orbitals was then calculated using the same settings as for the molecular dynamics calculations, and the electronic charge in each orbital was integrated. The error bars in Fig. 5.16 come from the standard deviation of the ratios. The total charge at the *s*-, *p*-, and *d*-orbitals enclosed by the Wigner-Seitz radius did not change with temperature.

Preliminary phonon DOS curves at each temperature were calculated from the Fourier transform of the velocity autocorrelation function after thermalization of the system. This information is presented in Fig. 5.17. Due to the size of the supercell and the number of time steps included in the calculation, the long wavelength modes below approximately 10 meV cannot be accurately reproduced. The AIMD calculations predict a large phonon softening, particularly at temperatures above 600 K. This includes only nonharmonic contributions, since the volume is constant for all temperatures.

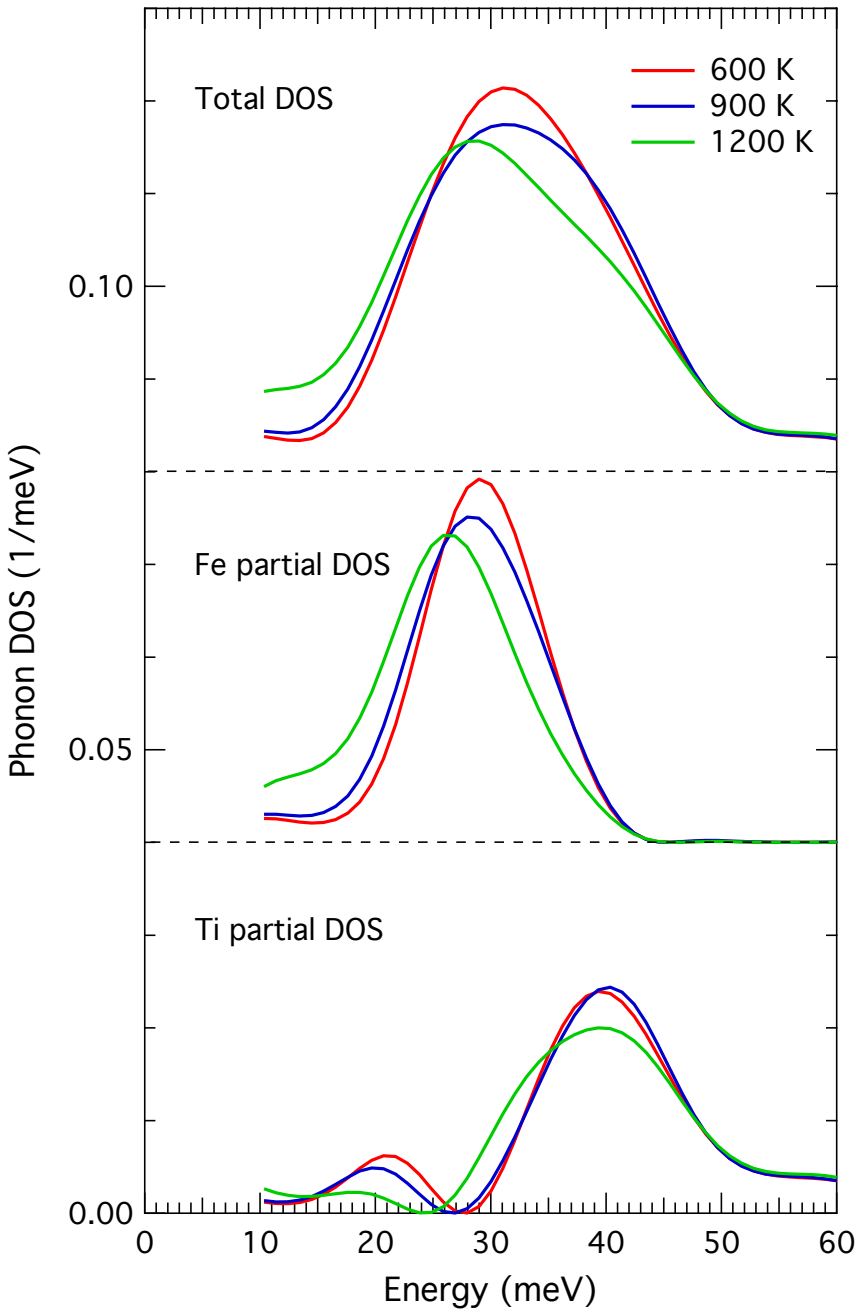

Figure 5.17: Preliminary phonon DOS curves for FeTi at elevated temperatures obtained from AIMD results.

5.6 Discussion

5.6.1 Grüneisen parameters

In this chapter, INS and NRIXS measurements of the phonons on FeTi at high temperature and at high pressure are presented. The main experimental observation is that the phonon DOS curves soften considerably more with temperature, as determined from the average phonon energy, than what the stiffening at high pressures can account for in the quasiharmonic model. As discussed in section 1.1.4, the quasiharmonic model is a mean-field model, so the volume dependence in introduced by essentially varying the interatomic distance in a Lennard-Jones potential. Nevertheless, the energy minima is still approximated by a harmonic potential. A measure of the explicit anharmonicity is given in Eq. 5.4, the partial derivative of the average phonon energy with respect to temperature at constant volume. It is straightforward to evaluate the anharmonicity of any system using this equation if both the temperature and the pressure dependence of the phonon DOS are available. Unfortunately, for most system these data are not available. Another approach is to look for a discrepancy between the thermal Grüneisen parameter γ_{th} (Eq. 5.3) and that obtained by the volume dependence of the average phonon energy measurements at elevated temperatures γ_T (Eq. 5.3). By both of these accounts, $B2$ FeTi strongly anharmonic.

The change in the average phonon energy of FeTi is negligible at temperatures below room temperature, as can be seen in Fig. 5.3, but it accelerates at higher temperatures. The Grüneisen parameter is, in fact, a function of the temperature, and ideally the average phonon energy should be measured continuously, but this is experimentally not feasible. Therefore, a value for γ_T was obtained by assuming a linear change between 300 and 750 K, and $\gamma_T = 2.9$. This value is within the normal range observed in metals. Nevertheless, it is considerably larger than $\gamma_{\mathrm{th}} = 1.9$, obtained from experimental values of several thermodynamic quantities. There are various sources of error in both of these values, most importantly the value of the bulk modulus. There is considerable variation in the results reported in the literature. The rest of the 'constants' in Eq. 5.3 are also temperature dependent. Nevertheless, the discrepancy is large enough to survive, and would probably increase if we could measure the average phonon energy continuously. At the minimum, the difference is 50%, but it could be as much as 100%.

The second approach using Eq. 5.4 also suffers from the lack of access to continuous temperature measurements of thermal parameters and a wide range of values for the bulk modulus. Additionally, the pressure data shown in Fig. 5.6, is only for the Fe motions, but the ab initio results discussed below show that the rates of change are the same for Fe and Ti motions. The Grüneisen parameter obtained for the pressure dependence is $\gamma_{\mathrm{Fe},P} = 2.0$. In this case too the discrepancy is large enough to survive corrections. From experimental phonon data, the value of the constant pressure derivative is $-8.90\times10^{-5}\,\mathrm{K}^{-1}$, while the constant temperature derivative is $-3.03\times10^{-5}\,\mathrm{K}^{-1}$. The

difference, about $-5.87\times10^{-5}\,\mathrm{K}^{-1}$ or 66%, is the phonon softening with temperature due to explicit anharmonicity.

The Grüneisen parameters were studied computationally in the quasiharmonic approximation. Phonon DOS curves were generated at different volumes, but considering only the harmonic force constants. In the case of increasing 'temperature,' the phonon free energy was considered to evaluate the volume-temperature relationship. The experimental and calculated values for the average phonon energy as a function of temperature are shown in Fig. 5.3, and those for the pressure dependence are shown in Fig. 5.6. The Grüneisen parameter is constant in the quasiharmonic approximation, so the temperature or pressure ranges chosen are irrelevant. The values of the calculated parameters are $\mathfrak{r}_T$=1.33 and $\mathfrak{r}_P$=1.60. (For the Fe-specific motions, $\mathfrak{r}_{\mathrm{Fe},P}$=1.69.). $\mathfrak{r}$ is used to distinguish calculated Grüneissen parameters from experimentally determined ones, denoted by γ. The agreement between the pressure parameters is satisfactory, but it is poor between the temperature ones. This supports the experimental evidence that indicates that the pressure behavior of FeTi is quasiharmonic, as is generally expected, but the temperature behavior is strongly anharmonic. The pressure behavior is not necessarily quasiharmonic. Recently, Invar anomalies have been identified as the source of nonlinear changes in the phonon spectra [336, 337], but these are uncommon exceptions. The mode-specific γ_j were not investigated, but they might provide additional information. The results presented in section 5.7 show that there is no broadening of the phonon DOS curves with temperature, usually associated with phonon-phonon cubic anharmonicity, and strongly suggesting that the nonharmonicity is due to electron-phonon interactions.

5.6.2 Force constants

As mentioned before, one of the peculiarities of the FeTi system is that, on average, the 2nn force constants are stiffer than those of the 1nn. This is a feature that it shares with Cr [310], with which it is isoelectronic. In fact, the magnitudes of the force constants are strikingly similar, if we use the average of the Fe–Fe and the Ti–Ti bonds 1nn force constants (for a comparison, see Ref. [320]). Additionally, the 2nn longitudinal force constant for Ti–Ti bonds is almost twice as strong as that for Fe–Fe bonds from experimental values, and almost three times stronger using calculated values (Table 5.1). Buchenau, et al. [320] noted that the 2nn transverse force constants are negative for Ti–Ti and positive for Fe–Fe, implying a repulsive force in the first case and an attractive force in the second.

We suggest that the peculiar 2nn longitudinal force constants in FeTi originate with the charge distribution. In crystals with the bcc structure, the electrons in the t_{2g} orbitals are mainly in the direction of the 1nn atoms (the [111] direction), while those in the e_g orbitals point mainly in the direction of the 2nn atoms (the [100] direction]). The ratio between the charge in both orbitals, usually called the asphericity of the system, is useful to assess the degree of directional bonding. As

mentioned in section 5.5.3, a ratio of 1.5 means that the distribution is perfectly spherical. In FeTi, this value at 0 K is 2.33 at the Fe sites and 2.01 at the Ti sites, as seen in Fig. 5.16. The average, 2.17, is among the highest values we found in the literature and implies that the charge is strongly localized between 1nn atoms. This screens the longitudinal motions along the [111] direction much more efficiently than the longitudinal motions along the [100] direction. The stiffer bond between Ti atoms is explained by the smaller number of Ti e_g electrons compared to Fe, which are 1.92 and 0.68 e^-/atom, respectively. (Jauch and Reehuis have done particularly thorough asphericity measurements on several elements. They obtained a value of 1.98 for Cr [338] and 1.67 for Fe [339].)

The results presented in the top plot in Fig. 5.10 show that the stiff 2nn longitudinal force constants in FeTi are unique among the $B2$-based alloys of Fe with other transition metals in the $3d$ row. The top plot in Fig. 5.11 show that the stiffness of the 1nn longitudinal force constant increases as the number of d-electrons in the system increases, although there is a small decrease in the last member of the series, FeCo. On the other hand, the stiffness of the average of the 2nn longitudinal force constants is less monotonic, but it generally decreases from its highest value in FeTi. This behavior can also be explained by the charge distribution in these system systems. In a simplistic model that nevertheless captures the essence of the problem, the electrons will fill the t_{2g} orbitals first, and additional electrons will start to fill the e_g orbitals. In FeTi, with 6 d-electrons/atom, all the electrons would fit in the t_{2g} orbitals with no spillover to the e_g ones. As the average number of electrons per atom increases, the e_g orbitals are gradually filled. This decreases the relative occupancy of the t_{2g} orbitals results in stiffer 1nn force constants, while the increase in the relative occupancy of the e_g orbitals results in softer 2nn force constants. The number of d-electrons/atom in FeTi makes the extremum of this trend. Pure Cr, also with 6 d-electrons/atom, might be in a similar situation.

The atomic site- and momentum-projected electronic DOS curves are shown in Fig. 5.9. Most of the integrated electronic density of both the t_{2g} and the e_g lies within 4 eV of the Fermi level, and of each side of the Fermi level, the shape of electronic DOS is similar to a Gaussian. The integrated electronic density for the t_{2g} orbitals from 4 eV below the Fermi level to the Fermi level is larger in the general case than that of the integration from the Fermi level to 4 eV above the Fermi level. The difference is particularly marked at the Fe sites, although the intensity is greater above the Fermi level at the Ti sites. For the e_g orbitals, the general trend is reversed and the integrated density is larger above the Fermi energy. In this case, this happens at both the Fe and the Ti sites. In the limiting case mentioned in the previous paragraph, all the integrated charge in the t_{2g} orbitals would lie below the Fermi level and that of the e_g orbitals would lie above. In this case, the number of electrons at the Fermi level would be zero. This is close to what happens in FeTi, in which the Fermi level lies at the bottom of a deep pseudogap. If a rigid band is also assumed, adding or removing electrons would increase the number of electronic states at the Fermi level.

The strong quasi-ionic bonding makes the FeTi intermetallic phase very stable, as mentioned in the introduction. The stability of the bond also makes the alloy very brittle, since atoms do not easily past one another. It is possible that the mechanical and lattice dynamical properties of other $B2$-ordered alloys with a number of electrons per atom close to 6, which would usually entail an element with less d-electrons than Cr and one with more, can be explained with the same model. In a dated publication [340], it was estimated that about 40% of all known $B2$-forming alloys fell under this category.

5.6.3 High temperature thermodynamics

Calculations of phonon DOS curves from the ab initio molecular dynamics simulations are shown in Fig. 5.15. The strong softening of the DOS curves with temperature can be observed, as is the fact that the rate of softening increases moderately with temperature, in agreement with the experimental results shown in Fig. 5.3. It is important to emphasize that these calculations were all performed at the same volume, so the softening is due exclusively to explicit anharmonicity, the last term of Eq. 5.4. The ab initio molecular dynamics simulations show that the pseudogap in the electronic DOS is gradually filled with increasing temperature (Fig. 5.15). This makes the number of electronic states at the Fermi level increase linearly with temperature, from 0.41 states/eV/unit cell at 0 K to 0.74 states/eV/unit cell at 1200 K, with a standard deviation of 0.15 states/eV/unit cell at the highest temperature. This represents an increase of about 80%.

The asphericity at the Fe sites decreases linearly with temperature, by 0.134 at 1200 K. At the Ti sites, the ratio decreases by 0.035 at 1200 K. Some authors report the percentage of the d-electron charge in the t_{2g} orbitals instead of the asphericity ratio. At the Fe sites, the t_{2g} occupancy decreases from 69.9% at 0 K to 68.6% at 1200 K. At the Ti sites, it decreases from 66.9% to 66.5% in the same temperature range. Considering the 8 d-electrons of Fe and the 4 d-electrons of Ti, we estimate that the charge transferred to the e_g orbitals from the t_{2g} orbitals at the Fe sites is about 0.1 e^-/Fe atom at 1200 K, but only one-fifth of this value at the Ti sites. This charge transfer to the bonds in the direction of the 2nn atoms is probably responsible for the preferential decrease of the real space 2nn longitudinal force constants derived from the Born-von Kármán fits to the data, shown in the top graph of Fig. 5.8. This preferential softening eventually makes the average of the 2nn longitudinal force constants softer than the 1nn force constant, which is the usual behavior in most materials. The softening of the Fe–Fe 2nn longitudinal force constants is greater than that of the Ti–Ti ones. This is also consistent with the larger decrease in the asphericity at the Fe sites. The 1nn force constant seems to stiffen slightly with temperature, although the change is very small. The high temperature behavior of the force constants is consistent with that observed in Cr [310]. The cross-over temperature at which the 2nn force constant become softer that the 1nn one is about 800 K in Cr (about 37% of the melting temperature), and about 500 K in FeTi (about 30% of the

melting temperature).

The analysis shown in section 5.5.1 and Fig. 5.9 provides more insight on the nature of the changes in the electronic structure. The 'thermal broadening' of the electronic DOS has been used before to simulate the effects of temperature in ab initio calculations CITE. In general we observe that the curves reproduce the trends observed in the electronic structure obtained from ab initio molecular dynamics, including the atom- and momentum-projected DOS curves. The pseudogap in the electronic DOS is filled at high enough temperatures, and the effect seems to be reproduced accurately by the set of curves marked '585 K.' At low temperatures (small ς) the filling is very slow, but at high temperatures it accelerates. The almost complete fill at the highest temperature in Fig. 5.9 is probably achieved beyond the melting point of FeTi, though. It is observed that most of the increase in the number of electrons at the Fermi level is due to t_{2g} electrons, although there is also an increase in the number of e_g electrons. In Cr, the modes that softened the most were the one of the transverse modes at the N point and the longitudinal modes two-thirds along the way in the Γ-H direction.

In the results shown in Fig. Fig. 5.9, there was no change in the asphericity as a function of broadening parameter, but this was observed when the electronic structure was calculated with different atomic positions obtained from 'snapshots' of the molecular dynamics results. The artificial broadening of the electronic DOS simulates an increase in the electron temperature, so this suggests that the charge transfer between orbitals is not because of thermal excitation of the electrons. Instead, the work suggest that it is an adiabatic effect: some charge is transferred to a another orbital to accommodate the lattice vibration, and the transfer is larger for larger atomic displacements.

5.7 Conclusion

High temperature and high pressure measurements of phonon spectra of $B2$-ordered FeTi were performed. It was observed that the softening with temperature is strongly anharmonic and not accounted for by the quasiharmonic stiffening upon compression. Born-von Kármán fits to the data showed that the average of the Fe–Fe and Ti–Ti 2nn longitudinal force constants is larger than that the 1nn longitudinal force constant, but the softening with temperature is larger for the 2nn force constants. Ab initio calculations of the force constants were in agreement with the experimental results at ambient conditions and suggest that the stiff 2nn longitudinal force constants result from a preferential distribution of the charge density along the direction of the 1nn atoms and a consequent depletion in the direction of the 2nn atoms. The changes in the phonon DOS curves at increasing pressures were well reproduced by quasiharmonic ab initio calculations, but the quasiharmonic model failed to reproduce the behavior at elevated temperatures. Ab initio molecular dynamics were performed at constant volume to obtain electronic structures and phonon DOS curves.

The anharmonic softening of the phonon DOS curves at high temperatures is accurately reproduced. An increase in the number of electrons at the Fermi level was observed, as well as a charge transfer from the electronic orbitals in the direction of the 1nn atoms to the orbitals in the direction of the 2nn atoms. This charge transfer was determined to be induce the preferential softening of the 2nn longitudinal force constants at high temperatures. The charge transfer is the response of the electrons in the adiabatic limit to a phonon perturbation. This might be the first case in which phonon-induced charge transfer has been investigated.

Bibliography

[1] P. M. Morse, *Thermal physics*, W. A. Benjamin, New York, 1962.

[2] L. Anthony, J. K. Okamoto, and B. Fultz, Phys. Rev. Lett. **70**, 1128 (1993).

[3] O. Delaire, M. S. Lucas, J. A. Muñoz, M. Kresch, and B. Fultz, Phys. Rev. Lett. **101**, 105504 (2008).

[4] R. F. Service, Science **335**, 1435 (2012).

[5] A. White, MRS Bull. **37**, 716 (2012).

[6] G. Ceder, Comput. Mater. Sci. **1**, 144 (1993).

[7] D. J. Wales and J. P. K. Doye, J. Phys. Chem. A **101**, 5111 (1997).

[8] T. S. Bush, C. R. A. Catlow, and P. D. Battle, J. Mater. Chem. **5**, 1269 (1995).

[9] S. Curtarolo, G. L. W. Hart, M. B. Nardelli, N. Mingo, S. Sanvito, and O. Levy, Nat. Mater. **12**, 191 (2013).

[10] G. Hautier, A. Jain, and S. P. Ong, J. Mater. Sci. **47**, 7317 (2012).

[11] H. L. Lukas, S. G. Fries, and B. Sundman, *Computational Thermodynamics: The Calphad Method*, Cambridge University Press, Cambridge, 2007.

[12] J. O. Andersson, T. Helander, L. Höglund, P. F. Shi, and B. Sundman, Calphad **26**, 273 (2002).

[13] F. Körmann, A. Breidi, S. Dudarev, N. Dupin, G. Ghosh, T. Hickel, P. Korzhavyi, J. A. Muñoz, and I. Ohnuma, in preparation.

[14] O. Delaire, J. Ma, K. Marty, A. F. May, M. A. McGuire, M.-H. Du, D. J. Singh, A. Podlesnyak, G. Ehlers, M. D. Lumsden, and B. C. Sales, Nat. Mater. **10**, 614 (2011).

[15] O. Delaire, M. S. Lucas, A. M. dos Santos, A. Subedi, A. S. Sefat, M. A. McGuire, L. Mauger, J. A. Muñoz, C. Tulk, Y. Xiao, M. Somayazulu, J. Zhao, W. Sturhahn, E. E. Alp, D. J. Singh, B. C. Sales, D. Mandrus, and T. Egami, Phys. Rev. B **81**, 094504 (2010).

[16] B. Fultz, personal communication, 2013.

[17] M. S. Lucas, G. B. Wilks, L. Mauger, J. A. Muñoz, O. N. Senkov, E. Michel, J. Horwath, S. L. Semiatin, M. B. Stone, D. L. Abernathy, and E. Karapetrova, Appl. Phys. Lett. **100**, 251907 (2012).

[18] A. van de Walle, Nature Mater. **7**, 455 (2008).

[19] P. Tiwary and A. van de Walle, Phys. Rev. B **87**, 094304 (2013).

[20] O. Delaire, M. Kresch, J. A. Muñoz, M. S. Lucas, J. Y. Y. Lin, and B. Fultz, Phys. Rev. B **77**, 214112 (2008).

[21] O. Delaire, K. Marty, M. B. Stone, P. R. C. Kent, M. S. Lucas, D. L. Abernathy, D. Mandrus, and B. C. Sales, Proc. Natl. Acad. Sci. U.S.A. 108 **108**, 4725 (2011).

[22] M. S. Lucas, J. A. Muñoz, O. Delaire, N. Markovskiy, M. B. Stone, D. Abernathy, I. Halevy, L. Mauger, B. Keith, M. L. Winterrose, Y. Xiao, M. Lerche, and B. Fultz, Phys. Rev. B **82**, 144306 (2010).

[23] J. Ashkenazi, M. Dacorogna, M. Peter, Y. Talmor, E. Walker, and S. Steinmann, Phys. Rev. B **18**, 4120 (1978).

[24] J. M. Wills and W. A. Harrison, Phys. Rev. B **28**, 4363 (1983).

[25] M. Born and T. von Kármán, Z. Physik **13**, 297 (1912).

[26] M. Born and K. Huang, *Dynamical theory of crystal lattices*, Claredon Press, Oxford, 1954.

[27] G. Venkataraman, L. A. Feldkamp, and V. C. Sahni, *Dynamics of Perfect Crystals*, MIT Press, Cambridge, 1975.

[28] P. Brüesch, *Phonons: Theory and Experiments I*, Springer-Verlag, Berlin, 1982.

[29] C. V. Raman, Proc. Indian Acad. Sci. **14A**, 317 (1941).

[30] L. Brillouin, C. R. Acad. Sci **191**, 292 (1930).

[31] D. L. Goodstein, *States of matter*, Prentice-Hall, Englewood Cliffs, New Jersey, 1975.

[32] A. T. Petit and P. L. Dulong, Ann. Chim. Phys. **10**, 395 (1819).

[33] A. Einstein, Ann. der Physik. (Berlin) **22**, 180 (1907).

[34] D. J. Griffiths, *Introduction to Quantum Mechanics*, Prentice-Hall, Upper Saddle River, 1995.

[35] C. Kittel, General introduction, in *Phonons in perfect lattices and in lattices with point imperfections*, edited by R. W. H. Stevenson, 1966.

[36] C. Kittel, *Quantum Theory of Solids*, John Wiley and Sons, New York, 1963.

[37] L. Kantorovich, *Quantum Theory of the Solid State: An Introduction*, Kluwer Academic Publishers, Dordrecht, The Netherlands, 2004.

[38] B. Fultz, Prog. Mater. Sci. **55**, 247 (2010).

[39] N. W. Ashcroft and N. D. Mermin, *Solid State Physics*, Holt, Rinehart and Winston, New York, 1976.

[40] J. E. Jones, Proc. R. Soc. Lond. A. **106**, 463 (1924).

[41] E. Grüneisen, Ann. Physik **344**, 257 (1912).

[42] D. C. Wallace, *Thermodynamics of Crystals*, Dover Publications, Mineola, New York, 1998.

[43] A. A. Maradudin and A. E. Fein, Phys. Rev. **128**, 2589 (1962).

[44] M. Zoli, G. Santoro, V. Bortolani, A. A. Maradudin, and R. F. Wallis, Phys. Rev. B **41**, 7507 (1990).

[45] X. L. Tang and B. Fultz, Phys. Rev. B **84**, 054303 (2011).

[46] C. W. Li, X. Tang, J. A. Muñoz, J. B. Keith, S. J. Tracy, D. L. Abernathy, and B. Fultz, Phys. Rev. Lett. **107**, 195504 (2011).

[47] W. Kohn, Phys. Rev. Lett. **2**, 393 (1959).

[48] S. Piscanec, M. Lazzeri, F. Mauri, A. C. Ferrari, and J. Robertson, Phys. Rev. Lett. **93**, 185503 (2004).

[49] J. M. Ziman, *Electrons and phonons*, Clarendon Press, Oxford, 1962.

[50] G. Grimvall, *The Electron-Phonon Interaction in Metals*, North-Holland, Amsterdam, 1981.

[51] N. Bock, *The Electron-Phonon Interaction in Metals*, PhD thesis, State University of New York at Buffalo, 2003.

[52] R. M. Martin, *Electronic Structure: Basic Theory and Practical Methods*, Cambridge University Press, New York, 2008.

[53] M. Born and J. R. Oppenheimer, Ann. Physik **84**, 457 (1927).

[54] P. Hohenberg and W. Kohn, Phys. Rev. B **136**, 864 (1964).

[55] W. Kohn and L. J. Sham, Phys. Rev. **140**, A1133 (1965).

[56] J. P. Perdew and K. Schmidt, AIP Conf. Proc. **577**, 1 (2001).

[57] D. M. Ceperley and B. J. Alder, Phys. Rev. Lett. **45**, 566 (1980).

[58] J. P. Perdew and A. Zunger, Phys. Rev. B **23**, 5048 (1981).

[59] S. H. Vosko, L. Wilk, and M. Nusair, Can. J. Phys. **58**, 1200 (1980).

[60] J. P. Perdew and Y. Wang, Phys. Rev. B **45**, 13244 (1992).

[61] R. O. Jones and O. Gunnarsson, Rev. Mod. Phys. **61**, 689 (1989).

[62] C. S. Wang, B. M. Klein, and H. Krakauer, Phys. Rev. Lett. **54**, 1852 (1985).

[63] W. Kohn, Rev. Mod. Phys. **71**, 1253 (1999).

[64] D. C. Langreth and J. P. Perdew, Phys. Rev. B **21**, 5469 (1980).

[65] J. P. Perdew, Phys. Rev. Lett. **55**, 1665 (1985).

[66] J. P. Perdew, K. Burke, and Y. Wang, Phys. Rev. B **54**, 16533 (1996).

[67] J. P. Perdew, K. Burke, and M. Ernzerhof, Phys. Rev. Lett **77**, 3865 (1996).

[68] J. P. Perdew, S. Kurth, A. Zupan, and P. Blaha, Phys. Rev. Lett. **82**, 2544 (1999).

[69] D. R. Hamann, M. Schlüter, and C. Chiang, Phys. Rev. Lett. **43**, 1425 (1979).

[70] P. E. Blöchl, Phys. Rev. B **41**, 5414 (1990).

[71] D. Vanderbilt, Phys. Rev. B **41**, 789 (1990).

[72] P. E. Blöchl, Phys. Rev. B **50**, 17953 (1994).

[73] G. Kresse and D. Joubert, Phys. Rev. B **59**, 1758 (1999).

[74] N. A. W. Holzwarth, G. E. Matthews, R. B. Dunning, A. R. Tackett, and Y. Zeng, Phys. Rev. B **55**, 2005 (1997).

[75] R. E. Watson and M. Weinert, Transition-Metals and Their Alloys, in *Solid state physics*, edited by H. Ehrenreich and F. Spaepen, 2001.

[76] E. R. Davidson, Methods in Computational Molecular Physics, in *NATO Advanced Study Institute, Series C*, edited by G. H. F. Diercksen and S. Wilson, 1983.

[77] B. Liu, The simultaneous expansion method for the iterative solution of several of the lowest eigenvalues and corresponding eigenvectors of large real-symmetric matrices, in *Numerical algorithms in chemistry: algebraic methods*, edited by C. Moler and I. Shavitt, 1978.

[78] M. P. Teter, M. C. Payne, and D. C. Allan, Phys. Rev. B **40**, 12255 (1989).

[79] D. M. Bylander, L. Kleinman, and S. Lee, Phys. Rev. B **42**, 1394 (1989).

[80] D. M. Wood and A. Zunger, J. Phys. A **18**, 1343 (1985).

[81] P. Pulay, Chem. Phys. Lett. **73**, 393 (1980).

[82] H. J. Monkhorst and J. D. Pack, Phys. Rev. B **13**, 5188 (1976).

[83] G. Kresse and J. Furthmüller, Phys. Rev. B **54**, 11169 (1996).

[84] G. Kresse and J. Furthmüller, Comput. Mat. Sci. **6**, 15 (1996).

[85] G. Gilat, J. Comput. Phys. **10**, 432 (1972).

[86] G. Gilat, Methods Comput. Phys. **15**, 317 (1976).

[87] A. H. MacDonald, S. H. Vosko, and P. T. Coleridge, J. Phys. C; Solid State Phys. **12**, 2991 (1979).

[88] P. E. Blöchl, O. Jepsen, and O. K. Andersen, Phys. Rev. B **49**, 16223 (1994).

[89] N. D. Mermin, Phys. Rev. **137**, A1441 (1965).

[90] K. M. Ho, C. L. Fu, and B. N. Harmon, Phys. Rev. B **29**, 1575 (1984).

[91] M. Methfessel and A. T. Paxton, Phys. Rev. B **40**, 3616 (1989).

[92] H. Wendel and R. M. Martin, Phys. Rev. Lett. **40**, 950 (1977).

[93] H. Wendel and R. M. Martin, Phys. Rev. B **19**, 5251 (1979).

[94] R. P. Feynman, Phys. Rev. **56**, 340 (1939).

[95] K. Kunc and R. M. Martin, Phys. Rev. Lett. **48**, 406 (1982).

[96] W. Frank, C. Elsässer, and M. Fähnle, Phys. Rev. Lett. **74**, 1791 (1995).

[97] G. Kresse, J. Furthmüller, and J. Hafner, Europhys. Lett. **32**, 729 (1995).

[98] K. Parlinski, Z. Q. Li, and Y. Kawazoe, Phys. Rev. Lett. **78**, 4063 (1997).

[99] S. Baroni, P. Giannozzi, and A. Testa, Phys. Rev. Lett. **58**, 1861 (1987).

[100] X. Gonze, Phys. Rev. A **52**, 1096 (1995).

[101] S. Baroni, S. de Gironcoli, A. Dal Corso, and P. Giannozzi, Rev. Mod. Phys. **73**, 515 (2001).

[102] S. H. Liu, R. P. Gupta, and S. K. Sinha, Phys. Rev. B **4**, 1100 (1971).

[103] M. Gupta and A. J. Freeman, Phys. Rev. Lett. **37**, 364 (1976).

[104] A. J. Freeman, T. J. Watson-Yang, and J. Rath, J. Magn. Magn. Mater. **12**, 140 (1979).

[105] J. Y. Rhee, X. Wang, and B. N. Harmon, Phys. Rev. B **51**, 15585 (1995).

[106] A. Landa, J. Klepeis, P. Söderlind, I. Naumov, O. Velikokhatnyi, L. Vitos, and A. Ruban, J. Phys.: Condens. Matter **18**, 5079 (2006).

[107] S. K. Sinha, Phys. Rev. **169**, 477 (1968).

[108] D. Bohm and D. Pines, Phys. Rev. **82**, 625 (1951).

[109] D. Pines and D. Bohm, Phys. Rev. **85**, 338 (1952).

[110] D. Bohm and D. Pines, Phys. Rev. **92**, 609 (1953).

[111] R. Kikuchi, Phys. Rev. **81**, 988 (1951).

[112] M. S. Lucas, *Cluster Expansion Applied to Inelastic Scattering Experiments*, PhD thesis, California Institute of Technology, 2008.

[113] R. Kikuchi and S. G. Brush, J. Chem. Phys. **47**, 195 (1967).

[114] J. A. Barker, Proc. R. Soc. **A216**, 45 (1953).

[115] J. Hijmans and J. De Boer, Physica **21**, 471 (1955).

[116] T. Morita, J. Phys. Soc. Jpn. **12**, 753 (1957).

[117] T. Morita, J. Math. Phys. **13**, 115 (1972).

[118] J. M. Sanchez, F. Ducastelle, and D. Gratias, Physica A **128**, 334 (1984).

[119] A. Gonis, P. P. Singh, and P. E. A. T. X. G. Zhang, Phys. Rev. B **51**, 2122 (1995).

[120] J. M. Sanchez, Phys. Rev. B **81**, 224202 (2010).

[121] J. M. Sanchez, Phys. Rev. B **48**, 14013 (1993).

[122] J. W. D. Connolly and A. R. Williams, Phys. Rev. B **27**, 5169 (1983).

[123] J. M. Ziman, *Models of Disorder: The Theoretical Physics of Homogeneously Disordered Systems*, Cambridge University Press, London, 1979.

[124] L. Nordheim, Ann. der Physik. (Lpz) **9**, 641 (1931).

[125] P. Soven, Phys. Rev. **156**, 809 (1967).

[126] B. Velicky, S. Kirkpatric, and H. Ehrenreich, Phys. Rev. **175**, 747 (1968).

[127] F. Aymerich, Phys. Rev. B **26**, 1968 (1982).

[128] M. Jaros, Rep. Prog. Phys. **48**, 1091 (1985).

[129] A. Zunger and J. E. Jaffe, Phys. Rev. Lett. **51**, 662 (1983).

[130] A. van de Walle and G. Ceder, Phys. Rev. B **61**, 5972 (2000).

[131] A. Zunger, S.-H. Wei, L. G. Ferreira, and J. Bernard, Phys. Rev. Lett **65**, 353 (1990).

[132] R. Arroyave and M. Radovic, Phys. Rev. B **84**, 1341123 (2011).

[133] J. von Pezold, A. Dick, M. Friák, and J. Neugenbauer, Phys. Rev. B **81**, 094203 (2010).

[134] K. A. Mäder and A. Zunger, Phys. Rev. B **51**, 10462 (1995).

[135] A. van de Walle and G. Ceder, J. Phase Equilib. **23**, 348 (2002).

[136] T. Lan, X. L. Tang, and B. Fultz, Phys. Rev. B **85**, 094305 (2012).

[137] H. J. C. Berendsen, J. P. M. Postma, W. F. van Gunsteren, A. DiNola, and J. R. Haak, J. Chem. Phys. **81**, 3684 (1984).

[138] H. C. Andersen, J. Chem. Phys. **72**, 2384 (1980).

[139] S. Nosé, J. Chem. Phys. **81**, 511 (1984).

[140] P. M. Morse, Phys. Rev. **34**, 57 (1929).

[141] R. A. Buckingham, Proc. R. Soc. Lond. A. **168**, 264 (1938).

[142] A. C. T. van Duin, S. Dasgupta, F. Lorant, and W. A. Goddard, J. Phys. Chem. A **105**, 9396 (2001).

[143] M. S. Daw and M. I. Baskes, Phys. Rev. Lett. **50**, 1285 (1983).

[144] M. S. Daw and M. I. Baskes, Phys. Rev. B **29**, 6443 (1984).

[145] M. S. Daw, S. M. Foiles, and M. I. Baskes, Mat. Sci. Rep. **9**, 251 (1992).

[146] C. Predescu, R. A. Lippert, M. P. Eastwood, D. Ierardi, H. Xu, M. Ø. Jensen, K. J. Bowers, J. Gullingsrud, C. A. Rendleman, R. O. Dror, and D. E. Shaw, Mol. Phys. **110**, 967 (2012).

[147] R. Car and M. Parrinello, Phys. Rev. Lett. **55**, 2471 (1985).

[148] D. A. McQuarrie, *Statistical mechanics*, University Science Books, Sausalito, CA, 2000.

[149] D. L. Abernathy, M. B. Stone, M. J. Loguillo, M. S. Lucas, O. Delaire, X. Tang, J. Y. Y. Lin, and B. Fultz, Rev. Sci. Instr. **83**, 015114 (2012).

[150] B. N. Brockhouse, Neutron scattering by phonons, in *Phonons in perfect lattices and in lattices with point imperfections*, edited by R. W. H. Stevenson, 1966.

[151] B. Fultz and J. Howe, *Transmission Electron Microscopy and Diffractometry of Materials*, Springer, Berlin, 2012.

[152] G. L. Squires, *Introduction to the theory of thermal neutron scattering*, Dover, Mineola, New York, 2012.

[153] S. Lovesey, *Theory of neutron scattering from condensed matter*, Claredon Press, Oxford, 1984.

[154] L. V. Hove, Phys. Rev. **95**, 249 (1954).

[155] B. Fultz, T. Kelley, J. Lin, J. Lee, O. Delaire, M. Kresch, M. McKerns, and M. Aivazis, Experimental inelastic neutron scattering: Introduction to DANSE, http://docs.danse.us/DrChops/ExperimentalInelasticNeu-tronScattering.pdf, 2009.

[156] M. Kresch, O. Delaire, R. Stevens, J. Y. Y. Lin, and B. Fultz, Phys. Rev. B **75**, 104301 (2007).

[157] M. G. Kresch, *Temperature Dependence of Phonons in Elemental Cubic Metals Studied by Inelastic Scattering of Neutrons and X-Rays*, PhD thesis, California Institute of Technology, 2009.

[158] R. L. Mössbauer, Z. Physik **151**, 124 (1958).

[159] K. S. Singwi and A. Sjölander, Phys. Rev. **120**, 1093 (1960).

[160] W. Sturhahn and V. G. Kohn, Hyperfine Interact. **123/124**, 367 (1999).

[161] S. L. Ruby, J. Phys. **35**, 209 (1974).

[162] M. Seto, Y. Yoda, S. Kikuta, X. W. Zhang, and M. Ando, Phys. Rev. Lett. **74**, 3828 (1995).

[163] W. Sturhahn, T. S. Toellner, E. E. Alp, X. W. Zhang, M. Ando, Y. Yoda, S. Kikuta, M. Seto, C. W. Kimball, and B. Dabrowski, Phys. Rev. Lett. **74**, 3832 (1995).

[164] A. I. Chumakov, R. Rüffer, H. Grünsteudel, H. F. Grünsteudel, G. Grübel, J. Metge, O. Leupold, and H. A. Goodwin, Europhys. Lett. **30**, 427 (1995).

[165] P. Kirkpatrick and A. V. Baez, J. Opt. Soc. Am. **38**, 766 (1948).

[166] A. I. Chumakov and W. Sturhahn, Hyperfine Interact. **123/124**, 781 (1999).

[167] W. Sturhahn and V. G. Kohn, Hyperfine Interact. **125**, 149 (2000).

[168] D. W. Johnson and J. C. H. Spence, J. Phys. D: Appl. Phys. **7**, 771 (1974).

[169] G. D. Garbulsky and G. Ceder, Phys. Rev. B **53**, 8993 (1996).

[170] L. Anthony, L. J. Nagel, J. K. Okamoto, and B. Fultz, Phys. Rev. Lett. **73**, 3034 (1994).

[171] B. Fultz, L. Anthony, J. L. Robertson, R. M. Nicklow, S. Spooner, and M. Mostoller, Phys. Rev. B **52**, 3280 (1995).

[172] B. Fultz, L. Anthony, L. J. Nagel, R. M. Nicklow, and S. Spooner, Phys. Rev. B **52**, 3315 (1995).

[173] L. J. Nagel, L. Anthony, and B. Fultz, Philos. Mag. Lett. **72**, 421 (1995).

[174] L. J. Nagel, L. Anthony, J. K. Okamoto, and B. Fultz, J. Phase Equilib. **18**, 551 (1997).

[175] L. J. Nagel, B. Fultz, and J. L. Robertson, Philos. Mag. B **75**, 681 (1997).

[176] M. E. Manley, B. Fultz, and L. J. Nagel, Philos. Mag. B **80**, 1167 (2000).

[177] M. S. Lucas, J. A. Muñoz, L. Mauger, C. W. Li, A. Sheets, Z. Turgut, J. Horwath, D. L. Abernathy, M. B. Stone, O. Delaire, Y. Xiao, and B. Fultz, J. Appl. Phys. **108**, 023519 (2010).

[178] D. D. Morgan, *Computational studies of alloy phase stability*, PhD thesis, University of California, Berkeley, 1998.

[179] R. Ravelo, J. Aguilar, M. Baskes, J. Angelo, B. Fultz, and B. L. Holian, Phys. Rev. B **57**, 862 (1998).

[180] A. van de Walle, G. Ceder, and U. V. Waghmare, Phys. Rev. Lett. **80**, 4911 (1998).

[181] G. J. Ackland, Vibrational entropy of ordered and disordered alloys, in *Alloy Modeling and Design*, edited by G. M. Stocks and F. E. A. Turchi, 1994.

[182] V. Ozoliņš, C. Wolverton, and A. Zunger, Phys. Rev. B **58**, R5897 (1998).

[183] F. Cleri and V. Rosato, Philos. Mag. Lett. **67**, 421 (1993).

[184] E. J. Wu, *Applications of lattice dynamics theory : calculating vibrational entropy in alloys and dielectric losses in ceramics*, PhD thesis, Massachusetts Institute of Technology, 2002.

[185] L. Shaojun, D. Suquing, and M. Benkun, Phys. Rev. B **58**, 9705 (1998).

[186] J. A. Muñoz, M. S. Lucas, O. Delaire, M. L. Winterrose, L. Mauger, C. W. Li, A. O. Sheets, M. B. Stone, D. L. Abernathy, Y. Xiao, P. Chow, and B. Fultz, Phys. Rev. Lett. **107**, 115501 (2011).

[187] L. J. Nagel, B. Fultz, J. L. Robertson, and S. Spooner, Phys. Rev. B **55**, 2903 (1997).

[188] J. Z. Liu, G. Ghosh, A. van de Walle, and M. Asta, Phys. Rev. B **75**, 114117 (2007).

[189] J. I. Seki, M. Hagiwara, and T. Suzuki, J. Mater. Sci. **14**, 2404 (1979).

[190] J. M. Sanchez, M. C. Cadeville, V. Pierron-Bohnes, and G. Inden, Phys. Rev. B **54**, 8958 (1996).

[191] A. Mustaffa and D. A. Read, J. Magn. Magn. Mater. **5**, 349 (1977).

[192] M. V. Nevitt and A. T. Aldred, J. Appl. Phys. **34**, 463 (1963).

[193] J. C. Krause, J. Schaff, M. I. Costa, and C. Paduani, Phys. Rev. B **61**, 6196 (2000).

[194] M. Shiga and Y. Nakamura, J. Phys. F **8**, 177 (1978).

[195] I. Mirebeau and G. Parette, J. Appl. Phys. **53**, 1960 (1982).

[196] T. Ziller, G. Le Caër, O. Isnard, P. Cénédèse, and B. Fultz, Phys. Rev. B **65**, 024204 (2001).

[197] F. Kajzar, J. Phys. F: Metal Phys. **7**, 1623 (1977).

[198] D. D. Johnson, F. J. Pinski, and J. B. Staunton, J. Appl. Phys. **61**, 3715 (1987).

[199] R. G. Jordan, X. Wang, A. M. Begley, S. L. Qiu, and Y. Liu, Solid State Commun. **78**, 1045 (1991).

[200] V. L. Moruzzi and P. M. Marcus, Phys. Rev. B **45**, 2934 (1992).

[201] J. C. Krause, C. Paduani, J. Schaff, and M. I. Costa, Phys. Rev. B **57**, 857 (1998).

[202] N. S. Yartseva, S. V. Yartsev, N. G. Bebenin, and C. Demangeat, Phys. Rev. B **71**, 144428 (2005).

[203] J. F. Smith, Fe-V phase diagram, http://www1.asminternational.org/AsmEnterprise/APD, 1991.

[204] W. Sturhahn, J. Phys.: Condens. Matter **16**, S497 (2004).

[205] M. L. Lind, *Ultrasonic Investigation of the Elastic Properties and Liquid Fragility of Bulk Metallic Glasses in the Supercooled Liquid Region*, PhD thesis, California Institute of Technology, 2008.

[206] B. E. Warren, *X-ray diffraction*, Addison-Wesley, Menlo Park, CA, 1969.

[207] J. P. Smith, Bull. Alloy Phase Diagrams **5**, 184 (1983).

[208] M. S. Lucas, A. Papandrew, B. Fultz, and M. Y. Hu, Phys. Rev. B **75**, 054307 (2007).

[209] M. S. Lucas, M. Kresch, R. Stevens, and B. Fultz, Phys. Rev. B **77**, 184303 (2008).

[210] C. Jiang, C. Wolverton, J. Sofo, L. Q. Chen, and Z. K. Liu, Phys. Rev. B **69**, 214202 (2004).

[211] F. Birch, Phys. Rev. **71**, 809 (1947).

[212] S. K. Sinha, R. P. Gupta, and D. L. Price, Phys. Rev. Lett. **26**, 1324 (1971).

[213] H. Krakauer, M. Posternak, and A. J. Freeman, Phys. Rev. Lett. **43**, 1885 (1979).

[214] P. Zhang, S. G. Louie, and M. L. Cohen, Phys. Rev. Lett. **94**, 225502 (2005).

[215] W. Ku, T. Berlijn, and C. C. Lee, Phys. Rev. Lett. **104**, 216401 (2010).

[216] J. Lindhard, Det Kgl. Danske Vid. Selskab, Matematisk-fysiske Meddelelser **28, No. 8** (1954).

[217] J. L. Bentley, Commun. ACM **18**, 509 (1975).

[218] M. H. Halloran, J. H. Condon, J. E. Graebner, J. E. Kunzler, and F. S. L. Hsu, Phys. Rev. B **1**, 366 (1970).

[219] C. Lehmann, S. Sinning, P. Zhan, H. Wonn, and I. Mertig, Fermi surface explorer, http://www.physik.tu-dresden.de/∼fermisur/, 2001.

[220] T. S. Choy, J. Naset, J. Chen, S. Hershfield, and C. Stanton, The Fermi surface database, http://www.phys.ufl.edu/fermisurface/, 2007.

[221] T. S. Choy, J. Naset, J. Chen, S. Hershfield, and C. Stanton, Bull. Am. Phys. Soc. **45**, L36 (2000).

[222] W. Koester and W. Gmoehling, Z Metallkd. **51**, 385 (1960).

[223] C. Wolverton and V. Ozoliņš, Phys. Rev. Lett. **86**, 5518 (2001).

[224] K. M. Ho, C. L. Fu, and B. N. Harmon, Phys. Rev. B **28**, 6687 (1983).

[225] P. B. Allen and J. C. K. Hui, Z. Physik B **37**, 33 (1980).

[226] D. C. Wallace, *Statistical physics of crystals and liquids. A guide to highly accurate equations of state*, World Scientific, Singapore, 2002.

[227] J. Bardeen, L. N. Cooper, and J. R. Schrieffer, Phys. Rev. **108**, 1175 (1957).

[228] N. Bock, D. Coffey, and D. C. Wallace, Phys. Rev. B **72**, 155120 (2005).

[229] N. Bock, D. C. Wallace, and D. Coffey, Phys. Rev. B **73**, 075114 (2006).

[230] W. L. McMillan, Phys. Rev. **167**, 331 (1968).

[231] C. H. Cheng, C. T. Wei, and P. A. Beck, Phys. Rev. **120**, 426 (1960).

[232] N. D. Markovskiy, J. A. Muñoz, M. S. Lucas, C. W. Li, O. Delaire, M. B. Stone, D. L. Abernathy, and B. Fultz, Phys. Rev. B **33**, 174301 (2011).

[233] J. M. Ziman, *Principles of the theory of solids*, Cambridge University Press, London, 1964.

[234] P. Bujard, R. Sanjines, E. Walker, J. Ashkenazi, and M. Peter, J. Phys. F **11**, 775 (1981).

[235] L. Huang, M. Ramzan, L. Vitos, B. Johansson, and R. Ahuja, J. Phys. Chem. Solids **71**, 1065 (2010).

[236] B. P. Schweiss, B. Renker, E. Schneider, and W. Reichardt, Phonon spectra of A-15 compounds and ternary molybdenum chalcogenides, in *Superconductivity in d- and f-band metals*, edited by D. H. Douglass, 1976.

[237] V. L. Moruzzi, J. F. Janak, and K. Schwarz, Phys. Rev. B **37**, 790 (1988).

[238] V. J. Minkiewicz, G. Shirane, and R. Nathans, Phys. Rev. **162**, 528 (1967).

[239] R. Colella and B. W. Batterman, Phys. Rev. B **1**, 3913 (1970).

[240] B. M. Powell, P. Martel, and A. D. B. Woods, Phys. Rev. **171**, 727 (1968).

[241] J. Prakash, L. P. Pathak, and M. P. Hemkar, Aust. J. Phys. **28**, 57 (1975).

[242] J. Crangle and W. R. Scott, J. Appl. Phys. **36**, 921 (1965).

[243] S. Mehendale, Y. Girard, V. Repain, C. Chacon, J. Lagoute, S. Rousset, M. Marathe, and S. Narasimhan, Phys. Rev. Lett. **105**, 056101 (2010).

[244] V. Cannella and J. A. Mydosh, Phys. Rev. B **6**, 4220 (1972).

[245] U. Larsen, Phys. Rev. B **18**, 5014 (1978).

[246] K. C. Zhang, Y. F. Li, G. B. Liu, and Y. Zhu, Phys. Lett. A **376**, 1898 (2012).

[247] M. Chen, S. Yamamuro, D. Farrell, and S. A. Majetich, J. Appl. Phys. **93**, 7551 (2003).

[248] I.-C. Chiang and D.-H. Chen, Adv. Func. Mater. **17**, 1311 (2007).

[249] H. L. Liu, J. H. Wu, J. H. Min, and Y. K. Kim, J. Appl. Phys. **103**, 07D529 (2008).

[250] H. Liu, P. Hou, W. Zhang, Y. K. Kim, and J. Wu, Nanotechnology **21**, 335602 (2010).

[251] Y.-N. Wu, D.-H. Chen, X.-Y. Shi, C.-C. Lian, T.-Y. Wang, C.-S. Yeh, K. R. Ratinac, P. Thordarson, F. Braet, and D.-B. Shieh, Nanomed: Nanotechnol **7**, 420 (2011).

[252] E. E. Connor, J. Mwamuka, C. J. M. Anand Gole, and M. D. Wyatt, Small **1**, 325 (2005).

[253] B. H. de Mayo, J. Phys. Chem. Solids **35**, 1525 (1974).

[254] M. Bienzle, T. Oishi, and F. Sommer, J. Alloys Compd. **220**, 182 (1995).

[255] C. Wolverton and A. Zunger, Comput. Mater. Sci. **8**, 107 (1997).

[256] C. Colinet, J. Eymery, A. Pasturel, A. T. Paxton, and M. van Schilfgaarde, J. Phys.: Condens. Matter. **6**, L47 (1994).

[257] R. Tetot and A. Finel, The Gaussian Cluster Variation Method and its Application to The Thermodynamics of Transition Metals, in *Stability of Materials*, edited by A. Gonis, P. Turchi, and J. Kudrnovsky, volume 355 of *NATO ASI Series*, page 197, Springer, 1996.

[258] M. Asta and S. M. Foiles, Phys. Rev. B **53**, 2389 (1996).

[259] J. R. Clinton, E. H. Tyler, and H. L. Luo, J. Phys. F: Met. Phys. **4**, 1162 (1974).

[260] R. A. Oriani, Acta Metall. **3**, 232 (1955).

[261] J. M. Sanchez, J. P. Stark, and V. L. Moruzzi, Phys. Rev. B **44**, 5411 (1991).

[262] T. L. Swan-Wood, O. Delaire, and B. Fultz, Phys. Rev. B **72**, 024305 (2005).

[263] O. Delaire, T. L. Swan-Wood, and B. Fultz, Phys. Rev. Lett. **93**, 185704 (2004).

[264] P. D. Bogdanoff, B. Fultz, and S. Rosenkranz, Phys. Rev. B **65**, 014303 (2001).

[265] P. D. Bogdanoff, T. L. Swan-Wood, and B. Fultz, Phys. Rev. B **68**, 014301 (2003).

[266] D. G. Howard and R. H. Nussbaum, Phys. Rev. B **9**, 794 (1974).

[267] P. Mannheim, Phys. Rev. **165**, 1011 (1968).

[268] B. R. Cuenya, W. Keune, R. Peters, E. Schuster, B. Sahoo, U. von Hörsten, W. Sturhahn, J. Zhao, T. S. Toellner, E. E. Alp, and S. D. Bader, Phys. Rev. B **77**, 165410 (2008).

[269] E. E. Alp, W. Sturhahn, and T. S. Toellner, Hyperfine Interact. **135**, 295 (2001).

[270] B. R. Cuenya, L. K. Ono, J. R. Croy, A. Naitabdi, H. Heinrich, J. Zhao, E. E. Alp, W. Sturhahn, and W. Keune, Appl. Phys. Lett. **95**, 143103 (2009).

[271] J. A. Muñoz, M. S. Lucas, L. Mauger, I. Halevy, J. Horwath, S. L. Semiatin, Y. Xiao, P. Chow, M. B. Stone, D. L. Abernathy, and B. Fultz, Phys. Rev. B **87**, 014301 (2013).

[272] E. Raub and P. Walter, Z. Metallk. **41**, 234 (1950).

[273] W. B. Pearson, *A Handbook of Lattice Spacings and Structures of Metals and Alloys*, Pergamon Press, New York, 1958.

[274] E. R. Jette, W. L. Bruner, and F. Foote, Trans. A. I. M. M. E. **111**, 354 (1934).

[275] H. Okamoto, T. B. Massalski, L. J. Swartzendruber, and P. A. Beck, Fe-Au, http://www1.asminternational.org/ AsmEnterprise/APD, 1990.

[276] B. Window, Phys. Rev. B **6**, 2013 (1972).

[277] M. S. Lucas, L. Mauger, J. A. Muñoz, Y. Xiao, A. O. Sheets, S. L. Semiatin, J. Horwath, and Z. Turgut, J. Appl. Phys. **109**, 07E307 (2011).

[278] M. S. Lucas, L. Mauger, J. A. Muñoz, I. Halevy, J. Horwath, S. L. Semiatin, M. B. Stone, D. L. Abernathy, Y. Xiao, P. Chow, and B. Fultz, J. Appl. Phys. **113**, 17A308 (2013).

[279] Y. Tsunoda, Y. Kurimoto, M. Seto, S. Kitao, and Y. Yoda, Phys. Rev. B **66**, 214304 (2002).

[280] T. Tanaka, A. Tajima, R. Moriizumi, C. Oshima, Y. Tsunoda, M. Seto, S. Kitao, and T. Mitsui, J. Phys. Soc. Jpn. **74**, 1762 (2005).

[281] J. Zarestky and C. Stassis, Phys. Rev. B **35**, 4500 (1987).

[282] J. W. Lynn, H. G. Smith, and R. M. Nicklow, Phys. Rev. B **8**, 3493 (1973).

[283] B. Grabowski, T. Hickel, and J. Neugenbauer, Phys. Rev. B **76**, 024309 (2007).

[284] A. Togo, F. Oba, and I. Tanaka, Phys. Rev. B **78**, 134106 (2008).

[285] A. A. Quong, Phys. Rev. B **49**, 3226 (1993).

[286] E. A. Brandes and G. B. Brook, editors, *Smithells Metals Reference Book*, Butterworth-Heinemann Ltd., Oxford, 1992.

[287] W. A. Harrison and S. Froyen, Phys. Rev. B **21**, 3214 (1980).

[288] N. W. Ashcroft, Phys. Lett. **23**, 48 (1966).

[289] J. Friedel, Transition metals: Electronic structure of the d-band, in *The Physics of Metals*, edited by J. M. Ziman, 1969.

[290] J. Creuze, F. Berthier, R. Tétot, B. Legrand, and G. Tréglia, Phys. Rev. B **61**, 14470 (2000).

[291] V. Ozoliņš, C. Wolverton, and A. Zunger, Phys. Rev. B **57**, 6427 (1998).

[292] M. Seto, Y. Kobayashi, S. Kitao, R. Haruki, T. Mitsui, Y. Yoda, S. Nasu, and S. Kikuta, Phys. Rev. B **61**, 11420 (2000).

[293] M. S. Lucas, personal communication, 2012.

[294] J. Yamashita and S. Asano, Prog. Theor. Phys. **48**, 2129 (1972).

[295] D. A. Papaconstantopoulos and D. J. Nagel, Int. J. Quantum Chem. **S5**, 515 (1972).

[296] D. A. Papaconstantopoulos, Phys. Rev. B **11**, 4801 (1975).

[297] G. N. Kamm, Phys. Rev. B **12**, 3013 (1975).

[298] E. A. Starke, C. H. Cheng, and P. A. Beck, Phys. Rev. **126**, 1746 (1962).

[299] E. V. Mielczarek and W. Winfree, Phys. Rev. B **11**, 1026 (1975).

[300] E. Källne, J. Phys. F **4**, 167 (1974).

[301] J. H. Weaver and D. T. Peterson, Phys. Rev. B **22**, 3624 (1980).

[302] W. J. Buehler and R. C. Wiley, Trans. Am. Soc. Met. **55**, 268 (1962).

[303] F. E. Wang, W. J. Buehler, and S. J. Pickart, J. Appl. Phys. **36**, 3232 (1965).

[304] R. Eibler, J. Redinger, and A. Neckel, J. Phys. F: Met. Phys. **17**, 1533 (1987).

[305] A. Kellou, Z. Nabi, A. Tadjer, N. Amrane, N. Fenineche, and H. Aourag, Phys. Stat. Sol. (b) **239**, 389 (2003).

[306] J. J. Reilly and R. H. Wiswall, Inorg. Chem. **13**, 218 (1974).

[307] O. Eriksson, J. M. Wills, and D. Wallace, Phys. Rev. B **46**, 5221 (1992).

[308] G. Grimvall, M. Thiessen, and A. Fernandez-Guillermet, Phys. Rev. B **36**, 7816 (1987).

[309] A. Fernandez-Guillermet and G. Grimvall, Phys. Rev. B **44**, 4332 (1991).

[310] J. Trampenau, W. Petry, and C. Herzig, Phys. Rev. B **47**, 3132 (1993).

[311] A. Heiming, W. Petry, J. Trampenau, M. Alba, C. Herzig, H. R. Schober, and G. Vogl, Phys. Rev. B **43**, 10933 (1991).

[312] A. Heiming, W. Petry, J. Trampenau, M. Alba, C. Herzig, H. R. Schober, and G. Vogl, Phys. Rev. B **43**, 10948 (1991).

[313] H. Ohtani, N. Hanaya, M. Hasebe, S. I. Teraoka, and M. Abe, CALPHAD: Comput. Coupling Phase Diagrams Thermochem. **30**, 147 (2006).

[314] H. K. Mao, J. Xu, V. V. Struzhkin, J. Shu, R. J. Hemley, W. Sturhahn, M. Y. Hu, E. E. Alp, L. Vodadlo, D. Alfè, G. D. Price, M. J. Gillan, M. Schwoerer-Böhning, D. Häusermann, P. Eng, G. Shen, H. Giefers, R. Lübbers, and G. Wortmann, Science **292**, 914 (2001).

[315] R. A. Forman, G. J. Piermarini, J. D. Barnett, and S. Block, Science **176**, 284 (1972).

[316] L. Merrill and W. A. Bassett, Rev. Sci. Instrum. **45**, 290 (1974).

[317] E. Sterer, M. P. Pasternak, and R. D. Taylor, Rev. Sci. Instrum. **61**, 1117 (1990).

[318] C. Stassis, D. Arch, B. N. Harmon, and N. Wakabayashi, Phys Rev. B **19**, 181 (1979).

[319] L. F. Zhu, M. Friák, A. Dick, B. Grabowski, T. Hickel, F. Liot, D. Holec, A. Schlieter, U. Kün, J. Eckert, Z. Ebrahumi, H. Emmerich, and J. Neugebauer, Acta Mater. **60**, 1594 (2012).

[320] U. Buchenau, H. R. Schober, J.-M. Welter, G. Arnold, and R. Wagner, Phys. Rev. B **27**, 955 (1983).

[321] J. Liebertz, S. Stähr, and S. Haussühl, Krist. Tech. **15**, 1257 (1980).

[322] D. B. Sirdeshmukh, L. Sirdeshmukh, and K. G. Subhadra, *Micro- and macro-properties of solids*, Springer, Berlin, 2006.

[323] K. Ikeda, T. Nakamichi, and M. Yamamoto, J. Phys. Soc. Jpn. **37**, 652 (1974).

[324] P. Gillet, P. Richet, F. Guyot, and G. Fiquet, J. Geophys. Res. **96**, 11805 (1991).

[325] M. Kresch, M. Lucas, O. Delaire, J. Y. Y. Lin, and B. Fultz, Phys. Rev. B **77**, 024301 (2008).

[326] W. Petry, A. Heiming, J. Trampenau, M. Alba, C. Herzig, H. R. Schober, and G. Vogl, Phys. Rev. B **43**, 10933 (1991).

[327] J. Trampenau, A. Heiming, W. Petry, M. Alba, C. Herzig, W. Miekeley, and H. R. Schrober, Phys. Rev. B **43**, 10963 (1991).

[328] M. M. McKerns, L. Strand, T. Sullivan, A. Fang, and M. A. G. Aivazis, Building a framework for predictive science, in *Proceedings of the 10th Python in Science Conference*, edited by S. van der Walt and J. Millman, 2011.

[329] L. Mauger, M. S. Lucas, J. A. Muñoz, S. J. Tracy, M. Kresch, and B. Fultz, in preparation.

[330] M. V. Nevitt, J. Appl. Phys. **31**, 155 (1960).

[331] J. Eckert, L. Schultz, and K. Urban, J. Non-Crys. Solids **127**, 90 (1991).

[332] K.-M. Ho, C. L. Fu, B. N. Harmon, W. Weber, and D. R. Hamman, Phys. Rev. Lett. **49**, 673 (1982).

[333] I. Calizo, A. A. Baladin, W. Bao, F. Miao, and C. N. Lau, Phys. Rev. Lett. **93**, 185503 (2004).

[334] X. Huang, C. Bungaro, V. Godlevsky, and K. M. Rabe, Phys. Rev. B **65**, 014108 (2001).

[335] R. D. King-Smith, M. C. Payne, and J. S. Lin, Phys. Rev. B **44**, 13063 (1991).

[336] M. L. Winterrose, M. S. Lucas, A. F. Yue, I. Halevy, L. Mauger, J. A. Muñoz, J. Hu, M. Lerche, and B. Fultz, Phys. Rev. Lett. **102**, 237202 (2009).

[337] M. L. Winterrose, L. Mauger, I. Halevy, A. F. Yue, M. S. Lucas, J. A. Muñoz, H. Tan, Y. Xiao, P. Chow, W. Sturhahn, T. S. Toellner, E. E. Alp, and B. Fultz, Phys. Rev. B **83**, 134304 (2011).

[338] W. Jauch and M. Reehuis, Phys. Rev. B **73**, 085102 (2006).

[339] W. Jauch and M. Reehuis, Phys. Rev. B **76**, 235121 (2007).

[340] M. V. Nevitt, Alloy chemistry, in *Electronic structure and alloy chemistry of the transition elements*, edited by P. A. Beck, 1963.